

# **Advanced chemical and structural Characterization of Nuclear Waste Materials related to the Nuclear Fuel Cycle**

Zur Erlangung des akademischen Grades eines

DOKTORS DER NATURWISSENSCHAFTEN

(Dr. rer. nat.)

der Fakultät für Chemie und Biowissenschaften

des Karlsruher Instituts für Technologie (KIT)

genehmigte

DISSERTATION

von

Dipl.-Chem. Sebastian Peter Bahl

aus

Kirchheimbolanden

KIT-Dekan: Prof. Dr. Willem Klopper

Referent: Dr. Tonya Vitova (KIT Associate Fellow)

Korreferent: Prof. Dr. Horst Geckeis

Tag der mündlichen Prüfung: 28.04.2017



This document is licensed under the Creative Commons Attribution – ShareAlike 4.0 License (CC BY-SA 4.0): <https://creativecommons.org/licenses/by-sa/4.0/deed.de>

*Meinem Vater und meiner Mutter*



# Erklärung

Hiermit erkläre ich wahrheitsgemäß, dass diese Arbeit im Rahmen der Betreuung durch Prof. Dr. Horst Geckeis selbstständig von mir verfasst wurde, keine anderen als die angegebenen Quellen und Hilfsmittel verwendet, die wörtlich oder inhaltlich übernommenen Stellen als solche kenntlich gemacht sowie die Regeln zur Sicherung guter wissenschaftlicher Praxis des Karlsruher Instituts für Technologie (KIT) beachtet wurden, die elektronische Version der Arbeit mit der schriftlichen übereinstimmt und die Abgabe und Archivierung der Primärdaten gemäß Abs. A (6) der Regeln zur Sicherung guter wissenschaftlicher Praxis des KIT beim Institut gesichert ist.

Karlsruhe, 04.11.2017



# Abstract

This dissertation reports structural and speciation investigations of simulated and genuine nuclear wastes. Chapters 4 and 5 emphasize on the very first application of the bulk U, Np and Pu  $M_{4,5}$  absorption edge high-energy resolution X-ray absorption near edge structure (HR-XANES) method for characterization of U, Np and Pu oxidation states in model and genuine nuclear waste glasses and spent nuclear fuel (SNF). Chapters 6 and 7 address volatilization and precipitation challenges occurring during vitrification of fission products (FP) like Cs, Tc, Ru and Pd. Various approaches are discussed and potential solutions are proposed.

Chapter 4.1 describes the results from the studies of Pu doped borosilicate glasses. Pu(III), Pu(IV) and Pu(VI) are for the first time characterized simultaneously present in a borosilicate glass using Pu  $M_5$  edge HR-XANES. It is illustrated that the method can be very efficiently used to determine Pu oxidation states which control the solubility limit of Pu in a glass matrix. HR-XANES results show that the addition of excess  $Si_3N_4$  is not sufficient for complete reduction of Pu to Pu(III) which has a relatively high solubility limit (10-25 wt%  $PuO_2$ ) due to its network-modifying behavior in glasses. It is provided evidences that the initially added Pu(VI) is partly preserved during vitrification at 1200/1400 °C in Ar atmosphere. Pu(VI) could be very advantageous for immobilization of Pu rich wastes since from U(VI) vitrification a possible glass solubility limit of up to 40 wt% can be deduced.

Chapter 4.2 reports the characterization and the structural differences between U, Np and Pu doped model and genuine nuclear waste glasses. The U, Np and Pu  $M_{4,5}$  edge HR-XANES reveals predominant U(VI) and Pu(IV) species in all glasses. But ordered structures involving U, O and likely Si are found only in the genuine waste glass by U  $L_3$  EXAFS analyses. Strong synchrotron X-ray induced radiation damage leading to reduction of U(VI) to U(IV) is detected also only for the genuine waste glass by U  $M_4$  HR-XANES. This effect might be related to differences in the radioactivity and/or the local atomic U environments in the model and the waste glasses. It might be explained with transfer of electronic charge to U from binding ligands and/or free charges as well as possible U reactions with radicals or charged species. Such reduction of U and potentially other *An* elements might be inducible by  $\alpha$ ,  $\beta$  and/or  $\gamma$  irradiation processes on a long-time scale and are hence of relevance for the *An* speciation in HLW glasses stored in an underground repository.

Chapter 5 discusses the speciation of U and Pu in commercial and special irradiated high burn-up SNF samples as well as of unirradiated  $UO_2$  reference materials. The bulk sensitivity of the *An*  $M_{4,5}$  edge HR-XANES technique is unambiguously demonstrated, whereas X-ray

photoelectron spectroscopy (XPS) is sensitive only to species formed on the surface. The U  $M_{4,5}$  HR-XANES method can clearly distinguish between U(IV) and U(V) as well as Pu(IV) and Pu(V)/Pu(VI), which is not always possible with the conventional U and Pu  $L_3$  XANES. U(IV) and U(V) likely in the form of  $U_4O_9$  are found in the two commercial SNF samples. It is shown that the U oxidation continues in ambient conditions as a function of time due to the small particle size of the samples. No phase transformation from  $UO_2$  to  $U_3O_8$  or  $UO_3$  is observed for any of the studied SNF samples. The special irradiated high burn-up sample stored in atmosphere with ca. 1%  $O_2$  for 20 years has only very minor amount of U(V) which illustrates its high stability against oxidation being advantageous in case of a potential cladding failure scenario for example in extended interim storage. For the first time it is demonstrated that along Pu(IV) also Pu(VI) is present in the bulk of presumably all SNF samples. This Pu(VI) is unlikely formed by oxidation in air but rather is a result of the neutron absorption and subsequent nuclear reactions.

Chapter 6 reports studies of HLW residual materials from a reprocessing and a vitrification plant. They are simulated and the formed compounds are characterized as well as possible host matrices for their immobilization are reviewed. The challenge of Cs and Tc volatilization loss is addressed by careful selection of immobilization processes, i.e., addition of reducing agent and application of host matrices with low melting temperature. A selection of suitable immobilization materials is made with regard to minimized FP volatilization behavior. Potential leaching performance is discussed considering composition and macroscopic appearance of the synthesized samples.

Chapter 7 presents insights obtained from the X-ray CT *in-situ* study of a vitrification process with emphasize on the precipitation of noble metal particles (NMP) which are known to cause severe problems in industrial vitrification processes in form of drain plugging and short-circuits. Results indicate the formation of the particles at 600-700 °C in the lower part of the cold-cap. An exceptional large precipitated specie is observed and described. Its formation might have an impact on the NMPs sedimentation behavior. For the first time, *in-situ* tracking of their movement in a glass melt is reported. The designed setup has the potential to unambiguously reveal the highly debated NMP sedimentation mechanism. Two counter-measures on the particles formation are tested. The use of glass powder instead of glass beads and the addition of 1 wt% Si as reducing agent decreased the NMP precipitation by 40% and 30%, respectively, and simultaneously retain Re used as a surrogate of Tc by a factor of 2-3.

# Zusammenfassung

Die vorliegende Dissertation beschreibt makroskopische und mikroskopische Untersuchungen von simulierten und tatsächlichen radioaktiven Abfallformen mit dem Ziel zu deren sicherer Zwischen- und Endlagerung beizutragen.

Dabei konzentriert sich der erste Teil der Arbeit auf die erstmalige Anwendung einer synchrotronbasierten Röntgenabsorptionsspektroskopie mit hoher Energieauflösung (HR-XANES) zur Aufklärung von U, Np und Pu Oxidationszuständen und deren lokaler Umgebungsstruktur in simulierten und tatsächlichen radioaktiven Abfallgläsern sowie in abgebranntem Kernbrennstoff. Mithilfe der beschriebenen Methode wird dabei in einem hochdotierten Pu Borosilikatglas-System zum ersten Mal die simultane Präsenz von Pu(III), Pu(IV) und Pu(VI) nachgewiesen. Der Einfluss des eingesetzten Reduktionsmittels auf die Pu Speziation wird diskutiert und deren Relevanz auf die Pu Löslichkeitsgrenze in Glas wird hervorgehoben. Mittels HR-XANES Untersuchungen an einem radioaktiven Abfallglas aus der Produktion einer industriellen Verglasungsanlage, werden die Actiniden U und Pu überwiegend in ihren hexa- bzw. tetravalenten Oxidationsstufen identifiziert, wohingegen Np vermutlich als Mischung seiner tetra- und pentavalenten Spezies vorliegt. Bei den Analysen wird ein durch die synchrotronbasierte Röntgenstrahlung induzierter, signifikanter U Reduktionsprozess beobachtet. Dieser kann auf die ausgeprägte radioaktive Natur des Materials zurückgeführt werden. Es wird vermutet, dass dieser Effekt eine Relevanz für die Langzeit-Actinidenspeziation in Abfallgläsern besitzt.

Der zweite Teil der Arbeit beschäftigt sich mit Herausforderungen, die bei der Verglasung von Spaltproduktlösungen auftreten. So wurden im Zuge der Reststoffproblematik in einer Wiederaufarbeitungs- und Verglasungsanlage mögliche Reststoffe simuliert, identifiziert sowie verschiedene Herangehensweisen zu deren Immobilisierung vorgeschlagen und auf ihre Tauglichkeit hin überprüft. Kriterien hierbei sind die Flüchtigkeit der Spaltprodukte Cs und Tc, sowie die Eignung der Immobilisierungsprodukte zur Endlagerung aufgrund einer ausreichenden Korrosionsbeständigkeit.

Zuletzt wird der Einsatz einer neuartigen *in-situ* Röntgentomographie-Methode zur Aufklärung von Bildungs- und Sedimentationsprozessen von Edelmetallpartikeln demonstriert. Diese Partikel, die bei der Verglasung von Flüssigabfällen aus der Wiederaufbereitung von abgebranntem Kernbrennstoff auftreten, sind in der Lage, schwerwiegende Probleme bei der Prozessführung zu verursachen. Zwei erfolgsversprechende Maßnahmen, die die Bildung dieser Partikel reduzieren, konnten zielführend getestet werden.



# Acknowledgements

Zu allererst gilt mein Dank Herrn Prof. Geckeis für das entgegengebrachte Vertrauen, die Unterstützung und die Möglichkeit, meine Promotion am INE anzufertigen. Meiner Betreuerin Tonya Vitova bin ich sehr dankbar für die intensive jahrelange Betreuung und ihr enormes Engagement für die Gruppe und jeden Einzelnen. Den Doktoranden des INE danke ich sehr für den guten Zusammenhalt und die Unterstützung untereinander. Zusammen mit den restlichen Kollegen haben sie eine sehr angenehme Arbeitsatmosphäre im Hause geschaffen. Die kurzen Dienstwege und der familiäre Umgang im INE habe ich immer sehr zu schätzen gewusst. Besonders hervorheben möchte ich diesbezüglich die gute Zusammenarbeit und das besondere Engagement von Elke Bohnert für unsere Gruppe. Der Analytik-Gruppe des INE danke ich für ihre freundliche, kompetente und effektive Arbeitsweise. Für die außerordentlich große Unterstützung bei Synchrotron-Messzeiten möchte ich sowohl dem Team um Kathy Dardenne und Jörg Rothe recht herzlich danken, als auch den Kollegen aus der Arbeitsgruppe, Tim Prüßmann und Ivan Pidchenko.

Insbesondere möchte ich mich bei Günther Roth bedanken, der immer und überall ein offenes Ohr für mich und meine Anliegen hatte und keine Gelegenheit ausließ mich zu fördern. Es war stets eine große Bereicherung für mich aus dem enormen Erfahrungsschatz von Herrn Roth und Herrn Weiseburger zu schöpfen, den sie bereitwillig mit mir teilten.

Mein Dank gilt ebenso allen Menschen, die sich Zeit genommen haben und mich bei der Korrektur meiner Dissertation unterstützten (Kai, Carmen, Ayla, Franzi, Barbara, Julian, Meike, Alex, Lotti, Herr Kienzler, Ernesto, V. Rondinella, F. Cappia, Herr Weisenburger)

Frau Monika Becker bin ich sehr dankbar für all die Privilegien, die sie mir in der Fachbibliothek Chemie hat zukommen lassen. Meinen Leidensgenossen Ayla und Jörg danke ich für die gemeinsame Zeit der letzten Monate und ihre umfangreiche Unterstützung und Ablenkung.

Großen Dank schulde ich ebenfalls allen Kooperationspartnern und Mitarbeitern, die bereit waren, gemeinsame Projekte zu initiieren und Proben für mich zu präparieren. Ohne sie wäre meine Arbeit so nicht zustande gekommen. Zu nennen sind insbesondere Ernesto, N. Müller, M. Herm, E. Bohnert, JRC-Karlsruhe (J. Somers, C. Boshoven, F. Cappia, F. Mairead, K. Popa), ESRF (K. Kvashnina), UAIC (M. Ignat), CEA Marcoule (S. Peugeot, P. Jollivet, P. Chevreux, A. Laplace, J. Delrieu) und TIT Tokyo (Prof. Yano, T. Kishi, Takuma, Shinya, Tsutaru). Außerdem danke ich den Studenten Veronika Koldeisz, Paul Estevenon und Aaron Beck für ihre Unterstützung meines Projekts. Die Zusammenarbeit hat mir stets Freude bereitet.

Ich bedanke mich auch sehr herzlich bei der KTE GmbH und im Besonderen bei Marco Klipfel für die angeregten Diskussionen und den Austausch von Daten und Erkenntnissen im Rahmen der Reststoffproblematik.

Herrn Akira Sakai möchte ich für das sehr herzliche Verhältnis und die unvergessene Zeit in Japan danken. Dem Karlsruhe House of Young Scientists (KHYS) danke ich für die Förderung meines Auslandsaufenthalts.

Zuletzt, und das von ganzem Herzen, möchte ich mich bei meinen guten Freunden und meiner Familie bedanken, die mich in dieser besonders schweren Zeit begleitet und mir unendlich viel Geduld entgegengebracht haben. Ohne sie wäre ich diesen Weg nicht gegangen. Im Besonderen Denis, Carmen und Nadine, die mich schon so lange begleiten, waren immer für mich da und haben mir Kraft gegeben. Danke!

# Table of Content

1.	Introduction and aims .....	1
2.	Background .....	5
2.1.	Disposal of high-level radioactive wastes (HLW) .....	5
2.1.1.	Direct disposal of spent nuclear fuel (SNF) .....	6
2.1.1.1.	Composition of SNF .....	6
2.1.1.2.	Evolution of SNF.....	7
2.1.1.3.	SNF behavior in repository conditions .....	8
2.1.2.	Disposal of vitrified waste from spent nuclear fuel (SNF) reprocessing.....	10
2.1.2.1.	Glasses as host matrix for nuclear waste immobilization .....	10
2.1.2.2.	Glass structure and immobilization mechanisms .....	13
2.1.2.3.	Vitrification technology.....	15
2.1.2.4.	Waste glasses in repository conditions.....	17
2.2.	Fundamental principles of X-ray absorption and X-ray emission spectroscopy.....	19
2.2.1.	X-ray absorption spectroscopy (XAS) .....	19
2.2.2.	Resonant inelastic X-ray scattering (RIXS) and high-energy resolution near edge structure (HR-XANES) technique .....	23
2.2.3.	General setup and X-ray emission spectrometer .....	30
3.	Experimental section.....	35
4.	Actinide (An) characterization in a Pu rich and genuine nuclear waste glass.....	41
4.1.	Pu rich borosilicate glass.....	41
4.1.1.	Experimental.....	43
4.1.2.	Results .....	46
4.1.3.	Discussion.....	51
4.1.4.	Conclusion .....	54
4.2.	Genuine nuclear waste glass.....	54
4.2.1.	Experimental.....	57
4.2.2.	Results .....	62
4.2.3.	Discussion.....	75
4.2.4.	Summary and Conclusion.....	77
5.	Actinide (An) oxidation states investigations of spent nuclear fuel (SNF) .....	79
5.1.	Experimental.....	86
5.2.	Results and Discussion .....	90

5.3. Summary and Conclusion .....	99
6. Simulation and vitrification of solid high-level waste (HLW) residuals remaining from reprocessing and vitrification activities .....	101
6.1. Mo and Cs rich residuals from reprocessing .....	102
6.1.1. Experimental.....	104
6.1.2. Results and Discussion.....	107
6.1.3. Conclusion.....	113
6.2. Tc and Cs rich residuals from vitrification .....	114
6.2.1. Experimental.....	116
6.2.2. Results .....	120
6.2.3. Discussion .....	127
6.2.4. Immobilization.....	129
6.2.4.1. Ba rich borosilicate glass at 950 °C .....	129
6.2.4.2. Alternative approaches .....	135
7. In-situ observation of noble metal particle (NMP) formation and their fate in a borosilicate melt .....	145
7.1. Experimental.....	149
7.2. Results .....	156
7.3. Discussion .....	165
7.4. Conclusion.....	171
8. Summary and Outlook.....	172
Appendix .....	177
List of Tables and Figures .....	191
List of Symbols and Abbreviations.....	201
List of Publications and Contributions.....	203
Curriculum Vitae.....	205
List of References.....	207

## 1. Introduction and aims

Detailed characterization of the mechanical, physical and chemical properties of nuclear waste is essential to understand how it interacts with the environment. Almost all high-level radioactive waste (HLW) is present as either vitrified waste from reprocessing residues or spent nuclear fuel. Such waste forms account for approximately 95% of the total radioactivity produced in the process of electricity generation,<sup>1, 2</sup> emphasizing the necessity for extensive knowledge about their properties and behavior in storage conditions.

Most disposal strategies envisage disposal of nuclear waste in a deep geological rock formation comprising a multi-barrier system in which the waste matrix is the innermost barrier.<sup>3</sup> In case of ground water intrusion the waste will come to contact with water and potential corrosion, dissolution and precipitation processes will be initiated. The release of toxic radionuclides depends mainly on the nature of the waste material and the given leaching conditions (cf. **Section 2.1**). Due to their long half-life and their  $\alpha$ -radiotoxicity the actinide elements (*An*) are of great concern with respect to their intermediate storage and disposal for thousands of years.

The use of advanced sensitive techniques enables comprehensive characterization of waste materials. Standard laboratory based microscopic and spectroscopic techniques such as light and electron microscopy, Raman spectroscopy, Infrared spectroscopy (IR), ultraviolet-visible spectroscopy (UV-Vis), X-ray diffraction (XRD), inductively coupled plasma atomic absorption and emission spectroscopy (ICP-AAS/OES) and mass spectroscopy (MS) provide a solid base for macroscopic and microscopic characterization of HLW materials. Their potential for speciation analyses, especially for amorphous matrices such as waste glass, is however limited. Precise characterization of the *An*'s oxidation states in the waste forms is of importance for predicting their properties, evolution and finally the interaction with the environment.<sup>4</sup> The X-ray photoelectron spectroscopy (XPS) spectroscopy is often applied since it is able to identify the oxidation states of the *An* elements. However, requirements such as vacuum conditions and a clean sample surface are prerequisites for this method which cannot be always fulfilled for radioactive materials. In addition, only the surface of the material is probed with a maximum depth of 10 nm. This part of the sample is not necessarily representative for the bulk of the probed material.

Synchrotron-based techniques are well suited for investigations of HLW materials.<sup>5</sup> XANES and EXAFS spectroscopy methods enable the electronic and structural characterization of the elements of interest. They are sensitive to the local atomic environment of the absorbing atom

and do not require long range order in the material as for example X-ray diffraction. Heterogeneous materials can be investigated with high spatial resolution by combining spectroscopy and microscopy. The X-ray absorption (XAS) techniques are described in detail in **Section 2.2**.

The  $An M_{4,5}$  HR-XANES technique has not been yet extensively applied for speciation investigations of  $An$  elements. This bulk method has high sensitivity to minor contributions of several  $An$  oxidation states present in the same material.<sup>6</sup> Herein, it has been used for the first time for characterization of three different Pu oxidation states mixed in the same glass. The experiments are performed in a He atmosphere and ambient pressure; no special sample preparation is required. These advantages make the technique a valuable tool for oxidation states characterization of  $An$  elements being constituents of HLW materials (cf. **Section 4** and **5**).

In the context of HLW conditioning several other challenges can be addressed using microscopic and spectroscopic techniques. X-ray radiation is used for generation of 3D tomographic images. Prof. T. Yano from TIT University, Tokyo, developed a setup enabling the *in-situ* observation of a vitrification process.<sup>7</sup> This tool is applied to trace formation and sedimentation of platinum group metals (PGM) in molten borosilicate glass (cf. **Section 7**). As most waste streams contain considerable amounts of PGMs they are of great concern when vitrifying high level liquid waste (HLLW) generated during spent nuclear fuel (SNF) reprocessing in a Joule-heated ceramic melter (JHCM).<sup>8</sup> They form immiscible separated phases in the glass melt depositing on the bottom of the glass pool where they form a highly viscous sludge causing severe processing problems. The deposits can plug the melters' drains and interfere with the heating mechanism which leads in the worst case to an outage of the vitrification facility. The formation and deposition mechanisms of the PGM particles in the glass melters are not yet understood and still debated.<sup>9</sup>

Another object of concern in industrial vitrification processes are volatile fission product (FP) elements such as Cs and Tc. They are released from the glass melt and accumulate in the exhaust process components as for example in the *Reprocessing and Vitrification Facility Karlsruhe* (WAK and VEK).<sup>10</sup> Both Cs and Tc represent a predominant part of the radioactivity of the collected residual waste stemming mainly from scrubbing solution concentrates. A second type of material has also remained from the reprocessing activities of the WAK. Mo, Cs and Zr rich precipitates are deposited on the bottom of HLLW storage tanks exhibiting enormous radioactivity contents. The analysis and handling of this residual material is a challenge for the upcoming decontamination and dismantling activities of the facility due to

the intense radiation fields. Tailored conditioning strategies have to be developed for their safe and reliable immobilization (cf. **Section 6**).

The main aims of this doctoral project are:

- 1) To develop and demonstrate the feasibility of an experimental procedure for the preparation of HLW samples and their investigation by *An* M<sub>4,5</sub> edge HR-XANES and *An* L<sub>3</sub> edge EXAFS spectroscopy techniques (cf. **Section 4.1.1, 4.2.1** and **5.1**).
- 2) To characterize genuine HLW materials from industrial processes such as SNF and nuclear waste glass with regard to the *An* speciation, e.g., the U, Pu and Np oxidation states and local atomic structure with emphasis on the application of the *An* M<sub>4,5</sub> edge HR-XANES technique; to prepare reference systems like series of UO<sub>2</sub> samples and U and Pu doped model glasses with the same base glass composition as a genuine nuclear waste and to compare their structural properties with the complex system. The relevance of the obtained results for conditioning, storage and disposal of HLW will be discussed (cf. **Section** ).
- 3) To simulate and characterize residual materials from industrial reprocessing and vitrification processes. Suitable immobilization conditions for retention of the volatile Cs and Tc will be considered and experimentally reviewed (cf. **Section 6**).
- 4) To investigate the formation and sedimentation behavior of PGM particles in a liquid glass melt by X-ray CT and other techniques. Based on the results several countermeasures will be experimentally reviewed (cf. **Section 7**).

The thesis in hand is structured as follows:

**Section 2** reports the background of the work with regard to high level waste forms and general aspects of nuclear waste management.

**Section 3** describes experimental methods and techniques as well as sample preparation procedures.

**Section 4** provides results obtained for the chemical state of *An* in vitrified waste glass.

**Section 5** shows results of SNF characterization using high-energy resolution X-ray spectroscopy.

**Section 6** deals with simulation and immobilization of residual radioactive waste types by vitrification methods.

**Section 7** reports in-situ X-ray tomographic investigations on the behavior of PGMs in glass melt.

**Section 8** contains a short summary and an outlook to potential further investigations on the basis of results obtained within the present thesis.

## 2. Background

### 2.1. Disposal of high-level radioactive wastes (HLW)

In 2015 over 430 commercial nuclear power reactors in 31 countries produced ca. 10% of the world's electricity demand.<sup>3</sup> Most of the fuel used in the nuclear power plants consist of UO<sub>2</sub> which is enriched with respect to U-235 up to 5 wt%. The fission of U-235 releases around 200 MeV per nucleus, a million-fold increase in energy release compared to chemical reactions, e.g., the combustion of fossil fuels. Although the nuclear process does not generate CO<sub>2</sub> or other greenhouse gases it yields its own waste in form of highly radioactive SNF leading to the requirement of the investigation and establishment of manageable waste forms and disposal concepts. Worldwide approximately 10000 metric tons of SNF are produced by nuclear power plants each year, 300000 metric tons are already stored in intermediate storage facilities, emphasizing the importance of advancing the progress of reliable final disposal concepts.<sup>11</sup> Most of the inventory is destined for long-term storage in geological repositories. Such direct disposal routes are described in more detail in **Section 2.1.1**. In August 2011, the Federal Parliament and Federal Council of Germany decided to abandon the civilian use of nuclear fission power for the generation of electricity in Germany ("*Atomgesetz*"). The Federal Government of Germany has to provide suitable facilities and a reliable concept for the safe final disposal of all nuclear waste. The prevailing political target in Germany is to dispose all radioactive waste in deep geological rock formations. The former iron ore pit Konrad in Salzgitter is under continuous construction, aiming to serve as a final disposal facility for nuclear waste with negligible heat-generation. Its license envisages the disposal of up to 303000 m<sup>3</sup> of low and medium level waste from 2022 on. In July 2013 the German parliament passed a site-selection-law with the aim to identify a suitable site for the disposal of heat-generating HLW. Its operation is planned from 2050 on.<sup>12</sup>

Some major western countries such as the UK or France pursue the closed fuel cycle with regard to the finite availability of U. The "red book" of U resources from the *International Atomic Energy Agency*, IAEA,<sup>13</sup> predicts an availability of U resources on earth for approximately 150 years. In contrast to one-time fuel cycles where only few percent of the employed U are actually utilized reprocessing and recycling of SNF allows for a U use in fast reactors of up to 75% for fission energy generation.<sup>14</sup> The waste remaining from reprocessing procedures contains mainly highly radioactive FPs which are vitrified in glass matrices. Worldwide these remainders of nuclear fuel recycling are beside the direct disposal of SNF the second major HLW dedicated for final disposal in a geological repository. They are further discussed in **Section 2.1.2**.

## 2.1.1. Direct disposal of spent nuclear fuel (SNF)

### 2.1.1.1. Composition of SNF

To assess the fate of SNF stored in a geological disposal for several hundred to thousands of years its behavior under the expected conditions must be evaluated and understood. Such behavior is essentially influenced by both the repository specific parameters such as host rock, container, geoengineered barrier, groundwater characteristics, etc. and the nature of the fuel itself. Due to its service in the nuclear reactor its characteristics and composition are drastically changed compared to fresh  $\text{UO}_2$  fuel. Understanding the interdependency of the SNF with the variety of disposal conditions is essential to assess the safety of different disposal concepts.<sup>3</sup>

The SNF composition is determined by two fundamental reactions: 1) fission of fissile components such as U-235 and Pu-239, and 2) neutron capture and sequential  $\beta$ -decay generating transuranium elements (mainly Pu-239 from U-238). Hence, the Pu concentration increases with irradiation duration. About one-third of the total energy produced in a typical light-water reactor (LWR) is released by the fission of neutron generated Pu-239. The FPs are highly radioactive and are main radioactivity components of the SNF as well as of the reprocessing waste at least for several hundreds of years. The final SNF composition depends on the type of fuel, initial composition and enrichment, neutron energy spectrum and the burn-up. In the past fuel elements were typically burned up to ca. 45 GWd/tU. Nowadays, the efficiency of the material flow processes is increased by burning the U up to 55-60 GWd/tU. The radioactivity of irradiated fuel and its cladding is initially dominated by the short-lived fission (e.g., I-131, Cs-137 or Sr-90) and activation products (e.g., Co-60 and Ni-63). In the long-term the radioactivity is dominated by the  $\alpha$ -decaying long-lived transuranium elements (e.g., Pu-239, Np-237 and Am-241).<sup>3</sup> The FPs, activation products and transuranium elements are present in many different phases in the SNF.<sup>15, 16</sup> Gaseous FPs (e.g., Xe and Kr) can form dispersed bubbles in the fuel matrix; metallic FPs (e.g., Mo, Ru, Pd) form immiscible metallic precipitates, so-called  $\epsilon$ -phases. The remaining FPs generate oxidic precipitates or solid solutions within the  $\text{UO}_2$  host (cf. **Figure 1**): Transuranium and rare earth elements can be incorporated into the  $\text{UO}_2$  lattice. Due to a temperature gradient of ca. 400 °C to 1100 °C from the rim to the center region of a single 10 mm fuel pellet as well as of the burn-up, the elemental composition and the macroscopic characteristics of the material are heterogeneously distributed.<sup>17</sup> Anomalies of the pellet rim region are further discussed in **Section 5**. Thus, the SNF has rather complex properties with respect to crystal structures, mechanical behavior, heat conductivity, chemistry and phase distribution as results of its irradiation history.

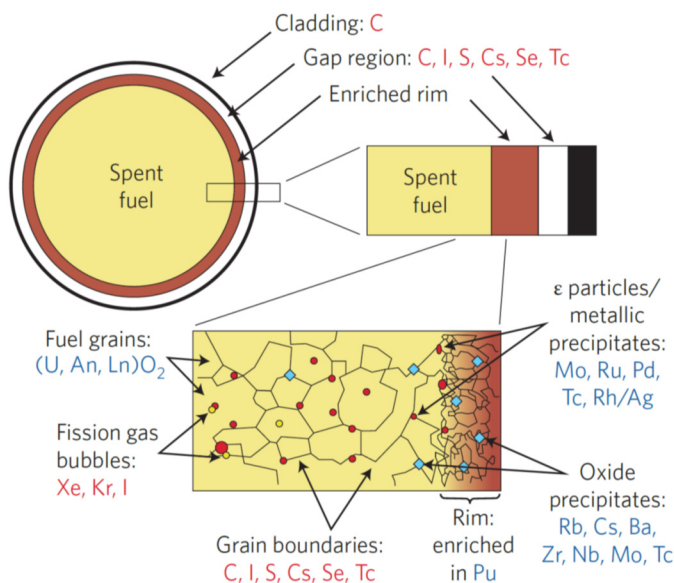


**Figure 1** Illustration of SNF microstructure and distribution of FPs and An. (Reproduced with permission from Ref. 3)

Every year ca. 20-30 t of SNF are unloaded from a typical LWR. Disregarding some important countries such as France, the UK, Russia, Japan, China and India, most other countries in the world use a once-through fuel cycle in which burned fuel is not reprocessed but instead destined for direct disposal in a geological repository. While the long-term storage in a repository will be necessary for hundreds of thousands of years, the SNF might be in intermediate storage for tens to hundreds of years at interim storage sites. During the whole time the chemical and physical properties evolve due to the accumulation of radioactive decay events, the decreased thermal output and the altered radiation field.

#### 2.1.1.2. Evolution of SNF

As time passes the short-lived FPs decay and the radioactivity will be dominated by the  $\alpha$ -decaying An, mainly Pu-239 and Am-241, after ca. 500 years (cf. **Figure 93** in the **Appendix**).<sup>18</sup> The heat generation of the FP decay (ca. 2MW/t after discharge from the reactor) causes the fuel elements to remain hot after the removal from a nuclear reactor, requiring its storage in water pools. After five to ten years, depending on its burn-up, the fuel elements can be unloaded and placed in metal containers. Due to the not yet existing final repositories in countries all over the world, the extended interim storage of SNF in these dry casks becomes an undesired reality. Gradually the waste packages can lose their intended protective function. Self-radiation damage and He build-up caused by  $\alpha$ -decay might lead to a significant pressurization inside the fuel rod, threatening the integrity of the fuel cladding.<sup>19</sup> Especially as radiation damage and the reactivity of generated hydrogen provoke an embrittlement of the

Zircaloy cladding.<sup>20</sup> Cladding failure complicates the repacking and the conditioning of the SNF prior to final disposal.

The most challenging issue the safety assessment of a potential geological repository is the timescale of hundreds of thousands of years. Within this time-frame the SNF undergoes significant changes which cannot be evaluated in real time experiments.

### 2.1.1.3. SNF behavior in repository conditions

Parallel to the evolving properties of the SNF also the repository conditions change likewise. The installation of a geological disposal and the emplacement of nuclear waste disturbs fundamental properties of the surrounding host rock. Tunnels create fractures; pore water will start moving and corrosion or alteration of barriers as well as the radiation modify the groundwater chemistry. Radiolytic species are generated in the aqueous solution, establishing oxidizing conditions at the waste surface, favoring the *An* dissolution.<sup>21</sup>

A HLW repository system usually consists of several barriers: 1) The conditioned waste form, 2) the container, 3) a geoengineered barrier/backfill, 4) seals, and 5) the host rock and overlaying geological layers. Depending on the disposal concept, the individual barriers take over different functions such as prevention or delay of water access to the waste form and retarding or even retaining dissolved radionuclides. A multi-barrier system is therefore a tuned system being optimized for a specific host rock and site.

Dissolution and transport mechanisms of radionuclides originating from SNF have been extensively studied.<sup>22-25</sup> The release of radionuclides can be grouped in the instantaneous and the long-term release. After water has breached the metal container, fission gasses (e.g., Kr, Xe) and mobile elements (e.g., Cs, I, Cl) which have been migrated to the grain boundaries and rim zone are rapidly released (so-called instant release fraction). After this initial release the dissolution of the UO<sub>2</sub> matrix takes place. This slower process consists of several major steps: 1) oxidation of U(IV) to U(VI), 2) bulk dissolution of UO<sub>2</sub> and release of FPs and transuranium elements, 3) dissolution of segregated oxides and metal phases, and 4) formation of secondary alteration products. The presence of radiolytic aqueous species generated by the ionizing radiation plays a major role in the matrix corrosion process. Water is broken down into reactive species such as H<sub>2</sub>O<sub>2</sub>, H<sub>2</sub> and H<sub>3</sub>O<sup>+</sup> drastically changing the water redox conditions at the fuel surface. The competing chemical reaction manifold is complex.<sup>21</sup> **Figure 2** gives a brief overview on possible processes occurring in the system.

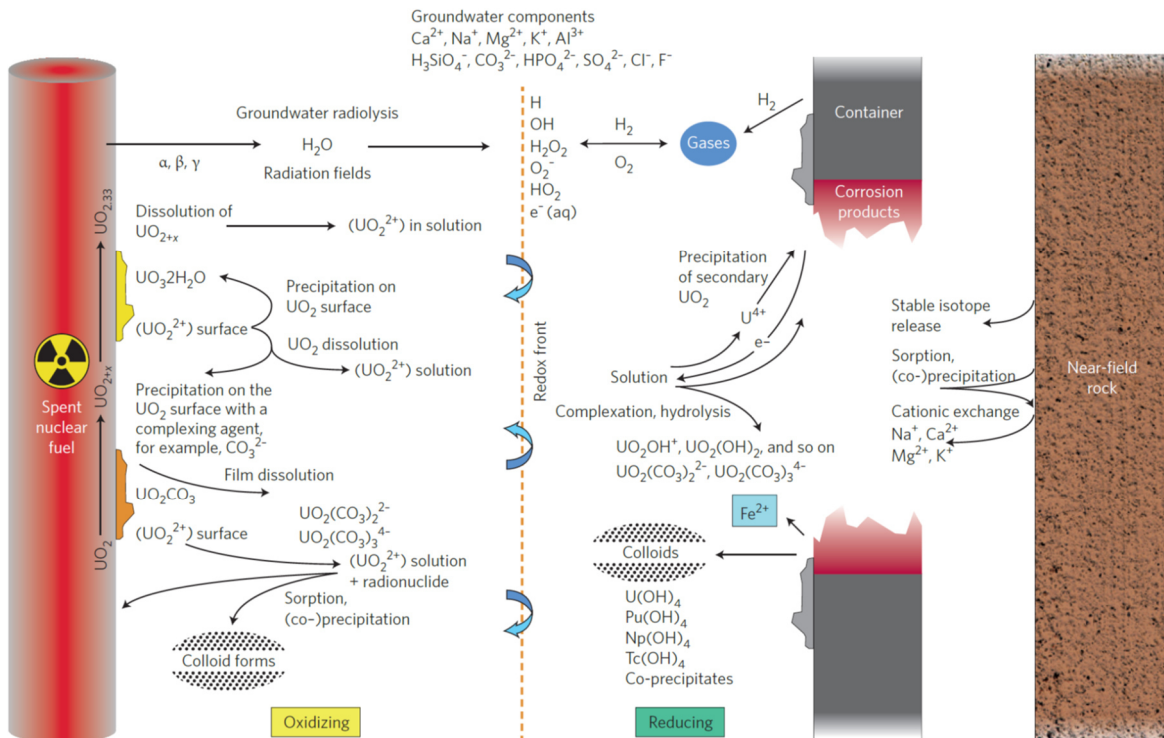


**Figure 2** Schematic illustration of chemical processes involved in the SNF material dissolution in the near-field of a geological repository. (Reproduced with permission from Ref. 26)

Defining a time scale for repository evolution is challenging.<sup>27</sup> The Belgian SAFIR 2 study distinguishes three discrete post-closure time frames for the final disposal of SNF and vitrified HLW in Boom clay (clay of the Boom sediment formation in Europe):<sup>28</sup>

- 1) In the **thermal phase** the decay of FPs and *An* keep the waste on a temperature of several hundred degrees. The thermal gradient prevents water access to the waste, so the HLW remains contained. The thermal phase is estimated to last approximately 1000 years.
- 2) In the **isolation phase** it is expected that almost no activity will be released from the repository. Although radionuclides are leached from the waste matrix after water has reached it, the slow release from the waste and the low migration rates through the engineered and natural barriers prevent the release from the system for long time. Most of the FPs have decayed after 2000-3000 years (Tc-99, I-129 and Cs-135 will still be present), so the radioactivity in this period is dominated by the *An*  $\alpha$ -decay. For the Boom clay the isolation phase is estimated to last over a period of ca. 10000 years.
- 3) The release of radionuclides to the environment and to surface water by migration is expected in the **geological phase**.

In the long-term of the geological phase, the boundary conditions influencing radionuclide mobility will be set by the local geology. Possibly, these conditions might be suddenly or

gradually changed by certain events. Depending on the position of the repository, tectonic disruptions or climate change can affect them. A fluctuation in the ground water flow might increase or decrease the dissolution of the waste. As most FPs will have decayed at that time mainly the *An* migration has to be considered. Their solubility largely depends on the prevailing redox conditions.<sup>29</sup> The oxidation states of the *An* have a dramatic effect on their solubility, transportation and bioavailability behavior.<sup>30</sup> U is known to exist in its tetra- and hexavalent form in reducing and oxidizing conditions, respectively. In contrast, Pu might be present in up to four different oxidation states from trivalent to hexavalent form. In general it can be said that *An* with lower oxidation states (e.g., tetravalent) form solid phases with low solubility whereas higher oxidation states (e.g., hexavalent) form well soluble dissolved species.<sup>31</sup>

## 2.1.2. Disposal of vitrified waste from spent nuclear fuel (SNF) reprocessing

### 2.1.2.1. Glasses as host matrix for nuclear waste immobilization

FPs and minor *An* (MA) generated during fuel irradiation represent only 5% of the SNF weight but 98% of its radioactivity. By reprocessing of the fuel these FPs and MA end up in concentrated HLLW solutions. These can be stored for several decades in stainless steel storage tanks equipped with cooling and stirring systems. Nevertheless, such a procedure requires continuous monitoring, maintenance and cannot be extended to a timescale of hundreds of thousands of years when the radioactive decay is significantly advanced. In addition, the liquid state of the HLLW is a major safety issue. In the 1950s major western countries such as USA, the UK, France, Canada, etc. started strategies for the immobilization of the FP and MA containing HLLW. Several host materials were considered with a rapid convergence on glass.<sup>32</sup>

Glasses are amorphous non-stoichiometric solid materials which tend to show a fragile rupture behavior. Characteristically, they show a glass transition temperature  $T_g$ . It describes an unusual phase transition which does not occur at a certain temperature but over a temperature range. In contrast to usual phase transitions, it does not go along with a discontinuous change in structure. As an amorphous material, glass does not have any long-range order, causing some of its unique properties. Glass can be made by several methods. Most glasses are formed by quenching a melt fast enough below its  $T_g$ , leaving no time to form a crystalline phase. During cooling, the viscosity of the melt increases progressively until the material solidifies. A glass can therefore also be characterized as “rigidified supercooled liquid”. Thus, glasses are kinetic

metastable materials. In practice, metastability is not a concern as most oxide glasses are much longer stable than any timescale of our universe. While silicate based glasses are formed at relatively slow cooling rates ( $10^{-2}$  K/s), the formation of an amorphous solid material from a metal melt require extremely high cooling rates of more than  $10^6$  K/s. Due to the tremendously high viscosity of solid glass at room temperature, relaxation processes are inhibited. Internal stress which builds up in the glass when its melt is quenched can be preserved in glasses for several thousands of years.<sup>32, 33</sup>

After ceramics, glasses are one of the oldest processed materials known to mankind. Natural glasses such as obsidian, formed by volcanic eruptions or impact of meteorites, were used to manufacture knives and arrow heads. Glazed stone beads used by humans have been dated to 12000 BC.<sup>33</sup> The first man-made glass was dated back to 4500 BC.<sup>32</sup> In Egypt, the pharaohs established a glass industry in 1500 BC. Since then, glass became an irreplaceable material in our everyday life. Due to some of its unique properties glass was discovered for a very new application in the 20<sup>th</sup> century: The immobilization of nuclear waste. Michael Faraday described glass as a solution of different substances in one and another.<sup>33</sup> This reflects very well its ability to be very tolerant to changes in its composition. Glasses and their properties change continuously and smoothly with composition variations. In combination with their physical and chemical durability, glasses were found to be a well suitable host matrix for the reliable immobilization of toxic waste such as long-lived highly radioactive waste.

No other material combines all advantages for the immobilization of nuclear waste:

- High capability to sustainably immobilize a broad range of elements in considerable amounts
- Small volume of the final waste glass product
- High chemical and physical durability
- High radiation tolerance
- Available production technology from industrial glass manufacturers

The exact composition of the glasses used for the immobilization of nuclear waste is tailored according to the waste composition, the melting process, the acceptance criteria for final disposal etc. **Figure 3** depicts the field of constraints and requirements a waste glass has to consider and to fulfill, respectively, and in which the glass formulation has to find the best compromise.

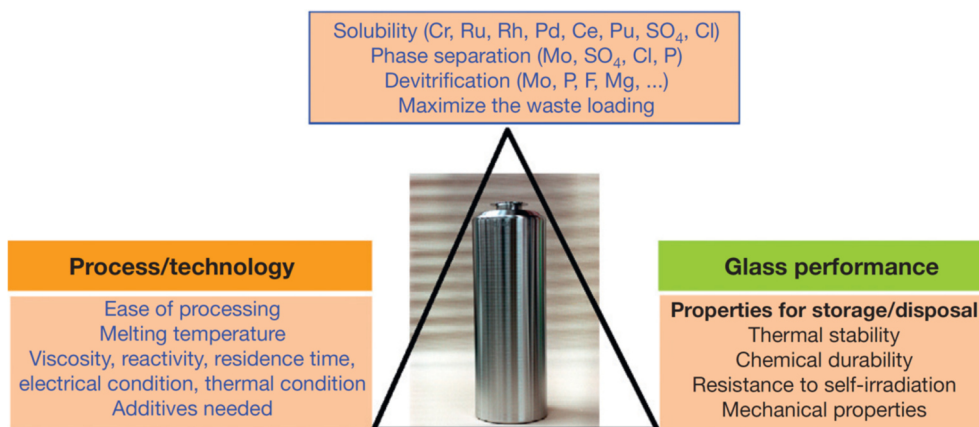


**Figure 3** Field of constraints and requirements a glass formulation has to consider and to fulfil, respectively, in order to serve as a reliable host matrix for nuclear waste. (Reproduced with the permission from Ref. <sup>32</sup>)

For most cases, alkali borosilicate glasses represent the best compromise for the immobilization of radioactive waste and have therefore been selected by most countries as reference matrix (France, the UK, USA, Germany, etc.). Another immobilization matrix are phosphate glasses. As their melt is very corrosive, their applicability is limited, yet they are suitable for the immobilization of Al rich wastes and are applied in Russia.<sup>32</sup>

The aqueous alteration of waste glass is the only considerable release process for the incorporated radionuclides. Thus, the leaching performance of the glass is a paramount criterion as it ensures low radionuclide release rates in any water exposure scenario. Leaching describes the process of washing out glass constituents into water. It depends on several parameters, but typical normalized leaching rates are below  $10^{-5} - 10^{-6}$  g/cm<sup>2</sup> day. This excellent corrosion-resistant property provides a high degree of environmental protection.

Waste glasses are not necessarily completely homogenous materials such as optical glasses. The waste contaminants are incorporated into the macro- and micro-structure of the glass matrix by either dissolution or encapsulation. As most elements from nuclear waste reprocessing are well soluble in glass, they participate in the network formation either as network formers or modifiers. Other immiscible elements with low solubility limits in glass melts such as sulfates, chlorides and molybdates as well as noble metals like Ru, Rh and Pd do not (completely) dissolve in the glass melt and become encapsulated. Depending on the nature of the encapsulated components, the leaching performance of the waste product might be negatively influenced.<sup>33</sup>

### 2.1.2.2. Glass structure and immobilization mechanisms

Within the last 40 years countries in Europe and all over the world (Belgium, Canada, Germany, China, India, Japan, Russia, etc.) used vitrification processes for immobilization of their HLLW. In most cases borosilicate glasses were used as host material. Their selection is based on their excellent properties in terms of waste immobilization: High flexibility with regard to waste loading and incorporation of many different waste elements, good glass-forming ability, chemical durability, mechanical integrity and thermal as well as radiation stability. The major compound of borosilicate glass is  $\text{SiO}_2$  with ca. 50 wt% and  $\text{B}_2\text{O}_3$  with ca. 15 wt%.  $\text{Na}_2\text{O}$  is typically included at approximately 10 wt%. As the glass components usually exist as oxidic species, their concentration is always given as oxide species, notwithstanding the fact that the element might be present in another speciation (e.g., U is usually given as  $\text{UO}_2$  even if it is incorporated in the glass as hexavalent U). In addition,  $\text{CaO}$ ,  $\text{MgO}$ ,  $\text{Na}_2\text{O}$  and  $\text{Al}_2\text{O}_3$  are present in smaller amounts.  $\text{SiO}_2$ ,  $\text{B}_2\text{O}_3$  and  $\text{Al}_2\text{O}_3$  build up the network as they establish strong covalent bonds to each other involving  $\text{SiO}_4$ ,  $\text{AlO}_4$ ,  $\text{BO}_4$  tetrahedral and  $\text{BO}_3$  triangles. The oxygen atoms cross-linking these building units are called bridging oxygens (BO). As the network does not establish a regular structure like in crystalline materials, the formed chains spread in all directions and have various lengths. Some of the building units exhibit one, two or even three non-bridging oxygen (NBO) atoms. Those NBO are only attached to one cation such as Si and carry a single negative charge. They compensate for the positive charge of free cations which are incorporated in the gaps of the network. These cations are called network modifiers as they modify the glass network by breaking bonds, increasing the number of NBO. This process is called depolymerization of the glass network. Network modifier can be alkali or earth-alkali elements, transition metals and ions with high charge as for example  $An$  elements. **Figure 4** illustrates the structure of a borosilicate glass with BO and NBO.<sup>33</sup> The ability of a cation to serve as a network modifier or a network former is characterized by its field strength  $F$  (also called Dietzel field strength):<sup>34</sup>

$$F = \frac{Z}{a^2} \quad (1)$$

Where  $Z$  is the charge and  $a$  the ionic radius ( $\text{\AA}$ ) of the cation. Cations with lower field strength (0.1–0.4, e.g., alkali) act as network modifiers, whereas ions with higher  $F$  (1.5–2.0, e.g., Si, B, etc.) are network formers. Field strength values for the different elements can be found in the literature.<sup>33, 35</sup>

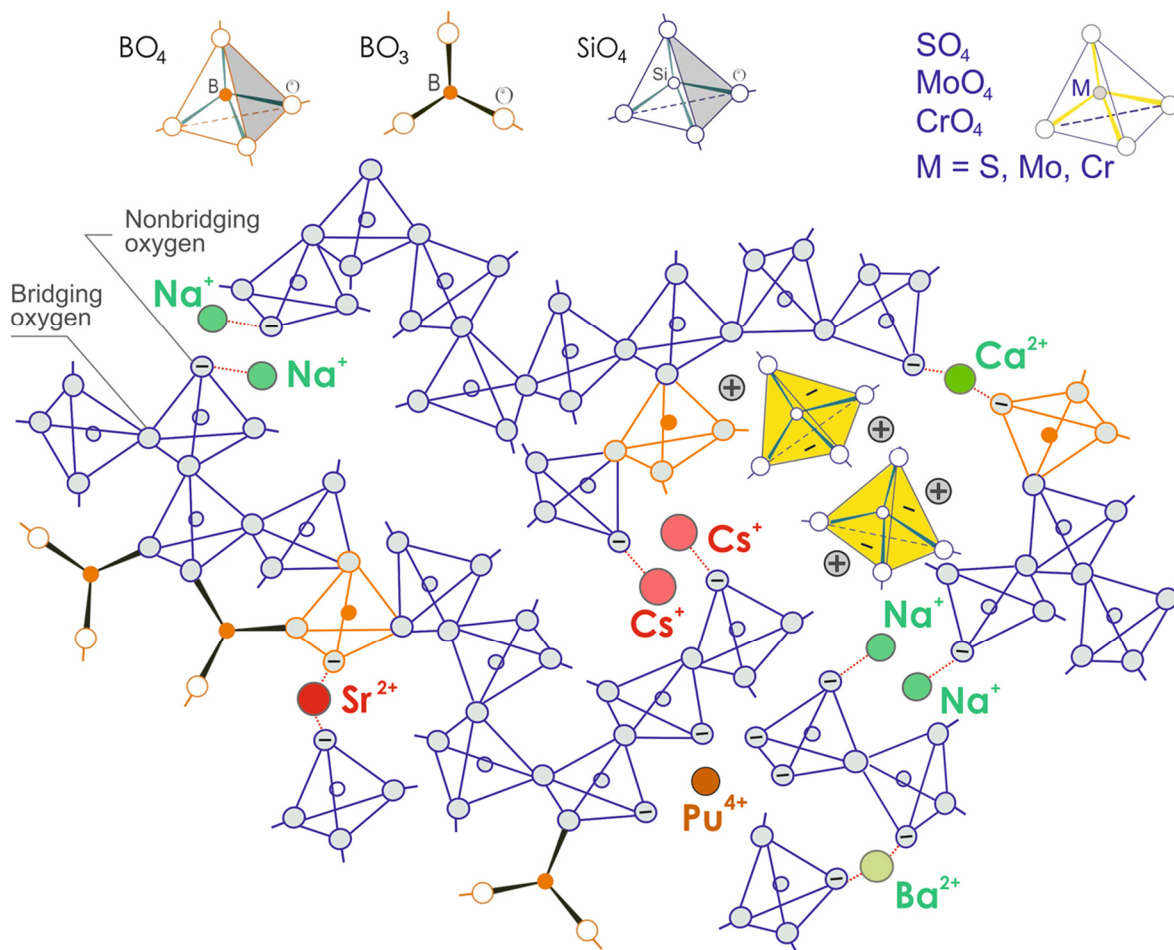


**Figure 4** Schematic illustration of an alkali-silicate glass network. The blue tetrahedral structures represent  $\text{SiO}_4$  network forming units, B atoms form either  $\text{BO}_3$  trigonal planar or  $\text{BO}_4$  tetrahedral units. Charged S, Mo or Cr tetrahedra are not connected to the glass network but incorporated in its gaps. Free cations such as alkali and earth-alkali elements compensate the negative charge of NBO. (Illustration by S. Weisenburger)

Some elements do not tend to incorporate in the glass matrix, neither as network modifier nor former. They end up in separated phases due to the very low solubility limits in the glass melt of their formed constituents (e.g.,  $\text{SO}_4$ ,  $\text{MoO}_4$ ,  $\text{RuO}_2$ ). They are considered as troublesome elements in a nuclear waste vitrification process. S can be incorporated in the glass matrix up to approximately 1 wt% in terms of  $\text{SO}_4$ . Above, separated water-soluble phases are formed. Together with cations like Na, the elements S, Mo or Cr form glass-insoluble so-called “yellow phases” amongst others, floating on the surface of the glass melt or accumulating at the bottom of the melting cavity (e.g.,  $\text{Na}_2\text{Mo}_4$ ). Additionally, “yellow phases” can incorporate several other components such as chromates and alkali elements. From the definition of the cation field strength it can easily be recognized that the oxidation state has a major influence on its incorporation behavior. Similar accounts for its solubility limit in the glass phase. The dependency of the glass solubility on the element oxidation states will be discussed in detail in **Section 4**. If Ru is present in the waste, it forms small needle-like  $\text{RuO}_2$  particles which are

encapsulated by the glass. They can agglomerate with Pd and sediment to the bottom of the glass melter causing serious problems due to its high viscosity and electrical conductivity. The vitrification of insoluble noble metals is discussed in detail in **Section 7**.

### 2.1.2.3. Vitrification technology

The vitrification process for the immobilization of nuclear waste comprises several steps, depending on the nature of the waste and the applied process. As most of the HLLW which is dedicated for immobilization is present as nitric acid solution, the first step of the vitrification process consists of the evaporation of the excess water. It is followed by calcination, glass melting and finally by pouring and cooling of the waste glass product. Calcination of the waste describes the thermal decomposition of its nitrates and other salts and thermal transformation to oxides. Vitrification processes which are performed nowadays can be either one-stage or two-stage processes. In the first case, the liquid waste is mixed with glass-forming additives (e.g., a pre-synthesized base glass, called glass frit) and fed into the melter, or the HLLW is fed separately from glass frit onto the glass pool surface where the mixing, evaporation, calcination and glass melting takes place. In the second case, prior to the described procedure, the liquid HLLW is dried and calcined in a so-called calciner (two-stage process). The calcine is then fed together with the glass-forming additives into the melter. For heating of the glass melt two conceptual different melters are used at nuclear waste vitrification plants: The JHCM or the induction-heated metallic melter. While the former is used in some facilities, the latter is known for reliable operation in the large-scale vitrification plants in France and the UK. **Figure 5** illustrates a cross-section of a JHCM developed by the Institute for Nuclear Waste Disposal of the Karlsruhe Institute of Technology (KIT-INE). Bottom and side electrodes heat the glass melt by an electrical current. HLLW and glass frit are fed onto the surface of the glass melt, where they are forming a so-called cold-cap floating on top of it. In the lower area of the cold-cap, the waste glass is formed and melts continuously into the glass pool.

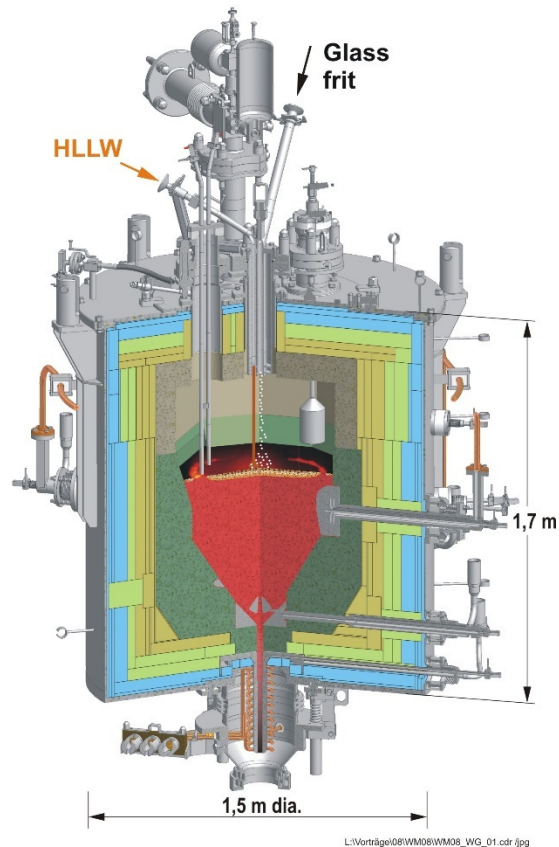


**Figure 5** Cross-section of a JHCM developed by KIT-INE within the VEK project.(Illustration adapted from Grünewald *et al.*)<sup>36</sup>

The melting of nuclear waste glass must be performed below temperatures of 1200 °C due to the volatility of certain elements and process handling. Nevertheless, Cs, Ru and Tc already form constituents at such temperatures ( $\text{Cs}_2\text{O}$ ,  $\text{RuO}_4$ , etc.) which are volatile and can leave the cold-cap and the glass melt in significant quantities. They are trapped by the melter off-gas treatment system and need to be recycled into the process. The readily melted glass is poured into stainless steel containers and cooled down within a few days. Glass cracks formed during the cooling process of the canisterized glass, lead to an increased surface area, potentially prone to the attack of water. Nevertheless, the glass product is sufficiently durable to ensure a suitable degree of radionuclide retention. The volume reduction factor (VRF, final waste glass product volume compared to initial HLLW volume) for vitrification processes is about five. The VRF is an important factor measuring the efficiency of the waste immobilization process and is correlated to its economic aspects.<sup>33</sup>

#### 2.1.2.4. Waste glasses in repository conditions

When nuclear waste glass is disposed in a final geological repository, water intrusion has to be taken into account. The time scale for which the water intrusion has to be expected depends significantly on the host rock formation and the emplacement concept. In the earlier parts of the German final storage concept, the conditions in a salt dome repository have been considered. In earlier safety analysis scenarios, it was assumed that approximately after 500 years groundwater brine has breached the container barriers and will contact the glass which will have a temperature of approximately 150 °C. In case of an earlier container failure, the corrosion of the glass might start untimely. For the long-term corrosion of more than 1000 years, temperatures below 80 °C are expected for the considered emplacement concept. The glass dissolution process is a combination of a variety of mechanisms discussed for example by Kienzler *et al.* and Vernaz *et al.*<sup>25,32</sup> The leaching behavior of a glass substrate can be assessed by so-called leaching tests during which glass samples are contacted with water under a large range of experimental conditions. The performance of several materials in leaching tests can only be compared under similar conditions of a given test. The test can either be performed static (glass sample is exposed to the same solution for the duration of the test), dynamic (glass is exposed to a flow of fresh leach, e.g., the “Soxhlet test”) or as integral test (glass leaching in the presence of natural environment materials). B is a good trace element for quantifying the dissolution rate of the glass matrix. In more diluted leaching solutions, also Na, Li and Mo can be used as tracer elements.<sup>32</sup>

When contacted by water, the main alteration processes of borosilicate glass occurring subsequently can be described as following:<sup>37,38</sup>

- Hydrolysis and exchange reaction of mobile glass components (alkali metals, B, etc.). This step occurs rapidly during the initial stage.
- Slower hydrolysis of Si driving the initial glass dissolution rate
- *In situ* condensation of hydrolyzed species (Si, Zr, Al, Ca, etc.) forming an amorphous gel layer at the glass/solution interface.
- The gel layer rapidly constitutes a barrier against the transport of water and solvated glass constituents. Especially for concentrated leaching solutions the transport-inhibiting effect of the gel layer becomes the alteration controlling factor.
- Mobilized glass components can precipitate forming secondary phases on the glass surface. By consuming the elements forming the protective layer the glass alteration is sustained.

The leaching behavior, especially in the initial phase, depends mainly on the glass composition, the temperature and the pH value of the solution. From 4 °C to 300 °C the initial leaching rate ranges over seven orders of magnitude. Thus, taking into account the temperature effect during the planning of leaching experiments is essential.

In case of the water renewal rate being very slow, as it expected for most geological repositories, silica saturation is observed in the leachate leading to a strong alteration rate drop. The decrease was related to a lower hydrolysis rate due to the increased solution concentrations and the formation of the gel layer serving as diffusive barrier.<sup>39</sup> Once the saturation conditions are established, a residual leaching rate, controlled by gel dissolution and secondary phase precipitation, is observed. The residual rate is typically rather low for borosilicate glasses (ca. 5 nm/year at 50 °C). In some cases, a resumption of the alteration is observed. When the equilibrium pH value is above 10 and the glass bears high Al concentrations, zeolite material can precipitate, leading to an increased cycle of adaptation.<sup>40</sup>

In a geological repository, the water chemistry inside the host rock is initially in equilibrium with the host rock. It is then disturbed by engineered materials such as concrete, steel, etc., and the heat produced by the deposited glass canisters. As a consequence, the glass dissolves in a system with evolving temperature, composition and water flow for at least ten thousand years.<sup>32</sup> The additional groundwater components may influence the glass dissolution by changing the gel layer formation,<sup>41</sup> increasing the hydrolysis rate of the silica network<sup>42</sup> or affecting the precipitation of secondary phases.

In a fractured host rock environment such as granite the water renewal rate would be the main environmental parameter. At this juncture the final disposal of vitrified waste in a granite host rock is contemplated only by a few countries (e.g., Russia and China). In a clay rock repository with low to no water flow, the formation of silica secondary phases serving as Si sink will be most relevant for glass dissolution. Numerous studies have investigated the effect of ionic strength and chemical composition of brine in a rock salt environment concluding lower glass dissolution rates compared with pure water.<sup>43-45</sup> In all environments, a high initial dissolution rate will be observed until the near field of the glass is saturated resulting in the residual leaching rate. This rate will determine the long-term dissolution of the waste glass. Predicting and modelling this final rate is a great challenge for science. Multiscale approaches are required as relevant space and times scales are too large to be modeled by a single model.<sup>25, 32</sup>

The effect of self-irradiation on the glass properties and its leaching behavior was studied for several decays in detail.<sup>32, 35, 46</sup> Main contributions to the irradiation dose of the waste glasses are due to the *An* ( $\alpha$ -decay), the FP ( $\beta$ -decay) and  $\gamma$ -transitions accompanying the  $\alpha$ - and

$\beta$ -decays. In order to evaluate their effect, glasses have been doped with relatively short-lived  $An$  such as Cm-244,<sup>47</sup> they were externally irradiated with electrons and heavy atoms<sup>48</sup> and the impact and recoil processes have been modelled on atomistic scale.<sup>49</sup> The studies determined irradiation effects to be of less relevance on the glass properties. In some cases the internal irradiation even improved the mechanical properties of the glasses.<sup>32</sup> Nevertheless, for the release of radionuclides – especially the long-lived  $An$  – the geochemical milieu is of more importance.<sup>25, 50</sup>

## 2.2. Fundamental principles of X-ray absorption and X-ray emission spectroscopy

### 2.2.1. X-ray absorption spectroscopy (XAS)

As electromagnetic radiation travels through matter it is attenuated due to its interaction with the material. This loss of intensity occurs according to the Lambert-Beer law:

$$I = I_0 e^{-\mu d} \quad (2)$$

Where  $I_0$  and  $I$  are the intensities of the incident and transmitted beam respectively,  $d$  is the thickness of the material and  $\mu$  the absorption coefficient.  $\mu$  depends highly on the energy  $E$  of the incident photons, the atomic number  $Z$ , the atomic mass  $A$  of the absorbing atoms and the density  $\rho$  of the material:

$$\mu \approx \frac{\rho Z^4}{AE^3} \quad (3)$$

According to this equation  $\mu$  decreases with increasing energy. However, at certain energies a sudden increase in  $\mu$  is observed, characteristic for the absorbing element (cf. Moseley's law). Due to their appearance in the absorption spectra these energies are called X-ray absorption edges (cf. [Figure 6](#)).

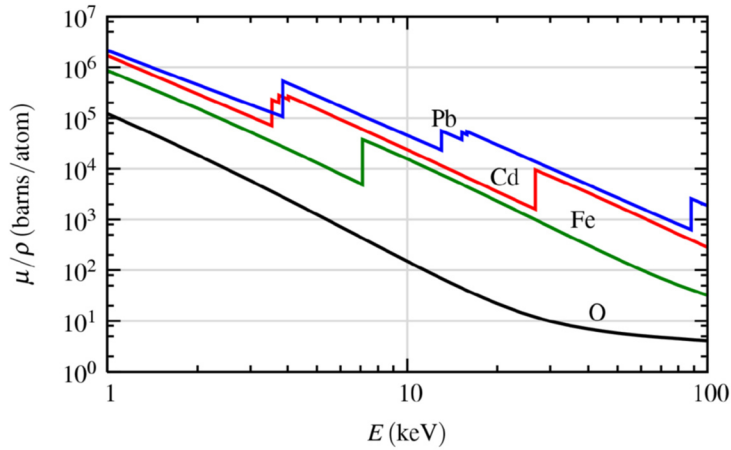


**Figure 6** Absorption cross-section  $\mu/\rho$  of Pb, Cd, Fe and O over a large X-ray energy range. The element specific absorption edges are can be recognized by a sharp rise in  $\mu/\rho$ . (Reproduced with permission from Ref. <sup>51</sup>)

The process describing the sudden change in  $\mu$  is the photoelectric effect, illustrated in **Figure 7**.<sup>52,53</sup> The energy of the X-ray photon is sufficiently high to excite an electron from its shell into a bound unoccupied states or the continuum. The created hole is filled by relaxation of a higher-shell electron. The energy difference between the electron levels is released either as emitted fluorescence (**Figure 7**, middle) or Auger electron (**Figure 7**, right).<sup>54</sup>

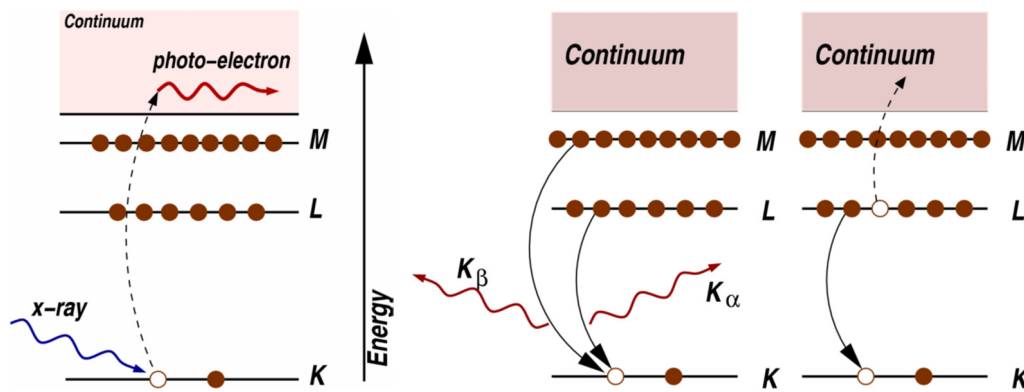


**Figure 7** Illustration of the photoelectric effect. A photon excites a core electron from the K shell into the continuum (left). The electron hole is filled by an outer M or L shell electron emitting either X-ray fluorescence (middle) or an Auger electron (right). (Adapted with permission from Ref. <sup>51</sup>)

The emission of Auger electrons is more probable for elements with low atomic  $Z$  number ( $Z < 30$ ) while the emission of fluorescence photons dominates for heavier elements.<sup>54</sup> In addition, the excitation with hard X-rays (more than 2 keV) favors the fluorescence effect rather than the Auger electron emission which is more likely for soft X-ray excitation.<sup>51</sup> X-ray absorption spectroscopy (XAS) is the measurement of the energy dependence of the absorption coefficient. It can be done in both transmission:

$$\mu(E) = \log(I_0/I) \quad (4)$$

and fluorescence mode:

$$\mu(E) \propto I_f/I_0 \quad (5)$$

where  $I_f$  is the intensity of the monitored fluorescence line.<sup>51</sup> In an XAS experiment the X-ray energy is tuned across an absorption edge of the element of interest. Corresponding to the principal quantum numbers  $n = 1, 2, 3, \dots$  of the main electron shell, these absorption edges are labelled K, L, M, etc. Transitions from different orbitals are numbered by subscripting 1, 2, 3 etc. to the edge label (e.g.,  $L_1, L_2, L_3$  edge). The excited electrons are labeled with their main quantum number  $n$  and the azimuthal quantum number  $l$  describing the orbital angular momentum (e.g.,  $2p_{3/2}$  for the  $L_3$  edge).<sup>54</sup> A schematic X-ray absorption spectrum is shown in **Figure 8**.

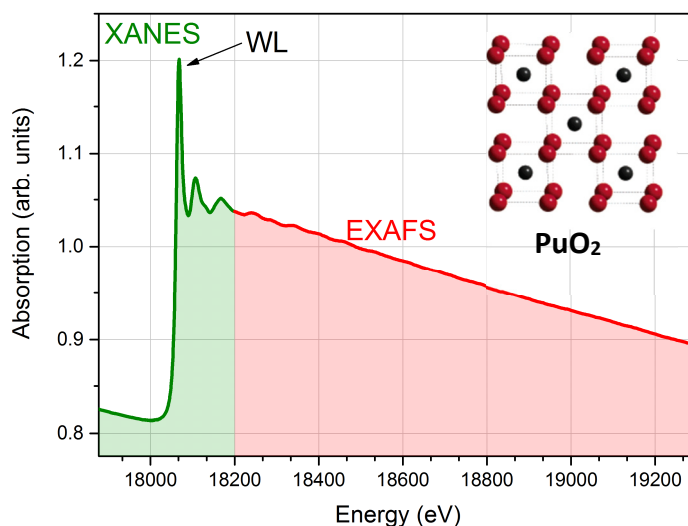


**Figure 8** XAS spectrum of PuO<sub>2</sub> (cf. Section 3). The XANES region is marked green, the EXAFS region red. The most intense peak in the XANES region is the WL. (Crystal structure of PuO<sub>2</sub> adapted with permission from Ref. <sup>55</sup>)

The most intense absorption feature is called WL. At this energy electron transitions take place following the dipole selection rules  $\Delta l = \pm 1$  (e.g.,  $2p \rightarrow nd$  transition for  $L_{2,3}$  edge). The incident energy is sufficient to excite electrons in unoccupied bound states. As that transition is very sensitive to the electronic configuration of the atom, the position of the WL can be used to determine the oxidation state of the absorbing atom. In addition, the shape of the WL fingerprints to some extent the coordination geometry of the absorbing atom.<sup>56</sup> Together with the region before the WL (approximately -50 eV relative to the WL), called pre-edge, and the region behind the WL (approximately 250 eV), called post-edge, it forms the so-called X-ray absorption near edge structure (XANES).<sup>57,58</sup> The region at higher energies is named extended X-ray absorption fine structure (EXAFS). It starts shortly after the WL, partially overlapping with the XANES region and continues to 1000 eV or more above the WL. In the EXAFS region

the electrons are excited into the continuum (cf. **Figure 7**, left). Due to interaction of the excited photoelectron with neighboring atoms, information about the local environment of the absorbing atom can be obtained. The photoelectron is considered as spherical wave which is scattered from surrounding atoms. The scattered electron waves interact with the initial wave causing interference. This is the origin of the oscillating part in the EXAFS spectrum.<sup>54</sup> The EXAFS spectrum contains information on the type, number and geometry (interatomic distances and angles) of the coordinating atoms relative to the absorbing atom.<sup>59</sup> As the photoelectron moves through the material it decays due to the finite lifetime of the core-hole and the interaction with the atoms.<sup>60, 61</sup> Therefore, the range of information is limited to distances smaller than 10 Å. As EXAFS spectroscopy probes the local atomic environment of every absorbing atom, no periodicity of the materials structure is required in contrast to for example X-ray diffraction. Thus, the EXAFS technique is predestined for the investigation of amorphous or liquid materials with only short-range atomic order.<sup>62</sup> As a results of approximations, an analytical expression of the EXAFS spectrum can be obtained.<sup>59</sup> Considering all atoms  $N_i$  with the same atomic number  $Z$  around the excited atom in shells at equal distances  $R_i$  from the absorbing atom, then the EXAFS signal  $\chi$  is given as a function of the photoelectron wave number  $k$  by:

$$\chi(k) = \sum_i \chi_i(k) \quad (6)$$

where each scattering path  $\chi_i$  of the photoelectron can be written as:

$$\chi_i(k) = \sum_i \left( \frac{N_i S_0^2}{k R_i^2} \right) F_i(k) \sin[2kR_i + \varphi_i(k)] \cdot e^{-2\sigma_i^2 k^2} e^{-2R_i / \lambda(k)} \quad (7)$$

The terms  $F_i(k)$ ,  $\varphi_i(k)$  and  $\lambda(k)$  are the scattering amplitude, the phase shift and the mean free path of the photoelectron, respectively. These parameters can be calculated by the *ab initio* quantum-chemical FEFF code based on the multiple-scattering theory.<sup>60</sup>

The distance  $R_i$  between the absorbing and the scattering atom is given by:

$$R_i = R_{0i} + \Delta R_i \quad (8)$$

It is equal to half the path length of the photoelectron in a single-scattering event.  $R_{0i}$  is half the path length used in the theoretical calculation modified by  $\Delta R_i$  which represents a change in the interatomic distance relative to the initial path length  $R_i$ .

$k$  is described by:

$$k = \sqrt{2m_e \frac{E - E_0 + \Delta E_0}{\hbar}} \quad (9)$$

The equation expresses the excess kinetic energy of the photoelectron in wavenumbers  $k$  taking into account the mass of the electron  $m_e$  and the Planck's constant  $\hbar$ .  $\Delta E_0$  relates to a change in the photoelectron energy and can be calculated by FEFF code. It aligns the energy scale of the theoretical spectrum to match the measured spectrum. The equation can be simplified by:

$$k \approx 0.51\sqrt{E - E_0} \quad (10)$$

$E$  is the incident energy of the exciting photon, and  $E_0$  is the binding energy of the emitted photoelectron.  $R_i$  can be determined by modelling the EXAFS spectrum.  $N_i S_0^2$  changes the amplitude of the EXAFS signal independent of  $k$ . The amplitude decreases with increasing the distance from the surrounding atoms by  $1/R_i$ .  $\sin[2kR_i + \varphi_i(k)]$  describes the oscillation in the EXAFS signal with a phase represented by  $2kR_i + \varphi_i(k)$ . The phase shift of the scattered photoelectron is taken into account by multiplying its path ( $2R_i$ ) by  $k$ .  $\varphi_i(k)$  considers the shift caused by the interaction of the photoelectron with the nuclei of the absorbing atom.  $\sigma^2$  is the mean-square displacement of the bond length between both atoms considering also contributions from thermal disorder and structural heterogeneity (Debye-Waller factor).  $\lambda(k)$  is the mean free path of the photoelectron, that means the average travel distance of the electron after its excitation. Thus, the term  $e^{-2R_i/\lambda(k)}$  accounts for its inelastic scattering due to excitation of the neighboring environment by adding exponential dumping to the EXAFS signal.<sup>63, 64</sup> The EXAFS signal in  $k$  range is Fourier transformed (FT) to  $R$  range and modeled using scattering paths (Equation 7) generated by the FEFF8.2 code. The *ARTEMIS* and *ATHENA* programs parts of the IFFEFIT program package are used for extraction of the EXAFS spectrum and the modeling procedure.

### 2.2.2. Resonant inelastic X-ray scattering (RIXS) and high-energy resolution near edge structure (HR-XANES) technique

The combination of the electron excitation process and subsequent relaxation of the system by emission of a photon is called resonant inelastic X-ray scattering (RIXS).<sup>65-67</sup> Different RIXS processes are illustrated in Figure 9 on the example of the lanthanide elements ( $L_n$ )  $L_3$  edge.

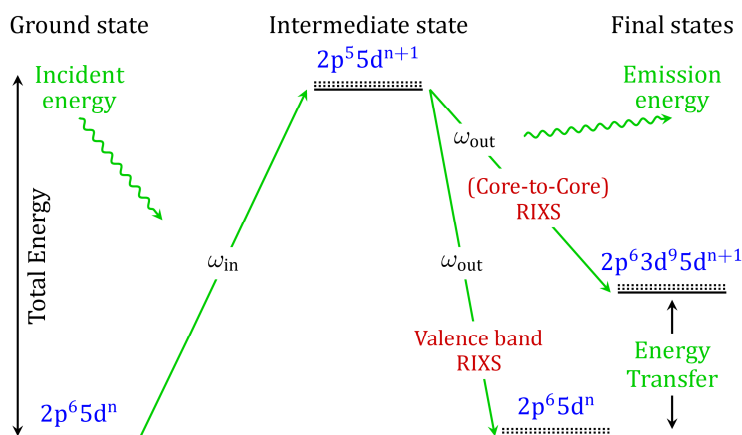


**Figure 9** Schematic illustration of the two-step RIXS processes. (Adapted with permission from Ref. <sup>54</sup>)

The incident photon excites an electron from the  $2p^6 5d^n$  ground state into the valence band creating an electron hole in the ground state. The intermediate state has an electron configuration of  $2p^5 5d^{n+1}$ . If the electron core-hole is filled by an electron from an intermediate level – in this example the  $3d$  state – the process is called Core-to-Core RIXS (throughout this work referred to as RIXS). The final state has a  $2p^6 3d^9 5d^{n+1}$  configuration. Its energy difference to the ground state is called energy transfer, i.e., the remaining energy which was transferred to the system.<sup>54</sup> If the core-hole is filled by an electron from the populated valence band (VB), the process is called valence band RIXS (VB-RIXS).<sup>68</sup> The measurement of the emission energy as a function of the excitation energy provides information about the electronic levels as its difference directly refers to the energy transfer. **Figure 10** shows a RIXS contour map of  $\text{PuO}_2$ . The fluorescence intensity is presented as function of the excitation and emission energy.

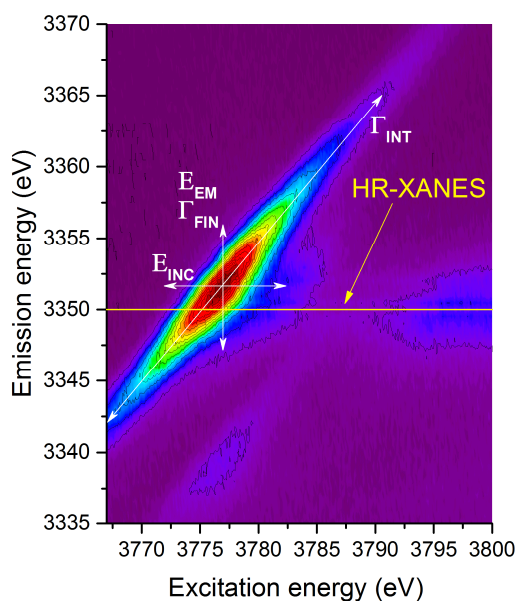


**Figure 10**  $3d4f$ RIXS of  $\text{PuO}_2$ .<sup>69</sup> The colors represent the intensity of fluorescence from blue (low) to red (high). The yellow horizontal line indicates the emission energy at which Pu  $M_5$  edge HR-XANES spectra are measured.

By recording the intensity of the emitted fluorescence as a function of the excitation energy at the “normal emission energy”, the XANES spectrum can be obtained. This correlates to a horizontal line in the RIXS spectrum.<sup>69</sup> The normal emission is determined as maximum of the emission line recorded at excitation energies well above the absorption edge. The broadening of the features visible in the RIXS spectrum (cf. **Figure 10**) depends on the finite lifetime of the core-hole due to the Heisenberg uncertainty relation ( $\Delta E \Delta t > \hbar/2$ ). With a rise in atomic number  $Z$ , the lifetime of the core-hole for one specific absorption edge decreases leading to an increased broadening.<sup>70, 71</sup> Both the broadening of the intermediate ( $\Gamma_{INT}$ ) and the final state ( $\Gamma_{FIN}$ ) determine the overall inherent broadening ( $\Gamma_{TOT}$ ) for fluorescence mode experiments.<sup>72</sup> It can be estimated as the full width at half maximum (FWHM) of a Lorentzian-type profile:

$$\Gamma_{TOT} = \frac{1}{\sqrt{\frac{1}{\Gamma_{INT}^2} + \frac{1}{\Gamma_{FIN}^2}}} \quad (11)$$

The excitation energy is by nature larger than the relaxation energy causing a higher energy uncertainty for  $\Gamma_{INT}$  than for  $\Gamma_{FIN}$ . As in transmission mode measurements, only the larger  $\Gamma_{INT}$  is considered, fluorescence mode experiments show always lower inherent spectral broadenings.<sup>54</sup>

The excitation and relaxation transitions for the  $L_3$  and  $M_{4,5}$  absorption edges which are most relevant for the investigation of  $An$ , are depicted in **Figure 11**. Electron core-holes are less stable and have therefore a shorter lifetime when located closer to the nucleus of the atom. Hence, the  $2p_{3/2}$  core-hole for  $L_3$  transitions has a total inherent core-hole broadening of ca. 3.2 eV whereas the  $3d_{3/2}$  or  $3d_{5/2}$  core-hole at the  $M_{4,5}$  edge has a significant lower broadening of approximately 1 eV.<sup>56</sup> Hämäläinen *et al.* were the first to utilize this advantage during the recording of XANES spectra of  $Ln$  with increased resolution.<sup>73</sup>

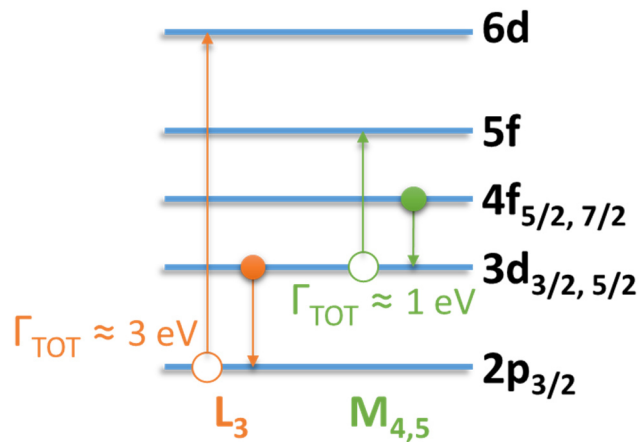


**Figure 11** Schematic illustration of electron transitions at the  $An$   $L_3$  and  $M_{4,5}$  edges.

The total broadening of the spectrum is a combination of the inherent core-hole lifetime broadening  $\Gamma_{TOT}$  and the experimental energy bandwidth  $E_{TOT}$ , which depends on the incident ( $E_{INC}$ ) and emission ( $E_{EM}$ ) energy bandwidth:

$$E_{TOT} = \sqrt{E_{INC}^2 + E_{EM}^2} \quad (12)$$

While  $E_{INC}$  is defined by the resolution of the double crystal monochromator (DCM) and the size of the incident beam spot on the sample,  $E_{EM}$  depends significantly on the detection method. In conventional measurements a solid state detector (SSD) with an energy resolution of typically more than 100 eV is used. In this case, the broadening of the spectrum is dominated by the immense experimental broadening. Exchanging the SSD by a multi analyzer crystal spectrometer (MAC-spectrometer) increases the experimental resolution to ca. 1-3 eV. Spectra recorded with a MAC-spectrometer are called high-energy resolution XANES (HR-XANES) spectra (also named partial fluorescence yield (PFY-XANES) or high-energy resolution fluorescence detected XANES (HERFD-XANES)). With this setup,  $E_{EM}$  depends on the geometry of the spectrometer and on the crystals. The setup of a MAC-spectrometer is discussed in **Section 2.2.3**. A table listing experimental parameters, absorption edges, broadenings and resolutions for the investigations presented in this study is shown in the experimental section (cf. **Table 32** in the **Appendix**). Calculated broadenings relevant for the investigation of  $Ln$  and  $An$  are listed by Prüßmann.<sup>54</sup>

The evaluation of HR-spectra greatly benefits from the enhanced energy resolution. **Figure 12** compares the U  $M_4$  edge spectra of metaschoepite ( $UO_3 \cdot 1-2H_2O$ ) recorded with conventional and HR-setup.

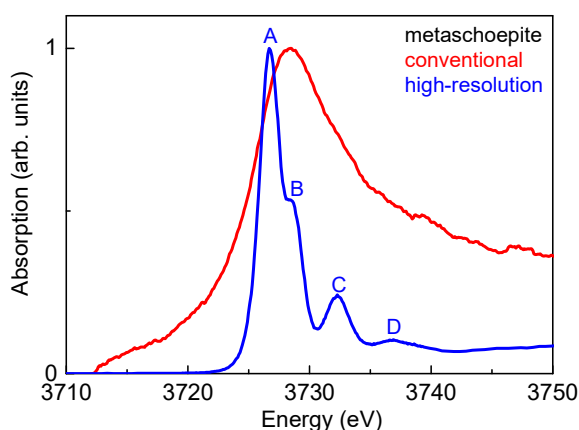


**Figure 12** XANES spectra of Metaschoepite measured with conventional and high-energy resolution setup.

The HR-spectrum reveals a sharper, more intense main peak and in the conventional measurements indistinguishable features are now well resolved and separated. In M edge

spectra, the region comprising the features **A**, **B**, **C** and **D** has a narrow energy range (approximately 20 eV). Consequently, this region is referred to as WL. Therefore, the most intense feature (cf. feature **A** in [Figure 12](#)) will be called main peak in the following discussions of M edge spectra.

As demonstrated in [Figure 11](#), the  $An$   $L_3$  edge probes unoccupied  $6d$  states and is sensitive to the coordination and crystal field splitting. Due to the short core-hole lifetime of the  $2p_{3/2}$  intermediate state it has an inherent spectral broadening of approximately 3.2 eV.<sup>70</sup> For  $An$  structural investigations the  $L_3$  edge has been used in numerous studies.<sup>5, 74-76</sup> However, the most interesting properties of the  $An$  originates from the participation of the  $5f$  valence states in the chemical bonding.<sup>77, 78</sup> The  $5f$  states can directly be probed by measuring  $An$  XANES spectra at the  $M_{4,5}$  edge recording  $4f_{5/2} \rightarrow 3d_{3/2}$  or  $4f_{7/2} \rightarrow 3d_{5/2}$  emissions.<sup>66</sup> The reduced inherent broadenings of the M edge enable the recording of very well resolved HR-XANES spectra (e.g., the core-hole lifetime broadening of the  $4f_{5/2}$  final state is approximately 0.37 eV (U  $M_4$  edge)).<sup>79</sup> As the M edge transition directly probes the  $5f$  valence states, the energy position of main spectral features is very sensitive to the oxidation state of the element. The HR-XANES spectra are an excellent instrument for the identification of  $An$  oxidation states mixed in the same material. The spectral features also contain information about the local atomic environment of the probed atom.<sup>6, 68, 76, 80</sup>

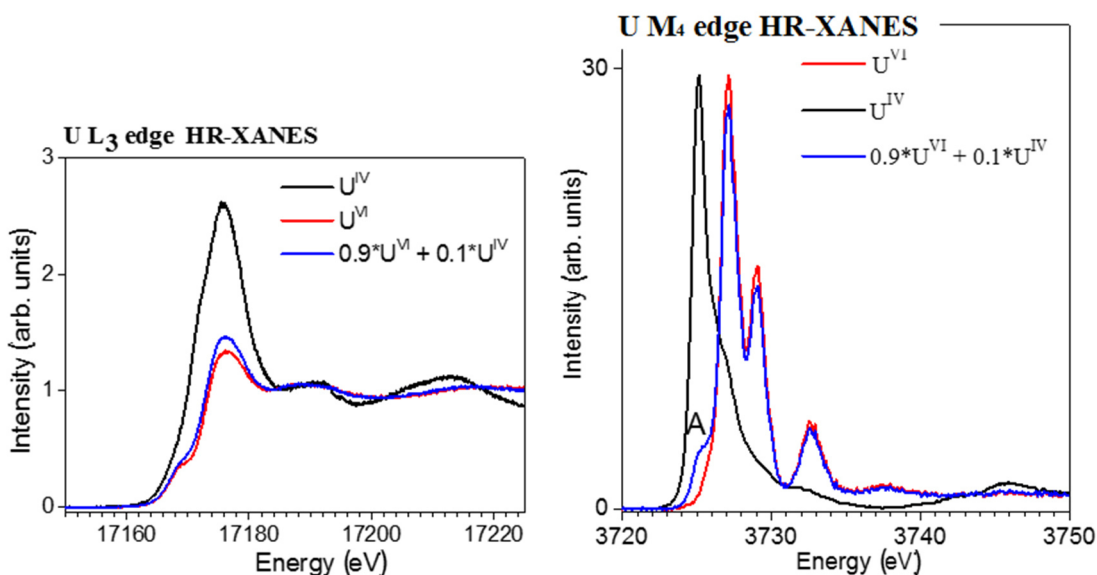


**Figure 13** U  $M_4$  edge (left) and  $L_3$  edge (right) HR-XANES spectra of U compounds containing different, pure U oxidation states shown in red and black. The blue spectrum is derived by linear combination modelling of 90% U(VI) and 10% U(IV) of the pure spectra.

**Figure 13** (left) shows the U  $L_3$  edge HR-XANES spectra of U(IV) and U(VI) reference compounds and a mixed U spectrum with 10% U(IV) and 90% U(VI) ( $0.1 \cdot U(IV) + 0.9 \cdot U(VI)$ ). The

simulated spectrum exhibits only slight differences in intensity compared to the U(VI) spectrum. Therefore, it is not possible to clearly detect and quantify the U(IV) contribution. The situation at the U  $M_4$  edge using HR-XANES is vastly superior. **Figure 13** (right) has additional absorption resonance **A** characteristic for U(IV). By performing linear combination least squares fit analyses quantitative determination of less than 10% U(IV) is possible. It was recently demonstrated that the HR-XANES technique enables to distinguish between U(IV), U(V) and U(VI) oxidation states with high sensitivity in a material containing mixed U oxides.<sup>66</sup> Therefore, the  $An M_{4,5}$  HR-XANES technique is a powerful tool for the investigation of  $An$  containing materials. The additional effort caused by the HR-setup is justified by the value of the obtained information.

It should be noticed that for the evaluation of the spectra suitable references measured in comparable conditions are essential. These references are not only necessary to determine the oxidation states but also to align sample spectra in order to compare them to each other. An example is given in **Figure 14**. The RIXS contour map was integrated at the normal emission energy for variable widths from 0.05–10 eV. The integration windows are illustrated in **Figure 14**, left. The obtained spectra are depicted in **Figure 14** right. As a function of the integration width, the main peak of the spectra shifts towards higher energies and additionally the shape of the spectrum also changes. As the position of the main peak is one of the most necessary parameters for the evaluation of the spectra it is important to measure the reference materials with the same energy resolution as the samples. The relative shifts of samples and references can then be evaluated. By aligning reference spectra with similar energy resolution, experimental spectra from different setups and with different calibrations can be shifted accordingly and compared to each other. Such processing was – for example – necessary in **Section 5**.

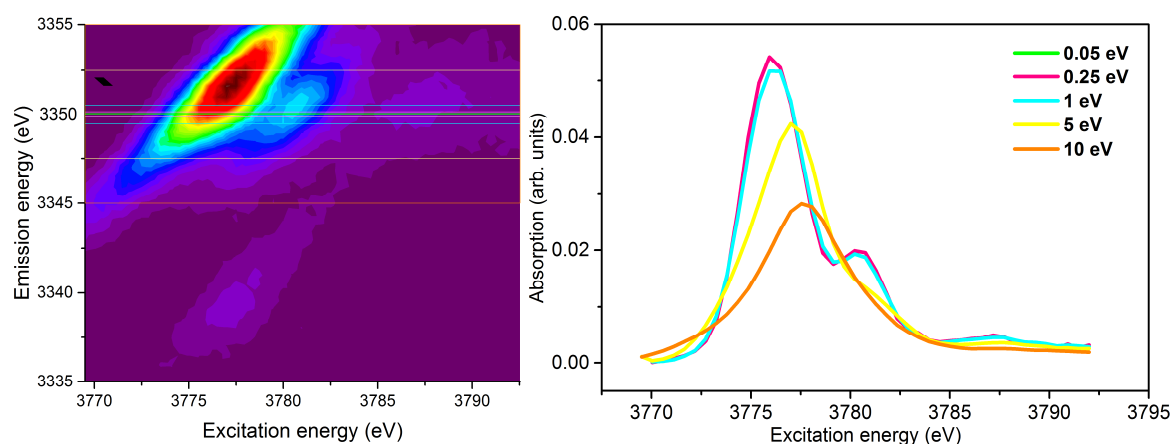


**Figure 14**  $3d4f$  RIXS contour map of  $\text{PuO}_2^{2+}$  (left). When integrated with different emission energy width (green: 0.05 eV, pink: 0.25 eV, cyan: 1 eV, yellow: 5 eV, orange: 10 eV) HR-XANES spectra with different energy resolution can be obtained (right).

It is well known in the literature, that performing an XAS experiment on a certain material, might change its properties and the speciation of its elements.<sup>81, 82</sup> The probability for X-ray induced redox process increases with increasing the X-ray flux and is more pronounced for organic compared to inorganic materials. Those induced processes are called radiation damage and can dramatically challenge the experiments and potentially lead to false results. Therefore, it is very important to evaluate the probed materials with regard to radiation damage to determine the reliability of the obtained data. An example is shown in **Figure 15**. The U(VI) containing mineral umohoite ((UO<sub>2</sub>)MoO<sub>4</sub>·H<sub>2</sub>O) was investigated by U M<sub>4</sub> HR-XANES with regard to the U oxidation state. The sample was investigated at a beamline with a very high X ray photon flux of more than 10<sup>13</sup> photons/s. The first spectrum shows a U(VI) characteristic pattern. After 5 s a shoulder at the low energy side of the main peak appears accompanied by an intensity decrease of the two main features. This trend continues when measured for another 60 s. The last spectrum reveals a very pronounced pre-edge. As this energy position is characteristic for the contribution of U(IV), it can be concluded that the exposure to the X-ray beam induces the reduction of U(VI) to U(IV). By recording preliminary spectra with short measuring time from fresh unexposed sample, comparing them with spectra recorded after long exposure time, the potential effect of radiation damage on the material can be evaluated (cf. **Figure 15**). This was done for the samples discussed in the present thesis.

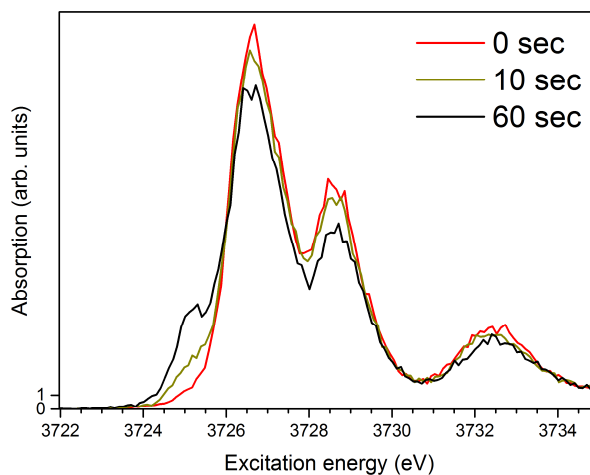


**Figure 15** U M<sub>4</sub> edge HR-XANES spectra of the U mineral umohoite. The spectra were recorded after the sample was exposed to intense X-ray radiation of the measurement for 0, 10 and 60 s.

### 2.2.3. General setup and X-ray emission spectrometer

X-ray absorption spectroscopy requires a precisely tunable X-ray source. One possibility are laboratory based installations as for example a laser-produced plasma source.<sup>83</sup> A synchrotron radiation facility is able to provide radiation of a very broad spectral range with very high intensity. High-energy electrons are deflected in magnetic fields, losing energy in a form of synchrotron radiation. A scheme of a typical synchrotron is shown in **Figure 16**. All synchrotron facilities differ in their setup, electron energy, mode of operation, etc. Typically they consist of:<sup>71</sup>

1. An electron gun (1)
2. A linear electron accelerator (2)
3. A booster ring which accelerates the electrons to their final energy (3)
4. A storage ring in which the electron beam is maintained on a specific orbit (4)
  - a. Magnetic fields focus the beam and keep the electrons in that orbit
  - b. Wiggler or undulator devices which produce the synchrotron radiation by deflecting the electrons in magnetic fields
5. Beamlines tangential to the storage ring at the wiggler/undulator positions to receive the generated light beam

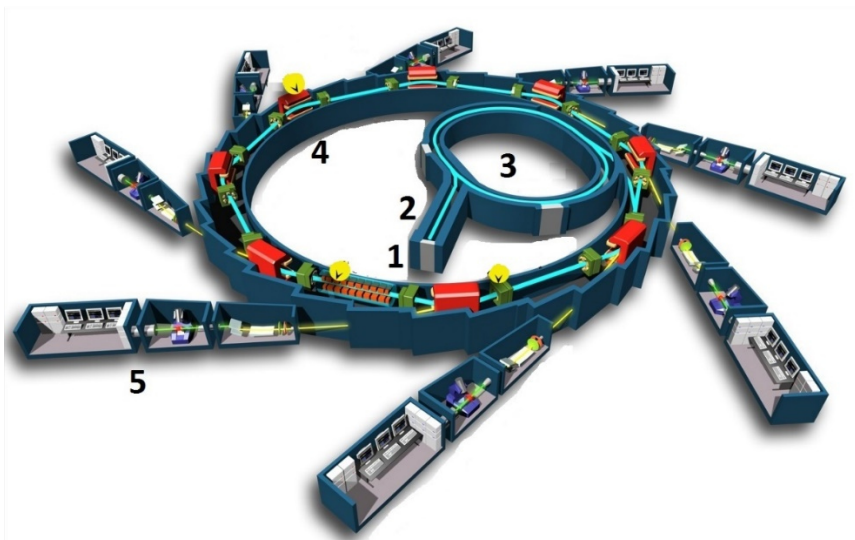


**Figure 16** Schematic illustration of a synchrotron facility. It consists of an electron gun (1), a linear accelerator (2), a booster ring (3), a storage ring (4) and several beamlines (5). (© SOLEIL synchrotron. Adapted with permission from Ref. <sup>84</sup>)

As the electron beam is deflected by the magnetic fields of a bending magnet/wiggler/undulator, it emits a spectrum of radiation along its path which is received by the beamline, schematically illustrated in **Figure 17**. One of the first components of a beamline

is a cooled slit serving as an aperture. This is necessary to reduce the heat load which is otherwise deposited on the following optical components. In the optical hutch the beam is collimated by a first mirror. In the DCM the beam is diffracted according to the Bragg law

$$n\lambda = 2d \sin(\theta) \quad (13)$$

on both crystals ( $n$  – positive integer giving the order of diffraction,  $\lambda$  – wavelength of the incident beam,  $d$  – distance between the lattice plane,  $\theta$  – diffraction angle). The monochromatized beam is then focused by the second mirror onto the sample in the experimental hutch. The first ionization chamber measures (cf. **Figure 17**), the intensity of the incident beam. There are different experimental modes for measurement of an X-ray absorption spectrum.

In transmission mode the absorption of the sample is measured before and after the sample with the help of the first and the second ionization chambers (**Equation 4**). Between the second and third ionization chambers a reference compound, commonly a thin metal foil, is positioned. This reference which has its absorption edge close to the edge of the investigated element is used for calibration of the DCM beamline and alignment of the spectra. In a fluorescence mode measurement, the emitted fluorescence of the sample is detected using a solid-state fluorescence detector. This detector records a complete emission spectrum. The energy range corresponding to the emission line of the element of interest is selected. Both modes can be considered as conventional XAS setup.<sup>71, 85</sup> For advanced HR-XANES investigations, the fluorescence detector is exchanged with a MAC-spectrometer.<sup>54</sup>

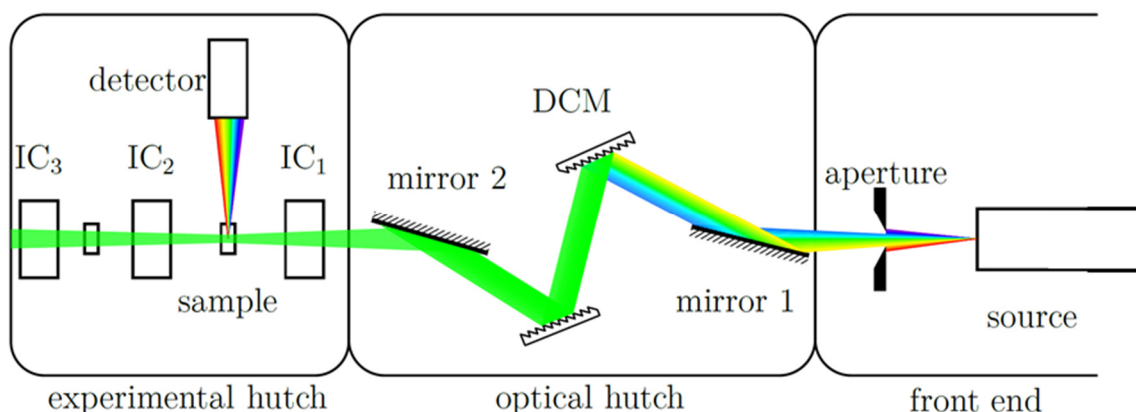


**Figure 17** Schematic illustration of a typical beamline (angles and distances are not to scale). The synchrotron ring with its radiation producing devices are named as “source”. The ionization chambers are abbreviated as IC<sub>n</sub>. (Reproduced with permission from Ref. <sup>54</sup>)

In the following section, the MAC-spectrometer build and installed by the Helmholtz Young Investigator Group (HYIG) with principle investigator Tonya Vitova is described.<sup>86</sup> The

spectrometer (cf. **Figure 18**) has been commissioned at the INE-Beamline for Actinide Research<sup>5</sup> at Angströmquelle Karlsruhe (ANKA)<sup>87</sup> synchrotron radiation facility as part of the doctoral project of Prüßmann.<sup>54</sup> In 2016 it was moved to the recently built and commissioned ACT-Beamline at ANKA (cf. **Figure 19**).<sup>88</sup>

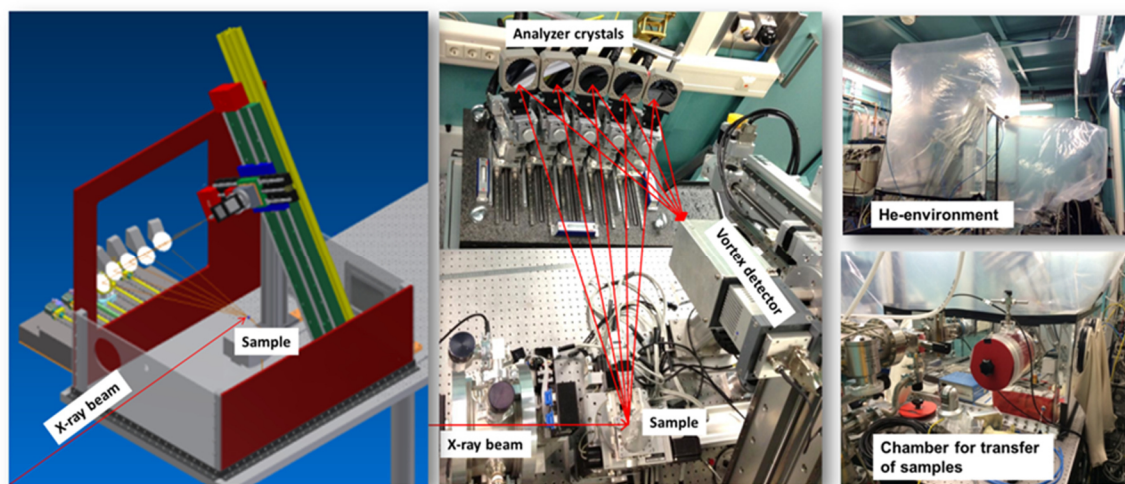


**Figure 18** 3D CAD model (left) and pictures of the MAC-spectrometer setup including the He environment chamber.

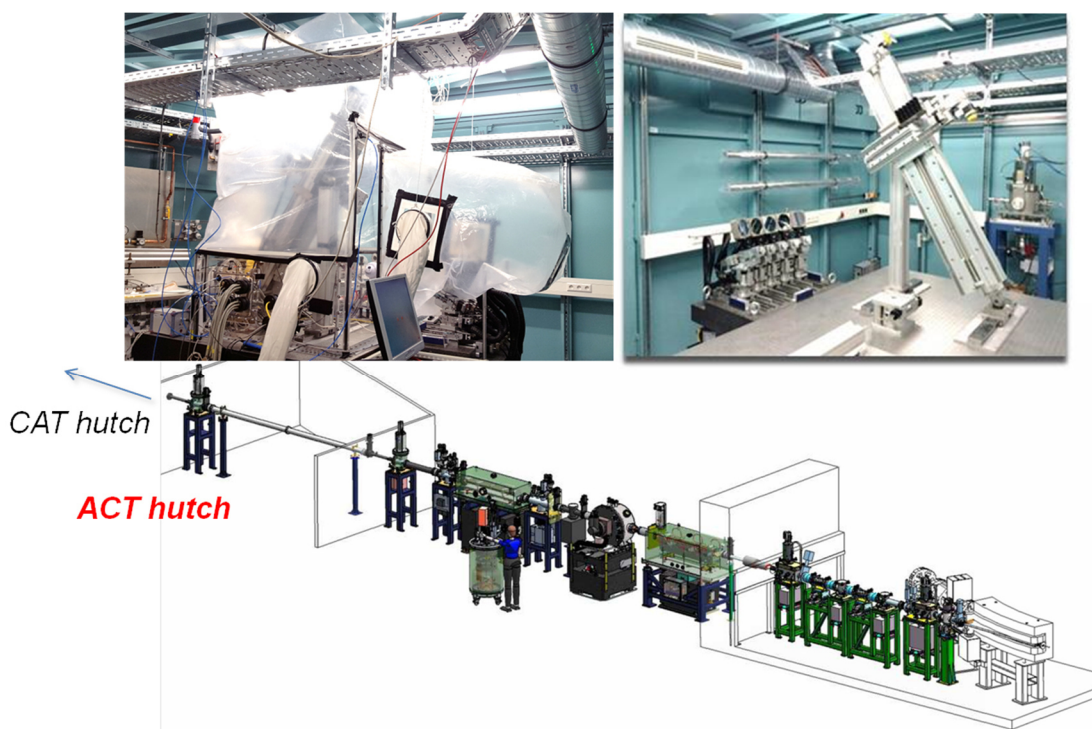


**Figure 19** Schematic illustration of the ACT-Beamline and photographic pictures of the installed spectrometer including He environment chamber.

The spectrometer is an adapted design of the spectrometer used at the ID26-Beamline at the European Synchrotron Radiation Facility (ESRF).<sup>67</sup> It is built in Johann geometry<sup>89</sup> for up to five spherically bent analyzer crystals with 1 m bending radius. Sample, crystal and detector are

positioned on a Rowland circle, whose diameter equals the bending radius of the crystal (cf. **Figure 20**).

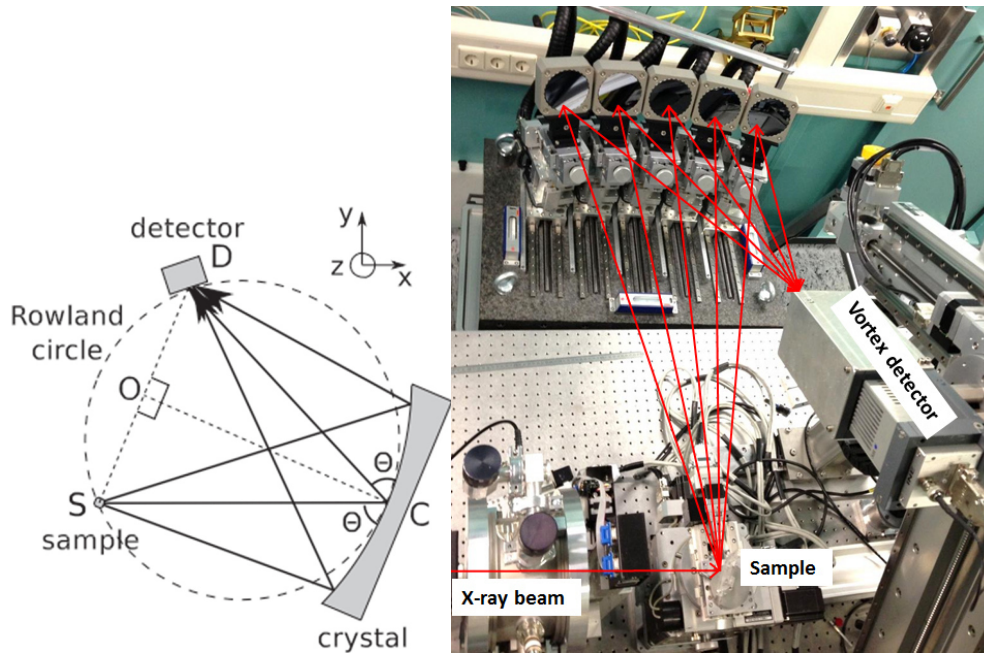


**Figure 20** Schematic illustration of the Johann geometry applied for the MAC-spectrometer (left). (Reproduced with permission from Ref. <sup>90</sup>) Picture of the installed spectrometer at the INE-Beamline at ANKA. The paths of the incident and fluorescence X-ray beams are indicated in red.

The selection of an emission energy can be achieved via the same diffraction principle as in the DCM. The position of the individual crystal is calculated according to the type of crystal (Si/Ge) used and the required Bragg angle.<sup>90</sup> Each of the five crystals possesses four degrees of freedom as shown in **Figure 21**.

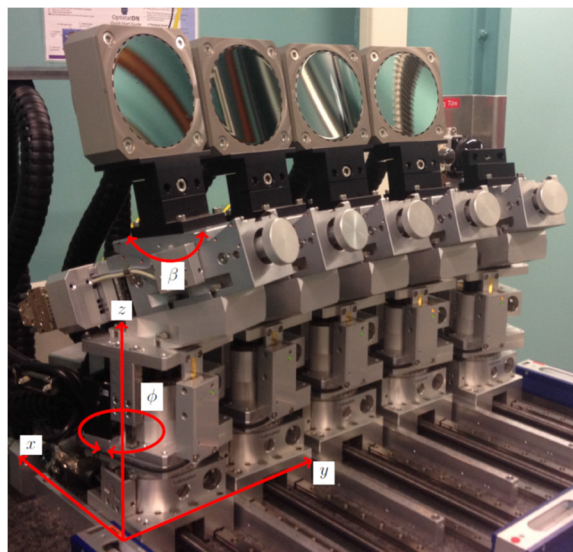


**Figure 21** Crystal positioning stages with four degrees of freedom for each crystal to fulfil the Bragg condition for the desired energy. Only four of the five crystals are mounted. (Figure taken from Prüssmann, doctoral thesis)<sup>54</sup>

For *An* M edge HR-XANES investigations a He atmosphere is essential as photons with an energy of 3–4 keV are absorbed in air within several centimeters.<sup>91</sup> Therefore, a He environment setup has been designed and assembled comprising the HYIG MAC-spectrometer and maintaining a 99% He-atmosphere (cf. [Figure 22](#)).



**Figure 22** He environment for the MAC- spectrometer for low energy HR-XANES measurements with energies of 3-4 keV.

### 3. Experimental section

#### Methods and Materials

##### Raman Spectroscopy

The polarized Raman spectra were measured at room temperature with a *SENTERRA Dispersive Raman-Microscope* equipped with an *Andor CDD* detector and a 10x or 20x objective with spectral resolution of 3-5  $\text{cm}^{-1}$ . Either a green ( $\lambda = 532 \text{ nm}$ ) or a red ( $\lambda = 785 \text{ nm}$ ) laser diode with a power of 10/25 mW (green laser) and 50 mW (red laser) was used for excitation. Spectra recorded in a spectral range of 90-1560  $\text{cm}^{-1}$  (green laser) and 60-1560  $\text{cm}^{-1}$  (red laser). For evaluation of the data the *OPUS* program (*Bruker*) was used.<sup>92</sup> If not stated otherwise, the spectra were neither background corrected nor normalized.

##### X-ray photoelectron spectroscopy (XPS)

XPS spectra were recorded with an *ULVAC-PHI, VersaProbe II* spectrometer, X-ray source: monochromatic Al  $K_{\alpha}$  ( $h\nu = 1486.7 \text{ eV}$ ), ellipsoidal shaped monochromator, source power 31 W, with an electron take-off angle of  $45^{\circ}$  (sample surface plane relative to analyzer). The X-ray beam had a diameter of 200  $\mu\text{m}$ . Survey spectra were collected with an analyzer pass energy of 187.85 eV and a step size of 0.8 eV, high resolution spectra with an analyzer pass energy of 23.5 eV and a step size of 0.1 eV (FWHM Ag  $3d_{5/2}$  line 0.67 eV).

##### Scanning electron microscope (SEM) and energy-dispersive X-ray spectroscopy (EDX)

Scanning electron microscopy images were recorded on a *FEI Quanta 650 FEG* instrument equipped with a field emission electron source and an *Everhart-Thornley-Detector* for secondary electron detection in high vacuum. Images were recorded by a backscattered electron detector. In **Environmental Scanning Electron Microscope (ESEM)** mode, an atmosphere of 50 or 60 Pa of water vapor was maintained inside the analysis chamber. EDX was performed with a *Thermo Scientific UltraDry Silicon* drift detector and the data were evaluated by the *NSS* software, version 3.3 (*Thermo Scientific*).

##### Transmission electron microscopy (TEM)

Samples for transmission electron microscopy (TEM) were crushed in a mortar, mixed with ethanol and dispersed on a carbon thin film on a Cu grid sample holder. The electron beam was accelerated with 200 kV in a *FEI Tecnai G2 F20 X Twin* microscope.

### X-ray powder diffraction (XRD)

The X-ray powder diffractograms were recorded with a *Bruker Advance D8* diffractometer using Cu-K $\alpha$ -radiation ( $\lambda = 0.15406$  nm) and Bragg-Brentano ( $\theta$ - $2\theta$ )-geometry (U= 40 kV, I = 40 mA). If not stated otherwise, the samples were measured at room temperature with a step size of  $0.01^\circ$  while rotated with  $15 \text{ min}^{-1}$ .

### Infrared spectroscopy (IR)

The IR spectra were recorded at room temperature with a *Bruker IFS55 Equinox* spectrometer in a *Pike MIRacle ATR* cell in a spectral range of  $400\text{-}4000 \text{ cm}^{-1}$  with a spectral resolution of  $4 \text{ cm}^{-1}$  and a scanning speed of 5 kHz. The instrument is equipped with a *DLaTGS* detector. Powder samples were investigated. For evaluation of the data the OPUS program (*Bruker*) was used. For better identification spectra were stretched along the y-axis.

### Extended X-ray absorption fine structure spectroscopy (EXAFS)

An L $_3$  EXAFS investigations are described in **Section 4.1.1** and **4.2.1**, respectively.

### High-energy resolution X-ray absorption near edge structure (HR-XANES)

U M $_4$  (3728 eV), Np M $_5$  (3664 eV) and Pu M $_5$  (3775 eV) edge HR-XANES experiments have either be performed at INE-Beamline<sup>5</sup> or at the CAT-ACT-Beamline<sup>88</sup> both at ANKA synchrotron radiation facility in Karlsruhe, Germany. Some of the U M $_4$  HR-XANES measurements were carried out at the ID26-Beamline<sup>93</sup> at ESRF synchrotron in Grenoble, France.

The same reference material was measured before and/or after each sample. If an energy shift was detected, the spectra of the sample were shifted accordingly. This procedure enables the comparison of spectra of one sample measured in different injection runs and experimental campaigns. Comparison of spectra measured at different beamlines is also possible following this procedure but any differences in the experimental energy resolution needs to be taken into account during the analyses.

*PyMca* software package<sup>94</sup> was used for data evaluation and merging of the spectra which were then plotted with the *Origin* software<sup>95</sup>.

### ID26-Beamline, ESRF<sup>93</sup>

At the ID26-Beamline, the DCM was equipped with two Si(111) crystals. Higher harmonics were rejected by three Si mirrors at an angle of  $3.5 \text{ mrad}$  (U M $_4$  edge) relative to the incident beam. The beam size was focused to ca.  $0.150 \text{ mm}$  vertical and  $0.450 \text{ mm}$  horizontal size. An identical in construction MAC-spectrometer as installed at INE- and later CAT-ACT-Beamline

and described in **Section 2.2.3** was also used at ID26-Beamline. A bag made of synthetic foil and filled with He gas was installed between the sample, the crystals and the detector to minimize intensity losses due to scattering and absorption of photons in the tender X-ray regime. The X-rays entered and left the He bag via polypropylene windows.

The energy resolution was determined to be 0.7 eV by measuring the FWHM of the elastic peak (cf. **Table 1**).

#### *INE-Beamline, ANKA<sup>5</sup>*

The INE-Beamline covers an energy range of 2.1-25 keV. A 1.5 T bending magnet generates a photon flux of  $10^{10}$  photons/s at the Pu L<sub>3</sub> edge. The primary X-ray beam was vertically collimated by a cylindrically bent Rh coated mirror, monochromatized by a Si(111) DCM and focused by a toroidal double-focusing Rh coated mirror to  $0.5 \times 0.5$  mm<sup>2</sup> onto the sample (cf. **Table 1**). A detailed description of the INE-Beamline is reported by Rothe *et al.*<sup>5</sup>

#### *CAT-ACT-Beamline, ANKA<sup>88</sup>*

The primary X-ray beam was vertically collimated by a cylindrically bent Si coated mirror, monochromatized by a Si(111) DCM and focused by a toroidal double-focusing Si coated mirror to  $1 \times 1$  mm<sup>2</sup> onto the sample (cf. **Table 1**). A detailed description of the INE-Beamline is reported by Zimina *et al.*<sup>88</sup>

#### *HR-XANES experiments*

U M<sub>4</sub> (3728 eV), Np M<sub>5</sub> (3664 eV) and Pu M<sub>5</sub> (3775 eV) edge HR-XANES spectra were recorded by using a MAC-spectrometer, described in **Section 2.2.3**. The same spectrometer is used at the INE-Beamline and the CAT-ACT-Beamline. The X-ray fluorescence was diffracted by five spherically bent Si(220) crystal analyzers (Saint-Gobain Crystals, France) with 1 m bending radius and focused onto the single diode VITUS KETEK silicon drift detector (SDD). The crystals were aligned at the Bragg angles listed in **Table 32** in the **Appendix**. The sample, crystals and detector were arranged in 5 vertical Rowland circles intersecting at the sample surface and the detector entrance window.<sup>90,54</sup> A gas tight box enclosing the spectrometer and the sample maintaining a constant He atmosphere during all measurements was installed to avoid intensity losses due to scattering and absorption of photons in the tender X-ray regime.

For Pu M<sub>5</sub> and U M<sub>4</sub> edge HR-XANES studies, the DCM was calibrated by assigning 3775 eV and 3728 eV to the maximum of the main peak of the spectrum of a PuO<sub>2</sub> and a UO<sub>2</sub> reference sample, respectively.

At the CAT-ACT-Beamline to achieve the highest resolution, the beam size was confined to 500 x 500 μm size by applying a pinhole in front of the sample and additional masks giving access only to the central section of the analyzer crystals.

Details about the Np M<sub>5</sub> HR-XANES studies are reported in **Section 4.2.1**.

**Table 1** Beamtime characteristics of the An M<sub>4,5</sub> HR-XANES measurements.

Date	Beamline	DCM	Spot size (mm <sup>2</sup> )	Pinhole	Focusing mirror	Energy resolution	Photon flux (photons/s)
April '14	ID26, ESRF	Si(111)	0.15 x 0.45	-		0.7 eV elastic scattering	10 <sup>13</sup> (4 keV)
June '14	ID26, ESRF	Si(111)	0.15 x 0.45	-		0.7 eV elastic scattering	10 <sup>13</sup> (4 keV)
Sept '14	INE, ANKA	Si(111)	0.5 x 0.5	-	Rh	3.73 eV FWHM PuO <sub>2</sub>	10 <sup>10</sup> (18 keV)
March '15	INE, ANKA	Si(111)	0.5 x 0.5	-	Rh	1.2 eV elastic scattering (3349 eV)	10 <sup>10</sup> (18 keV)
Nov '15	INE, ANKA	Si(111)	0.5 x 0.5	1 mm	Rh	1.65 eV elastic scattering (3341.0 eV), 3.27 FWHM PuO <sub>2</sub>	10 <sup>10</sup> (18 keV)
Nov '16	CAT-ACT, ANKA	Si(111)	1 x 1	500 x 500 μm slit	Si	2.73 eV FWHM PuO <sub>2</sub>	10 <sup>12</sup> (20 keV)

### Redox references

The Pu(IV)O<sub>2</sub> reference sample **#1** was prepared as follows: PuO<sub>2</sub> powder was filled in the hole of a stainless steel washer with 15 mm diameter which was glued on a Kapton tape. Washer and PuO<sub>2</sub> powder were covered with 13 μm Kapton foil and sealed with a Kapton tape. Two more washers were used to create a second independent containment by using 8 μm Kapton foil and a Kapton tape. Pu(III) and Pu(VI)O<sub>2</sub><sup>2+</sup> reference solutions **#2** (0.02 M each) were electrochemically prepared in 1 M HClO<sub>4</sub>/NaClO<sub>4</sub>. They are denoted as Pu(III)<sub>aq</sub> and Pu(VI)<sub>aq</sub>.<sup>56, 69</sup> The Pu(III) and Pu(VI) oxidation states were confirmed (99% purity) by Vis-NIR spectroscopy. The preparation and characterization of the PuO<sub>2</sub> reference sample **#3** is described by Prieur *et al.*<sup>96</sup>. For pellet pressing, 1 mg PuO<sub>2</sub> was mixed with 20 mg BN. The sample was placed in the inner parts of Al cell (cf. **Figure 46**). The inner and outer compartments of the cell were covered with Kapton windows with 13 and 8 μm thick Kapton foils, respectively.

The preparation and characterization of the PuO<sub>2</sub> reference sample **#3** is described by Prieur *et al.*<sup>96</sup>. For pellet pressing, 1 mg PuO<sub>2</sub> was mixed with 20 mg BN. The sample was placed in the inner parts of Al cell (cf. **Figure 46**). The inner and outer compartments of the cell were covered with Kapton windows with 13 and 8 μm thick Kapton foils, respectively.

The preparation and characterization of the solid samples **#4**, **#5**, and **#6** NpO<sub>2(am,hyd)</sub><sup>97</sup>, Ca<sub>0.5</sub>NpO<sub>2</sub>(OH)<sub>2</sub>·1.3H<sub>2</sub>O<sup>98</sup> and Na<sub>2</sub>Np<sub>2</sub>O<sub>7(cr)</sub><sup>99</sup> are described in Fellhauer *et al.*<sup>100, 101</sup> 2 mg of Np containing suspension was used for each Np sample. The samples were placed in the inner parts of Al cells (cf. **Figure 46**). The inner and outer compartments of the cells were covered with Kapton windows with 13 and 8 μm thick Kapton foils, respectively.

$\text{NpO}_2$  crystallizes in the same  $\text{CaF}_2$ -type lattice as  $\text{UO}_2$ . Np is thereby coordinated by eight O atoms in a distance of ca. 2.35 Å.<sup>102</sup> The Np(V) reference compound exhibits neptunyl structure with two short-bound O atoms similar to the uranyl structure.  $\text{Na}_2\text{Np}_2\text{O}_7$  forms a monoclinic crystal lattice in which Np is bound to O atoms in 1.64 Å and 2.55 Å distance in a neptunate structure.<sup>103</sup>

U containing metastudite mineral served as a U(VI) reference #7. The material was crushed, mixed with cellulose powder and pressed to a 13 mm pellet with approximately 1 mm thickness by a hand press.

The  $\text{UO}_2$  pellet #8 had a mass of 900 mg and an activity of ca. 11000 Bq. It was kept at ambient conditions. It was sealed in a containment of 8 µm and 13 µm Kapton foil by Kapton tape.  $\text{U}_4\text{O}_9$  and  $\text{U}_3\text{O}_8$  (#9 and #10) were provided by *JRC-Karlsruhe*.  $\text{U}_3\text{O}_8$  was prepared by oxidizing  $\text{UO}_2$  powder in air at 1000 °C for 8 h. The obtained powders were pressed and sintered in air.  $\text{U}_4\text{O}_9$  was prepared by mixing  $\text{UO}_2$  and  $\text{U}_3\text{O}_8$  powder in order to obtain a  $\text{UO}_{2.25}$  stoichiometry, followed by pellet pressing and heating at around 400 °C in an  $\text{H}_2/\text{H}_2\text{O}$  or  $\text{CO}/\text{CO}_2$  atmosphere maintaining a suitable O potential to obtain  $\text{U}_4\text{O}_9$ .

**Table 2** Redox reference samples used in different beamtimes.

No.	Reference	Oxidation state	Provided by	Used in beamtime
#1	$\text{PuO}_2$	Pu(IV)	KIT-INE (Bohnert/Bahl)	March '15
				Nov '15
				Nov '16
#2	$\text{Pu(III)}_{\text{aq}}$ and $\text{Pu(VI)}_{\text{aq}}$	Pu(III) and Pu(VI)	KIT-INE (Pidchenko)	Sept '14
#3	$\text{PuO}_2$	Pu(IV)	JRC-Karlsruhe (Prieur)	Sept '14
#4	$\text{NpO}_{2(\text{am})}$	Np(IV)	KIT-INE (Fellhauer/Gaona)	March '15
#5	$\text{Ca}_{0.5}\text{NpO}_2(\text{OH})_2 \cdot 1.3\text{H}_2\text{O}$	Np(V)	KIT-INE (Fellhauer/Gaona)	March '15
#6	$\text{Na}_2\text{Np}_2\text{O}_7$	Np(VI)	KIT-INE (Fellhauer/Gaona)	March '15
				Sept '14
				Nov '15
#7	Metastudite	U(VI)	KIT-INE (Pidchenko)	Nov '16
				Nov '15
				Nov '16
#8	$\text{UO}_2$	U(IV)	KIT-INE (Bohnert/Bahl)	Nov '15
				Nov '16
				April '14
#9	$\text{U}_4\text{O}_9$	U(IV) and U(V)	JRC-Karlsruhe	March '15
				Nov '15
				Nov '16
#10	$\text{U}_3\text{O}_8$	U(V) and U(VI)	JRC-Karlsruhe	April '14
				March '15
				Nov '15
#11	$\gamma\text{-UO}_3$	U(VI)	JRC-Karlsruhe (Cameco)	Nov '16
				Nov '15
				April '14
#12	$\text{UO}_2$	U(IV)	JRC-Karlsruhe	Sept '14
				April '14

The preparation of the  $\text{UO}_2$  reference **#8** is described in **Section 5.1** (sample **U3**). **#9** to **#12** were pressed cellulose pellets with diameter of 4 mm and 5 wt% U.  $\gamma\text{-UO}_3$  (**#11**) was commercially obtained (*Cameco Corp.*) while **#9**, **#10** and **#12** were synthesized by *JRC-Karlsruhe*.

## 4. Actinide (*An*) characterization in a Pu rich and genuine nuclear waste glass

### 4.1. Pu rich borosilicate glass

High-level nuclear waste with low Pu content is typically generated from reprocessing of commercial spent nuclear fuel (SNF) and is commonly immobilized in glass matrices (cf. **Section 2.1.2**). Borosilicate glass is most often applied for example in France, USA, India and UK.<sup>32, 33, 104, 105</sup> The quantity of Pu is well below 1 wt% in these waste glass products and Pu management is of less consideration compared to highly radioactive fission products and volatile (e.g., Cs and Tc) as well as low-soluble (e.g., Mo, Pt, Ru etc.) constituents of SNF.

Pu enriched defense waste is of high concern and requires tailored immobilization strategies.<sup>3</sup> Waste products of chemically and microstructurally homogenous nature are often an essential requirement for its safe long-term disposal in an underground nuclear waste repository (cf. **Section 2.1**). Beside crystalline ceramics, borosilicate glasses are also discussed as appropriate matrices.<sup>106</sup> However, formation of separate phases heterogeneously distributed in the glass can lead to differential swelling and/or poor leaching performance in a worst case scenario of ground water intrusion.<sup>35, 50</sup> The Pu solubility is restricted to a few weight percent in most common glasses. Vienna *et al.* composed an aluminosilicate glass, which is able to incorporate up to 11 wt% of PuO<sub>2</sub> in its matrix.<sup>107</sup> A higher Pu loading was only reported by Feng *et al.*<sup>108</sup> By reducing Pu to its trivalent state, during vitrification, an equivalent to 10-25 wt% PuO<sub>2</sub> was homogeneously incorporated in a glass matrix without forming any Pu rich agglomerates. This study illustrates that not only the glass composition, but even to higher extent the oxidation state of Pu is the crucial factor for the Pu solubility in glass matrices. Likewise Schreiber and Balazs demonstrated that up to 40 wt% U(VI) can be incorporated, whereas the solubility limit for U(IV) does not exceed 9 wt%.<sup>109</sup> This behavior can be explained by the mechanism describing the accommodation of the actinide (*An*) elements in the glass network. Depending on their oxidation state, the *An* can play the role of either network-forming or network-modifying elements and thereby their solubility limits can be greatly variable (cf. **Section 4.2**). Deschanel *et al.* concluded, that the way of incorporation can be predicted for all cations according to their charge and distance to the next oxygen atoms (Dietzel's field strength).<sup>35</sup> The Pu(III) resembles the network-modifying elements while the Pu(IV) species has more a network-forming behavior.

Tailored glass compositions and vitrification processes leading to desired oxidation states of the *An* elements require sensitive characterization methods. One of the widely used tools for

determination of the oxidation states of the *An* elements is the *An* L<sub>3</sub> edge X-ray absorption near edge structure (XANES) technique (cf. **Section 2.2.1**). However, due to the large spectral core-hole lifetime broadening contributing to the *An* L<sub>3</sub> edge XANES (7.8 eV)<sup>70</sup>, the spectrum is insensitive to the presence of minor amounts of *An* oxidation states.<sup>57, 110</sup>

Deschanel *et al.* studied the Pu solubility in borosilicate glass and prepared several homogeneous glasses with increasing Pu content (0.85-8 wt% PuO<sub>2</sub>) and variable amount of reducing agent.<sup>35</sup> They characterized the Pu oxidation state by the Pu L<sub>3</sub> edge XANES technique and reported stabilization of Pu in its tetra- and trivalent oxidation states. We have reexamined the oxidation states of Pu in the same glass samples reported by Deschanel *et al.* applying the more advanced Pu M<sub>5</sub> edge high-energy resolution XANES (HR-XANES) method. The *An* M<sub>4,5</sub> HR-XANES technique recently emerged as a valuable direct probe of the *An* 5f valence orbitals, which are largely responsible for the chemical bonding in the *An* compounds.<sup>5, 6, 68, 69, 78</sup> It was demonstrated that the spectra are very sensitive to the *An* oxidation states and allow, e.g., to distinguish between U(IV), U(V) and U(VI) species when mixed in the same material, not easily possible with other spectroscopy techniques (cf. **Section 2.2.2**).<sup>6, 110, 111</sup> This method probes the bulk of the material (1 μm penetration depth) and does not require vacuum conditions as, e.g., the laboratory based surface sensitive X-ray photoelectron spectroscopy (1-10 nm penetration depth). Due to the drastically reduced core-hole lifetime broadening (0.5 eV)<sup>69</sup> contributing to the spectrum compared to the Pu L<sub>3</sub> absorption edge (7.8 eV)<sup>70</sup> and the improved experimental energy resolution, the spectral resolution is significantly enhanced, providing more reliable access to the *An* oxidation states.

We provide new insights into the redox behavior of Pu, which controls its solubility in glass matrices. The Pu oxidation state and its local atomic environment, probed with Pu L<sub>3</sub> edge EXAFS, are correlated to the applied vitrification conditions and the added amount of reducing agent. The first application of the Pu M<sub>5</sub> edge HR-XANES technique for oxidation state characterization of Pu with the specific example of Pu incorporated into borosilicate glasses is reported. We demonstrate the need for development and application of such advanced methods for investigations of complex nuclear waste products.

### 4.1.1. Experimental

#### Preparation of samples

The Pu doped glasses were synthesized and prepared in the Atalante laboratories of the *Commissariat à l'énergie atomique et aux énergies alternatives* (CEA) Marcoule Centre, France. The chemical composition of the Pu glass and the preliminary structural analyses can be found in the publication of Deschanel *et al.*<sup>35</sup>

**Table 3** Glass frit compositions used to vitrify Pu.<sup>35</sup>

(a) Complex composition (wt%)					
SiO <sub>2</sub>	45-46	Li <sub>2</sub> O	2	Cs <sub>2</sub> O	1
B <sub>2</sub> O <sub>3</sub>	14-15	Fe <sub>2</sub> O <sub>3</sub>	3	BaO	0.5-0.6
Na <sub>2</sub> O	10-11	MoO <sub>3</sub>	2-3	SrO	0.3-0.4
Al <sub>2</sub> O <sub>3</sub>	5	ZrO <sub>2</sub>	2-3	REE oxides	3-4
CaO	4	ZnO	2-3	Other oxides	2-3

(b) Simplified composition (wt%)					
SiO <sub>2</sub>	59	Al <sub>2</sub> O <sub>3</sub>	4.3	ZnO	3.2
B <sub>2</sub> O <sub>3</sub>	18	CaO	5.2	ZrO <sub>2</sub>	0.7
Na <sub>2</sub> O	7	Li <sub>2</sub> O	2.6		

Two different base glass compositions were used for the synthesis. For the glasses molten at reducing conditions (**G2-G4**, cf. **Table 3** (b)) a simplified composition was used instead of the complex composition applied for the **G1** glass (cf. **Table 3** (a)). As the simplified composition contains the major constituents of the complex composition, both glasses are considered to be structurally similar. This was additionally shown by molecular dynamics calculations.<sup>112</sup>

Pu-239 oxide (cf. **Table 33** in the **Appendix**) dissolved in 1.6M nitric acid solution under aerobic conditions was added to the glass frit before melting. No redox state adjustment and no redox state analysis was performed for the Pu solutions. Reducing conditions were obtained by adding Si<sub>3</sub>N<sub>4</sub> for the **G2-G4** samples (cf. **Table 4**). R corresponds to the quantity of Si<sub>3</sub>N<sub>4</sub> used in relation to the amount of Pu. It was experimentally optimized by studying the reduction of Ce(IV) to Ce(III) in the same glass and synthesis conditions but without HNO<sub>3</sub> feeding.<sup>113</sup> A theoretical R value of 0.07 did not yield any Ce(III). Therefore, the reducing agent was applied with threefold excess obtaining predominantly Ce(III). For application to the Pu glass the required amount was calculated and increased across-the-board 50% to consider the feeding via HNO<sub>3</sub>. The nitrate salts are reduced to NO<sub>x</sub> species, consuming addition electrons. As every Si<sub>3</sub>N<sub>4</sub> molecule delivers at least 20 electrons (assuming the N oxidation to NO), per Pu atom ca. 0 (**G1**), 14 (**G2**), 22 (**G3**) and 29 (**G4**) electrons were available without considering the nitrate reduction and oxidation processes by air which cannot be quantified with the available

data. As redox processes in glass melts are always influenced by several parameters, the stoichiometric reaction control is challenging. Therefore, these values are only for orientation and the redox system was optimized by using the Ce(III) surrogate system. R is listed along with the Pu loading in [Table 4](#).

The four Pu doped glass samples **G1-G4** were mounted in a Plexiglas cell equipped with Kapton windows with 13 and 8  $\mu\text{m}$  thickness serving as inner and outer containment, respectively (cf. [Figure 94](#) in the [Appendix](#)). This preparation was performed in the glove boxes of the Atalante laboratories by S. Peugot and J. Delrieu. The custom-made sample holder was designed by A. Gensch and S. Bahl in the KIT-INE.

**Table 4** Fabrication characteristics of Pu doped glasses;  $R = m(\text{Si}_3\text{N}_4)/m(\text{PuO}_2)$ .

Sample	Melting temperature ( $^{\circ}\text{C}$ )	$m(\text{PuO}_2)$ (wt%)	Atmosphere	Crucible material	R
<b>G1</b>	1200	0.85	Ar	Pt	0
<b>G2</b>	1400	2.00	Ar	Pt	0.37
<b>G3</b>	1400	4.00	Ar	Pt	0.56
<b>G4</b>	1400	8.00	Ar	Pt	0.73

## Methods and Materials

### *Pu M<sub>5</sub> edge HR-XANES spectroscopy*

The samples were investigated at the INE-Beamline and CAT-ACT-Beamline in November 2015 and 2016, respectively, according to the setup described in [Section 3](#).

The used Pu references are listed in [Table 2](#). For measurement of the Pu M<sub>5</sub> edge HR-XANES (3775 eV) spectra the MAC-spectrometer described in [Section 2.2.3](#) was used. Spectra were recorded with three different experimental energy resolutions, which we denote as “low” (recorded in September 2014 beamtime), “medium” (recorded in November 2015) and “high” (recorded in November 2016). The Pu(III)<sub>aq</sub> and Pu(VI)<sub>aq</sub> spectra were measured at the INE-Beamline with low energy resolution. The spectra of the **G1-G4** glasses and the PuO<sub>2</sub> reference material were recorded with both medium (INE-Beamline) and high (CAT-ACT-Beamline) experimental energy resolutions (cf. [Section 3](#), [Table 2](#)). The differences in the resolution are due to variations in the beam size on the sample and the experimental energy resolution of the DCMs at the two beamlines. To achieve the highest resolution, the beam size was confined to 500 x 500  $\mu\text{m}$  size by applying a pinhole in front of the sample and additional masks giving access only to the central section of the analyzer crystals. For the medium experimental energy resolution, the FWHM of the incident beam (3341.0 eV) elastically scattered from a Teflon

sample was 1.65 eV. The most intense absorption resonances of PuO<sub>2</sub> spectra measured with the three different experimental energy resolutions exhibit a FWHM of 3.73 (low), 3.27 (medium) and 2.73 eV (high resolution), respectively (cf. **Section 3, Figure 23**).

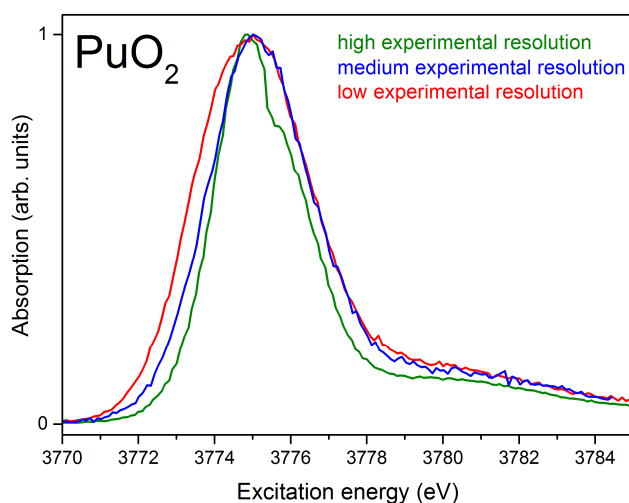


**Figure 23** Pu M<sub>5</sub> HR-XANES spectra of PuO<sub>2</sub> measured with different experimental energy resolutions.

Pu M<sub>5</sub> HR-XANES spectra for the PuO<sub>2</sub> reference were measured after each Pu glass analysis to verify the calibration of the DCM. Spectra were recorded from 3760-3835 eV with varying step sizes (3760-3770 eV: 0.5 eV; 3770-3790 eV: 0.1 eV; 3790-3835 eV: 0.5 eV) and 10 (medium resolution)/ 30 (high resolution) s/step integration time. Typically, two to three scans were collected at room temperature and averaged. All spectra were normalized to the maximum absorption intensity. The energy positions of the different absorption resonances were obtained by fitting the spectra with several Gaussian and one arctangent function. The fit was performed with the Fityk curve fitting software v.0.9.8 (<http://fityk.nieto.pl/>) which uses the Levenberg–Marquardt least-squares algorithm (cf. **Table 34** in the **Appendix**). **Figure 95** in the **Appendix** depicts exemplarily the **G1** spectrum and its fit.

#### Pu L<sub>3</sub> edge XAS spectroscopy

Pu L<sub>3</sub> edge XANES and EXAFS experiments were also performed at the INE-Beamline. The DCM, which is equipped with a D-MOSTAB, was used with two Ge(422) crystals and the spectra were recorded in transmission detection mode using three ionization chambers filled with Ar. Zr (K edge = 17998 eV) foil was simultaneously measured with all samples to control the energy calibration of the DCM. Four to six scans were collected at room temperature and averaged for each sample in the range of 17877-19306 eV; a 0.5 eV step size was used in the XANES region of the spectra and equidistant k steps (0.04 Å<sup>-1</sup>) in the post edge EXAFS region. The averaged Pu L<sub>3</sub> edge XANES scans were normalized by subtraction of a linear background function from the featureless pre-edge region and normalization of the edge jump to unity. The

WL energy position was obtained by determining the x-axis intercept of the first derivative spectra.

The EXAFS spectra ( $\chi(k)$ ) were extracted, Fourier transformed and modelled using the ATHENA and ARTEMIS programs included in the IFEFFIT program package.<sup>114</sup> The spectra were weighted by  $k = 1, 2$  and  $3$  within the  $k = 2.4\text{-}10.3 \text{ \AA}^{-1}$  range. Hanning windows with  $dk = 2 \text{ \AA}^{-1}$  sills were used ( $dk$  is the width of the sill used in the FT windows)<sup>115</sup>. The fit was performed in R space for  $R = 1.3\text{-}2.46 \text{ \AA}$  range. The single scattering paths used in the modelling were generated with the FEFF8.2 code using the  $\text{PuO}_2$  fluorite structure (ICSD collection code 55456).<sup>116</sup> The first coordination sphere was modeled by varying the distance to the absorbing atom, the Debye Waller (DW) factor and the energy shift of the ionization potential while the coordination number was fixed. In a second step, the coordination number was varied simultaneously with the DW factor obtained from the first step and the energy shift whereas the distance was fixed. The obtained goodness of fit (r factor) is 0.1% ( $r = 0.001$ ) or 0.2% ( $r = 0.002$ ), corresponding to the difference between data and model (cf. [Table 35](#) in the [Appendix](#)).

#### 4.1.2. Results

##### *Pu L<sub>3</sub> edge XANES*

[Figure 24](#) depicts the Pu L<sub>3</sub> edge XANES spectra of the Pu doped **G1-G4** glass samples and the  $\text{Pu(III)}_{\text{aq}}$ ,  $\text{Pu(IV)O}_2$ ,  $\text{Pu(VI)}_{\text{aq}}$  reference materials. The Pu L<sub>3</sub> edge XANES spectra mainly describe dipole allowed electronic transitions from 2p to unoccupied 6d orbitals ( $2p_{3/2} \rightarrow 6d$ ). The energy positions of the abrupt increase in absorption (absorption edge) and the most intense absorption resonance typically shift to higher energies by reduction of the electronic density in the vicinity of the Pu atom nucleus; this energy shift of the spectrum is commonly used for oxidation state analyses. However, the spectra can also shift due to changes in the short and long-range atomic environment around the absorbing atom. For example, Conradson *et al.* found up to 2 eV energy shift of the WLs of the Pu L<sub>3</sub> edge XANES spectra of several Pu(IV) materials with varying coordination environments.<sup>117, 118</sup>

A well-known challenge is to differentiate between Pu(IV) and Pu(VI), where the latter tends to form short trans-dioxo bonds with lengths of  $1.75 \text{ \AA}$  (Pu-yl, plutonyl) in both solid and liquid states (cf. [Figure 27](#)).<sup>119,120</sup> Due to the strong covalence of the plutonyl bond, there is an accumulation of electronic charge on the Pu atoms. As a result, the 2p core-hole is well screened

and the WL positions of the Pu(VI) and the Pu(IV) spectra can coincide (cf. [Figure 24](#)). Note that the Pu L<sub>3</sub> edge XANES of Pu(V) trans-dioxo species (axial bond length around 1.94 Å) is even shifted to lower energies compared to the spectrum of Pu(IV).<sup>117</sup>

A trend indicated with solid black arrows can be observed in the spectra. The energy position of the WL of the **G1** spectrum is slightly shifted to lower energies compared to the WL of the Pu(IV) reference spectrum suggesting contributions of Pu(III) in the **G1** sample. For R values below 0.73 (**G1-G3**), mixtures of most likely tri- and tetravalent Pu are formed. The energy positions of the WLs of the **G4** and the Pu(III) spectra coincide affirming the efficient reduction of Pu(IV) to Pu(III) in the **G4** glass caused by the reducing agent (R = 0.73) (cf. [Table 4](#)).

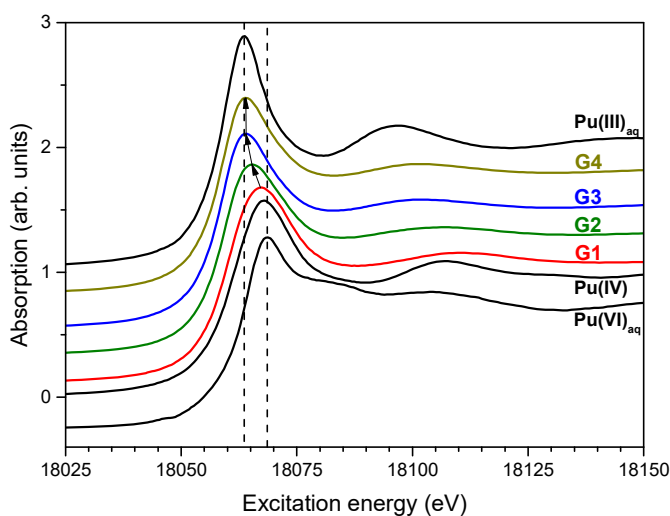


**Figure 24** Pu L<sub>3</sub> edge XANES spectra of the **G1-G4** glasses and the Pu(III), Pu(IV), Pu(VI) references.

These results are in good agreement with the report of Deschanel *et al.*, who also applied the Pu L<sub>3</sub> edge XANES technique to investigate the Pu oxidation states in the glasses **G1-G3**.<sup>35</sup> However, these analyses cannot exclude potential stabilization of minor amounts of higher Pu oxidation states.

#### *Pu M<sub>5</sub> edge HR-XANES*

**Figure 25** (left) depicts the Pu M<sub>5</sub> edge HR-XANES spectra of the **G1-G4** glass samples and the Pu(III)<sub>aq</sub>, Pu(IV)O<sub>2</sub>, Pu(VI)<sub>aq</sub> reference materials. The Pu M<sub>5</sub> edge HR-XANES spectra describe the dipole allowed transitions of 3d electrons to 5f unoccupied orbitals (3d<sub>3/2</sub> → 5f), which contain most of the *An* valence electrons participating in the chemical bonding. The valence electronic configuration of metallic Pu is 7s<sup>2</sup>5f<sup>6</sup>. In contrast to the Pu L<sub>3</sub> edge XANES spectra, the Pu M<sub>5</sub> edge HR-XANES reference spectra clearly shift to higher energies in the order Pu(III),

Pu(IV), Pu(VI); Pu(V) is difficult to stabilize, therefore no reference spectrum is presented. The spectra of the Pu(III)<sub>aq</sub> and Pu(VI)<sub>aq</sub> references were recorded with lower experimental energy resolution. This results in a larger broadening of the spectra. Considering the PuO<sub>2</sub> spectra measured with variable experimental energy resolutions (cf. [Figure 23](#)) a shift towards lower energies of up to 0.1 eV can be expected for Pu(III)<sub>aq</sub> and Pu(VI)<sub>aq</sub> spectra if measured with a resolution comparable to the glass spectra.

The **G1** and the Pu(IV) spectra have very similar energy positions (cf. [Figure 25](#), left), line **B**), which is a strong indication that Pu(IV) is the main species in the **G1** sample. The **G2-G4** spectra are shifted to lower energies with increasing R; the spectrum of **G4** peaks at about the energy position of line **A** (3774.1 eV) marking the most intense absorption resonance of the Pu(III) reference spectrum. This general trend suggests a reduction of the Pu oxidation state going from **G1** to **G4** in agreement with the Pu L<sub>3</sub> edge results.<sup>6</sup> However, the **G1-G4** spectra have asymmetric shapes. There are shoulders on the low (3774.1 eV) and high energy (3776.5 eV) sides of the **G1** spectrum, which increase and decrease in intensity, respectively, going from the **G1** to the **G4** spectrum. These additional spectral features point to mixtures of Pu(III) (line **A**), Pu(IV) (line **B**) and a higher oxidation state of Pu. We infer that this spectral contribution is likely due to the presence of Pu(VI) (line **C**). Note that the shoulder positioned next to line **C** on the high energy side of the main peaks of the **G1** and **G2** spectra (3776.5 eV) nearly coincides with the main peak of the Pu(VI) reference. Pu(V) is less probable but it might be potentially stabilized in the glass matrix as well, therefore we cannot completely exclude its presence.

We recorded the **G1**, **G4** and PuO<sub>2</sub> spectra with even higher experimental energy resolution. These spectra are depicted in [Figure 25](#) (right). The shoulder **C** is well pronounced in the **G1** spectrum, affirming the formation of Pu species with an oxidation state higher than IV. The low energy shoulder corresponding to minor contribution of Pu(III) is now clearly distinguishable in the **G1** spectrum.

The high-energy resolution enables also distinct detection of Pu(III) and Pu(IV) in the **G4** glass. The spectrum demonstrates formation of similar amounts of Pu(III) and Pu(IV). As the spectra of **G1** and **G4** in [Figure 25](#) (right) were measured with a higher experimental resolution, a 0.3 eV shift of the spectra towards lower energies can be expected compared to the Pu glass spectra measured with medium experimental resolution (cf. [Figure 25](#), left). [Figure 23](#) depicts PuO<sub>2</sub> spectra recorded with different resolutions from which this shift can be deduced. The post-edge feature **D** in the Pu(VI) reference spectrum is characteristic for plutonyl<sup>69, 78</sup> and describes transitions to the sigma antibonding ( $\sigma^*$ ) molecular orbital.<sup>78</sup> A similar peak was reported recently also for uranyl by Vitova *et al.*<sup>78, 121</sup> As feature **D** is not present in the spectra

of **G1** and **G2**, we conclude that the potential Pu(VI) species does not form a plutonyl type of bonding. It is more likely that the Pu-O distances are elongated and the Pu is coordinated by a more symmetric set of O atoms than in the plutonyl case, i.e., in a plutonate structure.<sup>122</sup> For example Pu can form  $\text{PuO}_6^{n-}$  polyhedra with octahedral coordination of six equidistant O atoms.<sup>123</sup> It was previously shown that this peak is not present for U(V)/U(VI) species in  $\text{U}_3\text{O}_8$ , (U(V) and U(VI)) and  $\text{U}_4\text{O}_9$  (U(IV) and U(V)), which are characterized by orthorhombic space group<sup>124</sup> and cuboctahedron coordination,<sup>125</sup> respectively.<sup>6</sup>

Based on these experimental evidences we conclude that Pu(IV) mainly contributes to the **G1** and **G2** glasses. This finding is in good agreement with literature reporting the formation of Pu(IV) in Pu doped borosilicate glasses melted in ambient conditions without reducing agent.<sup>113, 126</sup> Adding  $\text{Si}_3\text{N}_4$  to the vitrification feed mixture increases significantly the Pu(III) content as previously reported.<sup>35</sup> Pu(III) then becomes a major constituent of the **G3** and **G4** glasses. When considering the redox balance of the  $\text{Si}_3\text{N}_4$  reaction with  $\text{Pu}(\text{NO}_3)_4$ , the reductant is in significant excess only in sample **G4**. Apparently, this is not sufficient to reduce all Pu to Pu(III).

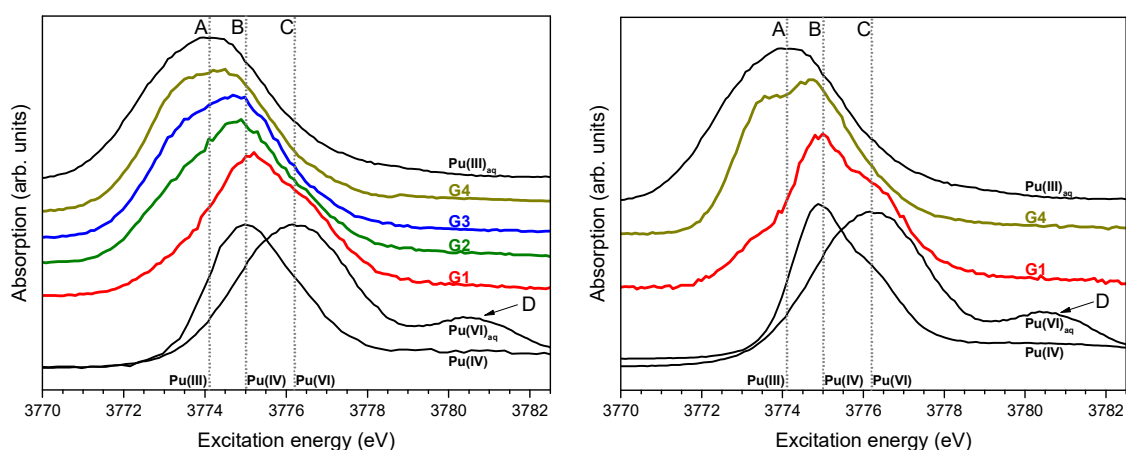


**Figure 25** (a) Pu M<sub>5</sub> edge HR-XANES spectra of the **G1-G4** glasses and (b) the **G1, G4** glasses recorded with medium and high experimental energy resolutions, respectively. The Pu(III)<sub>aq</sub> and Pu(VI)<sub>aq</sub> spectra were measured with low experimental energy resolution.

### *Pu L<sub>3</sub> edge EXAFS investigations*

The EXAFS spectra of the **G1-G4** glasses and their best fits are shown in k space in **Figure 26** (left). The analysis of the EXAFS region of the XAFS spectra provides quantitative information about the number and type of neighboring atoms as well as their distances to the absorbing Pu atom. The usable k-range is restricted by a signal at around  $11 \text{ \AA}^{-1}$ , which results from a minor (less than 0.2 % of the Pu amount) Am-241 contamination in the glasses. The Fourier transformed EXAFS (FT-EXAFS) spectra are depicted in **Figure 26** (right) (back-transformed

FT-EXAFS spectra cf. **Figure 96** in the **Appendix**). In all samples the Pu atoms are coordinated by ca. 5.5 O atoms (cf. **Table 35** in the **Appendix**). The average Pu-O distance however changes from 2.25-2.27 Å for samples **G1-G2** to 2.34 Å for samples **G3-G4**. This trend indicates that the effective charge on the Pu atoms decreases resulting in an increased bond length. This observation can be explained by the continuous reduction of Pu within the glass series as already revealed by the XANES/HR-XANES investigations. The fit results also illustrate that plutonyl bonds with lengths shorter than 1.8 Å are not formed, which is well in agreement with the results derived from Pu M<sub>5</sub> edge HR-XANES. Note that the Pu(VI)-O<sub>ax</sub> bond length of plutonyl in nitric acid solution initially added is assumed to be 1.69-1.77 Å.<sup>127</sup>

**Figure 27** depicts the distribution of Pu-O bond distances for ca. 100 Pu compounds reported in the Inorganic crystal structure database (ICSD). The bond lengths obtained from the fit to our spectra are indicated by arrows. Pu(IV) is likely a major constituent of **G1** and **G2**, whereas both Pu(III) and Pu(IV) are major constituents for the **G3** and **G4** glasses (cf. **Figure 27**, left). It is apparent that the increase of the Pu-O bond length with 0.09 Å from **G1** to **G4** leads to a bond length characteristic for Pu(III) compounds. No Pu(III) compound with Pu-O interatomic distances found for the **G1/G2** samples is reported in the ICSD database. The short Pu-O bond lengths typical for the Pu(VI) and Pu(V) plutonyl species are visible in **Figure 27** (right) below 2 Å.

The spectra display only one O coordination shell. Therefore, we can conclude that no Pu rich crystalline phases are formed in the glass matrix.

Pu(VI) compounds forming a plutonate structure are coordinated mainly octahedrally by six O atoms with an average distance of ca. 2.2-2.3 Å.<sup>123</sup> The finding of a Pu-O distance of 2.25 Å and 2.27 Å and a coordination of ca. 5.5 for samples **G1** and **G2** agrees well with the proposed Pu(VI) formation in a plutonate type of bonding. Those distances are, however, are also compatible with Pu-O distances in Pu(IV) compounds. A few Pu(V) compounds are listed in the database. The reported bond lengths are 0.17 Å longer than found for **G1** and **G2**.

Combining the outcome of HR-XANES and L<sub>3</sub> edge EXAFS results, we have to conclude that the Pu species characterized by the **C**-feature in HR-XANES must be assigned to Pu(VI).

The impact of the chemical composition of U on its speciation in glass vitrified in an Ar atmosphere has not been systematically investigated. But U(VI) nitrate solution and solid uranyl nitrate hexahydrate melted in aerobic conditions, at 1300 °C/1200 °C in borosilicate glass matrices form U-O<sub>ax</sub> bonds with 1.82 Å<sup>128</sup> and 1.84 Å (cf. **Section 4.2**) lengths,

respectively. Those are longer than the 1.77<sup>129</sup>/1.75<sup>130</sup> Å U-O<sub>ax</sub> bond lengths for the uranyl initially added. Hence, U(VI) and Pu(VI) appear to have similar behavior.

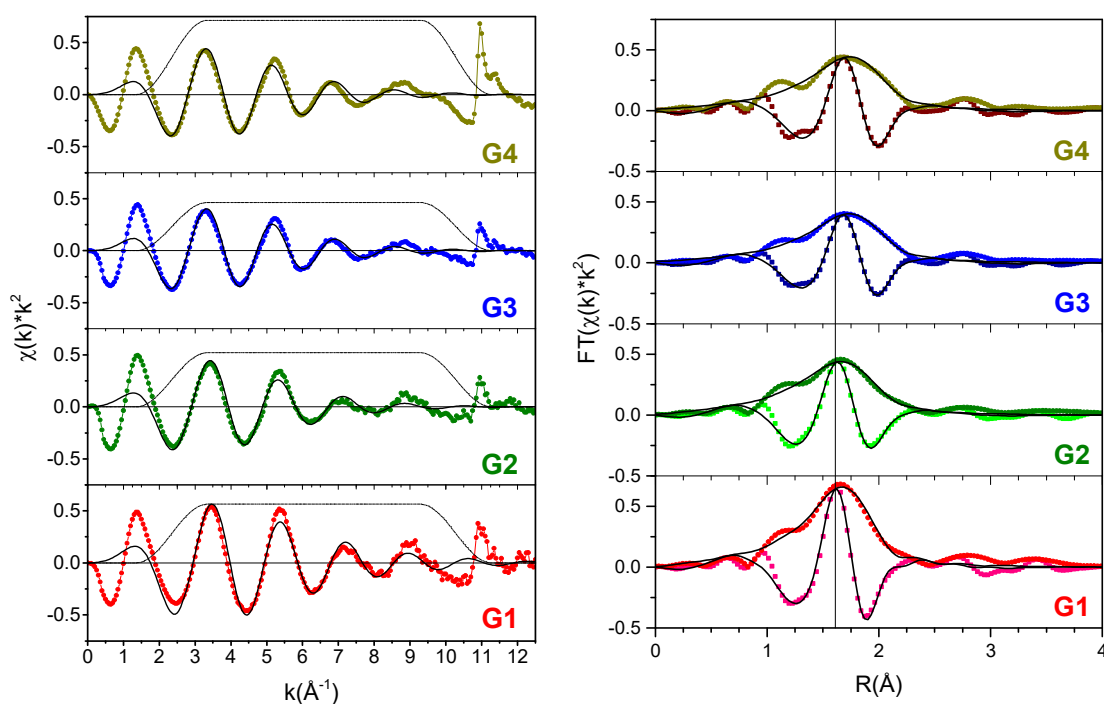


**Figure 26** (a) Pu L<sub>3</sub> edge EXAFS spectra of the **G1-G4** glass in k space, (b) magnitude and imaginary part of the experimental FT-EXAFS spectra and their best fits (right). Experimental data are shown with colored symbols whereas solid black lines represent fit results.

#### 4.1.3. Discussion

We report here for the first time that Pu(VI) can be stabilized during melting at 1200 °C (**G1**)/1400 °C (**G2**) in an Ar atmosphere. Stump *et al.* succeeded as well to incorporate major amounts of Pu(VI) during sol-gel synthesis at 100 °C obtaining a glass-like material.<sup>131</sup> However, successive heating to 800 °C completely reduced Pu(VI) to Pu(IV). UV-Vis spectroscopy was applied in this study to characterize Pu oxidation states, which is, however, not very sensitive for solid materials so that minor contributions of Pu(VI) cannot be excluded.

Conditions stabilizing Pu(VI) in a borosilicate glass matrix are controversially reported in the literature. Stevanovsky *et al.* performed in 2010 Pu L<sub>3</sub> edge XAS study and described partial Pu oxidation to Pu(VI) in a lanthanide borosilicate glass stored for more than 1.5 years in air.<sup>132</sup> On the contrary Hess *et al.* investigated 15 years old Pu doped borosilicate glass synthesized at 1200 °C with different  $\alpha$ -activities with Pu L<sub>3</sub> edge XAS spectroscopy and found unaltered Pu(IV), even for high  $\alpha$ -decay accumulations of  $8.8 \times 10^{15}$  to  $1.9 \times 10^{18}$   $\alpha$ -decays/g.<sup>126</sup> Our glass

samples were exposed to a slightly lower activity level of 1 to  $6 \times 10^{16}$   $\alpha$ -decays/g. In a similar manner, Bouty *et al.* studied  $\alpha$ -self-irradiation effects in an 8 years old Cm and Pu doped borosilicate glass synthesized at 1400 °C with around  $6 \times 10^{18}$   $\alpha$ -decays/g.

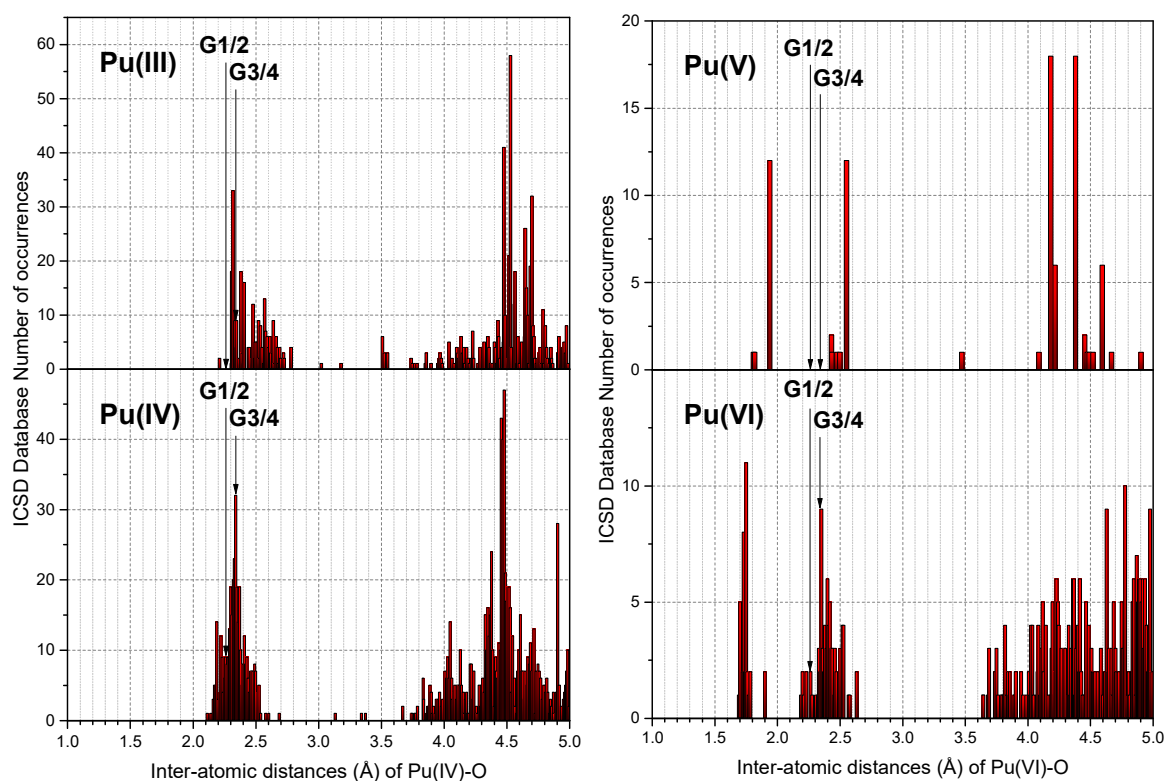


**Figure 27** Statistics of Pu-O distances for ca. 100 Pu containing compounds reported in the ICSD database.<sup>133</sup> The Pu-O distances obtained from the EXAFS fits for the G1-G4 samples are indicated with black arrows.

In agreement with Hess *et al.* no effect of the radiation on the tetravalent Pu oxidation state was found.<sup>46</sup> According to our investigations described above, it is apparent that the Pu L<sub>3</sub> XANES method is not sensitive to minor fractions of Pu redox species. As a result, minor Pu(VI) contributions possibly could not be resolved in those previous investigations. Due to the fact, that we found in our investigations Pu(VI) only in two samples, even though all four samples had the same storage and radiation exposure history, we suppose that Pu(VI) formation can be attributed to the synthesis process of the Pu-doped glasses rather than to storage conditions or radiation effects. It is more likely that Pu(VI) in our experiments forms due to the vitrification of Pu dissolved in 1.6M nitric acid. Tri-, tetra- and hexavalent Pu species can be stabilized in HNO<sub>3</sub> solution at pH values below 2.<sup>119, 123</sup> Despite melting under an Ar atmosphere Pu(VI) is apparently maintained in the glass. In case of the G1 glass sample redox active elements like Fe are present, while the G2 glass sample does not contain such components. The fact, that both glasses show the presence of Pu(VI), those elements seem to have minor impact on the Pu speciation.<sup>46</sup>

Our results suggest that when Pu dissolved in nitric acid is vitrified Pu(VI) species can be stabilized in nuclear waste glass along with other Pu redox species.

The potential to incorporate Pu(VI) in a stable manner in a waste glass product, might be of interest for designing vitrification processes for Pu rich waste.

The solubility behavior of Pu(VI) in borosilicate glass has not been systematically investigated so far. But as Pu cations in low oxidation states are believed to be incorporated in glass matrices in a similar manner as other *An* cations (e.g., U), it can be deduced that Pu(VI) is likely well soluble in borosilicate glass. Schreiber *et al.* reported a maximum U(VI) solubility in borosilicate glass of 40 wt%.<sup>109</sup> This would even exceed the Pu(III) solubility equivalent to 10-25 wt% PuO<sub>2</sub> reported by Feng *et al.* by far and opens up the opportunity to vitrify Pu rich nuclear wastes in a very efficient and economical way. Depending on the isotopic composition, the limiting factor of the Pu loading will be more likely the risk of criticality rather than its solubility in the glass matrix. The United States Department of Energy (DOE), for example, restricts its waste acceptance criteria by a very conservative limit of 987 g fissile material per cubic meter of glass (approximately 0.04 wt%).<sup>134</sup> Criticality issues could, however, be solved by addition of neutron absorbing elements like Gd and Hf, which is foreseen for the immobilization of Pu by incorporation in ceramics.<sup>135</sup>

A preferential mobilization of hexavalent Pu from glass when in contact with accessing solutions in a repository is certainly of less relevance. In the long-term the Pu leaching rate is governed by the overall glass matrix dissolution, and is independent from the Pu oxidation state.<sup>22</sup> The redox state of dissolved Pu species will then be determined by the given geochemical milieu and notably by the prevailing redox conditions. Usually, reducing conditions are expected due to iron canister corrosion resulting in relatively high concentrations of Fe(II) and H<sub>2</sub> in the leachates. Pu will then exist in reduced oxidation states exhibiting low solubility, strong sorption to surfaces and potentially formation of mobile colloidal species.

The Pu M<sub>5</sub> edge HR-XANES investigations show that, the increasing contribution of Pu(III) can be correlated with the rising amount of added reducing agent. The HR-XANES method illustrates that Pu(IV) remains as the main redox species, even though Si<sub>3</sub>N<sub>4</sub> is added in excess. A complete reduction to Pu(III) apparently requires the establishment of even stronger reducing conditions during the vitrification process.

#### 4.1.4. Conclusion

The Pu M<sub>5</sub> edge HR-XANES method is clearly capable of detecting Pu(III), Pu(IV) and Pu(VI) being simultaneously present in a simulated nuclear glass sample. Quantitative analyses of the Pu species with different oxidization states are possible when spectra of appropriate reference materials are recorded under the same experimental conditions. Our study demonstrates that this characterization method can be used for monitoring the redox conditions in vitrification processes upon reductant addition. A clear correlation of Pu oxidation state distribution and added reductant amount is revealed. By partial reduction to Pu(III) the solubility of Pu in the borosilicate glass was increased to more than 8 wt% whereby no separated Pu rich phases could be identified.

For complete reduction of Pu to the trivalent state in glass of similar chemical composition, it is necessary to add more reducing agent and to adjust R to a value higher than 0.73. This will most likely increase the Pu loading in the glass further.

We also clearly detected for the first time formation of Pu(VI) species in glasses synthesized upon addition of a Pu solution in nitric acid. Further experiments are needed to verify if Pu(VI) yields higher solubility as compared to Pu(III). In case of an analogy of Pu(VI) and U(VI) behavior in glass, a solubility limit around 40 wt% can be expected.

## 4.2. Genuine nuclear waste glass

Reprocessing of nuclear fuel generates HLLW, which is commonly immobilized in borosilicate glass matrices to generate disposable waste forms (cf. **Section 2.1.2**). The long-term radiotoxicity of U and Pu, which have the highest contribution among the *An* elements, is of great concern in safety concepts for a nuclear waste repository. In case of water intrusion and interaction with the glass matrix, different corrosion processes will take place and release of radioactivity into the environment can potentially occur (cf. **Section 2.1**). The redox nature of these *An* elements has an effect on their release mechanisms from the glass and the retention processes taking place in near and far field of the repository (cf. **Section 2.1.1.3**).

As part of safety assessment studies of a nuclear waste repository, self-irradiation effects of the waste forms have to be taken into account.  $\alpha$ -radiation, emerging from *An* decay processes, plays the most important role due to the high number of ion displacements (1000-2000) per  $\alpha$ -decay event.  $\beta$  and  $\gamma$  radiation, generated mainly by FP decay, produce in average less than one displacement per event and therefore it is a negligible part of the self-irradiation effects.<sup>136</sup>

But it might be able to induce charge transfer leading to changes of the chemical state of the radionuclides (cf. **Section 4.2.2**). Heating, ion displacement and the formation of He gas stresses the waste glass material and may affect its physical and chemical properties as well as its leaching behavior.<sup>47</sup>

In the concept of a closed fuel cycle, *An* are separated and recycled leaving low *An* containing HLLW for direct vitrification (cf. **Section 2.1.2**). Sources of *An* rich wastes are defense wastes or residues from transmutation processes. Immobilization of these wastes in solid matrices is challenging due to the *An* solubility limits restricting the loading capacity of the glass matrix. Safety requirements demand predominantly chemical and microstructural homogeneous glass products. Heterogeneities can raise differential swelling, enhanced leaching rates or stress corrosion, detrimentally affecting the long-term performance. Solubility limits of *An* are influenced by their oxidation states, the vitrification temperature and vary also in a wide range as a complex function of the glass composition. Pu for example can be loaded in non-reductive conditions on most borosilicate glasses in relatively small amounts of a few wt%, rarely exceeding 1.5 wt%.<sup>35</sup> Possibilities to enhance the U and Pu solubility in glass are discussed in **Section 4.1**. The adjustment of the *An* oxidation state plays a decisive role thereby.

The oxidation state of metal species in borosilicate glasses depends on the redox conditions measured in oxygen fugacity  $f_{O_2}$ . In glasses synthesized under ambient conditions (air,  $f_{O_2} \approx 0.23$  atm), U occurs predominantly as hexavalent uranyl species  $UO_2^{2+}$ ; U forms characteristic short bonds with two axial  $O_{ax}$  ( $\approx 1.80$  Å) and longer bonds with four or five equatorial  $O_{eq}$  atoms ( $\approx 2.23$  Å). Lower oxidation states in glass are obtained for  $f_{O_2} = 10^{-3} - 10^{-7}$  atm (mild reducing) or even  $10^{-8} - 10^{-10}$  atm (reducing). Former conditions form U(VI) coexisting with U(V), which is found in a moderately distorted octahedral structure [ $d(U-O) \approx 2.19-2.24$  Å]. Latter results report exclusive formation of U(IV) species in a less distorted octahedral local symmetry [ $d(U-O) \approx 2.26-2.29$  Å].<sup>128</sup> The trivalent state of U does not seem accessible even under most reducing condition.<sup>137</sup> But ambiguous results suggesting stabilization of U(III) in a borosilicate glass were reported by Halse *et al.* for glasses reduced at  $f_{O_2} = 10^{-18}$  atm.<sup>138</sup> The reduction power, i.e., the oxygen fugacity, is changed by adding a reducing agent to the glass forming materials<sup>113</sup> or performing the synthesis in a reducing atmosphere such as  $H_2$ .<sup>139</sup>

Spectroscopic methods giving access to the local coordination environment of U are rare. Optical spectroscopy provides information on the local symmetry of U sites but often shows constraints with respect to certain oxidation states and is difficult to apply for solid samples. Most challenging is the investigation of mixed oxidation states. XANES and EXAFS spectroscopy

can provide information on the local atomic environment averaged over all species of the probed element (cf. **Section 2.2**). With the HR-XANES technique applied in this work we address this challenge and resolve mixed *An* oxidation states present in the same sample (cf. **Section 2.2.2**).

The aim of the here presented project is to probe the U, Np and Pu oxidation states and their local atomic environments in a genuine active waste glass obtained from an industrial vitrification process by U, Np and Pu  $M_{4,5}$  HR-XANES as well as U and Pu  $L_3$  EXAFS. Additionally, SEM-EDX, XRD and Raman spectroscopy will be applied. The HLW glass sample originates from the vitrification plant Karlsruhe (VEK), which was operational from 2009 to 2010 and vitrified approximately 55 m<sup>3</sup> of HLLW producing 50 t of waste glass (cf. **Section 6**). Understanding on the speciation of U, Np and Pu in the VEK glass with complex chemical and radionuclide compositions will be gained. To the best of our knowledge there is only one study investigating HLW glass by spectroscopic techniques.<sup>74</sup> Dardenne *et al.* applied *An*  $L_3$  edge XANES spectroscopy to investigate the *An* oxidation states in the VEK glass. This technique, however, is less sensitive to contributions of minor oxidation states in mixtures.

U and Pu model glasses, which do not contain FPs, but have the same base glass matrix as the VEK glass were also synthesized and investigated. The comparison between genuine and model glasses allows to detect changes in the *An* redox states due to interactions with FPs and/or induced by the intense irradiation. Finally, the suitability of model glasses as surrogate materials for *An* focused structural investigations of nuclear waste glass is discussed. For Np  $M_5$  edge HR-XANES a Np doped R7T7 borosilicate glass matrix was used. Due to the difference in glass composition, it is not considered as model glass but is discussed in comparison with results from VEK glass Np speciation.

Since we will gain molecular scale structural understanding of the inner waste barrier (the glass matrix) the results will contribute to the safety assessment of its storage and final disposal in a deep geological repository.

### 4.2.1. Experimental

#### Preparation of samples

##### VEK glass frit

The VEK glass frit<sup>140</sup> was synthesized from glass-forming oxides, carbonates and hydroxides (cf. **Table 5**). The mixture was homogenized in a shake-mixer (turbula) for 15 min, transferred to the Pt/Rh crucible, calcined for 1 h at 800 °C and heated up to 1200 °C for additional 2 h. The glass melt was quenched by pouring it on a stainless steel gutter. The remaining glass in the crucible was also quenched by pouring cold water on its outer wall. Contact between water and glass was avoided. Afterwards all the glass fragments were ground to powder in a vibratory disc-mill (1 min). To ensure homogeneity of the frit, the powder was re-melted for 2 h at 1200 °C, quenched and milled again. The obtained powder was then used in the vitrification process.

**Table 5** Glass forming precursors used to produce the VEK glass.

<b>compound</b>	<b>mass (g)</b>
SiO <sub>2</sub>	88.92
B <sub>2</sub> O <sub>3</sub>	26.08
Al(OH) <sub>3</sub>	7.02
Li <sub>2</sub> CO <sub>3</sub>	12.83
Na <sub>2</sub> CO <sub>3</sub>	31.11
CaCO <sub>3</sub>	14.02
MgO	3.26
TiO <sub>2</sub>	1.78
<b>Total</b>	<b>185.01</b>

##### U model glass

Three U doped samples (1.19, 3.0 and 5.0 wt% UO<sub>2</sub>) were prepared using uranyl nitrate (UO<sub>2</sub>(NO<sub>3</sub>)<sub>2</sub>·6(H<sub>2</sub>O)) and the produced VEK glass frit described in the previous section. Yellow UO<sub>2</sub>(NO<sub>3</sub>)<sub>2</sub>·6(H<sub>2</sub>O) crystals were pulverized and mixed with the VEK glass frit. The mixture was transferred to the Pt/Rh crucible, heated up to 1200 °C for 2 h and quenched afterward by pouring it on a stainless steel gutter. The remaining glass in the crucible was removed mechanically. Powder was obtained by grinding glass chips in an agate mortar. The target compositions are listed in **Table 6**. All preparations were performed in the controlled area of the KIT-INE by S. Bahl and V. Koldeisz.

### Pu model glass

Four Pu model glass samples were synthesized in the controlled area of the *Directorate of Nuclear Safety and Security, JRC-Karlsruhe* (European Commission). Inactive VEK glass frit was mixed with different amounts of PuO<sub>2</sub> to obtain glass samples with PuO<sub>2</sub> concentrations 0.2, 0.5, 1.5 and 1.5 wt% PuO<sub>2</sub> (cf. **Table 6**). Melting and annealing in a high-temperature furnace at 1200 °C (600 °C) for 3 h (3 h) as well as all the other manipulations were performed in a N<sub>2</sub> filled glovebox. Removal of the cold glass material from the Pt/Rh crucible took place without applying any mechanical force. The samples were partly crushed for further investigations. From each of the four samples, two fragments were embedded in resin for cutting and polishing, respectively. All preparations were performed in the controlled area of the *JRC-Karlsruhe* by C. Boshoven and S. Bahl. Embedding and polishing of the specimens was performed by M.-F. Mairead.

**Table 6** Target oxide composition of U and Pu model glass samples.

Oxides (wt%)	1.19 wt% UO <sub>2</sub>	3.00 wt% UO <sub>2</sub>	5.00 wt% UO <sub>2</sub>	0.2 wt% PuO <sub>2</sub>	0.5 wt% PuO <sub>2</sub>	1.0 wt% PuO <sub>2</sub>	1.5 wt% PuO <sub>2</sub>
SiO <sub>2</sub>	56.37	55.34	54.20	56.94	56.48	56.20	56.94
B <sub>2</sub> O <sub>3</sub>	16.53	16.23	15.89	16.70	16.56	16.48	16.70
Al <sub>2</sub> O <sub>3</sub>	2.91	2.85	2.80	2.94	2.91	2.90	2.94
Li <sub>2</sub> O	3.29	3.23	3.16	3.32	3.29	3.28	3.32
Na <sub>2</sub> O	11.53	11.32	11.09	11.65	11.55	11.50	11.65
CaO	4.98	4.89	4.79	5.03	4.99	4.96	5.03
MgO	2.07	2.03	1.99	2.09	2.07	2.06	2.09
TiO <sub>2</sub>	1.13	1.11	1.09	1.14	1.13	1.13	1.14
UO <sub>2</sub>	1.19	3.00	5.00	-	-	-	-
PuO <sub>2</sub>	-	-	-	0.20	0.50	1.00	1.50
<b>Total</b>	<b>100</b>						

### Np doped glasses

R7T7-type glass doped with 0.85 wt% Np-237 (2·10<sup>5</sup> Bq/g glass) was prepared in 1993 by the *Alternative Energies and Atomic Energy Commission* (CEA) in France and stored at INE for 23 years in form of powder. The glass was elaborated under oxidizing conditions. Due to its long half-life of 2·10<sup>6</sup> years, Np loss by decay can be neglected. The glass was prepared for HR-XANES measurements by fixing the powder on a Kapton tape and covering it by 13 µm and 8 µm thick Kapton foils respectively.

### VEK genuine waste glass

The investigated VEK glass sample originates from the hot vitrification activities of the VEK plant from 2009 and 2010. 55 m<sup>3</sup> of HLLW were vitrified in a borosilicate glass matrix resulting

in a glass product loaded with 16 wt% of waste oxide. The complete description of the retain samples from the glass pouring process as well as the transportation can be found in the INE annual report 2010.<sup>141</sup> A summary of the vitrification activities was reported by Roth *et al.*<sup>36</sup>

Due to very high activities of the material, a small particle was selected for HR-XANES investigations from the glass samples available at INE (container 57). The particle has 1 mm<sup>2</sup> size, a weight of approximately 1 mg and a dose of ca. 200  $\mu\text{Sv/h}$  in contact (cf. [Figure 29](#)). For SEM-EDX investigation, another particle from container 57 was prepared. It is described in the SEM-EDX experimental paragraph.

## Methods and Materials

### X-ray powder diffraction (XRD)

The samples were measured according to the description in **Section 3**. At room temperature the angular range of  $2\theta = 5-80^\circ$  was measured with an integration time of 6.6-9 s per point. Pu model glass diffractograms were recorded with a different *Bruker Advance D8 diffractometer* in a range of  $2\theta = 15^\circ-120^\circ$  with a step size of  $0.02^\circ$ .

### Scanning electron microscope (SEM) and energy-dispersive X-ray spectroscopy (EDX)

The samples were measured with the electron microscope described in **Section 3**. The VEK glass fragment was cleaned in a super-sonic bath (isopropanol) prior mounting on double sided graphite tape on a metallic sample holder. The VEK glass particle investigated by XANES and EXAFS was obtained from the same glass container (container 57) but was not identical with the specimen prepared for SEM-EDX analysis. U doped glasses were embedded in resin, cut and polished. To establish electric conductivity, all specimens were covered with a nm thick layer of C in vacuum. EDX analysis of the U doped model glasses was performed before their surface was sputtered with Cr. The measurements were performed with electrons with energy of 30 keV.

### X-ray photoelectron spectroscopy (XPS)

Glass samples were crushed by stainless steel and agate mortar and pestle. The powder was pressed into indium foil and mounted on a sample holder of the XPS spectrometer. XPS spectra were recorded as described in **Section 3**.

### Raman

The samples were measured according to the description in **Section 3**. The red laser with power of 25 mW and 50 mW was used for excitation and focused by the x10 objective onto the specimens.

### High-energy resolution X-ray absorption near edge structure (HR-XANES)

Pellets were prepared by mixing ca. 20-30 mg of U glass with 3–10 mg of cellulose powder and pressing it to a pellet of approximately 1 mm thickness and 7 mm diameter with a manual hand press. They were fixed on the sample holder by double-sided graphite glue tape and sealed with 10  $\mu\text{m}$  thin polypropylene film.

U  $M_4$  edge (3728 eV) HR-XANES measurements of the U doped glass samples and references were performed at the ID26-Beamline, ESRF, Grenoble, France,<sup>93</sup> in April and June 2014 (cf. **Section 3**). Short pre-measurements (1–10 s per spectrum) were performed and carefully analyzed to check for X-ray radiation damage of the sample. All U model glass samples were stable to X-ray radiation. Spectra were recorded at different spots of the pellet for 3722.4-3735.1 eV energy range with step size of 0.1 eV and a measuring time of ca. 2-5 min per spectrum. For each sample ca. 10 spectra were averaged.

Pu  $M_5$  edge (3775 eV) HR-XANES data were recorded at the ANKA INE-Beamline, Karlsruhe, Germany,<sup>5</sup> in Sept '14 (cf. **Section 3**). The used Johann type spectrometer is described in **Section 2.2.3**. Spectra were checked for X-ray radiation damage effects by comparing spectra rapidly recorded on the same sample spot in the energy range of 3760-3835 eV. Step sizes of 0.1 eV in the region of the WL and 0.5 eV for pre- and post-edge were used. Pu model glass samples were measured by setting the spectrometer to the maximum of the normal emission line (3350 eV). The VEK glass was recorded at the maximum of the emission line (3351.6 eV) exciting with an energy of 3777.2 eV (measured maximum of Pu  $M_5$  main peak) in the energy range of 3767-3791 eV. The difference led to a Pu main peak shift of the VEK spectrum towards higher energies of 1.7 eV which was corrected in the spectrum depict in **Figure 39** (cf. **Section 2.2.2**).

Np  $M_5$  edge (3664 eV) HR-XANES data were recorded at the ANKA INE-Beamline in March '15 at an energy range of 3654.0-3684.0 eV (VEK glass) and 3649.5-3728.5 eV (R7T7 glass). Step sizes of 0.1 eV in the region of the WL and 0.5 eV for pre- and post-edge were used. The samples were recorded by setting the spectrometer to the maximum of the normal emission line (3258.4 eV).

The Np redox references are described in **Section 3**.

#### Extended X-ray absorption fine structure spectroscopy (EXAFS)

EXAFS spectra of the U doped glasses have also been recorded at the ANKA INE-Beamline. The DCM, which is equipped with a D-MOSTAB, was used with two Ge(422) crystals and the spectra were recorded in transmission detection mode as a function of the incident photon energy, monitored by three ion chambers filled with Ar. A Y reference foil (K edge = 17038 eV) was simultaneously measured in transmission mode and used for energy calibration of the DCM. Typically, two to seven scans were collected at room temperature and averaged for each sample in the range of 16935-17924 eV with varying step sizes in the pre- and post-edge and WL region. No radiation damage was observed. The averaged U L<sub>3</sub> edge XANES scans were normalized by subtraction of a linear background function from the featureless pre-edge region and normalized to the edge jump of unity.

The oscillating  $\chi(k)$  EXAFS part of the XAS spectrum was extracted, processed by FT and modelled by using the *ATHENA* and *ARTEMIS* programs, respectively, parts of the *IFEFIT* program package.<sup>114</sup> The single scattering paths were generated with the *FEFF8* code.<sup>60</sup> The  $\chi(k)$  spectra within 2.6–14 Å<sup>-1</sup> range were weighted by  $k = 1, 2$  or  $3$ . Hanning windows with sills equal to 2 ( $dk = 2$ ) were used. The fit was performed in  $R$  space for 1.1–2.167 Å range. For each shell the coordination number was first fixed and the change in distance and the DW factors were varied. In a second step, the coordination number was varied simultaneously with the (obtained from the first step) DW factors, whereas the change in distance was fixed. The fit results are reported in **Table 36** in the **Appendix**.

#### Crucible

The crucibles for the synthesis of the U (Pu) model glasses are made of 90% Pt and 10% Rh by *Ögussa*. They have a diameter of 28 mm (20 mm) and a height of 32 mm (23 mm). The remaining U glass was removed from the crucible by mechanical treatment. Irrespective of a small amount in the orders of milligrams, all material could be removed. The crucible was reused. Four crucibles used for melting of the Pu glass samples were not reused and therefore not cleaned.

VEK glass frit was synthesized in a Pt/Rh 90:10 crucible with 6 cm diameter and 5 cm height. After mechanical removal of the remaining glass, the crucible was treated with 30% HF solution for approximately 12 hours for cleaning.

### Furnace

The furnace used for U glass synthesis was a *N20/HR* chamber furnace manufactured by *Nabertherm*. VEK frit was melted in a *HT 04/17* chamber furnace also by *Nabertherm*. Pu glass samples were synthesized in a N<sub>2</sub> atmosphere (less than 0.3% O<sub>2</sub>) in a customized (*Linn High Therm*) tube furnace with water cooled heat shielding in a glove box.

### Grinding tools

Both U and Pu glass were ground mechanically with agate mortar and pestle.

### Mill

A vibratory disc mill (*Pulverisette 09.003* by *Fritsch*) with tungsten carbide grinding tools was used to grind the VEK glass frit.

### Chemicals

The used chemicals were provided by *VWR International* and unless otherwise stated, used without further purification. PuO<sub>2</sub> was provided by the INE. The isotopic composition is as follows: Pu-238 2.16·10<sup>5</sup> Bq, Pu-239 7.70·10<sup>5</sup> Bq, Pu-240 4.47·10<sup>5</sup> Bq, Pu-241 2.31E·10<sup>7</sup> Bq (0.39 mg Pu).

## 4.2.2. Results

U and Pu loaded model glasses were synthesized in order to serve as a surrogate system of the genuine waste glass. In the following the characterization of the U and Pu model glasses is discussed followed by the investigation of the VEK glass. The Np doped R7T7 glass is only used for comparison of the Np oxidation states in the Np M<sub>5</sub> HR-XANES investigation and was not characterized with other methods.

The U and Pu doped model glass samples are depicted in **Figure 28**. It is known that a redox sensitive element can cause a glass to appear in different colors due to changes in excitation and transition energies in the range of visible light. The U model glass samples are colored predominantly yellow with a small contribution of green. These varieties of colors for U have already been known in 19<sup>th</sup> century. They were described by Franz Xaver Anton Riedel who produced the first U colored glass and named its varieties after his both daughters "Anna-gelb" (yellow) and "Eleonore-grün" (grün).<sup>142</sup> The color varies with the amount of impurities, the U

concentration, the oxidation state of the coloring element and the synthesis conditions. An amber-yellow color, as found in the U model glass, is characteristic for high U concentrations.

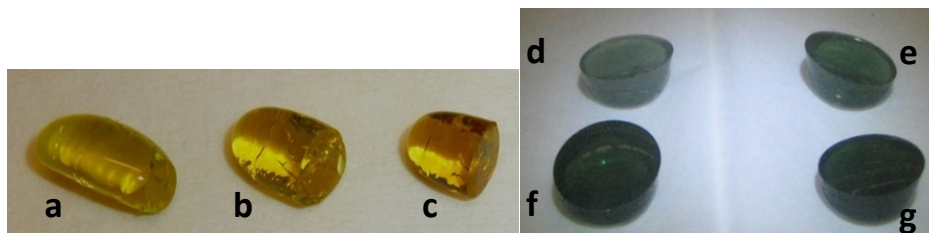


**Figure 28** Photographs of Pu and U model glasses. UO<sub>2</sub> content: a) 1.19 wt%, b) 3 wt%, c) 5 wt%. PuO<sub>2</sub> content: d) 0.2 wt% e) 0.5 wt% f) 1 wt% g) 1.5 wt%.

The four Pu model glass samples were synthesized by the *Directorate of Nuclear Safety and Security, JRC-Karlsruhe* (European Commission), in the framework of a *TALISMAN* project (*TALI\_C03-01*). The color of these glass products ranges from light green (0.2 wt% PuO<sub>2</sub>) to intensive dark green (1.5 wt% PuO<sub>2</sub>). All model glass samples appear transparent and do not show any visually detectable crystalline phases or phase separations.

The VEK glass particle ( $m \approx 1$  mg) is shown in **Figure 29**. Several optical dark heterogeneities can be detected in the predominantly green glass.

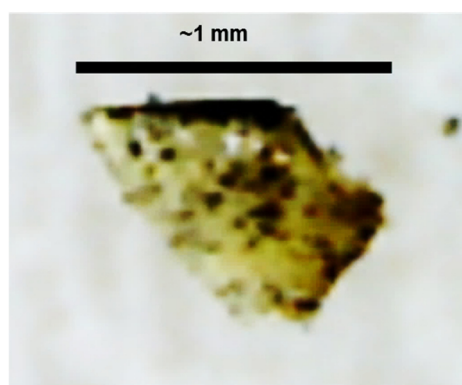


**Figure 29** Light microscope image of the VEK glass particle.

#### *Model U and Pu glasses XRD*

The amorphous nature of the synthesized U and Pu model glasses was verified by powder XRD (cf. **Figure 30**). An content in all samples is below the U and Pu solubility limit in borosilicate glass (cf. **Section 4.2.1**). The XRD pattern are characteristic for amorphous glass samples. For the Pu glasses low intensity reflexes at 2 Theta of approximately 22.2° arise from the resin in which the Pu glass powder was embedded, whereas the high background at low 2 Theta angles is caused by X-ray scattering from the air and the slits. The U doped glasses were measured without to be embedded in a resin. Two different diffractometers were used for the U and Pu measurements therefore there are variations of the background.

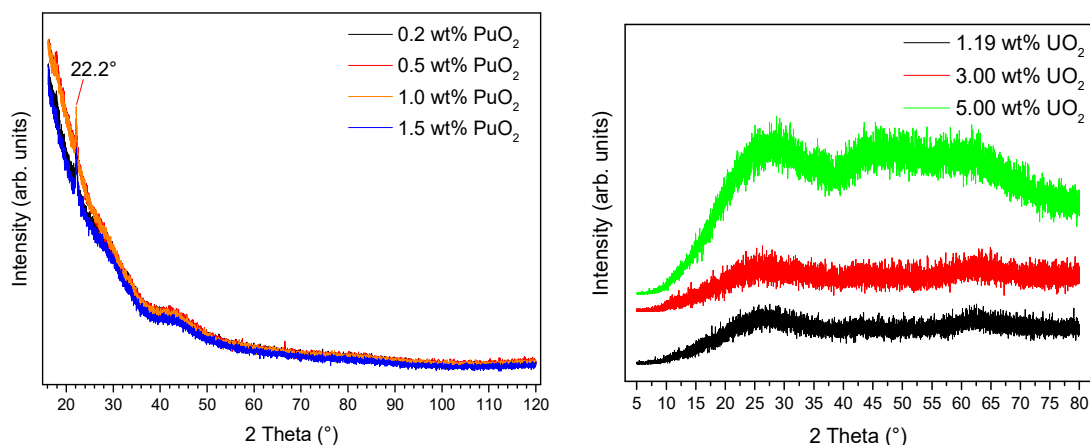


**Figure 30** Powder XRD diffractograms of the Pu and U model glasses.

### *U and Pu model glasses Raman*

It has been previously reported that the U-O vibrations can provide information about the local structure and coordination of U.<sup>143</sup> The Raman spectra of the U model glasses are dominated by a broad vibrational band at 767 cm<sup>-1</sup> (FWHM: 50 cm<sup>-1</sup>) with rising intensity as a function of the U loading (cf. **Figure 31**). The region above 1000 cm<sup>-1</sup> can be considered as a background. The 767 cm<sup>-1</sup> band is assigned to the  $\nu_1$  symmetric stretching mode of UO<sub>2</sub><sup>2+</sup> with wavenumbers ranging between 790 cm<sup>-1</sup> and 900 cm<sup>-1</sup> for most uranyl minerals.<sup>143</sup> High charge density anions such as SiO<sub>4</sub><sup>4-</sup> coordinated to U in the equatorial plane may cause elongation of the U-O<sub>ax</sub> bond length; as a result, the  $\nu_1$ (UO<sub>2</sub><sup>2+</sup>) stretching mode shifts towards lower wavenumbers. For example, kasolite, a uranyl mineral with SiO<sub>4</sub><sup>4-</sup> polyanion coordinated to the uranyl cation, is characterized by a U-O<sub>ax</sub> bond length of ca. 1.83 Å and the  $\nu_1$ (UO<sub>2</sub><sup>2+</sup>) appearing at 760 cm<sup>-1</sup>. The correlation between the frequency of the  $\nu_1$ (UO<sub>2</sub><sup>2+</sup>) and the U-O<sub>ax</sub> bond strength has been theoretically studied.<sup>144, 145</sup> The frequency in wavenumbers appears to be inversely correlated to the averaged U-O<sub>ax</sub> bond length. The appearance of the  $\nu_1$ (UO<sub>2</sub><sup>2+</sup>) stretching band at 767 cm<sup>-1</sup> suggests that the U-O<sub>ax</sub> is longer than 1.8 Å in the model glasses. Additional insights are gained from the EXAFS analyses.

Low intensity bands arising from bending modes  $\nu_2$  of UO<sub>2</sub><sup>2+</sup> expected between 200 cm<sup>-1</sup> and 340 cm<sup>-1</sup> were not observed due to the high background level.<sup>143</sup>

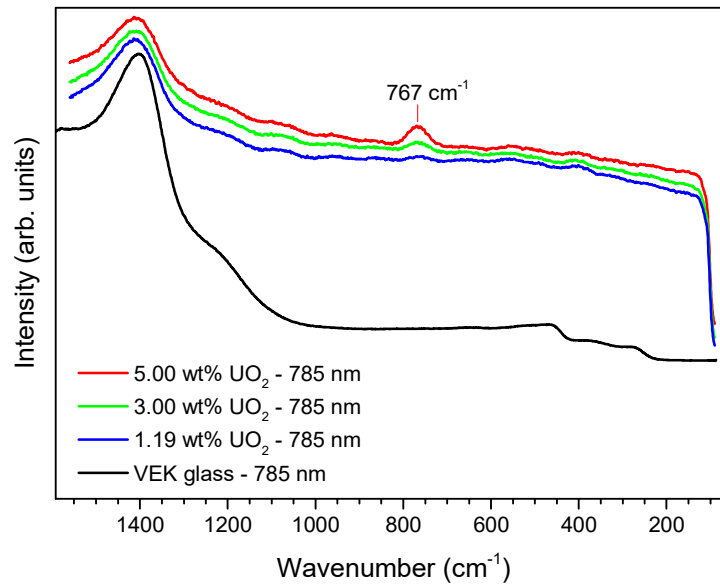


**Figure 31** Raman spectra of the VEK and U model glasses recorded with a 785 nm laser.

The Raman results confirm the presence of U(VI) with uranyl type of bonding in the glass. The formation of  $\text{UO}_2$  cannot be excluded on the basis of the obtained data, because a possible contribution of its most intensive  $T_{2g}$  vibration expected at approximately  $445\text{ cm}^{-1}$  might be superimposed by the intense background.<sup>146</sup>

The intensity of the  $767\text{ cm}^{-1}$  feature can be directly correlated to the U content in the glass. The maximum intensity of the peak as a function of the U concentration in the glass can be modeled by a linear function with slope of 2.03 and a y-intercept of -0.82. This empirical relation can be used as a tool for estimation of U content in highly loaded glass samples (cf. **Figure 32**). The lack of intensive sharp peaks confirms absence of any crystalline phases in the U mode glasses.

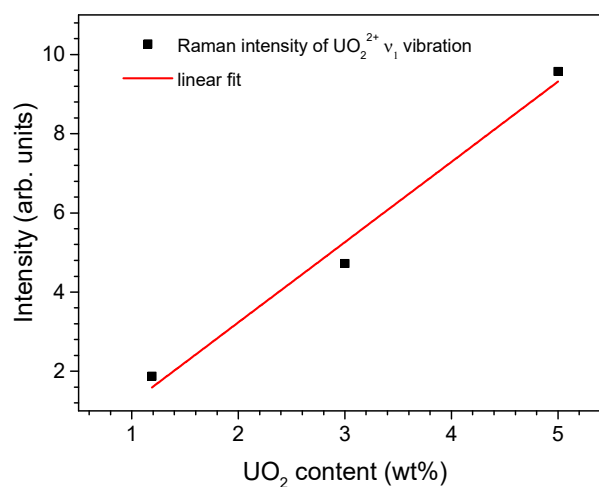


**Figure 32** Correlation diagram between vibration band intensity and U content in the three U doped model glass samples.

The XRD and the Raman results strongly suggest that U is distributed homogeneously in the model glass. Crystalline phases are also not identified by optical as well as SEM-EDX analysis (cf. **Figure 28** and **Figure 33**). EDX measurements were taken at 5 different spots of each sample in areas of approximately 50  $\mu\text{m} \times 50 \mu\text{m}$ . Results are shown in **Table 7**. The U content as determined by EDX deviates by  $\pm 0.25 \text{ wt}\%$  from the target doping level.

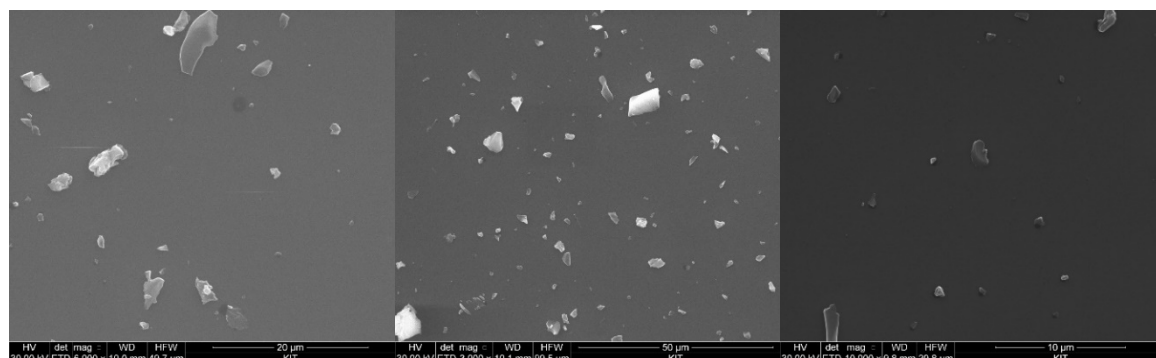


**Figure 33** SEM micrograph of the 1.19 wt% (left), 3 wt% (middle) and 5 wt% (right)  $\text{UO}_2$  model glasses. The homogenous surface is covered with small glass pieces and dust particles resulting from sample preparation.

**Table 7** Averaged EDX results from 5 measurements of U doped model glasses.

Element (wt%)	C	O	Na	Mg	Al	Si	Ca	Ti	U
1.19 wt% $\text{UO}_2$	8.0	46.7	8.1	0.9	3.3	27.4	3.9	0.8	exp.: 0.8 target: 1.1
3 wt% $\text{UO}_2$	4.0	46.9	8.7	1.0	4.0	27.9	4.0	0.8	exp.: 2.9 target: 2.6
5 wt% $\text{UO}_2$	6.5	46.2	8.3	1.0	2.6	26.3	3.8	0.8	exp.: 4.6 target: 4.4

Raman studies performed on the Pu model glasses show no vibration bands related to the glass samples (cf. **Figure 34**). The visible bands can be assigned to scattering from the containment materials. Due to radiation protection requirements, the samples had to be measured embedded in a resin matrix and covered by a Kapton foil. These results do not provide indications for the existence of any crystalline phases and are in agreement with the XRD results. A stretching mode characteristic for crystalline  $\text{PuO}_2$  would be expected at  $478 \text{ cm}^{-1}$ .<sup>146</sup>

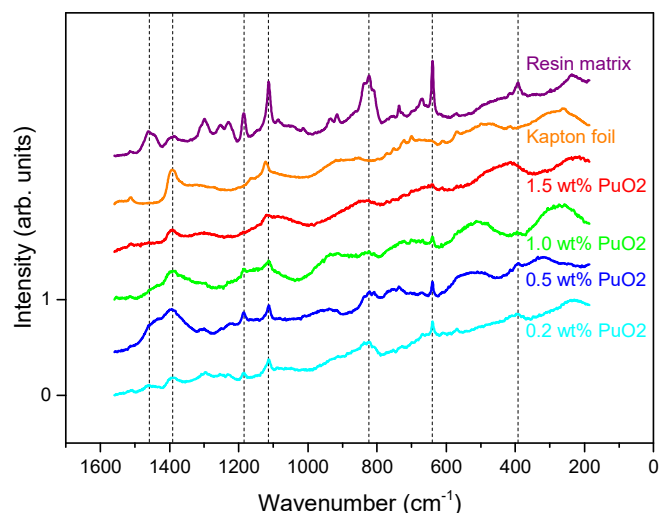


**Figure 34** Raman spectra of the Pu model glasses recorded with a 785 nm laser.

#### *U M<sub>4</sub> and Pu M<sub>5</sub> HR-XANES of model glasses*

The HR-XANES investigations of the glasses were performed at different synchrotron facilities. The Pu containing model glasses and the VEK glass were measured at the INE-Beamline at the ANKA synchrotron radiation facility, U model glasses were studied both at the ID26-Beamline at ESRF synchrotron radiation facility and at the INE-Beamline to verify the reproducibility of the spectra. Beside a higher quality of the ID26-Beamline data, this was the case. **Figure 35** depicts the HR-XANES M<sub>4,5</sub> edge spectra of the U and Pu model glasses.

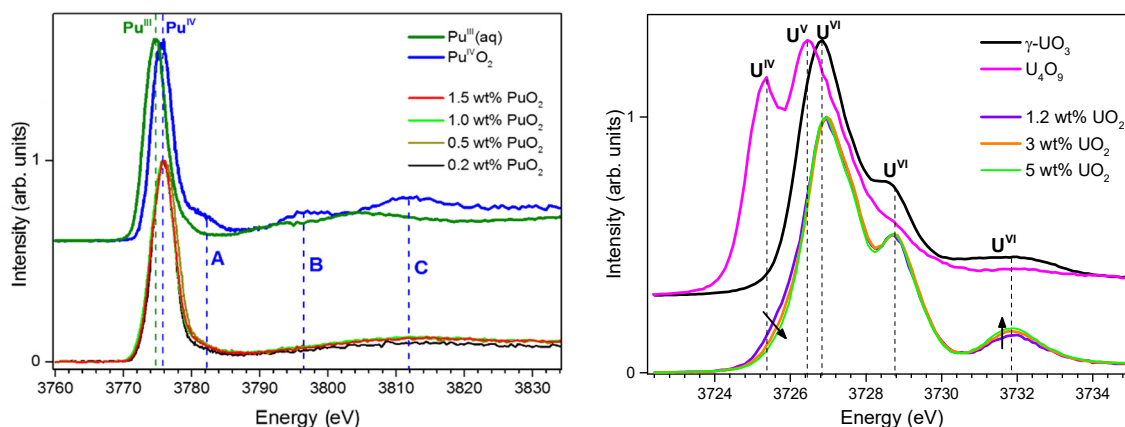


**Figure 35** Pu M<sub>5</sub> (left) and U M<sub>4</sub> (right) edge HR-XANES of model glasses and reference compounds.

The Pu M<sub>5</sub> edge spectra, left in the figure, do not reveal major differences as a function of the Pu content. The main absorption peak is located at 3776.0 eV, which coincides with the main peak position of PuO<sub>2</sub>. The main peak of the reference spectrum of Pu(III) in aqueous solution is shifted by 0.9 eV to lower energies. Pu(IV) is identified as the dominant Pu specie, which agrees with reported studies in the literature for Pu doped glass prepared in oxidative

conditions.<sup>126</sup> Post-edge features labelled **A**, **B** and **C** in the bulk PuO<sub>2</sub> spectrum arise from the scattering of the photoelectron from O and Pu atoms, which are periodically ordered in a crystal lattice (cf. **Section 2.2.1**). The absence of these features in the glass spectra confirm that Pu is dispersed in the glass and does not form Pu rich ordered clusters, for example in a form of PuO<sub>2</sub>. In **Section 4.1** minor amounts of Pu(VI) were found. Its presence was attributed to the Pu feeding via HNO<sub>3</sub> solution which oxidized the initial added PuO<sub>2</sub> partially. The hypothesis proposed in **Section 4.1** implies that a vitrification process performed in an inert gas atmosphere is able to maintain the initial Pu speciation. The obtained results are in agreement since Pu(IV) is found in the model glasses after adding PuO<sub>2</sub> to the vitrification feed mixture.

**Figure 35** right depicts the U M<sub>4</sub> edge HR-XANES spectra of the U model glasses compared to the spectra of the  $\gamma$ -UO<sub>3</sub> and U<sub>4</sub>O<sub>9</sub> references.  $\gamma$ -UO<sub>3</sub> is a U(VI) oxide with a trigonal crystal system in which U is coordinated by six O atoms (average U-O distance: 1.78 Å) in a distorted octahedral geometry.<sup>121</sup> Whereas U<sub>4</sub>O<sub>9</sub> is a mixed-valence U oxide consisting of U(IV) and U(V) crystallizing in a cuboctahedron crystal lattice with different U sites (U-O distance: 2.0-2.2 Å<sup>125</sup>) (cf. **Section 5**).<sup>6, 125</sup> The rising U content in the glasses does not influence the energy position of the most intense peak of the glass spectra. It is shifted by about +0.3 eV compared to the spectrum of  $\gamma$ -UO<sub>3</sub>, which indicates higher electronic density in the vicinity of the U atoms in the glasses. The glass spectra closely resemble that of the  $\gamma$ -UO<sub>3</sub> spectrum. Petiau *et al.* measured conventional U M<sub>4</sub> edge XANES of U doped glass samples.<sup>147</sup> They found the spectrum to have a symmetric main peak and a shift of +1±0.2 eV compared to the spectrum of the UO<sub>2</sub> reference. Optical spectra indicate the presence of U(V) and U(VI). The shift of the HR-XANES spectra reported in the present thesis is +1.8 eV (main peak of U in the glasses: 3726.9 eV, main peak of UO<sub>2</sub>: 3725.1 eV). These results suggest the predominant existence of U(VI) oxidation state in all U doped model glass samples. However, there is visible a weak pre-edge feature at ca. 3725.6 eV with decreasing intensity for high U content while the post-edge feature at 3731.8 eV rises. The behavior of this pre-edge shoulder as a function of the amount of doped U and the similarity of its energy position to the main peak of UO<sub>2</sub> indicate minor contribution of U(IV) in the samples. It is an unexpected finding since the glasses were melted in ambient conditions and no redox active elements were added. The samples are very resistant to irradiation with high photon flux hence we exclude the possibility that U(IV) is formed by X-ray induced radiation damage (cf. **Section 4.2.1**). Optical UV-Vis spectroscopy performed to substantiate the HR-XANES result did not provide useful information due to the low contribution of the potential U(IV) species. It is a very minor effect of less than 5% estimated by linear combination of U(VI) with U(IV) spectra and is more pronounced for low

U content. Structural defects in the amorphous glass matrix might cause a local structural distortion of the U environment leading to a small broadening of the main peak.

#### *U XPS of model glass*

Surface analysis of the samples were performed by XPS. Both as-prepared and freshly powdered U model glass samples were investigated. Spectra of the three U model glass samples demonstrate  $4f_{7/2}$  peaks at ca. 380 eV and 382 eV with similar intensity corresponding to U(IV) and U(VI), respectively; U(VI) satellite peak at 386 eV with low intensity is present too (cf. **Figure 36**). Modeling of the powder spectra leads to an U(IV):U(VI) ratio of approximately 1:1 for the 3 wt%  $\text{UO}_2$  glass sample (cf. **Table 8**).

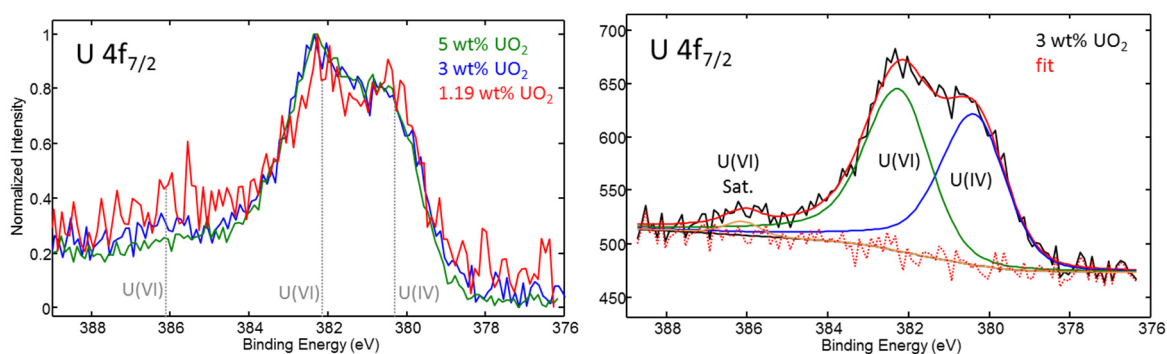


**Figure 36** XPS spectra of powdered U model glass samples (left) and fit of the 3 wt%  $\text{UO}_2$  sample XPS spectrum (right). Fit results are shown in **Table 8**.

**Table 8** Results from quantitative fit of the XPS spectrum of the 3 wt%  $\text{UO}_2$  glass sample shown in **Figure 36**.

Position (eV)	FWHM (eV)	Height	% Gauss	Area	% Area
380.37 U(IV)	1.81	141	80	352	47.03
382.25 U(VI)	1.81	152	80	379	50.64
386.11 U(VI)	0.98	13	80	17	2.33

Measurement of a 5 wt%  $\text{UO}_2$  glass chip reveals, that the U(IV) and U(VI) species are highly heterogeneously distributed on the glass surface. Five different positions on the glass chip were measured with a beam with diameter of approximately 200  $\mu\text{m}$  (cf. **Figure 37**). All spectra show clearly coexistence of both U(VI) and U(IV) species.

The high contribution of U(IV) found by XPS deviates from the results obtained with the  $\text{U M}_4$  edge HR-XANES for the bulk of the sample. U(IV) is also not expected due to the oxidative preparation conditions. Testing the sample's sensitivity to radiation damage caused by irradiation with the X-ray beam with approximately 1.5 keV energy did not reveal any formation of U(IV). In fact, the exposure of the sample to the X-ray beam induced oxidation

from U(IV) to U(VI) (cf. **Figure 36**, right). This fact excludes radiation damage as possible explanation for the high U(IV) content.

As XPS is a very surface sensitive method, probing the first few atomic layers of the specimens, a possible contamination with U(IV) containing material could explain the unexpected finding of large amounts of U(IV) and its heterogeneous distribution. Also the reduction of surface U by the preparation procedure might be possible. Ollier *et al.* detected a similar effect investigating a U doped borosilicate glass in oxidizing conditions.<sup>148</sup> The presence of unexpected U(IV) was determined by XPS analysis to ca. 20%. U M<sub>4</sub> HR-XANES (not yet published) by Bahl *et al.* revealed the exclusive presence of U(VI) in the bulk of the sample investigated by Ollier *et al.*

Another effect which might induce speciation artefacts in XPS measurements is the removing of O from the surface of certain materials by applying high vacuum to the sample. This might leave U in a reduced form while the O atoms are oxidized. This effect was used by Gasperi *et al.* to control the oxidation and reduction of Ce oxide thin films by changing the atmosphere from high-vacuum to a certain O<sub>2</sub> partial pressure from room temperature to ca. 750 °C and simultaneous characterization by Ce L<sub>3</sub> edge RIXS.<sup>149</sup>

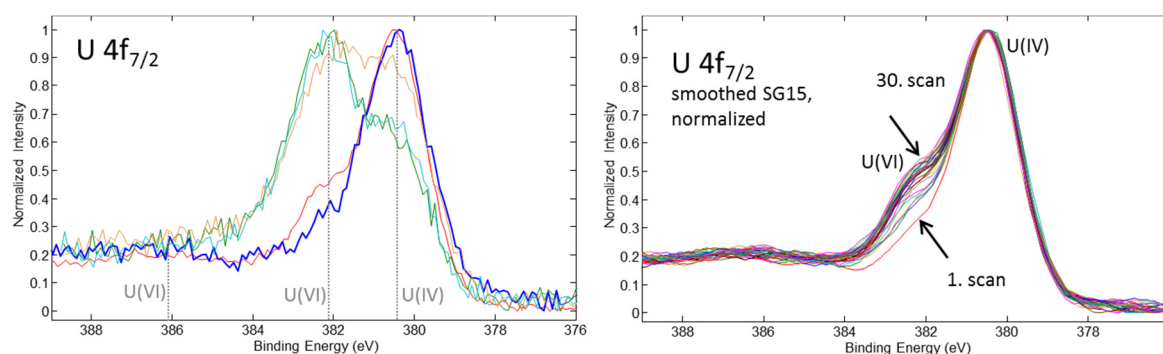


**Figure 37** XPS spectra of as-prepared glass chip sample 5 wt% UO<sub>2</sub> measured at 5 different positions (left) and 30 scans measured at one position of the same sample (right). Each scan took approximately 10 min.

Changes of the HR-XANES spectrum in **Figure 35** (right) can be also potentially caused by a structural distortion of the local U atomic environment as a function of the rising U content. This is probed by U L<sub>3</sub> edge EXAFS.

#### *U L<sub>3</sub> EXAFS of model glasses*

The FT EXAFS of the glass loaded with 5 wt% UO<sub>2</sub> and the fit to the spectrum are depicted in **Figure 38** as an example. The spectrum is dominated by one peak and no additional coordination spheres of U are detected, which confirms that similar to Pu, U is dispersed in the glass matrix and does not form any ordered oxidic clusters.

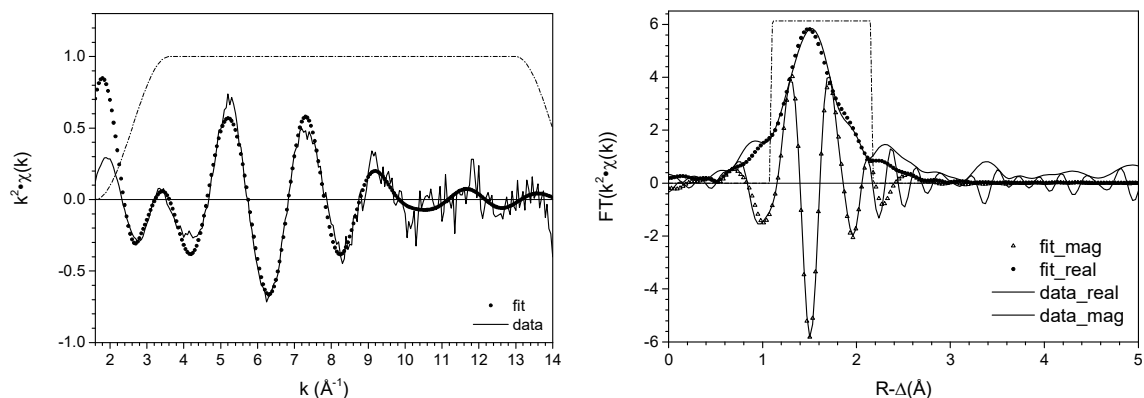


**Figure 38** U L<sub>3</sub> edge EXAFS spectrum of the U model glass sample with 5 wt% UO<sub>2</sub> in *k* space. Experimental data are shown as solid line whereas black symbols represent fit results (left). FT-EXAFS spectra of the same sample in *R* space. Magnitude and real part of the experimental data are shown as solid lines; symbols represent the fit results (right).

The first coordination sphere of the FT-EXAFS spectrum was modeled with three U-O distances, 2 O, 5.4 O and 3 O atoms at 1.84 Å, 2.29 Å and 2.62 Å, respectively (cf. **Table 36** in the **Appendix**). The obtained results for the U-O bond distances and coordination numbers do not reveal significant differences for all model glass samples. Therefore, the observed trend in the pre-edge region of the U M<sub>4</sub> edge HR-XANES spectra cannot be explained with a significant structural distortion in the direct vicinity of U.

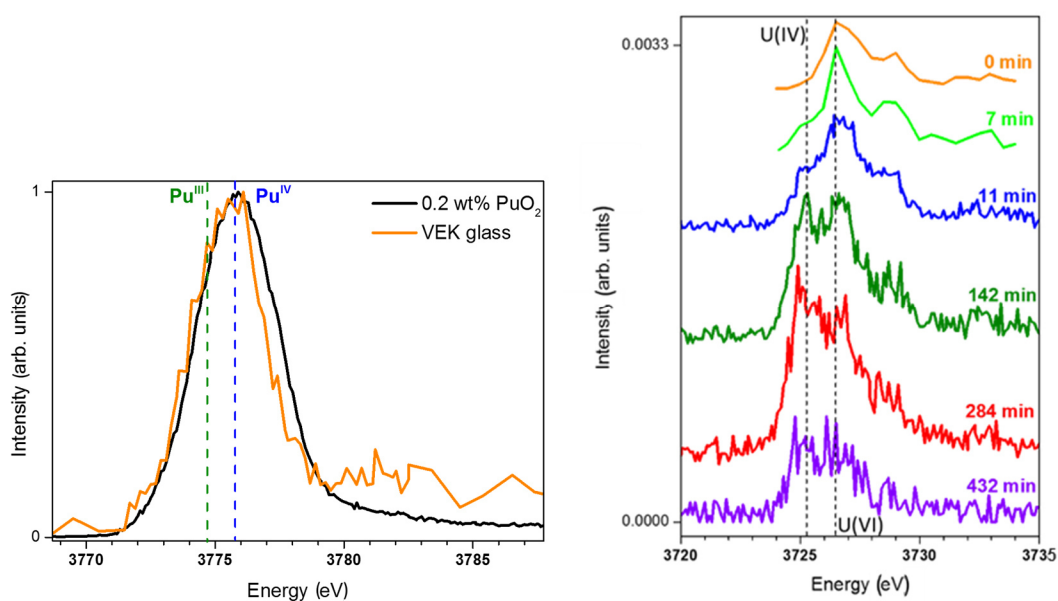


**Figure 39** Pu M<sub>5</sub> edge HR-XANES spectra of the VEK glass and the 0.2 wt% PuO<sub>2</sub> model glass (left), U M<sub>4</sub> edge HR-XANES spectra of the VEK glass recorded after different irradiation time of the same sample spot (right).

The U coordination for the U doped model glasses is consistent with literature data from Farges *et al.* who investigated several U doped silica glasses and reports similar results for the U-O bond distances.<sup>128</sup> Note that EXAFS probes the average local atomic environment of all U

atoms in the glass and it is not very sensitive to small structural changes. Therefore, the U(IV) species mainly visible for the lowest U concentration can be induced by minor local structural defects in the glass matrix, which are not detectable by EXAFS analyses.

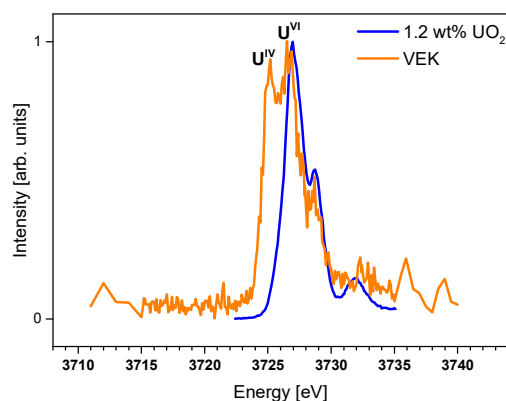


**Figure 40** U  $M_4$  edge HR-XANES spectrum of the VEK waste glass sample in comparison to the U doped glass with 1.19 wt%  $UO_2$ . The VEK glass spectrum represents the merged spectra depicts in **Figure 39** (right).

#### *VEK glass Pu $M_5$ and U $M_4$ HR-XANES*

The Pu  $M_5$  edge HR-XANES of the genuine VEK glass and the 0.2 wt% Pu doped glass sample are compared in **Figure 39**. No significant differences between the two spectra are identified. The obtained results confirm that Pu(IV) is the main species also in the VEK glass. These results agree with Pu  $L_3$  edge XANES studies performed by Dardenne *et al.* on the same material.<sup>74</sup> The low signal-to-noise-ratio due to the low Pu concentration of approximately 0.04 wt%  $PuO_2$ <sup>150</sup> does not allow reliable interpretation of the post-edge part of the spectrum. According to the hypothesis proposed in **Section 4.1**, it might be possible that minor amounts of Pu(VI) exist as the VEK glass was synthesized adding dissolved  $HNO_3$  waste. If the presence of an inert gas atmosphere, which was applied in **Section 4.1** but was not present in the VEK glass furnace, is required to obtain Pu(VI) remains unclear.

In **Figure 39** (right) the U  $M_4$  edge HR XANES spectra of the VEK glass are shown. They are measured after different irradiation time of one sample spot. A spectral feature at approximately 3725.2 eV characteristic for U(IV) gains intensity as a function of the irradiation time. X-ray induced radiation damage is known to occur when using highly intensive synchrotron radiation (cf. **Section 23**).<sup>151, 152</sup> However, the observed radiation damage is unusually strong for irradiation with a beam with low photon flux of  $10^9$  photons/s (at 3.7 keV) and appears after only a few minutes of exposure. Remarkable is also the fraction of the reduced U atoms. Taking into account the changes of intensity, at least 50% of the initially present U(VI) is converted to U(IV) which might even lead to a structural rearrangement. An average of the radiation damaged spectra yields the spectrum depicted in **Figure 40** in which

both oxidation states are well separated. Comparing the high-energy feature at approximately 3727 eV for the genuine and the U model glass with similar U concentration, U(VI) can be identified as initially present in the VEK glass. The effect seems to be reversible. After repeating the experiment 14 months later, U(VI) was found initially in the sample, which we once more reduced to U(IV) upon irradiation.

Clarification of the X-ray induced radiation damage mechanism is challenging. Conclusions can be drawn from the fact that radiation damage is observed for the VEK glass only but not for the U model glasses. The model glasses were irradiated with a three orders of magnitude higher photon flux at ESRF compared to the measurement of VEK glass at ANKA. The unlike behavior of U upon X-ray irradiation might be caused by differences in the U speciation in the model and the VEK glasses or by some other radiation induced electron transfer processes in the waste glass. The irradiation with X-ray photons at the U L<sub>3</sub> edge (17166 eV) did not show any change in the U oxidation within the studies of Dardenne *et al.*<sup>74</sup> This implies that the energy (3.7 keV) of the incident photons are of importance for the potential charge transfer process.

#### *VEK glass EXAFS*

Comparison of the EXAFS spectra of the VEK and the U model glasses (cf. **Figure 41** and **Figure 38**) reveals differences in the second coordination sphere at ca. 4 Å. Dardenne *et al.*<sup>74</sup> who analyzed the spectrum of the VEK glass, suggests Al or Si to be located in the vicinity of the U atom at a distance of 3.97 Å (cf. **Table 37** in the **Appendix**). EXAFS usually is not able to distinguish between elements with Z differences of ± 1. In order to obtain additional insights, compounds where U binds in a similar manner to entities containing O and Si/Al are compared. When units containing Si coordinate to U and the Si atoms are located in the second coordination sphere at approximately 3.63-3.89 Å, the equatorial U-O distance is contracted to 2.23–2.29 Å. This is comparable to the obtained 2.27 Å U-O distance for the VEK glass. Whereas when Al neighbors U in the second coordination sphere at 3.88 Å, the equatorial U-O distance averages at ca. 2.4 Å.<sup>153-156</sup> As Si and Al are generally not known as redox active elements, reduction of U by one of those is less likely. It is, however, known that charge can be transferred upon irradiation with X-rays leading to changes in the oxidation state of the probed element especially for soft X-rays due to its very high energy deposit.<sup>157, 158</sup>

The EXAFS analyses of the U model glasses do not reveal a second coordination sphere. In addition, the U-O distances and the coordination numbers for the first coordination shell for the VEK and the U model glasses are slightly different. The fit reveals 2 O at 1.80 Å, 5 O at 2.27 Å and 1.2 O at 2.82 Å for the VEK glass (cf. **Table 37** in the **Appendix**). This corresponds to a characteristic uranyl U-O bond length with an average distance of 1.80 Å for O<sub>ax</sub> and

2.28-2.47 Å for  $O_{eq}$ .<sup>120</sup> Whereas for the U model glasses the  $UO_2^{2+}$  cation with an axial  $U-O_{ax}$  bond distance of 1.84 Å can be considered as elongated, which was also found by the Raman investigations.

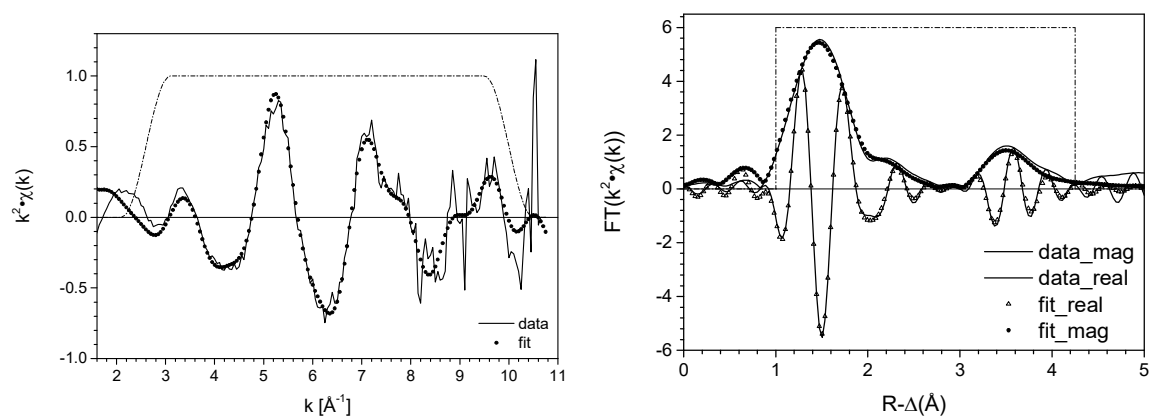


**Figure 41** U  $L_3$  edge EXAFS spectrum of the VEK glass in  $k$  space. Experimental data are shown as solid line whereas black symbols represent fit results (left). FT-EXAFS spectra of the same sample in  $R$  space. Magnitude and real part of the experimental data are shown as solid lines, symbols represent the fit results (right). Data were obtained and evaluated by Dardenne *et al.*

#### VEK SEM-EDX

EXAFS analyses reveal that U in the VEK glass is coordinated likely by silicate ligands with Si atoms residing in the second coordination sphere forming ordered agglomerates in the glass matrix. SEM-EDX analysis were performed to visualize and characterize the size and the chemical composition of these clusters. A glass particle with a size of approximately 1 x 1 mm was extensively explored but no isolated U containing phases were found. The glass has an amorphous glass matrix with numerous expected inclusions of  $RuO_2$  needles and spherical Pd particles (cf. **Section 7**). The chemical compositions of the  $RuO_2$  particles and the matrix glass revealed by the EDX analysis are listed in in **Table 9**. Due to the low U content and potentially small size of these U and Si rich particles, it is possible that they are not detected by SEM-EDX. TEM investigations in collaboration with Thierry Wiss (*JRC-Karlsruhe*) are planned.

#### VEK glass Raman

The Raman spectrum of the VEK glass excited with 785 nm laser diode recorded by González-Robles Corrales *et al.*<sup>159</sup> is also depicted in **Figure 31**. Neither evidences for crystalline phase separations are observed nor the symmetric stretching mode  $\nu_1(UO_2^{2+})$ . Although the  $UO_2$  content of the glass is estimated to be 1.19 wt%<sup>74</sup> the  $\nu_1(UO_2^{2+})$  might not be resolved due to a very high background caused by the numerous elements which are incorporated in the waste glass matrix. The use of a laser with a different wavelength, e.g., 532 nm, might decrease the background in the region of interest and reveal the  $\nu_1(UO_2^{2+})$  stretching.

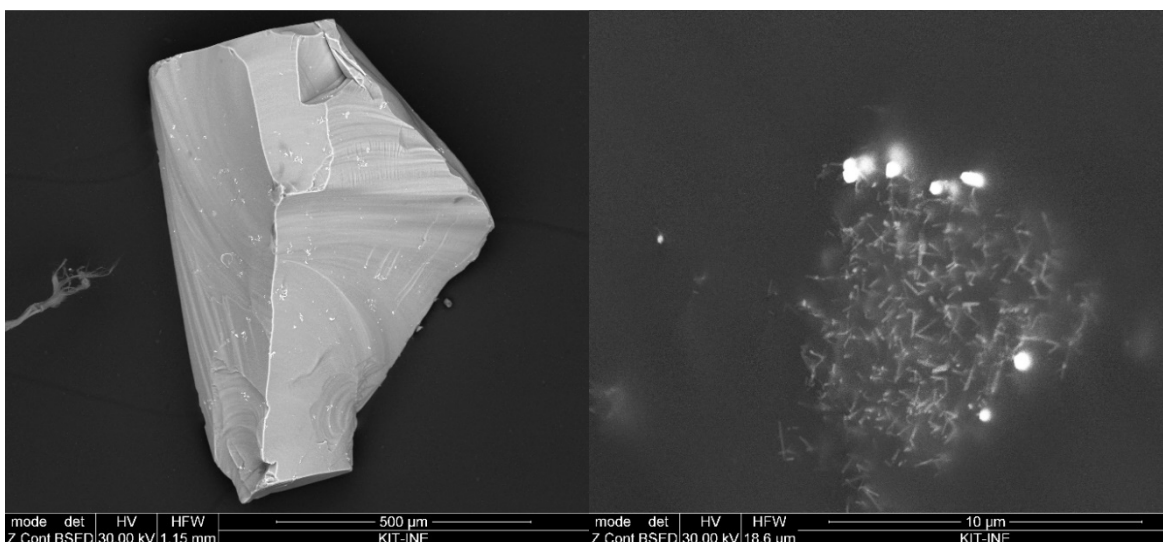


**Figure 42** Micrograph of a 1 mm VEK glass particle (left). NMP agglomerates of RuO<sub>2</sub> needles and spherical Pd particles (right).

**Table 9** EDX results of the NMPs and the glass matrix averaged from three measurements (only selected elements are listed).

Element (wt%)	O	Na	Mg	Si	Ca	Ru	Pd	U
RuO <sub>2</sub>	39.3	1.8	0.14	3.8	0.51	51.2	0	0.58
Glass	59.6	7.6	0.8	22.1	3.25	0	0	1.82

### 4.2.3. Discussion

The strong X-ray induced radiation damage observed only for the VEK glass might be explained by transfer of electronic charge leading to reduction of U(VI) to U(IV). The identified ordered U environment, involving U, O and likely Si, possibly contributes to the observed effect as it is not observed in the U model glass.

The X-ray beam can in addition induce transfer of free charges as for example trapped electrons to U or provoke reactions with radical constituents of the highly radioactive VEK glass. Such species are continuously build up by the radioactive decay. The reversibility of the effect shows that those transferred to U electrons can be again excited possibly due to internal transfer of energy and/or irradiation with visible light leading to formation of U(VI). Elucidation of the X-ray induced radiation damage mechanism can be of great interest as it can be correlated to the long-term changes of the U speciation in a repository. Similar processes can be potentially induced by the  $\alpha$ -,  $\beta$ - and  $\gamma$ -activity in a highly radioactive nuclear waste glass and be of importance in a long-time scale. Since U is present predominantly in its hexavalent state according to the present analysis, five years ageing of the VEK glass does not appear sufficient

to detect redox change of U. But as the glass will be exposed to ion radiation for hundreds of years the accumulated dose might be adequate for appreciable reduction of U and maybe other An. Taking into account the photon flux, the photon energy, the exposed sample volume and its density, the accumulated dose within a 2 h measurement can be estimated to approximately 1 MGy. The irradiation with X-ray photons at the U L<sub>3</sub> edge (17166 eV) did not show any change in the U speciation within the studies of Dardenne *et al.* which is a clear evidence that the energy of the electromagnetic radiation play an important role by the process.<sup>74</sup>

In addition to the U and Pu HR-XANES studies, Np M<sub>5</sub> edge HR-XANES investigations were performed. Np is present in very low concentrations (less than 0.02 wt% NpO<sub>2</sub>) in the glass. The Np-237 doped French R7T7 glass was used as a reference material since no Np model glass with the VEK glass frit was prepared. The chemical compositions and synthesis conditions of the two glass frits do not substantially differ as both glasses are borosilicate glasses with addition of Al, Li, Na, Ca, Mg and Ti, melted in ambient conditions.<sup>160</sup> The R7T7 glass is doped with ca. 0.85 wt% NpO<sub>2</sub>. In **Figure 43** Np M<sub>5</sub> edge HR-XANES spectra for the R7T7 glass and VEK glass are compared to spectra of Np redox references measured within the same experimental campaign: Np(IV)O<sub>2</sub>, Ca<sub>0.5</sub>Np(V)O<sub>2</sub>(OH)<sub>2</sub>·1.3H<sub>2</sub>O, Na<sub>2</sub>Np(VI)<sub>2</sub>O<sub>7</sub>.<sup>97-99</sup> Their preparation is described in the experimental section. While NpO<sub>2</sub> is similar to UO<sub>2</sub> and PuO<sub>2</sub>, the Np(V) and Np(VI) references reveal a neptunyl and neptunate structure, respectively. Likewise for uranyl and plutonyl<sup>80</sup>, the spectrum for neptunyl species exhibit characteristic features marked with **B** in **Figure 43**. Due to the similar energy distances between the main peak and feature **B** for the R7T7 glass and the Np(V) reference sample, it can be concluded that Np occurs dominantly in its pentavalent oxidation state in the French glass.

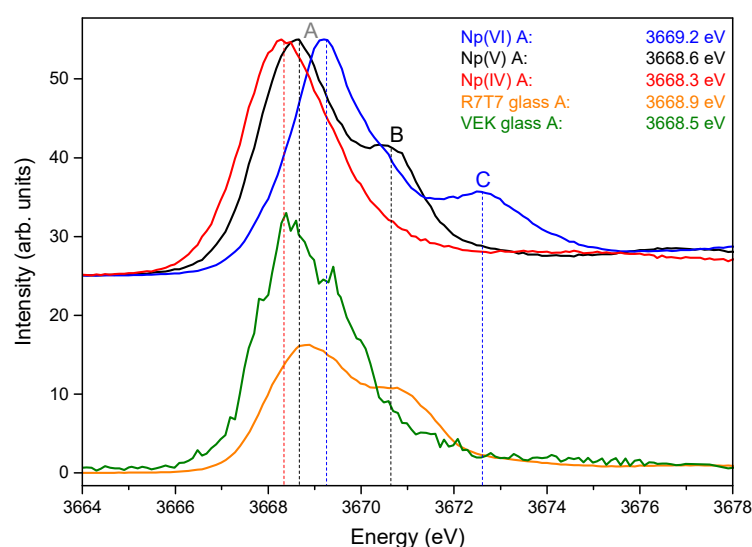


**Figure 43** HR-XANES spectra of the VEK glass and the Np doped R7T7 reference glass in comparison with Np redox references (Np(IV)O<sub>2</sub>, Ca<sub>0.5</sub>Np(V)O<sub>2</sub>(OH)<sub>2</sub>·1.3H<sub>2</sub>O and Na<sub>2</sub>Np(VI)<sub>2</sub>O<sub>7</sub>).

Dardenne *et al.* reported Np(V) as the predominant Np oxidation state in the VEK glass. The Np L<sub>3</sub> edge spectrum has a post-edge multiple-scattering feature indicating neptunyl speciation<sup>103</sup>. Neptunyl characterizes with 1.89 Å<sup>161</sup> and 1.74 Å<sup>162</sup> trans-dioxo bond distance (Np-O<sub>ax</sub>) for Np(V) and Np(VI) neptunyl, respectively. Np L<sub>3</sub> edge EXAFS analysis of the VEK glass was not possible due to the very low Np concentration. However, the Np(IV) and Np(V) L<sub>3</sub> edge XANES spectra have similar positions therefore contribution of Np(IV) cannot be excluded.

The Np M<sub>5</sub> edge HR-XANES spectrum of the VEK glass does not have the feature **B** characteristic for neptunyl. In contrast to the Np L<sub>3</sub> edge study, the spectrum strongly resembles Np(IV) not Np(V). The energy positions of the main peaks for the VEK and the NpO<sub>2</sub> spectra are similar. The VEK spectrum has a slightly asymmetric shape with a shoulder on the high-energy side at ca. 3669.4 eV, which might be explained by the presence of a minor amount of Np(V) oxidation state. It is possible that the X-ray induced radiation damage detected for U occurs also for Np and the initial Np(V) has reduced to Np(IV) upon irradiation. Seven spectra measured for 10 min/spectrum were recorded to verify this assumption but no clear reduction of Np(V) to Np(IV) was observed. Due to the low Np concentration, a more rapid acquisition of spectra was not possible. Future experiments at the CAT-ACT beamline might help to elucidate the question if Np shows a behavior similar to U in the VEK glass when analyzed by M<sub>5</sub> edge HR-XANES.

#### 4.2.4. Summary and Conclusion

The *An* M<sub>4,5</sub> edge HR-XANES method is applied here for the first time for bulk analyses of redox states of U, Np and Pu in a genuine waste glass sampled during vitrification of HLLW. Obvious discrepancies between the speciation of U and Np in the model and VEK glasses are found, which is an evidence that surrogate glasses are not necessarily suitable model systems, for example for leaching experiments.

Raman, SEM-EDX, XRD and HR-XANES investigations confirm the amorphous nature of the U and Pu model glasses. SEM-EDX analyses reveal RuO<sub>2</sub> needles and spherical metallic Pd particles embedded in the amorphous VEK glass matrix.

U is mainly identified as U(VI) in the VEK and the U model glasses.

The occurrence of U(VI) as predominant oxidation state agrees with published studies for glasses melted in oxidative conditions. Pu is found only as dispersed Pu(IV) species in both Pu doped model and VEK glass. The hypothesis proposed in **Section 4.1** suggests that the Pu speciation depends on the initial speciation of Pu when added to the vitrification mixture.

It agrees well with the Pu model glass as this glass was prepared from PuO<sub>2</sub>. The VEK glass was melted from a HLLW HNO<sub>3</sub> solution in which Pu is most likely present as predominantly Pu(IV). According to the results reported in **Section 4.1** a very minor formation of Pu(VI) can also be possible in the HNO<sub>3</sub> and therefore the glass product. Presumably due to the more complex composition and the presence of redox active elements no Pu(VI) contribution is observed in the VEK glass.

Ordered inclusions in the VEK glass comprising U, O and likely Si atoms are interpreted from EXAFS spectroscopy but are not detected by SEM-EDX analysis. Scheduled TEM investigations might help to better characterize these likely very small (less than 200 nm) ordered regions in the glass matrix. XAS spectroscopy at the Si and Al K absorption edges might further help to identify the chemical composition and structure of those particulate inclusions. EXAFS analyses are also of interest for Pu and Np but were not possible to perform at the INE-Beamline due to the low concentration and the limited incident beam intensity. Such investigations will be carried out in the near future at the Pu and Np L<sub>1</sub> edges at the CAT-ACT beamline, which provides at least two orders of magnitude higher photon flux at 22.4-23.1 keV compared to the INE-Beamline.

The reduction of U(VI) to U(IV) induced explicitly by tender X-ray radiation (3.7 keV) but not by 17 keV photons and observed only for the VEK glass but not for the model U doped glasses is of high interest. Elucidation of the origin of this effect is challenging. It is possible that it is correlated with the ordered U environment involving U, O and likely Si, found only in the VEK glass by U L<sub>3</sub> edge EXAFS. Free charges and/or radicals, which are continuously generated by the decay of radioisotopes, can be transfer to/react with U and therefore possibly contribute to the reduction effect.

Np forms predominately Np(V) in the Np doped R7T7 reference glass, whereas mixture of Np(IV) and likely Np(V) is identified for the VEK glass. It is possible that Np(IV) results from X-ray induced radiation damage process similar to the effect described for U. Although the distinct determination of the Np oxidation states is challenging, it is possible to demonstrate that there are differences in the Np oxidation states and coordination for the Np doped R7T7 glass compared to the VEK glass.

## 5. Actinide (An) oxidation states investigations of spent nuclear fuel (SNF)

"SNF is most probably one of the most complex materials which is known to human kind" – P. Carbol, GENTLE course "Nuclear Waste Management", INE Karlsruhe, Germany.<sup>163</sup>

SNF undergoes a variety of processes, therefore, its characteristics depend on a multiplicity of factors.<sup>163</sup> The chemical and physical properties of SNF are influenced by initial chemical composition (UO<sub>2</sub> or MOX), isotopic enrichment, irradiation (burn-up and power rating) as a result of fission and nuclear reactions, FP distribution, fission gas migration and release, temperature history after discharge and decay time. The thermochemical configuration of the irradiated fuel is strongly affected by the chemical properties of the fission products. A variety of phases is formed, e.g., grain boundary precipitates (oxide or  $\epsilon$ -phases). Mechanical stress as a result of swelling of the ceramic fuel pellet and thermal stresses lead to formation of cracks.

An axial cross-section of a 10 mm SNF pellet in its Zircaloy cladding is shown in [Figure 45](#). Due to the cylindrical geometry of the SNF pellet and the neutron energy spectrum, the outer rim region of a fuel pellet is a zone of increased neutron absorption by U-235 compared to the inner core area.<sup>164</sup> The elevated absorption causes a local enrichment of plutonium and other transuranium elements. The Pu presence leads to a higher fission density and consequent higher concentrations of FPs in the rim region. The local burn-up in this region of the fuel can be 2-3 times higher than the fuel pellet average burn-up. Upon reaching a local burn-up of about 50-75 GWd/t<sub>HM</sub> the fuel undergoes restructuring processes significantly altering the morphology of the SNF (cf. [Figure 44](#)).<sup>165</sup> This structure was first observed in the early 1960s by Bleiberg *et al.*<sup>166</sup>, typically at in the rim of the pellet (i.e., at its radial periphery). Due to its formation characteristics it was called rim-structure and later high burn-up structure (HBS).<sup>167</sup> Numerous studies have explored the properties of this material.<sup>164, 165, 168, 169</sup> It is characterized by sub-micron grains from 0.3-0.1  $\mu\text{m}$  which are formed from the initially present 10  $\mu\text{m}$  sized grains. Fission gases diffuses out from the subdivided grains and precipitates into finely dispersed intergranular bubbles, drastically increasing the local porosity of the material (up to values higher than 20%).<sup>170</sup> The thickness of the HBS highly depends on the irradiation history and the average fuel burn-up. The initially few micrometer thick layer propagates inwards with increasing local burn-up (e.g., it reaches 1200  $\mu\text{m}$  for the sample with 100 GWd/t<sub>HM</sub> average burn-up).<sup>171</sup> After the first observation in the late 1950s, the relevance of the HBS was reevaluated in the 1980s<sup>172</sup>, following the general trend of increasing the fuel discharge burn-up up to levels which encompass significantly the formation of the HBS. Questions arose concerning the safety of prolonged fuel operation. The need for extended knowledge of the HBS

properties and reactivity was highlighted. Since then, the HBS has remained object of studies worldwide.<sup>173-175</sup>

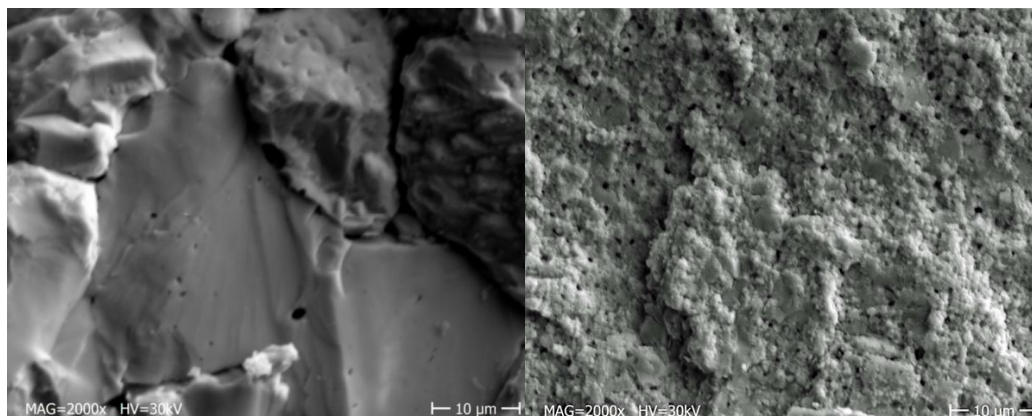


**Figure 44** SEM micrograph of high burn-up SNF from the core region of a pellet (left) and from the rim region of a pellet (right). The latter reveals the typical characteristics of the HBS morphology. These two radial pellet regions were used for preparation of samples **S1** and **S2**. (Reproduced with permission from Ref. <sup>176</sup>)

As a host for an increased amount of radiotoxic FPs, the HBS material is of particular interest in safety assessments of storage and disposal sites. It has to be considered for the interpretation of experimental results on SNF dissolution. One aspect of concern is the oxidation state (and evolution) of the irradiated fuel matrix during irradiation and storage. Chemical alteration of SNF may lead to significantly changed chemical and physical properties, affecting its long-term, but also intermediate storage performance (cf. **Section 2.1.1.3**).

The oxidation of unirradiated and irradiated  $\text{UO}_2$  are very complex processes which depend on numerous parameters. In the following an overview is given on relevant published studies investigating the oxidation behavior of unirradiated  $\text{UO}_2$ , SNF materials and  $\text{PuO}_2$ .

#### *Oxidation of unirradiated $\text{UO}_2$*

Oxidation processes take place when  $\text{UO}_2$  comes into contact with air. The oxidation of  $\text{UO}_2$  is influenced by several parameters such as temperature, moisture<sup>177</sup>,  $\text{O}_2$  partial pressure<sup>178, 179</sup>, microstructural morphology and density. McEachern *et al.*<sup>178</sup> discuss in their review that several key parameters affect the oxidation of  $\text{UO}_2$  below 400 °C, which is the highest expected temperature for SNF in dry storage.<sup>180</sup> They describe the oxidation of  $\text{UO}_2$  as a two-step reaction:



The first step of this reaction ( $\text{UO}_2 \rightarrow \text{U}_3\text{O}_7/\text{U}_4\text{O}_9$ ) occurs already at room temperature in ambient conditions. Above 250 °C, oxidation from the  $\text{U}_3\text{O}_7/\text{U}_4\text{O}_9$  to  $\text{U}_3\text{O}_8$  is observed.<sup>181, 182</sup> Up to 700 °C, the thermodynamically most stable product of the oxidation process in dry air is

$\gamma$ - $\text{UO}_3$ .<sup>183</sup> However, in practice this final oxidation process from  $\text{U}_3\text{O}_8$  to  $\gamma$ - $\text{UO}_3$  is hindered and  $\text{U}_3\text{O}_8$  is stable up to 1100 °C when it decomposes.<sup>178</sup> The reasons remain poorly understood. The  $\text{UO}_2$  matrix undergoes a change in its crystal structure from a fluorite type to a distinct different crystal structure with a 23% decreased density.  $\text{U}_3\text{O}_8$  has an orthorhombic crystal structure where U coordinates by six O atoms at 2.07-2.23 Å distances. The oxidation from  $\text{UO}_2$  to  $\text{U}_3\text{O}_8$  goes along with a net volume increase of 36%.<sup>184</sup> If occurring in actual spent nuclear fuel, this oxidation process could lead to failure of the cladding encapsulating the pellets, significantly complicating its handling and packaging.<sup>185-187</sup> The two step oxidation of  $\text{UO}_2$  is a complex reaction and is often observed to occur concurrently. The intermediate state of  $\text{U}_3\text{O}_7/\text{U}_4\text{O}_9$  forms as discrete layer on the surface of the material.<sup>188</sup> As its growing is limited by the rate of  $\text{O}_2$  diffusion, a parabolic reaction kinetic is observed.<sup>189, 190</sup> The formation of  $\text{U}_3\text{O}_8$  from this intermediate species is described as a nucleation-and-growth mechanism with sigmoidal reaction kinetics.<sup>186</sup> The superposition of both process kinetics has a more complex reaction progress which is discussed in details in the review of McEachern *et al.*<sup>178</sup>

With regard to the surface of the fuel, the oxidation from  $\text{UO}_2$  to the intermediate  $\text{U}_3\text{O}_7/\text{U}_4\text{O}_9$  species is found to occur with high reaction rates. The chemisorption of  $\text{O}_2$  on the matrix surface which is the first step of the oxidation process, was found to be a rapid and a highly exothermic process.<sup>191</sup> A oxidized layer of approximately 5 nm is rapidly formed on  $\text{UO}_2$ .<sup>178</sup> Due to its significant density difference, the  $\text{U}_3\text{O}_8$  which is formed subsequently for temperatures above 250 °C in dry air is observed to spall from the surface of sintered  $\text{UO}_2$  samples in form of fine powder. The duration until the first powder is visually observed is called “powder-formation time”.<sup>192, 193</sup>

Scientists from Pacific Northwest National Laboratory (PNNL) examined the oxidation performance of sintered unirradiated  $\text{UO}_2$  pellet stored in ambient conditions and at temperatures from 135 °C to 230 °C.<sup>194</sup> The oxidation at 230 °C in an ambient atmosphere showed a drastic change in oxidation kinetics towards faster reactions and higher oxidation states than  $\text{U}_3\text{O}_8$ . The reasons remain not yet fully understood.<sup>194</sup>

As both  $\text{O}_2$  chemisorption and diffusion controlled formation of  $\text{U}_3\text{O}_7/\text{U}_4\text{O}_9$  are highly dependent on the surface area, a smaller particle size of the material strongly increases the oxidation rate. This is shown by the pyrophoric behavior of 0.05  $\mu\text{m}$  sized  $\text{UO}_2$  powder at 0 °C<sup>195</sup> whereas sintered  $\text{UO}_2$  only forms a 1  $\mu\text{m}$  thick oxide layer at 250 °C after 24 h<sup>196</sup>.

Presence of  $\text{H}_2\text{O}$  drastically enhances the oxidation of the  $\text{UO}_2$  matrix. Water is a potential source for radiolytic oxidation products increasing oxidation reactions. In addition,  $\text{H}_2\text{O}$  can

incorporate in the structure, widening the variety of oxidation products which facilitate alternative kinetics and reaction paths.<sup>184, 194</sup>

#### *U speciation in simulated and genuine SNF*

Generally, significant fuel oxidation may occur only if the cladding is breached as in the case of defective fuel rods. Wasywich *et al.*<sup>197</sup> analyzed defective CANDU (CANada Deuterium Uranium) fuel bundles which were stored for up to 100 months in dry and a moist air atmosphere by microscopy, XPS and XRD. CANDU fuel consist of UO<sub>2</sub> pellets with natural U isotopic composition. Due to the use of heavy water as moderator, no U-235 enrichment is required. Most extensive U oxidation was found for areas in the periphery of the SNF pellets with high FP concentration and increased porosity characteristic for HBS. While in moist air the ratio U(VI)/U(IV) was found to be more than 1, suggesting formation of U<sub>3</sub>O<sub>8</sub>, in dry air the fuel oxidation stopped at the  $\alpha$ -U<sub>3</sub>O<sub>7</sub> phase (U(VI)/U(IV) < 1). U(V) was not considered in the study. However, while the moist oxidation affected mainly large surface areas of the material, the dry air oxidation penetrated the material via grain boundaries and fuel sheath gaps and had less impact on the surface.

Jegou *et al.* also investigated the oxidation behavior of U in SNF with respect to the HBS and the core material of a pellet (average burn-up of 60 GWd/t<sub>HM</sub>) by heating the materials with an external laser beam and performing Raman spectroscopy. They report that the HBS is more stable against oxidation processes compared to the core material of an irradiated UO<sub>2</sub> fuel pellet.<sup>198</sup> In the core material predominantly UO<sub>2</sub> was oxidized to  $\alpha$ -U<sub>3</sub>O<sub>8</sub> (U(V) and U(VI)) species, whereas the HBS areas were only oxidized to U<sub>4</sub>O<sub>9</sub> (U(IV) and U(V)). These phases, formed on the surface of the heated material, were identified with the help of their characteristic Raman spectra. The observed oxidation behavior might be attributed to the higher content of trivalent fission products and plutonium, stabilizing the fluorite structure of the UO<sub>2</sub> HBS matrix. However, Jegou *et al.* point out the different temperature conductivities of the materials due to variations in their compositions. Differences in thermal conductivity and microstructure leads to different local temperatures when the material is heated with a laser beam, potentially resulting in different oxidation behavior of UO<sub>2</sub>. Simultaneous temperature determination was not possible due to the technical setup.

Cobos *et al.*, who doped UO<sub>2</sub> pellets with additional elements in order to simulate different levels of burn-up, support the hypothesis for enhanced oxidation resistance.<sup>199</sup> The conversion of the simulated SNF to U<sub>4</sub>O<sub>9</sub> and U<sub>3</sub>O<sub>8</sub> was found to be strongly delayed for higher burn-ups at 1000 °C. However, the investigated SNF simulated material was synthesized as sintered pellets

with high density and low porosity, not comparable to the HBS morphology of genuine fuel. Therefore, it is questionable in which extent these results are transferable to irradiated fuel.

McEachern *et al.* discussed also the higher oxidation rate of submicrometric grains.<sup>178</sup> Due to the small particles size ( $\sim 0.1 \mu\text{m}$ ) of the HBS, the surface area was increased, enhancing oxidation reactions compared to SNF core material ( $\sim 10 \mu\text{m}$ ). The higher density of grain boundaries also likely led to increased oxygen diffusion. It is possible that the effect of larger porosity and smaller grains competes with oxidation state stabilizing effects from high concentrations of FPs and therefore only minor oxidation of U was observed in the HBS after heating.

Fanghänel *et al.*<sup>200</sup> concluded that the higher stability exhibited by the HBS is related also to the tight nature of the HBS grain boundaries, as shown for example in retained fission gas high temperature release tests.

Campbell *et al.*<sup>201</sup> compared the oxidation behavior of LWR SNF and unirradiated  $\text{UO}_2$  fuel by studying weight differences. The initial SNF weight gain rates at  $230 \text{ }^\circ\text{C}$  were found to be 50 times greater than those for  $\text{UO}_2$ . While initially delayed, compared to the  $\text{UO}_2$ , oxidation to  $\text{U}_3\text{O}_8$  was found by X-ray diffraction for all investigated SNFs. Taylor *et al.* explain this by the fact that the FPs are less soluble in a  $\text{U}_3\text{O}_8$  phase than in  $\text{UO}_2$ , delaying the oxidation process.<sup>202</sup> Exposure to a  $\gamma$ -radiation field increased the weight gain with both increasing temperature and exposure time. Material with high microporosity was preferentially oxidized. For 4000 h of air and radiation exposure at  $230 \text{ }^\circ\text{C}$ , the fuels exceeded a weight gain level of 4 wt%, indicating U oxidation to higher oxidation states than  $\text{U}_3\text{O}_8$ .<sup>201</sup>

#### *Oxidation of $\text{PuO}_2$*

$\text{PuO}_2$  is a stable phase at room temperature and ambient conditions. It is formed on the surface of Pu metal when exposed to dry air.<sup>123</sup> First, the  $\text{PuO}_2$  layer has a protective effect limiting the O diffusion. If a certain thickness of the layer is reached, stress-induced spallation processes are initiated.<sup>203</sup> When the material is transferred to inert conditions such as vacuum or an inert gas atmosphere, the  $\text{PuO}_2$  layer transforms rapidly within approximately 200 min into  $\text{Pu}_2\text{O}_3$ .<sup>123</sup> In moist air the oxidation rate of Pu is increased by 100 fold. The rate enhancement is attributed to formation of a  $\text{PuO}_{2+x}$  layer. In water,  $\text{PuO}_2$  is oxidized to a  $\text{PuO}_{2+x}$  phase which releases Pu(V) into the solution.<sup>204</sup> Subsequent processes may involve its disproportionation to Pu(IV) and Pu(VI) and Pu(VI) reduction. In a dry atmosphere  $\text{PuO}_2$  was found to be inert in the presence of  $\text{O}_2$ , ozone and nitrogen.<sup>203</sup> XPS, Auger electrons spectroscopy and XRD methods were mainly used in the reviewed studies to determine the different Pu oxide phases.

Mixed U-Pu oxide solid material was investigated by Vauchy *et al.* by TGA, XAS and XRD after exposure to low moisture and an O<sub>2</sub> containing atmosphere at room temperature. A fast oxidation of the grains surface was detected increasing the overall O content of the samples. Nevertheless, the Pu did not exceed the tetravalent oxidation state in the bulk of the material.<sup>205</sup>

Pu speciation in simulated and genuine SNF: Kropf *et al.* investigated UO<sub>2</sub> fuel irradiated within the *ATM-103 project* (Calvert Cliffs, USA)<sup>206</sup> by Pu high-energy resolution L<sub>3</sub> edge EXAFS using a Laue geometry analyzer. They found Pu occupying tetravalent U positions in the fuel matrix with Pu-O distances typical for PuO<sub>2</sub>. Np concentrations were too low for EXAFS analysis, but qualitative evaluation suggested that also Np is incorporated as UO<sub>2</sub>-like phase in the fuel matrix.<sup>207</sup> Also Fortner *et al.* reported the incorporation of Pu in its tetravalent state in SNF.<sup>208</sup> Anthonysamy *et al.* identified tetravalent Pu and Th along with oxidized U(IV) to U(V) in an U-Th-Pu MOX material in TGA-TDA experiments.<sup>209</sup>

There are still significant discrepancies in the oxidation behavior of UO<sub>2</sub> and SNF which are not yet fully understood.<sup>178</sup> As SNF is a highly challenging material to handle and the availability of techniques probing the bulk material with respect to the *An* oxidation states are limited, less is known about the U and Pu speciation in the bulk material. Current literature acts on the assumption that the majority of the UO<sub>2</sub> matrix remains in its tetravalent oxidation state and that the other *An* are formed in their lower stable oxidation states such as Pu(IV).<sup>210</sup> How the U and Pu speciation changes at high burn-ups is still a question of debate.

Mostly, speciation investigations of simulated SNF or material surface studies of genuine SNF are reported, which might not be comparable to irradiated bulk SNF. The U and Pu oxidation states are investigated with surface sensitive techniques like XPS probing only approximately 5 nm depth of the material. The interpretation of Raman spectra can be challenging. Detection of vibrational bands specific for the U and Pu species might be not possible due to various signals from the irradiated SNF with a complex chemical composition.<sup>198</sup> The probing depth of the Raman investigations on *An* materials was estimated to about 500 nm.<sup>2, 211</sup> Therefore, the method is bulk sensitive, but surface species still contribute significantly to the spectra. In addition the intensive laser light can heat the material up and induce changes of the *An* speciation as used by Jegou *et al.* in their U oxidation study.<sup>198</sup> Böhler *et al.* illustrated that the U/Pu L<sub>3</sub> edge XANES method is more sensitive to minor changes of U and Pu oxidation states in as prepared and melted UO<sub>2</sub>, PuO<sub>2</sub> and a UO<sub>2</sub>-PuO<sub>2</sub> system ( $0 \leq x(\text{PuO}_2) \leq 0.5$ ) in comparison to XRD and Raman spectroscopy.<sup>212</sup> *An* L<sub>3</sub> edge XANES is useful but has clear limitations (cf. **Section 4.1**). It is often not possible to detect minor contributions of one oxidation state in

mixtures. In addition, the spectra of for example U L<sub>3</sub> XANES of UO<sub>2</sub> and U<sub>4</sub>O<sub>9</sub> are almost identical. This can be overcome by the *An* M<sub>4,5</sub> edge HR-XANES method.

The aim of the here presented study is to provide insights into the U and Pu oxidation states in SNF, in both core and rim region (where the HBS is formed), using the U M<sub>4</sub> and Pu M<sub>5</sub> edge HR-XANES technique. This method is able to distinguish between different oxidation states even when mixed in the same material. The results will contribute to the understanding of complex SNF, which is necessary for safety assessment of its intermediate storage and final (long-term) disposal.

A SNF pellet irradiated up to approximately 50 GWd/t<sub>HM</sub> originating from a Swiss commercial pressurized water reactor was investigated. Two samples from the core and the rim, i.e. the HBS area, of this SNF pellet were prepared. The sampling positions are indicated in [Figure 45](#). Small particles with approximately 500 μm size were removed from the inner part of the pellet. The second sample was made by pressing the Zircaloy detached from the SNF against a Kapton tape; it contains particles with HBS characteristics (cf. [Figure 45](#)). This preparation procedure was followed in order 1) to reduce the dose of the samples, which simplifies their handling, and 2) to minimize self-absorption effects. The latter is of concern by investigations of highly concentrated samples.<sup>213</sup> In this case, the emitted photons are partly re-absorbed by neighboring atoms and the spectral intensity is damped.

Since the samples likely exhibit high surface-to-volume ratio and handling was performed partly in air, several unirradiated UO<sub>2</sub> benchmark samples (**U1-U3** and **UF1**, cf. [Table 10](#)) were prepared in order to evaluate the effect of the preparation procedure on the U and Pu oxidation states. In addition, a third sample with more bulk-like character originating from fuel irradiated within the international *High Burn-up Rim Project (HBRP)*<sup>165</sup> was studied. The 100 GWd/t<sub>HM</sub> burn-up of the material is similar to the burn-up level reached in the rim region of irradiated commercial fuels with an average burn-up of ca. 50 GWd/t<sub>HM</sub> and above. This material irradiated under conditions of radially homogeneous burn-up and temperature<sup>165</sup> consists of a completely transformed into HBS as demonstrated by previous studies.<sup>173</sup> A 4 mg fragment was washed with acetone to remove any dust particles and was prepared for U and Pu M<sub>4,5</sub> edge HR-XANES investigations. The preparation of all studied samples and references is described in **Section 5.1**.

## 5.1. Experimental

All samples and their descriptions are listed in **Table 10** in **Section 5.2**. The studied SNF samples **S1** and **S2** were obtained from the *SBS1108 N0204* fuel rod segment which was irradiated in the commercial pressurized water reactor Gösigen nuclear power plant in Switzerland. The irradiation was carried out in four cycles for a period of time of 1226 days with an average linear power rate of 260 W/cm achieving an average burn-up of 50 GWd/t<sub>HM</sub>. The fuel rod segment was discharged on 27<sup>th</sup> of May 1989 that implies a cooling time of 24 years before cutting and characterization of the segment. The characterization of the *SBS1108 N0204* fuel rod segment was performed and reported by Metz *et al.*<sup>214</sup> The fuel rod treatment, storage and preparation procedure after discharge is described by González-Robles *et al.*<sup>23</sup> A segment sample (of approximately 10 mm length) was cut in the gap between two adjacent pellets of the fuel rod. The cutting took place in a N<sub>2</sub>-atmosphere (O<sub>2</sub> content less than 1%). After storage for several years in an Ar filled container the fuel was mechanically de-cladded and fractured in a dry air atmosphere. The HBS sample **S1** was fabricated by trapping the SNF dust stuck on the inner cladding wall of the emptied cladding ring on a Kapton tape strip. The particles originate from the rim part of the pellet, that means the contact layer of the fuel with the cladding wall. The dust particles were removed from the wall by applying a mechanical shock to the cladding ring. The particle size was estimated by visual inspection and comparison with powders of known particle size. The average size of the dust particles is estimated by optical comparison (by eye) with powders of known particle size to be smaller than 100 µm. The second SNF sample **S2** was prepared by bringing a particle of several mm size, which was obtained from the fractured pellet core area, in contact with a Kapton tape. Some particles with sizes of ca. 500 µm were caught on the Kapton tape. Both samples then were covered in ambient conditions with 13 µm thick Kapton foil leaving little space for trapped air. They were mounted in a Plexiglas cell equipped with a Kapton window with 8 µm thickness. The prepared samples are shown in **Figure 45**. Their combined dose rate is below 30 µSv/h. All manipulations performed after the de-cladding and fracturing of the pellet took either place in dry air or ambient conditions in the controlled area of the KIT-INE and were mainly performed by E. Gonzalez-Robles and N. Müller.

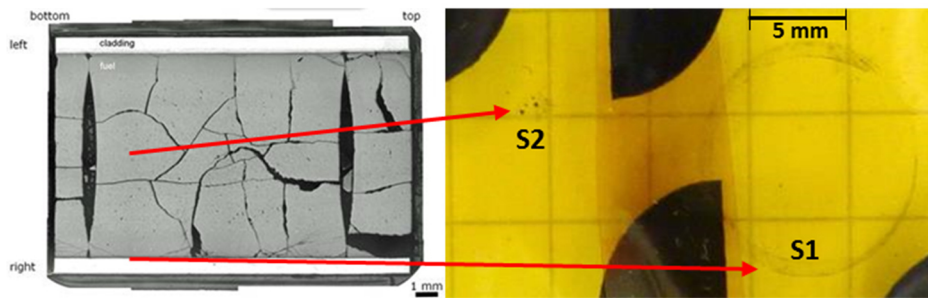


**Figure 45** Macrograph of the commercial irradiated SNF vertical cross section (left). Prepared footprint of core particle **S2** and HBS dust material **S1** on Kapton tape (right) for *An* M edge investigations. Red arrows indicate the origin of the footprint samples material. (Cross section image adapted with permission from Ref. <sup>215</sup>)

The sample **S3** was obtained from high burn-up SNF material prepared and investigated within the “High burnup rim project” (*HBRP*).<sup>173</sup> The U-235 enriched fuel (25.8 wt%) was irradiated from 1993 in the Halden reactor, Norway, at 560 °C to a burn-up of ca. 96 GWd/t<sub>HM</sub>. The special arrangement in the reactor ensured homogenous burn-up and temperature distribution. After discharge in 1996 the material was stored for approximately 20 years in the hot cells of *JRC-Karlsruhe* in a N<sub>2</sub> dry atmosphere with ca. 1% nominal O<sub>2</sub> impurity. The experimental investigations performed during the *HBRP* project have shown that the sample is fully restructured into the HBS.<sup>173</sup> A 4 mg particle of the SNF was washed three times with acetone in an ultrasonic bath in order to remove surface contaminations and dust before mounting it with double sided graphite tape in an Al cell equipped with two independent Kapton windows (cf. **Figure 46**). All manipulations were performed by F. Cappia within 1 hour and took place under a N<sub>2</sub> inert gas atmosphere (may. 10 ppm O<sub>2</sub>) in the laboratories of *JRC-Karlsruhe*.<sup>216</sup> The radiation dose measurement determined dose rates of 15400, 65.7, 8.66 and 6.16 μSv/h in 0, 30, 70 and 100 cm distance from the mounted sample.



**Figure 46** Sample holder for *An* M<sub>4,5</sub> edges HR-XANES (*CEA* design, acknowledgments to Philippe Martin, Philippe Valenza and Renaud Belin) measurements. (1) Outer containment (Al); (2) outer containment ring with 13 μm Kapton foil; (3) inner containment (Al) with a 3 mm dump for *An* sample; (4) inner containment ring with 8 μm Kapton foil; (5) Cover for the first containment; (6) Screws for the first containment ring (left). SNF sample **S3** mounted in the illustrated Al cell sealed with two Kapton windows (right).<sup>216</sup>

The unirradiated  $\text{UO}_2$  benchmark samples were prepared from several ceramic  $\text{UO}_2$  pellets, provided by KIT-INE, with a diameter of 5 mm and a small hole in the center by E. Bohnert (KIT-INE) according to the procedure used in previous studies.<sup>217</sup> They are labeled **U1** (0.3 g and 1.5 mm thickness), **U2** (0.2 g and 1.1 mm thickness) and **U3** (0.2g and 1.0 mm thickness). Pellet **U3** was subsequently broken and consists only of a quarter of the initial 0.2 g pellet. All three pellets were introduced into a high-temperature furnace (positioned in ambient air) and were heated for 6 h at 1150 °C in  $\text{H}_2/\text{Ar}$ -flow (8%  $\text{H}_2$ ). The  $\text{H}_2/\text{Ar}$  stream maintained during cooling. After 1 h the pellets were quickly transferred in the  $\text{H}_2/\text{Ar}$  stream to glass vials filled with Ar. The vials were closed with screw caps. Pellet **U3** was then introduced in an Ar filled glovebox. **U2** was directly transferred to a vacuum chamber for XPS measurements. **U1** was exposed to air for 4 h. A footprint sample **UF1** was then prepared from **U1** by pressing the exposed pellet for some seconds on Kapton tape. Also the pellet **U1** was then transferred to the glovebox. Both **U1** and **U3** were glued onto a Plexiglas sample holder by double sided graphite tape. The pellets were covered by 13  $\mu\text{m}$  thick Kapton foil which was sealed on the edges with Kapton tape. The footprint of pellet **U1** was also covered by 13  $\mu\text{m}$  thick Kapton foil. Samples **U1**, **U3** and **UF1** then were mounted in two bigger cells sealed with a frame equipped with an 8  $\mu\text{m}$  thick Kapton foil window. **Figure 47** shows the sample cell of **U1** and **U3**. In-between the different measurement sessions the sample cell remained sealed in ambient conditions. From the manufacturer's specifications<sup>218</sup> a  $\text{O}_2$  permeability of approximately 1  $\text{cm}^3$  per year for the cell was calculated. Therefore, a partial oxidation of the sealed samples over the time cannot be excluded.



**Figure 47** Sample holder of  $\text{UO}_2$  benchmark sample **U1** and **U3**. The empty cell illustrating the containment concept is shown in **Figure 97** in the **Appendix**.

Sample **U3** served as U(IV) reference material for the U  $M_4$  edge HR-XANES measurements in November 2015 and 2016 (see text below in **Section Methods and Materials**), whereas in

March 2015 a different UO<sub>2</sub> pellet was used (cf. **Table 2** in **Section 3**). HR-XANES spectra of samples **U1**, **UF1**, **S1**, **S2** and **S3** were recorded either the INE-Beamline or the CAT-ACT-Beamline while **U2** was only used for the XPS measurement. An overview of the samples is given in **Table 10**.

## Methods and Materials

### *High-energy resolution X-ray absorption near edge structure (HR-XANES)*

An M<sub>4,5</sub> edge HR-XANES investigations of samples **S1** and **S2** were performed at the INE-Beamline in March 2014 and November 2015 as well as at the CAT-ACT-Beamline in November 2016 while the reference samples **U1-U3** and **UF1** were investigated only in November 2015 and 2016. **S3** was investigated exclusively at the CAT-ACT-Beamline in November 2016. The general beamline settings are described in **Section 3**.

The samples were measured by setting the spectrometer to the maximum of the normal emission line (U 3334.4 eV, Pu 3345.9 eV) and recording within the energy range of 3710-3789 eV (U) and 3759-3840 eV (Pu) with a step size of 0.1 eV in the WL region and 0.5 eV in the pre- and post-edge. No background correction was performed. All spectra were normalized to 1 in the post-edge region if not stated otherwise.

In order to check for homogeneity of sample **S1** five different positions of the ring-shaped sample were probed (cf. marks in **Figure 50**). As the recorded spectra coincide for all positions (cf. **Figure 98** in the **Appendix**) they were merged to obtain higher signal-to-noise ratio. The fluorescence map was recorded by exciting the U at the maximum of its main absorption peak and recording the M<sub>β</sub> fluorescence.

The modeling of the U M<sub>4</sub> edge HR-XANES spectra was performed with the *Fityk* curve fitting software v.0.9.8 (<http://fityk.nieto.pl/>) using six Gaussian and one arctangent functions. The Levenberg–Marquardt least-squares algorithm was used in the fit.

### *X-ray photoelectron spectroscopy (XPS)*

The XPS measurements were performed according to the information given in **Section 3**. The X-ray beam was scanned over the UO<sub>2</sub> sample for a length of 800 μm. C 1s (284.8 eV) of adventitious hydrocarbon was used as charge reference which corresponds to O 1s (oxide) 530.0 eV. Charge compensation was not necessary due to the semi-conducting properties of the material.

## 5.2. Results and Discussion

**Table 10** Overview of samples studied in this project and their description.

Sample name	Description
<b>U1</b>	UO <sub>2</sub> pellet, 4 h exposed to air
<b>U2</b>	UO <sub>2</sub> pellet used for XPS investigation
<b>U3</b>	UO <sub>2</sub> pellet used as U(IV) reference in U M <sub>4</sub> edge HR-XANES investigation (cf. <b>Table 2</b> )
<b>UF1</b>	Footprint from surface of pellet <b>U1</b> after air exposure
<b>S1</b>	Footprint of HBS SNF from commercial reactor
<b>S2</b>	Footprint of central pellet area of SNF pellet from commercial reactor
<b>S3</b>	HBRP project SNF HBS particle

### *UO<sub>2</sub> benchmark samples*

UO<sub>2</sub> pellets freshly reduced to stoichiometry were prepared to serve as reference and benchmark samples. Characterization of those samples was performed to examine the influence of sample preparation on sample alteration as pre-test for the subsequent investigations of SNF. As shown by previous UO<sub>2</sub> synthesis procedures<sup>217</sup> the reduction of ceramic UO<sub>2+x</sub> pellets to UO<sub>2</sub> in a H<sub>2</sub>/Ar atmosphere is completed after approximately 6 h at 1150 °C. Pellet **U2** was measured with XPS directly after the reduction procedure. The U 4f XPS spectrum and its best fit are shown in **Figure 48**. The fit to the spectrum provides quantitative information for the U speciation in the first few atomic layers (ca. 5 nm depth) of the sample; U(IV) 45 at%, U(V) 47 at% and U(VI) 8 at% are found (see **Table 38** in the **Appendix**). The surface of the pellet is significantly oxidized despite its transfer to the XPS vacuum chamber in an inert gas atmosphere. Apparently, sufficient amounts of O<sub>2</sub> were present for surface oxidation. The extent and the high oxidation rate are in good agreement with findings reported by McEachern *et al.* for UO<sub>2</sub> surface oxidation to U<sub>4</sub>O<sub>9</sub> (U(IV) and U(V))<sup>6</sup>.<sup>178</sup>

While the information depth of XPS lies in the approximate 10 nm range the penetration depth of the X-ray beam used for the An M<sub>4,5</sub> edge HR-XANES investigations is significantly higher. It can be calculated on the basis of the work of Henke *et al.*<sup>91</sup> With an energy of 3700 eV the radiation has an attenuation length of approximately 1 μm in a UO<sub>2</sub> matrix, i.e., the intensity of the incident X-ray beam is attenuated to  $1/e \approx 37\%$  of its original intensity. As the HR-XANES spectra are recorded in fluorescence mode the incident photons as well as the emitted photons need to overcome the UO<sub>2</sub> matrix and reach the detector in order to contribute to the spectrum. The photons on both paths are attenuated by 63%. Hence, information from a sample depth of 1 μm reach the detector with an intensity of less than 15% of the initial intensity. Thus, 1 μm

can be estimated as the maximum probed information depth for  $\text{UO}_2$  by the U  $M_4$  edge HR-XANES technique.

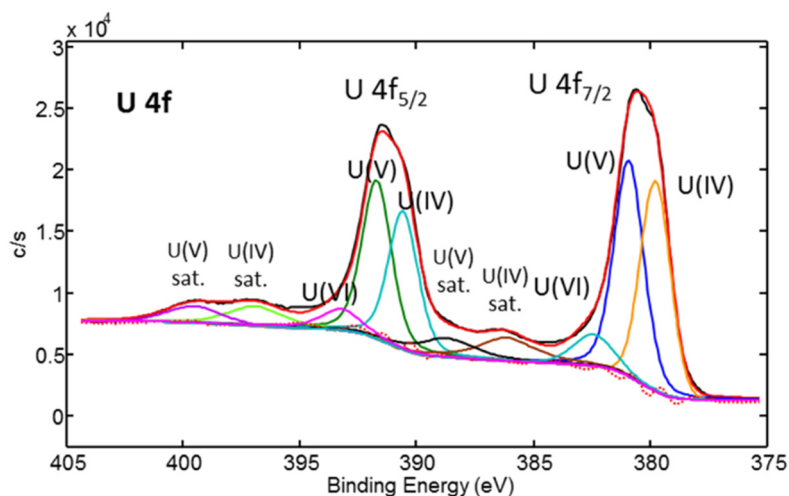


**Figure 48** XPS spectrum of **U2** (black). Fitting of the main and satellite peaks resulted in the fit spectrum shown in red. The evaluation results of the best fit can be found in **Table 38** in the **Appendix**.

The U  $M_4$  edge HR-XANES spectra of **U1**, **U3** and **UF1** are depicted in **Figure 49**. The freshly reduced  $\text{UO}_2$  sample denoted as **U1** was kept for 2 h in ambient conditions prior to the investigation. After exposure to air **U1** was used to prepare the footprint **UF1**. The pellet **U3** was reduced to stoichiometry and packed for the HR-XANES measurements in an inert gas atmosphere.

The **U1** and **U3** spectra appear similar and have one main peak whereas the **UF1** spectrum reveals two pronounced peaks. The main absorption peak located at approximately 3725.0 eV (**A**) for the **U1** and **U3** spectra is characteristic for U(IV). The second peak **B** in the **UF1** spectrum is at higher energy (3726.1 eV) indicating contribution of U in a higher oxidation state which can be potentially U(V) or U(VI). The energy position of this peak **B** coincides with the U(V) peak of the  $\text{U}_4\text{O}_9$  spectrum. In  $\text{U}_4\text{O}_9$  U is present in tetravalent and pentavalent oxidation states. Due to the limited resolution of the experiment the characteristic peaks for U(IV) and U(V) overlap and appear as one asymmetric peak. The peak **A** has a lower intensity compared to peak **B** in contrast to the reported spectrum by Kvashnina *et al.* where the two peaks have comparable heights.<sup>6</sup> This finding indicates that likely storage in ambient conditions led to partial oxidation of U(IV) to U(V) in the  $\text{U}_4\text{O}_9$  sample. Minor U(VI) contribution is possible too.

The post-edge region of the spectra is sensitive to the short but also long range atomic order around the absorbing U atom. The post-edge region above 3730 eV of the **UF1** spectrum is clearly different compared to the corresponding parts of the  $\text{U}_3\text{O}_8$  and  $\gamma\text{-UO}_3$  spectra but it is

similar to the  $U_4O_9$  shown in [Figure 49](#) too.  $U_4O_9$  has a cubic or cuboctahedral crystal structure (depending on its  $\alpha$  or  $\beta$  modification)<sup>219</sup> whereas  $U_3O_8$  and  $UO_3$  have orthorhombic<sup>183</sup> and tetragonal structures<sup>121</sup>, respectively. The exact crystallographic phase was not determined for this  $U_4O_9$  sample. The post-edge regions of the  $U_4O_9$  depicted in [Figure 49](#) (right) and the spectrum reported by Kvashnina *et al.* are identical.<sup>220</sup> They also did not identify the crystal modification of the investigated  $U_4O_9$ .

It can be concluded that **UF1** contains U(IV) and U(V). No crystal structure analysis was performed but it is very likely that  $U_4O_9$  is formed.  $U_3O_7$  with a complex crystal structure<sup>221</sup> is also discussed as one of the possible oxidized  $UO_2$  modifications at temperatures below 250 °C. Since no spectrum is available for this material it cannot be verified how similar it is to the **UF1** spectrum.

The point that the **UF1** and **U1** samples are distinctly different, i.e., no significant amount of U(V) is clearly visible in the **U1** spectrum, confirms that the U  $M_4$  edge HR-XANES technique probes substantially the bulk of the material. The spectra of **U1** and **U3** are also very alike which implies that the method is not very sensitive to variations in surface oxidation due to different preparation and handling procedures. XPS can be used as complementary technique as it is mainly sensitive to the surface. The XPS result for the U speciation in **U2** is very similar to the U  $M_4$  edge HR-XANES result for the **UF1** sample suggesting that surficial U oxidation of the  $UO_2$  pellets cannot be prevented by the sample handling procedure as applied in the present study

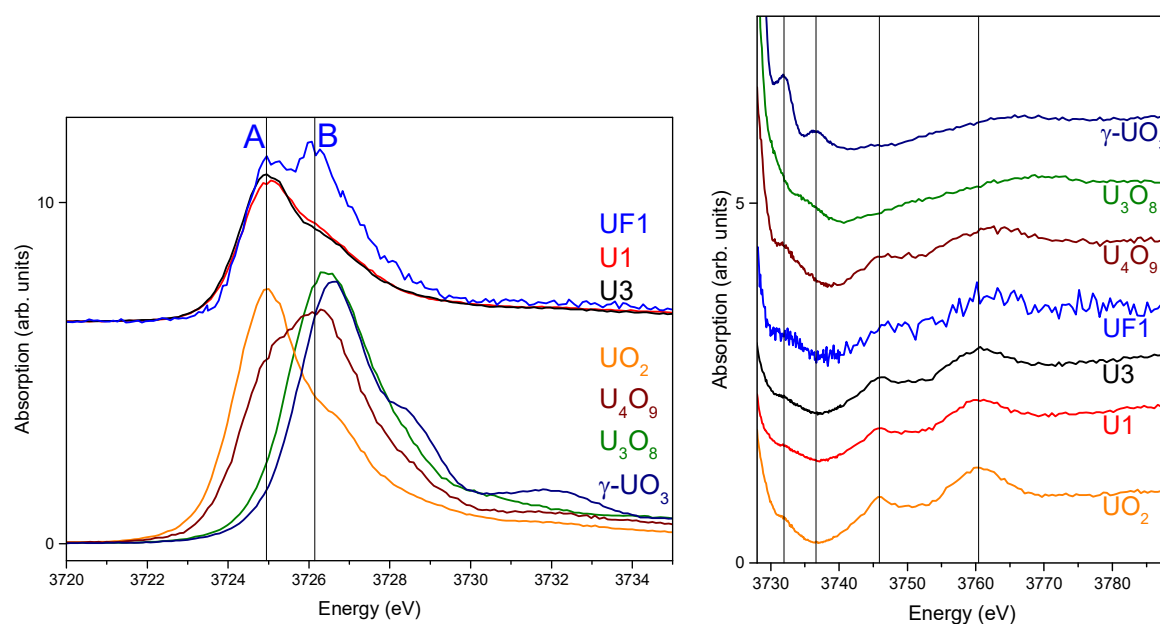


**Figure 49** U  $M_4$  edge HR-XANES spectra of samples **U1**, **U3**, **UF1** and different U oxide references samples with emphasize on the WL region (left) and on the post-edge region (right). The experimental resolution between the two sets of spectra differ slightly. The post-edge features are marked with solid black lines.

### Commercial SNF

U  $M_4$  edge HR-XANES spectra from the HBS (**S1**) and the central region (**S2**) of the SNF pellet were recorded in March 2015 a few days after the preparation of the samples and in two additional experiments performed in November 2015 and November 2016.

The U  $M_\beta$  fluorescence was recorded as a function of the position of the X-ray beam on the **S1** and **S2** samples. This fluorescence map reveals hotspots with high U content (cf. **Figure 50**).

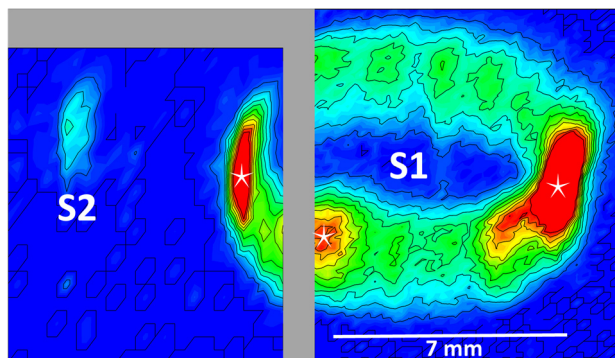


**Figure 50** U  $M_\beta$  fluorescence map of **S1** and **S2**. Blue and red indicate areas of low and high U fluorescence intensity, respectively. Sample **S1** was measured at positions marked with white stars. No fluorescence data were recorded for the area in grey.

To screen the chemical homogeneity of the **S1** sample U  $M_4$  edge HR-XANES spectra were measured at several positions marked in **Figure 50** (cf. **Figure 98** in the **Appendix**). Since the spectra are very similar they were merged to obtain a spectrum with high signal-to-noise ratio. The spectra of the **S1** and **S2** samples as well as of the  $UO_2$  (**U3** sample) reference are depicted in **Figure 51**. The spectra of the  $UO_2$  bulk sample measured in March/November 2015 and November 2016 are comparable. U(IV) is the main species for the **S2** sample too. An additional contribution appears as a shoulder on the high energy side of the main U(IV) peak of the **S2** spectra and slowly increases as a function of time. The post-edge regions above 3730 eV of the three **S2** spectra do not change notably and are similar to  $UO_2$ ; therefore this second contribution is likely U(V) which is described above for the **UF1** reference sample (cf. also **Figure 53**). This U(V) specie is well distinguishable in the **S1** spectrum measured in March 2015 and grows to become the main part of the **S1** spectrum measured in November 2016. Clearly oxide species possibly similar to  $U_4O_9$  form in both **S1** and **S2** samples.

The high energy position of the **S1** main peak of the spectrum measured in November 2016 suggests also presence of U(VI). The high surface reactivity of the presumably small particles might lead to oxidation and phase transformation<sup>178</sup> beyond  $U_4O_9$ , e.g., formation of  $U_3O_8$ . The formation of  $U_3O_8$  is generally not observed in the literature for SNF material below 250 °C in air.<sup>181</sup> Wasywich *et al.* found oxidation of CANDU fuel in moist air to a U(VI)/U(IV) ratio higher than 1 indicating the formation of  $U_3O_8$ .<sup>197</sup>

**Figure 52** depicts spectra for the **UF1** and **S1** footprint samples measured in November 2015 and 2016. The U oxidation changes more noticeably for the **S1** sample. The spectrum of **UF1** suggests that U(IV) has continued to oxidize only to U(V) while the **UF1** spectrum is still rather characteristic for  $U_4O_9$ . The inhibited oxidation of the unirradiated  $UO_2$  to U(VI) is in agreement with the studies of McEachern *et al.*<sup>178</sup> discussed in Section 5. Future measurements of the same **UF1** and **S1** samples will verify if this potential oxidation to U(VI) species lasts only in the **S1** sample.

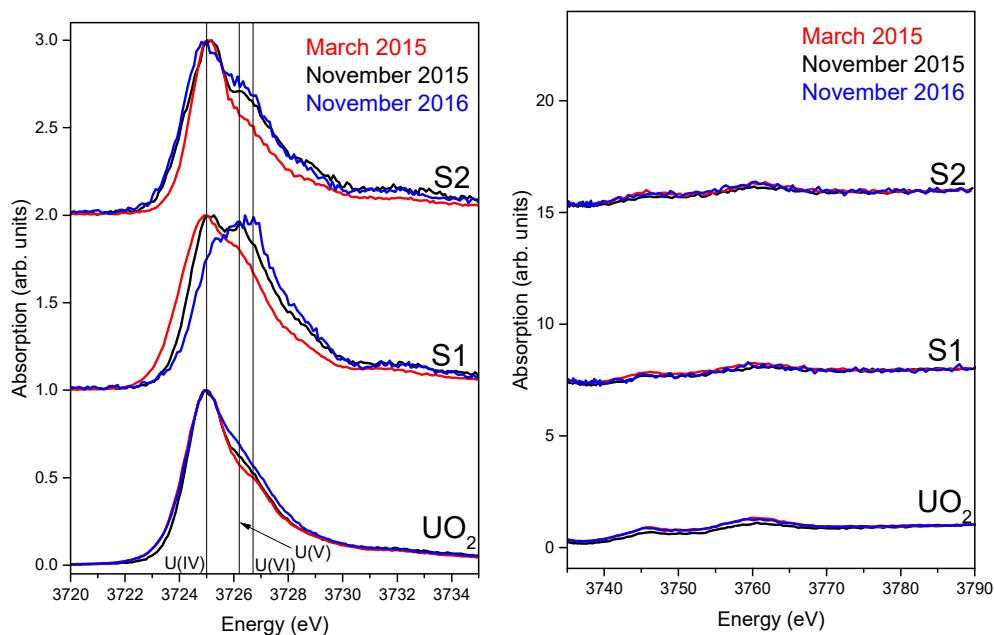


**Figure 51** U  $M_4$  edge HR-XANES spectra (short (left) and extended (right) energy range) of the HBS sample **S1**, SNF sample **S2** and the  $UO_2$  reference **U3** measured in March 2015, November 2015 and 2016. The energy positions of the most intense absorption peaks of U(IV) ( $UO_2$ ), U(V) ( $U_4O_9$ ) and U(VI) ( $\gamma-UO_3$ ) are marked with lines. The short energy range spectra are normalized by the maximum of the most intense absorption peak whereas the extended energy range spectra are normalized by the pre- and post-edge.

The question arises if the larger U(V) content in the **S1** compared to the **S2** sample can be attributed to structural, chemical and morphological differences of the HBS and the SNF samples. The faster oxidation kinetics for **S1** compared to **S2** might be explained with differences in the size of the particles. **S1** contains fine powder whereas the **S2** sample comprises several small particles of approximately 500  $\mu m$  diameter. **S2** can be considered for a bulk sample; however, presence of fine dust cannot be excluded since **S2** is a footprint of a large particle. The performed benchmark study on reference samples illustrate that footprints are only representative for the surface of the material.

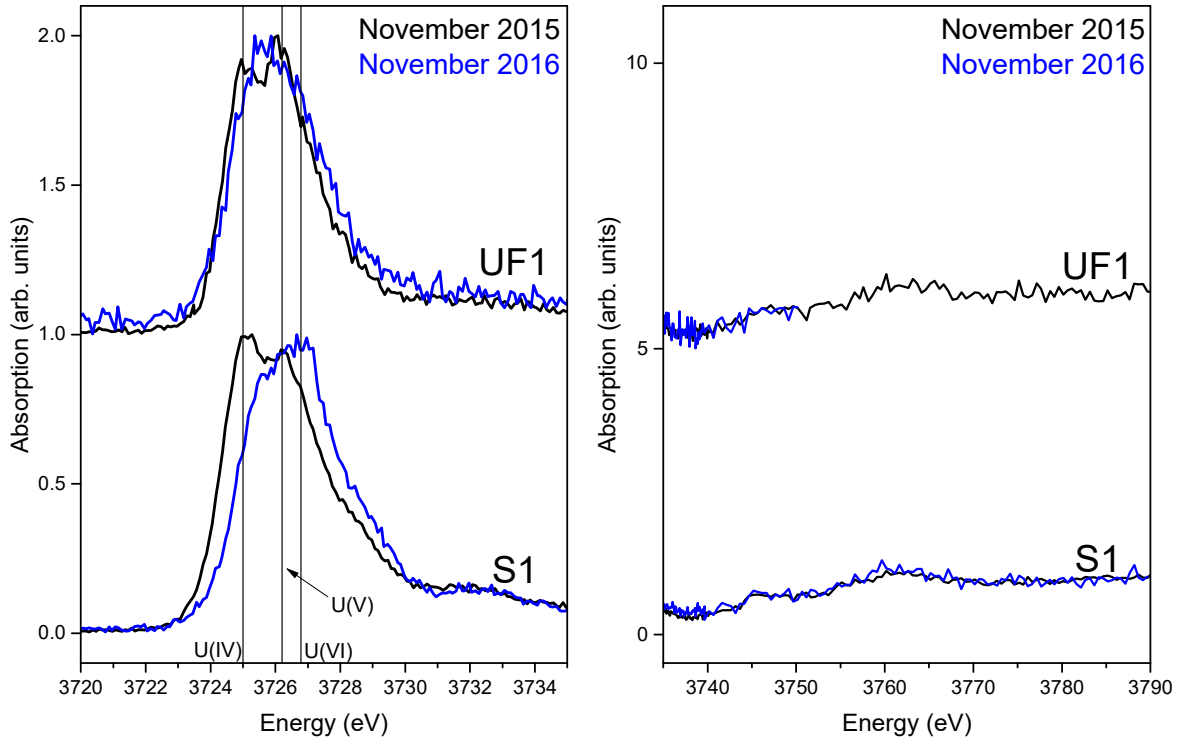


**Figure 52** U M<sub>4</sub> edge HR-XANES spectra (short (left) and extended (right) energy range) of the HBS sample **S1**, and unirradiated **UF1** measured in November 2015 and 2016. The energy positions of the most intense absorption peaks of U(IV) (UO<sub>2</sub>), U(V) (U<sub>4</sub>O<sub>9</sub>) and U(VI) ( $\gamma$ -UO<sub>3</sub>) are marked with lines. The short energy range spectra are normalized by the maximum of the most intense absorption peak whereas the extended energy range spectra are normalized by the pre- and post-edge. The November 2016 measurement of **UF1** was aborted prematurely.

### HBRP SNF

The question if the observed differences between the **S1** and **S2** samples are only a manifestation of different levels of surface oxidation caused by particle size variations is addressed with the investigation of sample **S3**. This sample consists of a 4 mg bulk particle removed from a SNF pellet which was pre-characterized as homogenous HBS material within the international *HBRP* project.<sup>173</sup> The sample stored for 20 years in an inert gas atmosphere with an average impurity of 1% O<sub>2</sub>. The fragment was washed with acetone to remove surface particles. **Figure 53** (left) depicts the U M<sub>4</sub> edge HR-XANES spectrum of **S3** recorded at the ACT-Beamline. The spectrum is very similar to the spectrum of UO<sub>2</sub> (**U3**) The most intense absorption peaks of the two spectra located at 3725 eV coincide. It can be concluded that **S3** contains predominantly tetravalent U. A clear difference between the spectra is the intensity of the high energy feature at ca. 3726.4 eV which is assigned to U(V) in the benchmark study. Comparing the intensity of this high energy feature relative to the main U(VI) peak it can be concluded that there is a somewhat higher U(V) contribution in the **S3** sample than in the UO<sub>2</sub> reference. This becomes clearer when the spectra are normalized to the maximum intensity of the main peaks (**Figure 53**, right).

The different intensities of the main peaks can be for example due to structural disorder in the **S3** sample as a result of more complex chemical composition and morphology compared to  $\text{UO}_2$ . Self-absorption effects, which occur for samples with high concentration and density of the probed element, can damp the spectral intensity. In the performed investigations the difference between **S3** and  $\text{UO}_2$  cannot be assigned to self-absorption as both materials have similar U concentration. In addition, **S3** has about 10% less density compared to  $\text{UO}_2$ .

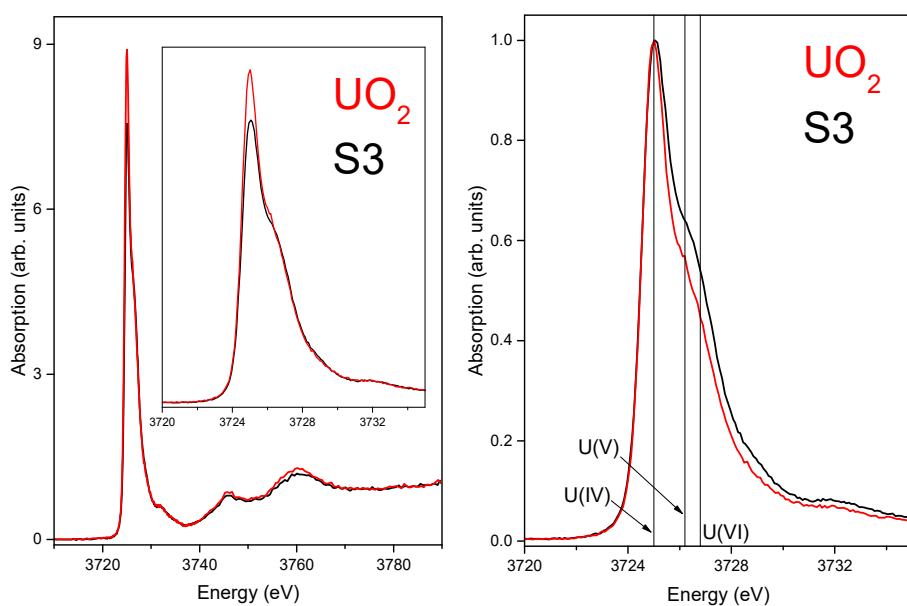


**Figure 53** U  $M_4$  edge HR-XANES spectra of **S3** and  $\text{UO}_2$  reference **U3** measured in November 2016. For evaluation, the spectra were normalized to the pre- and post-edge region (left) and to the maximum of the main peak (right). The energy position of the most intense absorption peaks of  $\text{UO}_2$  is marked with a vertical line.

In order to compare the intensities of the **B** shoulder features **A-F** of the spectra were modeled using six Gaussian and one arctangent function (cf. **Figure 54**). Two different approaches were followed: In the first approach the  $\text{UO}_2$  spectrum was fit by varying the parameters of the Gaussian functions; the height of the arctangent step function was fixed to 1. For fitting of the **S3** spectrum the obtained energy positions were applied and fixed while the remaining parameters of the Gaussian functions were varied.

In the second approach both  $\text{UO}_2$  and **S3** spectra were fit by varying the parameters of the Gaussian functions. The results of both approaches are comparable. The difference in the energy position of the main peak is below 0.15 eV; its intensity and area differ by less than 3% and 4%, respectively. As the results are similar only the second approach is illustrated in **Figure 54**. In order to evaluate the small differences of shoulder **B** its intensity is correlated to the intensity of the main feature **A**. Post-edge features **D-F** originate from scattering of the

photoelectron from atoms surrounding U; they probe the local atomic environment of U in the material (see also [Figure 49](#), right).

The results of the fitting procedure are given in [Table 39](#) in the **Appendix**. For the  $\text{UO}_2$  spectrum feature **B** has approximately 76% the intensity of feature **A**. For the **S3** spectrum this ratio is found to be ca. 87%. The difference of 11% can most likely be attributed to the minor formation of U(V) oxidation state in the SNF **S3** sample. The HBS SNF material was exposed for 20 years to atmosphere containing approximately 1%  $\text{O}_2$ : The results confirm only minor U oxidation state changes therefore it can be concluded that sample **S3** is rather stable against oxidation. It appears that the fast U oxidation kinetics observed for the **S1** and **S2** samples is induced by small particles with large reactive surfaces. Based on the current set of samples it cannot be concluded if the level of burn-up affects the U speciation. One challenge to detect minor U(V)/U(VI) is imposed by the fact that those are minor species whereas unaltered U(IV) is the dominant matrix element. A closer insight into the potential change of chemical state of the  $An$  in regions with high local burn-up can be obtained by investigations of other redox sensitive  $An$  elements. Pu is the ideal candidate since it has a considerably high concentration in SNF, hence the experiments are feasible.

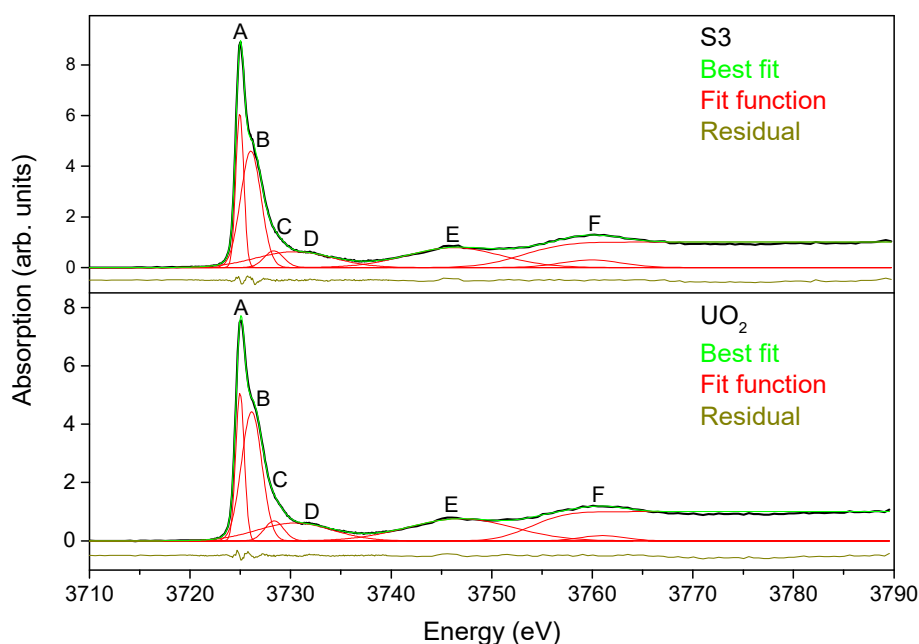


**Figure 54** **S3** and  $\text{UO}_2$  spectra (black) plotted with their best fit (green). The fitting functions used to fit features **A-F** are shown in red. The difference between the best fit sum and the experimental spectrum is given below the respective spectra as residual.

### *Pu M<sub>5</sub> edge HR-XANES of SNF samples*

The Pu speciation is investigated in samples **S1**, **S2** and **S3**. Pu is not part of the pristine fuel matrix but it builds up in the neutron irradiation process by neutron capture of U and subsequent decay. In the commercial SNF (sample **S1** and **S2**) it averages at ca. 1.04 wt% (cf. **Table 40** in the **Appendix**). The Pu content of the *HBRP* SNF was not calculated but it is estimated to be less than 1 wt%. Due to the high U-235 enrichment (ca. 26%<sup>216</sup>) the disk was exposed to less neutrons than materials with comparable burn-ups.

The Pu M<sub>5</sub> edge HR-XANES spectra of the **S1** and **S2** samples recorded in March 2015 are depicted in **Figure 55**. The main absorption peaks of the **S1** and **S2** spectra are shifted to higher energies compared to the spectrum of the PuO<sub>2</sub> reference. This behavior indicates a significant oxidation of Pu(IV) to Pu(V) and/or Pu(VI). The position of the main peak of electrochemically prepared Pu(VI) in HClO<sub>4</sub>/NaClO<sub>4</sub> is marked in the figure.<sup>56</sup> Although it is known that the shape and the energy position of the spectrum of aqueous Pu(VI) differs from Pu(VI) solid state spectra, the indicated position can be used as an orientation. According to the work of Vitova *et al.* the position of the main peak for the same oxidation state of U(VI) in solid state materials and in aqueous solution can shift approximately 0.2 eV.<sup>69</sup> Similar to the U studies Pu is more oxidized in the **S1** sample compared to the **S2** sample. This may be related to increased porosity, higher contribution of FPs and transuranium elements, smaller grain size, etc. of the HBS. The increased oxidation for Pu as for U is most likely a consequence of the larger surface area of the HBS **S2** sample which causes increased reaction rate. The intensity of the main peaks of the **S1** and **S2** spectra is much higher compared to the spectrum of PuO<sub>2</sub> due to prominent self-absorption effects for PuO<sub>2</sub>.

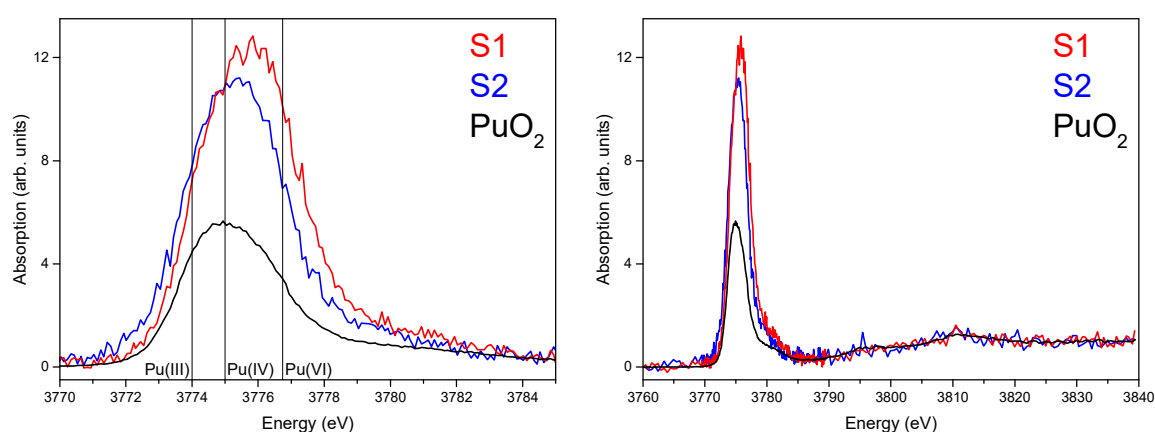


**Figure 55.** Pu M<sub>5</sub> edge HR-XANES spectra (short (left) and extended (right) energy range) of the HBS sample **S1**, SNF sample **S2** and the PuO<sub>2</sub> reference. The energy positions of the most intense absorption peaks of Pu(III), Pu(IV) and Pu(VI) is marked with vertical dashed lines.

The spectra measured for the bulk **S3** sample and the PuO<sub>2</sub> reference are shown in **Figure 56**. Due to the higher energy resolution of this more recent measurement a shoulder at the position of Pu(VI) can be identified. It is known that it is easier to oxidize U(IV) than Pu(IV)<sup>123</sup>. Since 20 years storage in atmosphere with 1% O<sub>2</sub> did not lead to significant oxidation of the UO<sub>2</sub> matrix it is unlikely that Pu(IV) will oxidize due to the storage conditions. One plausible hypothesis is that a part of Pu is initially formed in higher than Pu(IV) oxidation state while undergoing nuclear build-up reactions. The **S3** spectrum also reveals a small pre-edge feature marked in **Figure 56** which has a position characteristic for Pu(III). Due to the low signal-to-noise ratio of the spectrum and the low intensity of this peak it can be only speculated about existence of minor amount of Pu(III) in the **S3** sample. Future measurements with even high experimental energy resolution can help to elucidate this question. This can be achieved by reducing the size of the incident beam to less than 500 μm diameter.

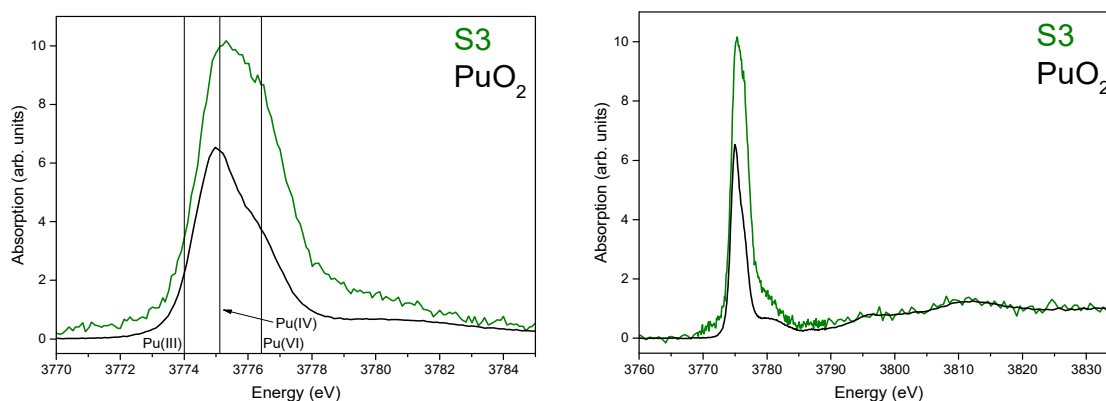


**Figure 56** Pu M<sub>5</sub> edge HR-XANES spectra (short (left) and extended (right) energy range) of the HBS sample **S3** and the PuO<sub>2</sub> reference. The energy positions of the most intense absorption peaks of Pu(III), Pu(IV) and Pu(VI) are marked with vertical dashed lines.

### 5.3. Summary and Conclusion

The performed investigations illustrate that the U/Pu M<sub>4,5</sub> edge HR-XANES method is mainly sensitive to the bulk part of the material in contrary to XPS which has a predominant surface sensitivity. The two methods provide complementary information; therefore, their combined application is beneficial.

The experiments showed in accordance with the literature that the UO<sub>2</sub> surface is very reactive in an ambient atmosphere. In the presence of even minor amounts of O<sub>2</sub> it is likely that the surface of a SNF pellet will be oxidized. A footprint sample contains species representative only for the surface of the SNF pellet and its large surface-to-volume ratio will favor oxidation of U

and Pu as a function of time. Hence, assigning results obtained from studies of  $\text{UO}_2$  and SNF footprint samples to the bulk of these materials can be misleading.

For all investigated reference and SNF samples only U(V) as part of most likely  $\text{U}_4\text{O}_9$  is found. The formation of  $\text{U}_3\text{O}_8$  or  $\text{UO}_3$  leading to change of the crystal structure is not observed. Minor contributions of U(VI) is detected for a footprint prepared from commercial SNF which is generally not expected and is likely caused by the large surface area related to the small SNF particles. Futures measurements will verify if the oxidation will continue or a steady state will be reached. Published studies report hindered  $\text{U}_3\text{O}_8$  formation by exposition of  $\text{UO}_2$  to air.<sup>202</sup>

The **S3** sample characterizing with high level of burn-up shows very minor U oxidation for a period of 20 years in atmosphere with 1%  $\text{O}_2$  when compared to unirradiated  $\text{UO}_2$ . This result strongly suggests that HBS is rather stable against oxidation. But the studies of the **S1** and **S2** samples demonstrate that for example in case of accident and direct contact of air and moisture with a SNF pellet surface oxidation of U is likely.

More significant Pu(V)/Pu(VI) contribution compared to U(V) is found in the **S3** sample. It is demonstrated that these higher oxidation states of Pu and U are formed in the bulk of the **S3** sample. As Pu is formed only by neutron capture and reactive decay processes its oxidation is proposed to be rather related to such processes than to result from reaction with  $\text{O}_2$ .

In order to get a more consistent and complete picture of oxidation processes of SNF further studies with systematic and comparative approaches have to be performed. As discussed,  $\text{UO}_2$  may serve as potential model system, however significant differences compared to the SNF oxidation behavior make the use of genuine SNF material indispensable to achieve well-founded scientific insights. The preparation and investigations of highly active SNF samples were realized in a cooperation between *JRC-Karlsruhe* and KIT-INE research facilities. An experimental procedure for preparation of irradiated SNF samples and their investigation was developed and its feasibility was demonstrated.<sup>216</sup> The gained knowledge and experience will facilitate future synchrotron based investigations of highly radioactive materials.

## 6. Simulation and vitrification of solid high-level waste (HLW) residuals remaining from reprocessing and vitrification activities

In the reprocessing pilot plant Karlsruhe (“Wiederaufarbeitungsanlage Karlsruhe”, WAK) nuclear fuel was reprocessed from 1971 to 1990. Approximately 200 t fuel from research and power producing nuclear reactors were treated and the separated U and Pu was recycled to the nuclear fuel cycle. The accumulated high-level liquid waste (HLLW) was stored for several years in storage tanks.<sup>10</sup> From 2009 to 2010 this liquid waste of approximately 55 m<sup>3</sup> was successfully immobilized by vitrification in the vitrification plant Karlsruhe (“Verglasungseinrichtung Karlsruhe”, VEK) on the same site.<sup>36</sup> In both facilities some solid radioactive residual material is still remaining:

- 1) Within the storage of the HLLW a considerable amount of solid state material precipitated from the solution and deposited at the bottom of the tanks (approximately 180 kg, more than 10<sup>15</sup> Bq and 300 Sv/h)<sup>222</sup>. Investigations performed by Van Winkel *et al.* found the precipitates to consist mainly of radioactive Cs and Mo. Water-insoluble Cs<sub>3</sub>PMo<sub>12</sub>O<sub>40</sub> was identified as a major component.
- 2) After vitrification of the HLLW the process components were rinsed by nitric acid in order to facilitate the future dismantling of the facility. An excess part of the rinsing solution was not recycled in the melter but collected in process tanks of the facility and sampled. Due to internal heating originating from the radioactive decay of the radionuclides and a continual dry-air flow the solution was evaporated to dryness (approximately 80 kg, more than 10<sup>15</sup> Bq). From the liquid chemical analysis it was concluded that the solid residue material remaining is rich in Tc and Cs. Both elements show volatile behavior in the vitrification process and deposited in the exhaust line where they were removed by the rinsing solution.

In the upcoming dismantling campaigns of the WAK and VEK facilities the removal and immobilization of these two types of residual material will be the key challenge. Both solid state deposits are carrier of the majority amount of nuclear radiation within the facilities.<sup>222</sup> The study here presented has the aim to 1) derive insights into the nature of the materials relevant for their removal and handling and 2) review a proposed suitable vitrification procedure for immobilization of the high-active waste materials. The simulation and immobilization of the Cs and Mo rich residue are discussed in **Section 6.1**, whereas the Tc and Cs rich one is dealt with in **Section 6.2** and **6.2.4**.

## 6.1. Mo and Cs rich residuals from reprocessing

The reprocessing of nuclear fuel materials generates HLLW (cf. **Section 2.1**). The storage of this FP rich solution led to the formation of water-insoluble precipitate accumulated at the bottom of the storage tanks of the WAK reprocessing plant.<sup>10</sup> The solid material contains mainly Cs and Mo forming the compound  $\text{Cs}_3\text{PMo}_{12}\text{O}_{40}$ ; its vitrification is challenging.<sup>223</sup> Mo is known to form crystalline, often water-soluble phases within the glass matrix (cf. **Section 2.1.2.2**).<sup>224</sup> These separated phases can serve as host for radionuclides with potential release in the near field of a deep geological repository in case of water intrusion and interaction with the waste product.

As discussed in **Section 2.1.2** borosilicate glasses are successfully applied for vitrification of a broad range of nuclear waste materials. The vitrification in laboratory conditions of the genuine radioactive solid residue is challenging due to the risk associated with the radiotoxic nature of the material. Within a previous study Bahl *et al.* investigated the vitrification of variable loadings of  $\text{Cs}_3\text{PMo}_{12}\text{O}_{40}$  and inactive nuclear waste simulate residue in borosilicate glass matrix and characterized glass product structures.<sup>225</sup> A multicomponent borosilicate glass developed at INE was used as a matrix.<sup>226</sup> It was found that the Keggin structure of  $\text{Cs}_3\text{PMo}_{12}\text{O}_{40}$  is decomposed at the applied 1300 °C vitrification temperature. Above 5.19 wt% molybdate loading crystalline and water insoluble Ba- and Ca-molybdate phases are formed. Additionally, due to the high volatility of Cs melting at 1300 °C for 2 h released ca. 40% of the Cs inventory to the atmosphere. Successful integration of the intact Keggin structure of  $\text{Cs}_3\text{PMo}_{12}\text{O}_{40}$  into the glass matrix may result in a glass product capable of incorporating Cs and suitable for final disposal.

The aims of the here presented investigations are 1) to identify melting temperatures preserving the Keggin structure, 2) to characterize the morphology of the glass product at different melting temperatures, 3) to quantify the Cs fraction incorporated in the glass as a function of the melting temperature and if possible to propose vitrification conditions suitable for immobilization of this specific radioactive waste. The here presented study was object of the master thesis of Veronika Koldeisz from *Department of Inorganic and Analytical Chemistry, Budapest University of Technology and Economics, Budapest, Hungary*.<sup>227</sup> It was performed under the supervision of S. Bahl.

$\text{Cs}_3\text{PMo}_{12}\text{O}_{40}$  is a molybdate compound with a thermodynamically stable Keggin-anion-structure illustrated in **Figure 57**. The central tetrahedral phosphate-unit is caged by 12

octahedral molybdate  $\text{MoO}_4^{2-}$  units. Depending on the cation these compounds possess characteristic properties.<sup>228-231</sup>

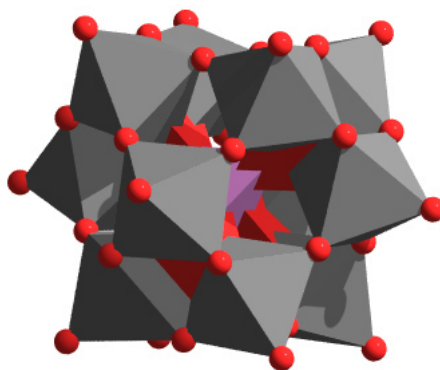


**Figure 57** Keggin structure of  $[\text{PMo}_{12}\text{O}_{40}]^{3-}$ . The tetrahedral  $\text{PO}_4^{3-}$ -unit (purple) is caged by 12 octahedral  $\text{MoO}_4^{2-}$ -units (grey). (Reproduced with permission from Ref. <sup>232</sup>)

For example, compounds with large counter-ions as Cs and ammonium exhibit a porous structure and therefore large specific surface.  $\text{Cs}_3\text{PMo}_{12}\text{O}_{40}$  is a highly water insoluble solid compound with intensive yellow color. On a microscopic level it consists of spherical nanoparticles with an approximate size of 50-1000 nm (**Figure 58**). Its synthesis, described in **Section 6.1.1**, is accessible by aqueous cation-exchange-reaction.<sup>230</sup> Time resolved XAS investigations at the Mo K edge do not detect changes of the crystal structure of  $\text{Cs}_3\text{PMo}_{12}\text{O}_{40}$  while heating the material up to its melting point (690 °C<sup>233</sup>).<sup>234</sup>

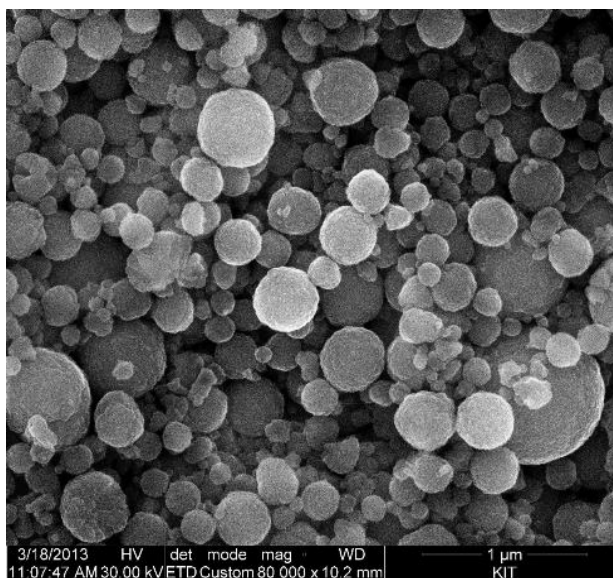


**Figure 58** SEM micrograph of  $\text{Cs}_3\text{PMo}_{12}\text{O}_{40}$  particles.

### 6.1.1. Experimental

In the following section the synthesis of the materials and the methods which were used for their characterization are described. **Section 3** give a general description of the applied characterization methods.

#### Preparation of samples

##### Cesium molybdophosphate

The  $\text{Cs}_3\text{PMo}_{12}\text{O}_{40}$  was synthesized by cation exchange reaction using phosphomolybdic acid and cesium nitrate according to the following reaction:



For that purpose 8.22 g  $\text{H}_3\text{PMo}_{12}\text{O}_{40}$  (1.00 eq., 4.50 mmol) was dissolved in 140 mL  $\text{H}_2\text{O}$  and a white insoluble solid, most probably an impurity, was removed by filtration. 4.40 g  $\text{CsNO}_3$  (43.22 eq., 194.69 mmol) was added while stirring in air the so far yellow transparent solution. After additional 10 min stirring the yellow solid (**Figure 59**) was obtained by centrifugation (2400 rpm 3 min, 2700 rpm 30 min, 2700 rpm 60 min) and three times washing the milky non-transparent suspension with  $\text{H}_2\text{O}$ . The solid was transferred into a crystallization dish and dried for 5 d at 180 °C and with air ventilation. It was pulverized and used without further preparation in the vitrification. It was obtained 73.78% corresponding to 7.37 g material.



**Figure 59** Powdered  $\text{Cs}_3\text{PMo}_{12}\text{O}_{40}$  in a beaker.

##### Glass frit

The glass frit was derived from glass-forming oxides and carbonates (**Table 11**). The mixture was homogenized in a shake-mixer (turbula) for 15 min, transferred to a Pt/Rh crucible, calcined for 1 h at 800 °C and heated up to 1250 °C for additional 2 h. The glass melt was quenched by pouring it on a stainless steel gutter. The remaining glass in the crucible was also

quenched by cooling the outside walls with cold water. Contact between water and glass was avoided. All the glass fragments were ground to powder in a vibratory disc-mill (1 min). To grant homogeneity to the frit, the powder was re-melted for 2 h at 1250 °C, quenched and milled again. The obtained powder was then used in the vitrification process.

**Table 11** Glass forming precursors used to synthesize the glass frit.<sup>226</sup>

<b>compound</b>	<b>m (g)</b>
SiO <sub>2</sub>	95.50
B <sub>2</sub> O <sub>3</sub>	62.10
Na <sub>2</sub> CO <sub>3</sub>	15.94
Li <sub>2</sub> CO <sub>3</sub>	11.51
Al(OH) <sub>3</sub>	12.02
CaCO <sub>3</sub>	25.54
MgO	9.32
BaCO <sub>3</sub>	9.60
Sb <sub>2</sub> O <sub>5</sub>	1.07
V <sub>2</sub> O <sub>5</sub>	3.20
<b>Total</b>	<b>245.80</b>

#### Vitrification of Cs<sub>3</sub>PMo<sub>12</sub>O<sub>40</sub>

Eight vitrified Cs<sub>3</sub>PMo<sub>12</sub>O<sub>40</sub> samples were prepared at different temperatures (600 °C, 700 °C, 800 °C, 900 °C, 1000 °C, 1050 °C, 1100 °C, 1200 °C). The eight samples are labelled as follows: **VK-03-600** – **VK-03-1200**, whereas the last number of the label corresponds to the vitrification temperature.

For the preparation of each sample powdered Cs<sub>3</sub>PMo<sub>12</sub>O<sub>40</sub> (0.6751 g) and frit (14.325 g), with total molybdate content of 3.5 wt%, were mixed, homogenized in the turbula (15 min) and transferred to the Pt crucible. The crucible was heated for 2 h at the temperatures listed above. If it was possible, the melt was quenched by pouring it on a stainless steel gutter. The high viscosity of the glass melted up to 1100 °C prevented its pouring. Therefore, the melt was quenched by a cool water flow on the outside of the crucible avoiding contact between water and glass. After mechanical removing of the glass from the crucible, about two-thirds of the sample was ground to powder (1 min, disc mill).

## Methods and Materials

### Raman Spectroscopy

The samples were excited by a green laser with 10 mW power. All Raman spectra were background corrected and normalized to their maximum.

### X-ray powder diffraction (XRD)

XRD diffractograms were recorded within the  $2\theta = 5-80^\circ$  range, with 7 s integration time per step; only for the **VK-03-900** and the **VK-03-1200** samples 30 s per step integration time was applied.

### Scanning electron microscope (SEM) and energy-dispersive X-ray spectroscopy (EDX)

For SEM-EDX studies the specimens were mounted on a metallic Siemens sample holder by an electrically conducting graphite glue. To avoid electric charging of the samples in high vacuum, its surface was covered by a few nm thick layer of chromium and electric conductivity was established by connecting the metallic sample holder and the surface by the graphite glue or metallic wires to record SEM images. EDX measurements were mainly performed on uncovered surfaces, i.e., before covering the surface with an electric conductive layer.

### Infrared spectroscopy (IR)

The IR spectra were recorded as described in **Section 3**.

### Transmission electron microscopy (TEM)

TEM images and electron diffractograms were recorded as stated in **Section 3**.

### Crucible

The crucible used for melting of the glass is made of 90 % platinum and 10 % rhodium and has a cylindrical form with a top diameter of 6 cm and a height of 5 cm. The crucible was cleaned from remaining glass by a procedure including mechanical removal followed by a chemical treatment in 30% HF-solution for approximately 12 hours.

### Furnace

The furnace used was a *HT 04/17* by the company *Nabertherm* with 5.2 kW power.

### Mill

A vibratory disc mill (*Pulverisette 09.003* by *Fritsch*) with tungsten carbide grinding tools was used.

### Centrifuge

The centrifuge *Varifuge 3.0 (Heraeus)* was used; 20 mL plastic tubes with screw cap were applied.

### Chemicals

The chemicals were provided by VWR International and unless otherwise stated, they are used without further purification.

## 6.1.2. Results and Discussion

The glass products were investigated by IR, Raman, XRD, TEM-EDX and elemental analysis in order to verify if the Keggin structure was preserved at specific vitrification temperatures. Photographic images of glass fragments from each sample are shown in [Figure 60](#). It is clearly visible that vitrification temperatures of 1100 °C and 1200 °C led to green transparent non-crystalline glass material. Samples **VK-03-1050** and **-1000** appear partially crystalline on the surface of the glass fragments. The bulk of these two samples is a transparent glass. The surface and bulk of **VK-03-900**, **-800** and **-700** are non-transparent but predominantly homogenous. On the contrary, sample **VK-03-600** produced at the lowest vitrification temperature is a highly porous white material with a few yellow submillimeter sized grains similar to the  $\text{Cs}_3\text{PMo}_{12}\text{O}_{40}$  powder. The appearance suggests structural properties which are more comparable to a porous aluminosilicate material than to a glassy material.



**Figure 60** Glass fragments of synthesized samples.

Vibrational spectra of three samples and two references are shown in [Figure 61](#). The  $\text{Cs}_3\text{PMo}_{12}\text{O}_{40}$  has a vibrational pattern characteristic for a Keggin type crystal structure. The

absorption bands can be assigned to the asymmetric stretching of the tetrahedral phosphate-unit ( $1061\text{ cm}^{-1}$ ), the asymmetric stretching of the terminal bound oxygen in  $\text{Mo}=\text{O}$  ( $959\text{ cm}^{-1}$ ) and the stretching of the bridging oxygen atoms  $\text{Mo}-\text{O}-\text{Mo}$  ( $861\text{ cm}^{-1}$ ,  $761\text{ cm}^{-1}$ ).<sup>231</sup>

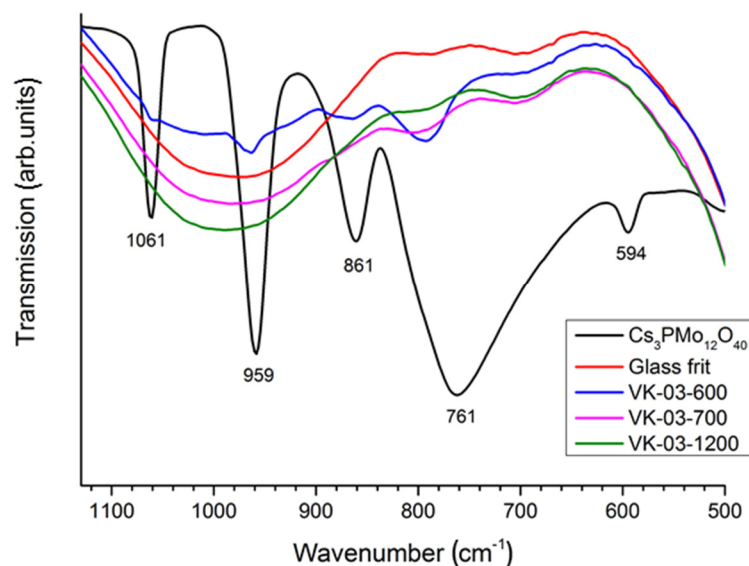


**Figure 61** IR-spectra of the glass frit,  $\text{Cs}_3\text{PMo}_{12}\text{O}_{40}$  and three glass samples.

The glass frit without Mo shows very broad absorption bands caused by the vibration of the dominating Si-O network. Sample **VK-03-1200** exhibits a similar spectrum with no evident Keggin structure pattern. These results strongly suggest that the vitrified  $\text{Cs}_3\text{PMo}_{12}\text{O}_{40}$  is decomposed. The spectrum of sample **VK-03-700** differs only by a low intensity broad band at around  $793\text{ cm}^{-1}$  implying decomposition of the Keggin structure too. On the contrary sample **VK-06-600** exhibits bands at  $1061\text{ cm}^{-1}$  and  $959\text{ cm}^{-1}$  characteristic for  $\text{Cs}_3\text{PMo}_{12}\text{O}_{40}$ . This result confirms that the Keggin structure is partially preserved during the vitrification at  $600\text{ }^\circ\text{C}$ . However, the vibration of the bridging oxygen atoms  $\text{Mo}-\text{O}-\text{Mo}$  at  $869\text{ cm}^{-1}$  and  $793\text{ cm}^{-1}$  is shifted to higher wavenumbers compared to  $\text{Cs}_3\text{PMo}_{12}\text{O}_{40}$ . A similar effect can be seen in the recorded Raman spectra shown in **Figure 62**. The main vibrational bands of  $\text{Cs}_3\text{PMo}_{12}\text{O}_{40}$  are found at  $983\text{ cm}^{-1}$  and  $967\text{ cm}^{-1}$  whereas sample **VK-03-600** shows narrower peaks shifted ca.  $6\text{ cm}^{-1}$  to higher wavenumbers ( $990\text{ cm}^{-1}$  and  $973\text{ cm}^{-1}$ ). This phenomenon might be caused by the interaction of the octahedral  $\text{MoO}_4^{2-}$ -units on surface of the  $\text{Cs}_3\text{PMo}_{12}\text{O}_{40}$  crystalline grains with the surrounding silica matrix leading to an increase of the vibrational energy. A change of the crystal structure, especially of the outer  $\text{MoO}_4^{2-}$ -units as indicated by IR spectroscopy, as a consequence of high temperature treatment like melting and recrystallization might also be a possible explanation. The Raman spectra of the glass samples are compared with spectra of the reference materials. The characteristic peaks for  $\text{Cs}_3\text{PMo}_{12}\text{O}_{40}$  are clearly visible only for the

**VK-03-600** spectrum.  $\text{CaMoO}_4$  has dominant contribution in almost all spectra except in spectra of the amorphous samples **VK-03-1100** and **-1200**.

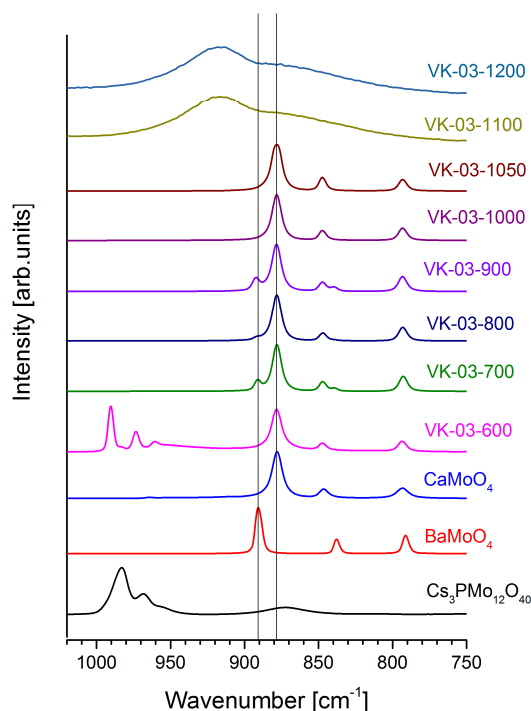


**Figure 62** Normalized and background corrected Raman spectra of the synthesized glass samples and three crystalline references.

Samples **VK-03-1100** and **-1200** do not contain any crystalline phases. Several Raman measurements at different sample positions confirm that samples **VK-03-800**, **-900**, **-1000** and **-1050** contain both amorphous glass and crystalline  $\text{CaMoO}_4$ .  $\text{BaMoO}_4$  is not found in samples prepared at temperatures higher than 900 °C. As it is found in the study of Bahl *et al.* the content of  $\text{CaMoO}_4$  phase dominates that of  $\text{BaMoO}_4$  in agreement with the five times higher Ca-content in the glass. The results from all measured Raman spectra are summarized in **Table 12**.

**Table 12** Summary of the results from Raman spectroscopy of samples **VK-03-600** to **-1200**.

Sample	Glass	$\text{CaMoO}_4$	$\text{BaMoO}_4$	$\text{Cs}_3\text{PMo}_{12}\text{O}_{40}$
<b>VK-03-600</b>		✓	✓	✓*
<b>VK-03-700</b>		✓	✓	
<b>VK-03-800</b>	✓	✓	✓	
<b>VK-03-900</b>	✓	✓	✓	
<b>VK-03-1000</b>	✓	✓		
<b>VK-03-1050</b>	✓	✓		
<b>VK-03-1100</b>	✓			
<b>VK-03-1200</b>	✓			

\*shifted  $\sim 6 \text{ cm}^{-1}$  to higher energies

The XRD results are in good agreement with the vibrational spectroscopy data (Figure 64).  $\text{CaMoO}_4$  is found up to 1050 °C,  $\text{BaMoO}_4$  can be clearly identified at 600 °C and 800 °C. A weak reflex at 26.08° for sample **VK-03-600**, which can be assigned to the Keggin structure, appears shifted ca. 0.08° to lower angles. Undissolved  $\text{Cs}_3\text{PMo}_{12}\text{O}_{40}$  grains can be seen by SEM (Figure 63) and were identified by EDX analysis for sample **VK-03-600**. Although this sample has a crystalline porous appearance, there are no further reflexes referring to any silicate crystalline material. Therefore, it is likely that this sample consists of an amorphous matrix incorporating crystalline  $\text{CaMoO}_4$ ,  $\text{BaMoO}_4$  and  $\text{Cs}_3\text{PMo}_{12}\text{O}_{40}$  components. The broad reflex at 21.80° in the diffraction pattern of sample **VK-03-800** is not identified via comparison with pattern of a crystal diffraction database.

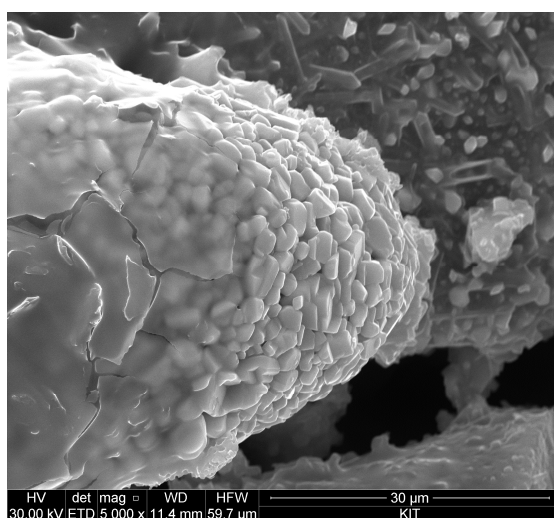


Figure 63 SEM picture of an undissolved  $\text{Cs}_3\text{PMo}_{12}\text{O}_{40}$  grain in sample **VK-03-600**.

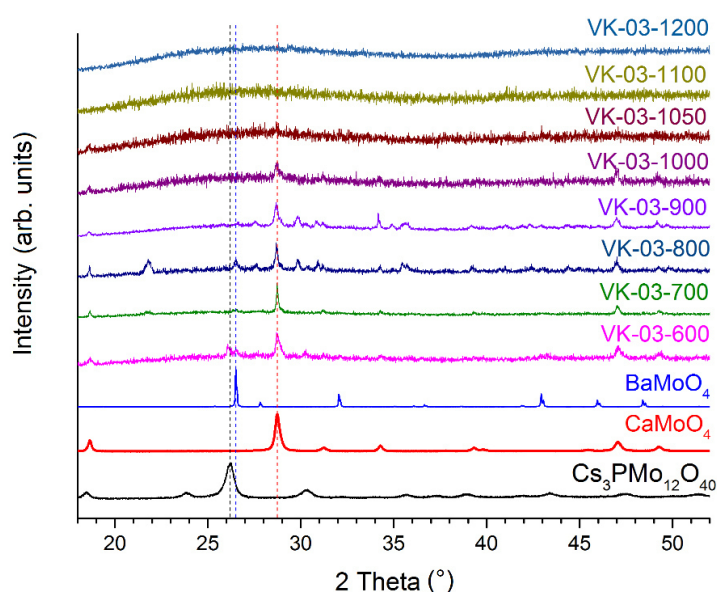
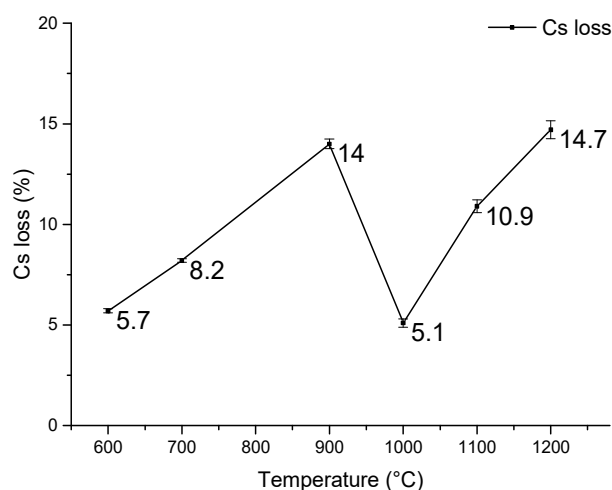


Figure 64 XRD pattern of the glass samples and three crystalline molybdate-references.

Elemental analysis was performed to correlate the Cs loss to the vitrification temperature. It is expected that the Cs volatilization increases with increasing temperature due to a higher evaporation pressure. As seen in **Figure 65** this trend could be observed for melting up to 900 °C. Unexpectedly, the Cs loss for synthesis at 1000 °C decreases by two-third from 14% to 5.1% in comparison to the previous sample in the series. For higher temperatures the system returns to the expected trend to reach a Cs loss of 14.7% at 1200 °C.



**Figure 65** Cs loss as function of the vitrification temperature determined by Cs AAS of the KOH digested glass samples.

A probable explanation for this anomaly can be deduced from the appearance of the materials (**Figure 60**). Samples synthesized at temperatures lower than 1000 °C do not show glassy appearance and suggest therefore that no glass melt is formed during the vitrification process. It is likely that the temperatures are sufficient to transform the components only into a porous silica material; this hypothesis is also confirmed by the Raman spectroscopy results. From this porous material more Cs can evaporate than from a liquid glass melt due to its high surface-to-volume ratio. For 1000 °C a glass melt is formed leading to a decreasing Cs loss. Higher temperatures favor formation of glass melt. However simultaneously the Cs vapor pressure increases and together with the reduced viscosity of the liquid melt might lead to increased Cs release.

XRD, Raman spectroscopy and SEM-EDX results confirm the presence of spherical structures of crystalline BaMoO<sub>4</sub> and CaMoO<sub>4</sub> with diameters ranging from 100 nm up to 2.45 μm both on the samples surface and in the bulk for vitrification temperatures up to 1050 °C.<sup>225</sup> Recently performed TEM investigations gain a new insight into the crystal structure of the crystalline regions on the nanometer scale. **Figure 66**(a) shows a bright-field image of a glass sample with a 12.28 wt% MoO<sub>3</sub> from a previous study. Relatively dark areas indicated by arrows

correspond to clusters of crystalline phases formed in the glass sample. The average size of these clusters is approximately 500 nm in diameter. **Figure 66(b)** shows a magnified image of the area indicated by the dotted square region in **Figure 66(a)**. The increased contrast in **Figure 66(b)** is due to a typical diffraction effect. **Figure 66(c-e)** depict selected-area electron diffraction (SAED) patterns taken from areas indicated by dotted circles **1-3** in **Figure 66(b)**. The SAED pattern of area **1** is indexed in terms of the tetragonal lattice of  $\text{CaMoO}_4$  ( $a = 0.5222 \text{ nm}$ ,  $c = 1.1452 \text{ nm}$ ,  $I4_1/a$ ). The crystalline zone axis is  $[201]$ . A SAED pattern taken from area **2** shows a similar SAED pattern to that of area **1**. However, the reflections of the  $[201]$  SAED pattern of area **2** appear at ca. 7% lower angles than that of area **1** which corresponds to the reflections of  $\text{BaMoO}_4$  ( $a = 0.5548 \text{ nm}$ ,  $c = 1.274 \text{ nm}$ ,  $I4_1/a$ .) In **Figure 66(e)** a SAED pattern taken from area **3** is shown where two SAED patterns taken from areas **1** and **2** overlap. The splitting of the reflections due to existence of two crystalline phases is clearly visible. EDX analysis identified these phases as  $\text{CaMoO}_4$  and  $\text{BaMoO}_4$ , respectively.

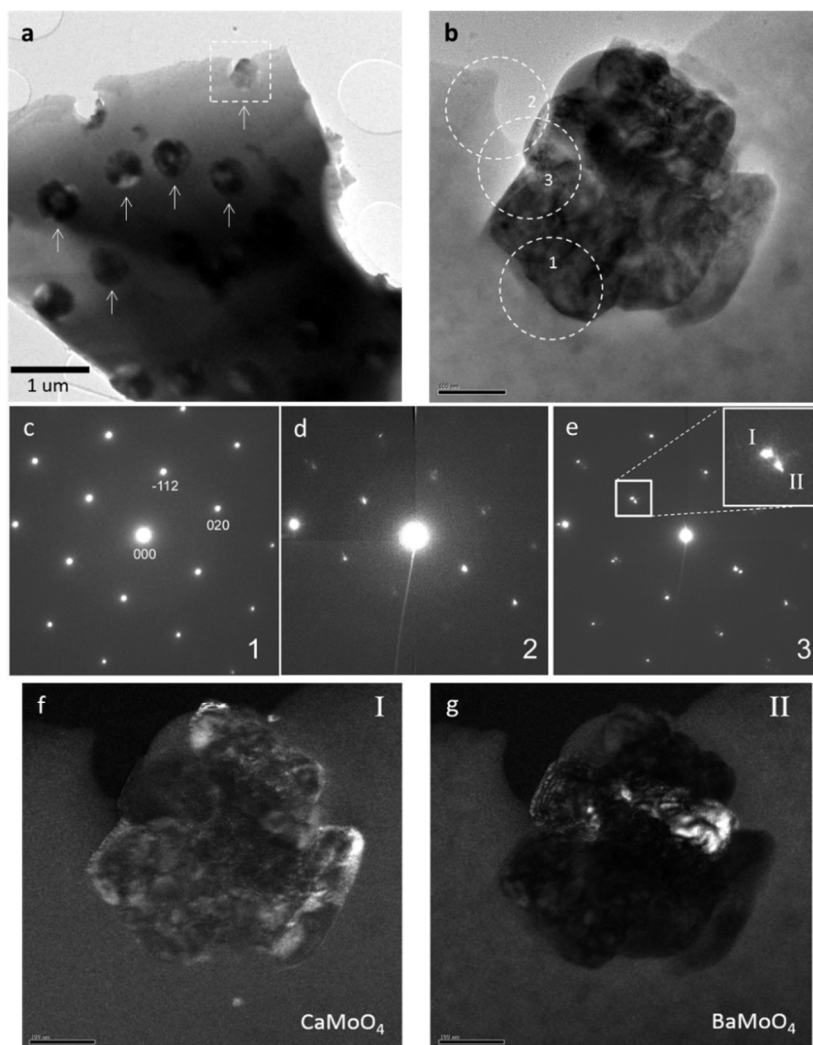


**Figure 66** (a) TEM image of a glass fragment with several crystalline structures. (b) One crystalline structure which was measured at different spots. (c-e) Diffraction pattern recorded at spots 1-3 (f-g) Dark field images which show the lattice distribution of  $\text{BaMoO}_4$  and  $\text{CaMoO}_4$ .

By separating the diffraction caused by the lattices using the  $(-1 -1 2)$  reflections (cf. **Figure 66(e)**) two images are obtained which show the spatial distribution of the identified compounds in a dark field image (cf. **Figure 66(f-g)**). The diffraction spot **II** in **Figure 66(e)** corresponds in real space to the larger lattice constant of  $\text{BaMoO}_4$ . Although the lattices are very similar they grow separately as indicated by **Figure 66(f)** and **Figure 66(g)**. The images are consistent with area **1** and **2** from the SAED patterns of **Figure 66(c-d)**.

### 6.1.3. Conclusion

The here presented investigations show that the Keggin structure of  $\text{Cs}_3\text{PMo}_{12}\text{O}_{40}$  is partially preserved for vitrification temperatures of 600 °C correlated with a low Cs loss of 5%. This result indicates that the Keggin structure retains most of the Cs. The released Cs originates from the decomposed fraction of the  $\text{Cs}_3\text{PMo}_{12}\text{O}_{40}$ . However, the high porosity of the obtained product suggests that its durability and as a consequence its long-term behavior in a deep underground repository might reveal a poor performance. Additionally, the results report approximately 5% Cs loss in the glass product obtained at 1000 °C vitrification temperature. In this case the immobilization mechanism of Cs is different compared to the 600 °C melted material as the Keggin structure is completely decomposed. It can be related to the dissolution of the Cs in the highly viscous glass melt. Crystalline agglomerates of  $\text{CaMoO}_4$  and  $\text{BaMoO}_4$  form below 1050 °C melting temperatures for a total  $\text{MoO}_3$  content of 3.50 wt%. These crystalline phases, having limited solubility in water, are able to incorporate and immobilize radionuclides (see Ref. <sup>235</sup>) and thus, act as a chemical barrier for radionuclide release from a nuclear waste repository. A TEM study using *Ln* homologues not presented in this work suggests that trivalent *An* will be mainly localized in these regions. In contrary, the undesirable product  $\text{NaMoO}_4$  which has a very high water solubility was not identified. Vitrification temperatures of more than 1050 °C led to the uniform dispersion of the molybdate in the amorphous glass matrix and result in Cs loss up to 15% due to higher vapor pressure and lower viscosity.

In summary, the results suggest that the used glass matrix is in principle appropriate for vitrification of the  $\text{Cs}_3\text{PMo}_{12}\text{O}_{40}$  rich waste at the VEK site by loading the glass with 3.5 wt% molybdate and applying 1000 °C melting temperatures. At these conditions the Cs release was minimized to 5% with the applied conditions. An active stirring of the melt is recommended to further prepare a more or less uniform dispersion of crystalline phases within the glass melt and to avoid phase separation as visible in **Figure 60**. The formed glass product is likely suitable for long-term disposal and can be described as a composite material containing

borosilicate glass with embedded  $\text{CaMoO}_4$  and  $\text{BaMoO}_4$  rich regions. This, however, must be proven in dedicated leaching and glass corrosion studies, respectively.

## 6.2. Tc and Cs rich residuals from vitrification

Rinsing of the process components and the piping in the main process area of the VEK plant after vitrification activities in 2009/2010 yielded around 3000 L of a radioactive solution containing significant activities of Cs-137 and Tc-99.<sup>236</sup> It was collected in an evaporator concentrate tank and probed by liquid sampling on 14<sup>th</sup> of March 2011. After sampling the liquid was distributed in equal volumes to the receipt tank and the evaporator concentrate tank. Due to the use of jet pumps and residual liquid in the pipes and tanks the total volume was increased by ca. 700 L. A constant dry-air flow was maintained in both tanks. Due to the internal energy release of the radioactive decay the solution temperatures averaged between 30 °C and 45 °C. Within one and a half year both solutions evaporated to dryness (approximately 80 kg solid material, more than  $10^{15}$  Bq). Both temperature and filling level of the tanks were monitored and are shown in [Figure 67](#).

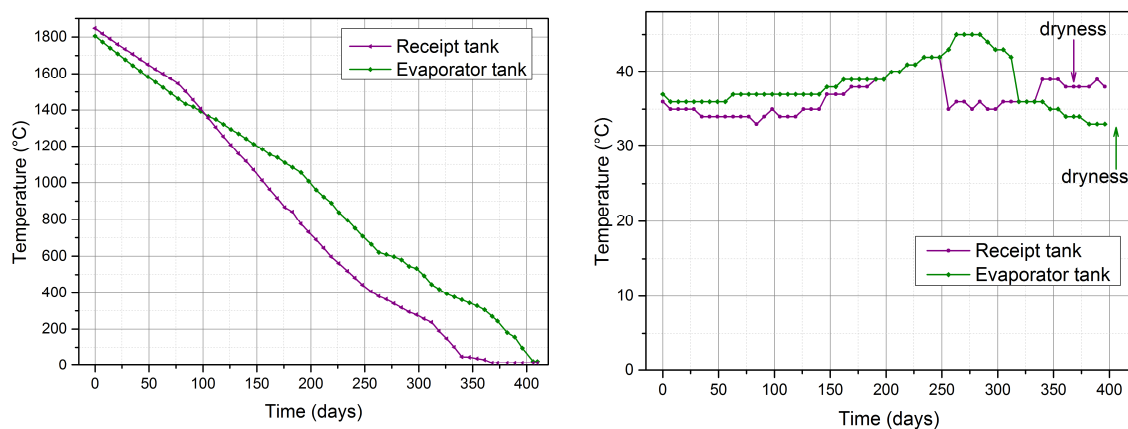


**Figure 67** Filling levels in the receipt and evaporator concentrate tank as function of the time (left). Temperature profile of the solutions in both tanks until dryness and beyond (right). The moment of dryness is indicated. (Data from KTE GmbH<sup>10</sup>)

### *Drying process of receipt tank*

When filled on 24<sup>th</sup> of October 2011, the tank contained 1847 L of the rinsing solution with a temperature of 36 °C. The filling level decreased approximately in a linear manner by approximately 5.6 L/day at a temperature of ca. 35–40 °C. Merely in June the temperature rose to 42 °C, most likely due to a temporary fluctuation in the dry-air flow.

### *Drying process of evaporator concentrate tank*

On 24<sup>th</sup> of October the tank contained 1805 L of the solution with a temperature at 37 °C. The drying rate was with 4 L/day at 35–45 °C lower than in the receipt tank. The reason is unknown.

### *Liquid sampling results*

The liquid sample obtained on 14<sup>th</sup> of March 2011 of the evaporator concentrate tank filled with 2970 L was analyzed at INE by ICP-MS<sup>237</sup>. The results are listed in **Table 13** in g/L and mmol/L. The solution contained nine major elements dominated by Tc and Cs on a quantity basis.

**Table 13** ICP-MS analysis results of liquid sampling of the evaporator concentrate tank on 14<sup>th</sup> of March 2011. The elements with the most relevant concentrations are listed. Standard deviations and more details results are listed in **Table 41** in the **Appendix**.

Element	Tc	Cs	Na	Fe	La	Cr	Ni	Ba	Mn	HNO <sub>3</sub>
c (g/L)	4.24	3.54	1.26	1.67	1.22	0.33	0.24	0.13	0.09	-
c (mmol/L)	43.3	26.7	55.0	29.9	8.8	6.4	4.1	0.9	1.6	2740

In addition to the elements listed minor amounts of *An* elements were found (0.0009 g/L Np-237, 0.002 g/L Pu-239, 0.00094 g/L Pu-240). Those elements have not been considered in the simulate synthesis due to their radioactivity and low concentration. The HNO<sub>3</sub> concentration was found to be 2.74 mol/L.

### *Aim of the project*

The drying of the solutions in the VEK process components was arranged in order to transform the radioactive material in a safer solid state. Most of the precipitated material will be most likely deposited on the bottom of the tanks while minor amounts could be attached to the walls. From their solubility limits the precipitation of CsTcO<sub>4</sub>, NaTcO<sub>4</sub> and several nitrate salts during evaporation is roughly estimated (cf. **Table 42** in the **Appendix**). At the moment there is no feasible way to visually evaluate or probe the residue material due to technical reasons in combination with the very high level of radioactivity. Before the tanks are opened and the dried residue is removed a safe handling and immobilization strategy has to be developed and the way of disposal of the materials has to be determined. This study has the aim to obtain valuable insights in the materials physical and chemical nature and to compare observed solid phase formation during drying with solubility limit calculations (cf. **Table 41** in the **Appendix**). Points addressed in this study are:

- Macroscopic properties of the residue material (form, layering, homogenous/heterogeneous, hygroscopic, consistency, hardness, ... etc.)
- Chemical composition and speciation of the solid
- Insights in the solubility and precipitation behavior of the studied elements

Those information is considered important for planning for and deciding on further treatment procedures related to the removal of the material from the vessel and further treatment and conditioning. A specific question was whether the main activity carriers Cs-137 and  $\text{ReO}_4^-$  could be selectively separated during evaporation. In order to tackle those question the rinsing solution was simulated in a laboratory scale experiment (4.86 L) on basis of the analysis results reported in **Table 13** and evaporated to dryness in a comparable temperature range. A stainless steel container was used so that the initial surface-to-volume ratio is similar to the genuine situation in the tanks. The characteristics of the resulting solid state material were then analyzed by several microscopic and spectroscopic techniques such as SEM-EDX, Raman, IR and XRD in addition to ICP-OES/AAS. In **Section 6.2.4** several approaches to the immobilization of the obtained residue material are discussed.

The here presented work was object to the GENTLE student research project of master student Paul Estevenon from *The National Graduate School of Chemistry, Montpellier, France*.<sup>238</sup> It was performed from June to September 2014 under the close supervision of S. Bahl. Its results were also reported in a summarized form within a contracted project with the KTE GmbH (permission for publication granted by Prof. Urban, KTE GmbH)<sup>10</sup>.

### 6.2.1. Experimental

In the following section the synthesis of the materials and the methods which were used for their characterization are described. **Section 3** give a general description of the applied characterization methods.

In the following section the methods which are used for characterization of the liquid and solid samples are described. For some information the reader is referred to **Section 3** describing the general setting of the techniques. Afterwards the synthesis of the simulate is described in addition to the performed drying process.

## Preparation of samples

### *Simulated solution*

The composition of the experimental solution is based on the results from the elemental analysis from the 14<sup>th</sup> of March 2011 of the evaporator concentrate tank (cf. **Table 13**). For the experiment the radioactive elements were surrogated by inactive elements on a mole-by-mole basis: Cs-133 for Cs-135/Cs-137 and Re-185 for Tc-99. The justified simulation of Tc by Re due to their similar chemical behavior is discussed elsewhere.<sup>239</sup> Np-237, Pu-239 and Pu-240 have also been identified in the in-tank solution. Because of their low concentration they were considered as negligible in the intended investigations and therefore surrogated by La. The target composition of the experimental solution is listed in **Table 14**.

**Table 14** Target composition of the experimental solution used for the drying experiment. It is based on the analysis results reported in Table 13.

Element	Re	Cs	Na	Fe	La	Cr	Ni	Ba	Mn
c (g/L)	8.06	3.54	1.26	1.67	1.22	0.33	0.24	0.13	0.09
c (mmol/L)	43.3	26.7	55.0	29.9	8.8	6.4	4.1	0.9	1.6

The amounts of chemicals which were used to prepare the solution are listed in **Table 15**. Rhenium was added by slowly dissolving metallic rhenium (extensive NO<sub>x</sub> formation) in 65% nitric acid according to the reaction:



The loss of H<sup>+</sup> was considered in the calculation of the solutions acidity of 2.74 mol/L. The other elements (Cs, Na, Fe, La, Cr, Ni, Ba and Mn) were added as nitrates to water as listed in **Table 15** and stirred until complete dissolution. Afterwards the Re solution was added to the aqueous solution of nitrate salts. In total, a clear blue solution of 4.86 L was obtained (cf. **Figure 68**).

**Table 15** Chemicals used for the synthesis of the experimental solution.

Compound	m <sub>th</sub> (g)	m <sub>exp</sub> (g)
Re	39.17	39.19
Ba(NO <sub>3</sub> ) <sub>2</sub>	1.20	1.20
CsNO <sub>3</sub>	25.35	25.35
NaNO <sub>3</sub>	22.68	22.69
La(NO <sub>3</sub> ) <sub>3</sub> ·6H <sub>2</sub> O	18.55	18.55
Mn(NO <sub>3</sub> ) <sub>2</sub> ·4H <sub>2</sub> O	1.95	1.96
Fe(NO <sub>3</sub> ) <sub>3</sub> ·9H <sub>2</sub> O	58.74	58.75
Ni(NO <sub>3</sub> ) <sub>2</sub> ·6H <sub>2</sub> O	5.73	5.74
Cr(NO <sub>3</sub> ) <sub>3</sub> ·9H <sub>2</sub> O	12.40	12.40
HNO <sub>3</sub> 65%	1319	1320
H <sub>2</sub> O	3835	3883

#### Drying of the solution

The solution was transferred into a stainless steel container with an inner diameter of 19.8 cm, a wall thickness of 3 mm and a height of 25 cm. The geometry of the container was designed in such a way that the solution has an initial surface-to-volume ratio of 0.64 dm<sup>2</sup>/L which was also the situation in the evaporation and receipt tanks of the VEK. The solution was heated in a sand bath to 50 °C in a fume hood and kept at constant temperature (cf. **Table 43** in the **Appendix**). The dried material was continuously heated to avoid re-liquefaction by air moisture. During the drying process the liquids volume and the temperature were recorded as well as 1 mL liquid samples was taken for elemental analysis by ICP-OES (cf. **Table 43** in the **Appendix**).

#### Solid state material sampling

The solid residue material revealed a very heterogeneous macroscopic appearance. Three major areas were observed on the surface of the residue. They will be described in more detail in **Section 6.2.2**. For SEM measurement, material was taken from the different characteristic areas. The samples were dried overnight in a furnace at 60 °C. To avoid hydration, the specimens were transferred to a desiccator for storage. It was observed that the samples contain remaining water so they were analyzed in the electron microscope in ESEM mode at 50 to 60 Pa water atmosphere. After SEM-EDX analysis, the same samples were also used for Raman spectroscopy analysis. Due to the hygroscopic and corrosive nature of the material only one XRD analysis was performed. Corrosion was observed after the measurement on the stainless steel parts of the XRD sample holder. For the measurement material from all

characteristic areas was collected and comminuted to a homogenous material. Solid samples from the different areas were dissolved in nitric acid and diluted in water for ICP-OES measurements. The liquid samples taken during the drying process were also analyzed by ICP-OES.

## **Methods and Materials**

### Raman Spectroscopy

A red laser was used with power of 50 mW in combination with the 20x objective for investigation of the simulated dried residue material. All spectra were background corrected and normalized to their maximum.

### X-ray powder diffraction (XRD)

XRD diffractograms were recorded within the  $2\theta = 10-70^\circ$  range with 0.7 s integration time per step. The spectrum was background corrected with the *OPUS* program (*Bruker*). Reference diffractograms collected in the *American Mineralogist Crystal Structure* (AMCSD) database were used.

### Scanning electron microscope (SEM) and energy-dispersive X-ray spectroscopy (EDX)

The SEM-EDX microscope was operated in ESEM mode with an H<sub>2</sub>O atmosphere of 50 to 60 Pa.

### Inductively coupled plasma optical emission spectroscopy (ICP-OES)

Elemental composition was determined by an *Optima 8300* optical emission spectrometer.

### Atomic absorption spectroscopy (AAS)

These studies were performed using a *Perkin Elmer 3300* atomic absorption spectrometer.

### pH measurements

pH measurements were performed using an *Orion 420A* pH-meter equipped with an *Orion 8103SC* pH electrode.

### Infrared spectroscopy (IR)

The IR spectra were recorded as stated in **Section 3**.

## 6.2.2. Results

### *Drying process*

The drying process is illustrated in **Figure 68**. The temperature of the solution was kept between 46 °C and 49 °C. With evaporation a change in color was observed caused by the transition metal ions in the solution (mainly Cr and Fe). Due to higher concentration of all components the liquid turned first to light then to dark green. After 8-9 days the solution was evaporated to dryness. An overview about the filling level, the sampling dates and the temperature profile is given in **Table 43** in the **Appendix**. The first crystals were observed after 5 days when around 75% of the solution was evaporated (cf. **Figure 68**, 3). A solid dark brown heterogeneous residue material was obtained as final product of the drying process as shown in **Figure 68**, 4.



**Figure 68** Photographs of the experimental solution in the drying process.

**Figure 69** shows the decrease of the solutions volume. The sampling frequency was increased towards the end as a higher possibility for precipitation events was expected. The results from liquid sampling **S1–S10** are listed in **Table 44** in the **Appendix**. Taking into account the volume of the solution the element inventory can be calculated. It accounts for **S1** to 16.4 g Cs, 36.8 g Re, 5.96 g Na and 7.8 g Fe. As the process of precipitation removes elements from the solutions inventory, the liquid sampling is a tool to identify and quantify precipitation from the solution.

The evolution of selected elements is shown in **Figure 70**. It was found that significant amounts of precipitate were formed at 0.34 L residual volume. This is equal to a 15 times higher concentration than in the initial state. Re was found to be present in high concentration of 150 g/L which agrees with its relative high solubility.<sup>239</sup> **Figure 70** also shows the decrease in element fraction from the inventory for low solution volumes. It can be noticed that precipitation occurs shortly before dryness between 0.35 L and 0.23 L.

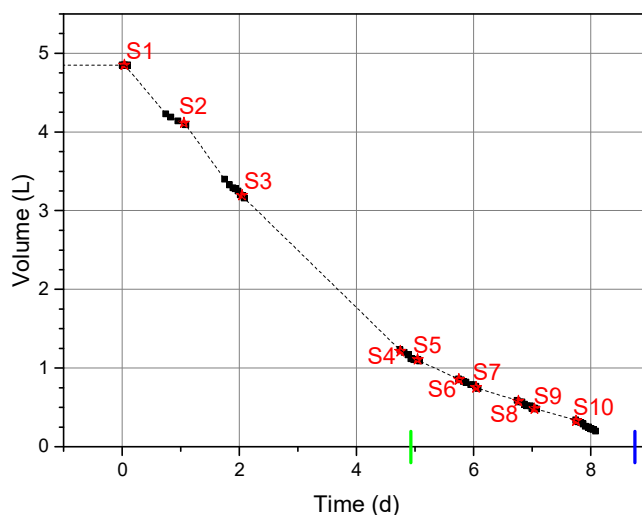


**Figure 69** Measurement of the volume decrease by time in black. The sampling time of sample **S1** to **S10** is indicated by labelled red marks. The first observation of floating crystals is indicated with a green vertical bar, the dryness of the material with a blue vertical bar.

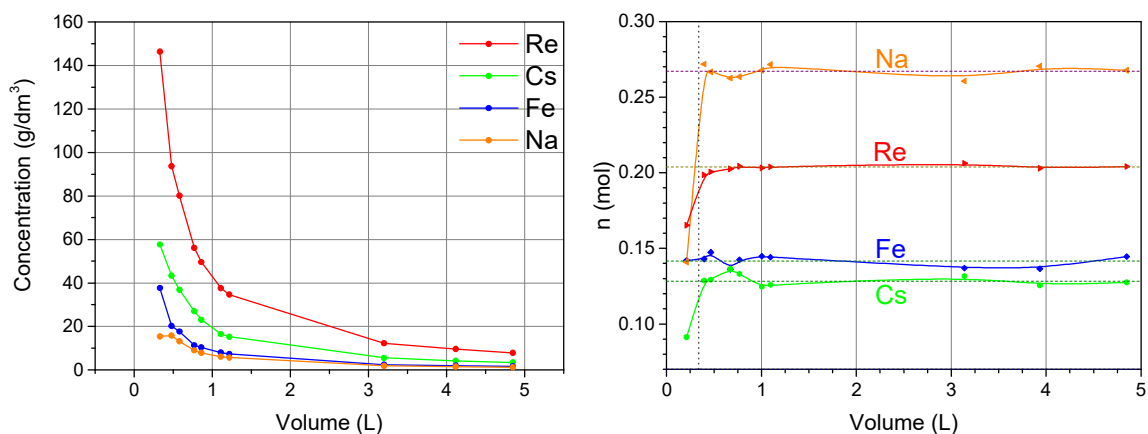


**Figure 70** Element concentration of selected elements Re, Cs, Fe and Na in the simulate solution as function of the solutions volume (left). Decrease of element fraction with decreasing volume (right). The volume of 0.34 L when most compounds start to crystallize is indicated with a vertical dashed black line.

In addition to the element concentration, the density of the solution and the  $\text{H}_3\text{O}^+$  concentration was determined by geometrical calculations and pH measurement, respectively. They are listed in **Table 16**. The  $\text{H}_3\text{O}^+$  concentration increased from initial 2.7 mol/L to 12.9 mol/L. The

density increased from 1.1 g/cm<sup>3</sup> to 1.67 g/cm<sup>3</sup>. As every sample taken from the solution had a volume of 1 mL the loss of elements can be considered as negligible.

**Table 16** H<sub>3</sub>O<sup>+</sup> concentration and solution density calculated for S1–S10.

Sample	S1	S2	S3	S4	S5	S6	S7	S8	S9	S10
c(H <sub>3</sub> O <sup>+</sup> ) (mol/L)	2.70	3.32	4.18	10.5	11.8	12.9	12.9	12.9	12.9	12.9
Density	1.10	1.12	1.16	1.39	1.41	1.46	1.48	1.53	1.56	1.67

### *Characterization of solid residual material*

As expected, most of the residual material is composed of perrhenates and nitrates. These compounds exhibit a very hygroscopic nature such as the material was re-liquidated after a few hours when exposed to an ambient air atmosphere. The solid residual showed a heterogenous macroscopic appearance. Three major areas could be identified:

- An area with significant layering. The top layer consists of a solid crust layer with big crystals. Below there was either two more bitumen like layers or another dark brown crust. This area consists of two or three different layers (cf. **Figure 71** left) and is therefore called “two layers area” and “three layers area” in the following.
- A one layer black and bitumen like area with big crystals inside the residue (cf. **Figure 71** middle). This area is called “one layer area”.
- An area which looks like the “one layer area” with a black color but with brown traces on the surface. This area revealed to have two layers, one with bitumen like black residue and a thin hard layer with green crystals (cf. **Figure 71** right). This area is called “brown area” in the following.



**Figure 71** Photographs of areas in the residual material with significant different characteristics. “Two layers area” (left), “one layer area” (middle) and “brown area” (right).

### *XRD analysis*

For identification of crystalline solid state compounds in the residual material samples from all characteristic areas were taken, homogenized and a XRD diffractogram was recorded

(cf. **Figure 72**). By comparison with known diffraction pattern from a database  $\text{CsReO}_4$  was clearly identified with its main reflex at  $24.8^\circ$ . The low intense reflex at  $29.4^\circ$  coincides with the main reflex of  $\text{NaNO}_3$ . Raman spectroscopy will support this finding. No further un-assigned reflexes can be observed. As this measurement lead to significant corrosion of the stainless steel sample holder no further samples could be investigated.

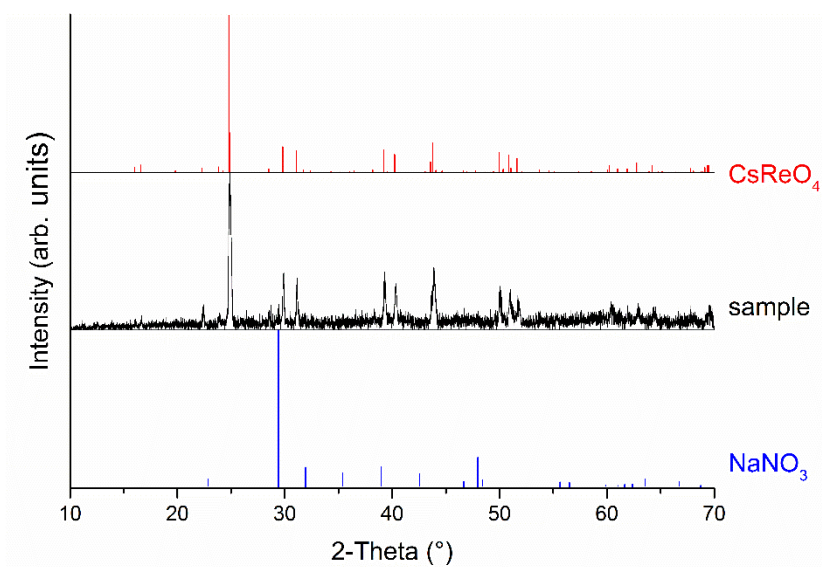


**Figure 72** XRD pattern of homogenized residual material in comparison with reflex positions obtained from AMCSD crystal structure database.

#### *ICP-OES and AAS analysis*

**Table 17** lists the results of the elemental analysis performed by solid state sampling, dissolution and ICP-OES and AAS measurement. Samples from all characteristic areas were taken. For the “two layer area” two samples were taken, respectively. As the results are very similar it can be assumed that the areas and layers itself are composed predominantly homogenously. In between the areas there are significant differences in elemental distribution. Cs differs from 9.97 to 26.94 at%, Re from 14.77 to 34 at%.

The “two and three layers area” top layers show similar chemical composition. The same accounts for their bottom layers. The middle layer of the “three layers area” has a composition between the composition of the top layer and the composition of the bottom layer. It can be considered as transition layer. Therefore, the “two layers area” and the “three layers” area were investigated as one area.

The “crystal belt area” (crystals which have grown on the walls of the steel container in an earlier stage of the drying process) has a composition which is comparable with the “two and three layers area” top layers but with less Na and more Fe and La.

The “brown area”, which did not seem to be very different from the “one layer area” during the first observations has a significantly different composition. The two layers which were observed contained a lot of Fe, Re and Cs (more than 75% in molar ratio for the considered elements).

In a general view of the residue the most important concentrations of Ba, Cr, Cs, Fe, Ni and Re can be found for the bottom layers (and the top layer of the “brown area”) indicating an early precipitation. More than 50 at% of Na is found in the crust top layers (excepted top layer of the “brown area”).

**Table 17** ICP-OES and AAS results from sampling of the solid residual material from different areas. The results are given in at%. The relative standard deviation of the Cs concentration is given by max. 2.74% whereas the deviation for the other elements is max. 5%.

Area	<i>two layers</i>	<i>two layers</i>	<i>crystal belt</i>	<i>brown</i>	<i>brown</i>	<i>three layers</i>	<i>three layers</i>	<i>three layers</i>	<i>one layer</i>	<i>target composition</i>
Layer	<i>crust</i>	<i>bottom layer</i>		<i>top layer</i>	<i>bottom layer</i>	<i>top layer</i>	<i>middle layer</i>	<i>bottom layer</i>		
Ba	0.03	0.47	0.16	0.14	0.63	0.02	0.53	1.07	0.25	<b>0.54</b>
Cr	2.11	4.58	2.69	4.33	3.00	1.97	4.09	4.73	4.87	<b>3.61</b>
Fe	9.63	20.45	12.89	20.14	13.56	9.02	18.13	21.37	21.80	<b>16.93</b>
La	2.84	5.51	9.03	2.43	3.90	4.42	8.00	6.14	5.19	<b>4.99</b>
Mn	0.60	1.14	0.64	1.13	0.85	0.53	0.95	1.10	1.12	<b>0.91</b>
Na	54.36	24.00	45.50	14.71	15.03	57.95	32.34	23.00	24.74	<b>31.09</b>
Ni	1.53	3.20	1.86	3.19	2.12	1.36	2.76	3.20	3.23	<b>2.29</b>
Re	16.92	25.60	16.74	28.68	33.98	14.77	21.27	24.54	25.00	<b>24.52</b>
Cs	11.99	15.05	10.50	25.26	26.94	9.97	11.94	14.84	13.79	<b>15.12</b>

### *SEM observation and EDX analysis*

SEM analyses were performed for twenty different samples from the solid residue. The heterogeneous appearance in a macroscopic scale is also reflected in the micrometer scale. Large dark NaNO<sub>3</sub> crystals of 1–3 mm have often been found embedded in a matrix of paste with non-crystalline appearance (cf. **Figure 73** left). These crystals were mainly observed in the top layers of the material in accordance with the elemental analysis. The paste was found in nearly all the sample areas and has more or less constant composition of: 5-10 at% Cr, 35-45 at% Fe, 0.5-1 at% La, 1-2 at% Mn, 5-10 at% Na, 5-7 at% Ni, 25-30 at% Re, 5-10 at% Cs. As it transformed and moves slightly under the electron beam the paste still contained water which is heated and vaporized by the electron beam. Another notable structure which often appeared is a bright crust on the surface of the sample (cf. **Figure 73** right). In this crust-like

material high concentrations of Re were correlated with Cs and some Fe. Thus, most likely the already identified  $\text{CsReO}_4$  is one of its main components.

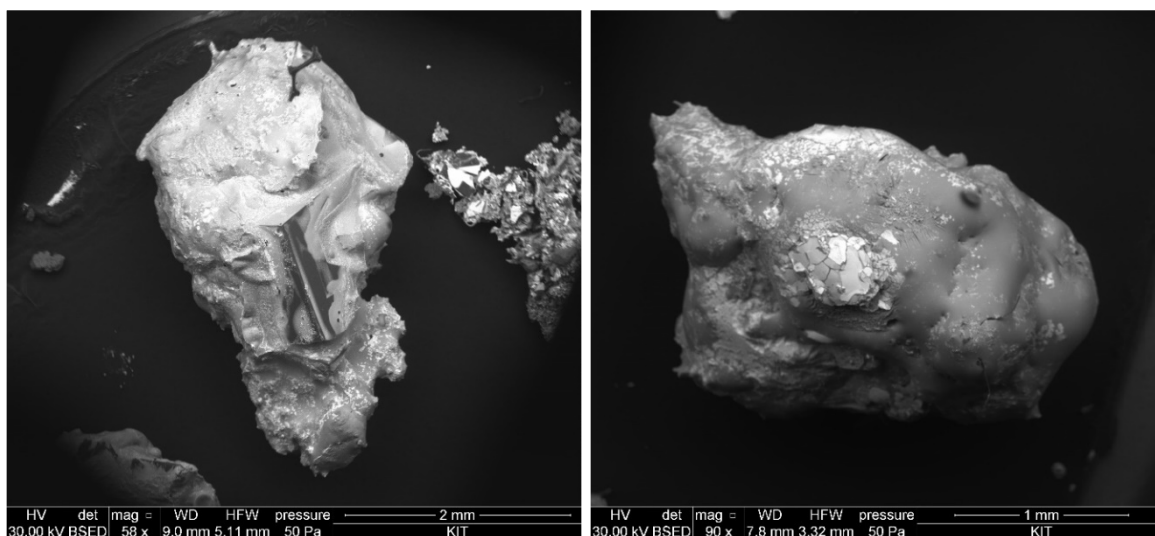


**Figure 73** SEM images of sample material from crust of the “two layer area” (left) and the middle layer of the “three layer area” (right).

La was observed correlated with Na in ca. 100  $\mu\text{m}$  sized crystals inside the non-crystalline paste (cf. **Figure 74**). Under continuous electron irradiation the well-shaped crystals cracked and degraded.

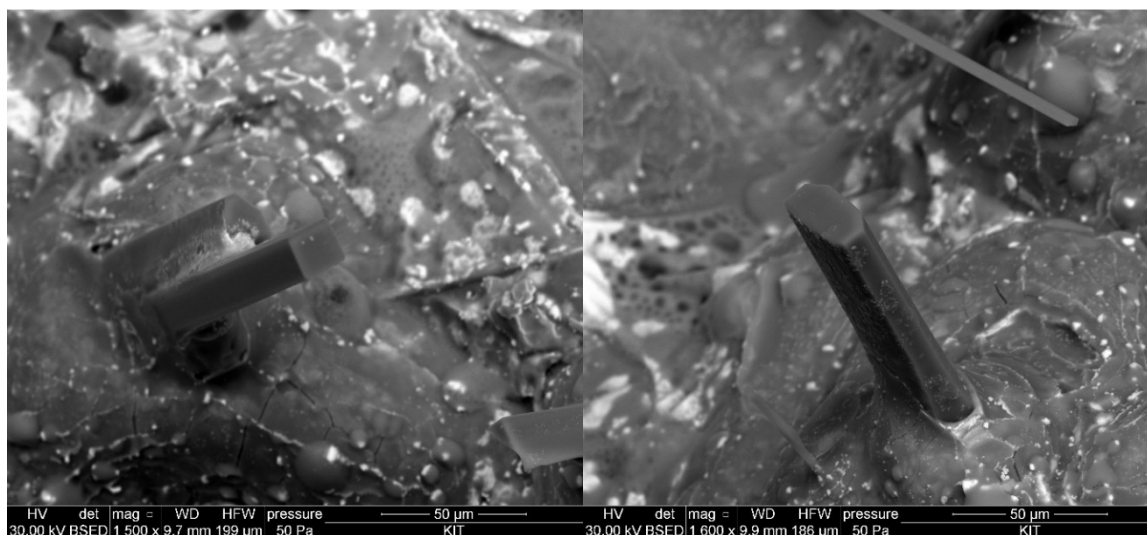


**Figure 74** SEM images of La and Na rich crystals in non-crystalline matrix.

### *Raman spectroscopy analysis*

Raman spectroscopy turned out to be very suitable to determine the heterogeneous nature of the residue material. Several samples were taken from the characteristic areas of the material and analyzed by Raman spectroscopy. The obtained spectra are compared with pure spectra of several commercially obtained reference compounds such as  $\text{CsReO}_4$ ,  $\text{NaNO}_3$ ,  $\text{CsNO}_3$ ,

$\text{Fe}(\text{NO}_3)_3 \cdot 9\text{H}_2\text{O}$ , etc.  $\text{CsReO}_4$  and  $\text{NaNO}_3$  are found to be present in nearly all samples (cf. **Figure 75**). The vibrational bands of the references and the samples clearly coincide for  $\text{CsReO}_4$  (190, 730 and  $1070 \text{ cm}^{-1}$ ) and  $\text{NaNO}_3$  (330, 900, 920 and  $970 \text{ cm}^{-1}$ ). For some samples a broad band at  $1050 \text{ cm}^{-1}$  can be observed. A comparison with Raman spectra of several nitrate compounds such as La, Fe, Cr, Ni, Mn, Ba and Cs nitrate reveals that their main feature is positioned at this wavenumber. Therefore, the formation of nitrate compounds can be assumed. As the solubility limit for  $\text{NaReO}_4$  is relatively low compared to the limit of  $\text{NaNO}_3$  (cf. **Table 42** in the **Appendix**), its formation under drying conditions is expected (**Table 41** in the **Appendix**) beside  $\text{CsReO}_4$ . But even though the total molar concentration of Cs is clearly lower than that of Re (ratio: ca. 0.65), no evidence for the formation of  $\text{NaReO}_4$  is found in the spectra. It might form non-crystalline  $\text{Re}_2\text{O}_7/\text{Fe}(\text{ReO}_4)_3$  species or solid mixed phases in lower concentration which would be superimposed by the main  $\text{CsReO}_4$  peak at  $1070 \text{ cm}^{-1}$ . The Raman results support the assumptions drawn from XRD analysis and prove the presence of  $\text{NaNO}_3$ .

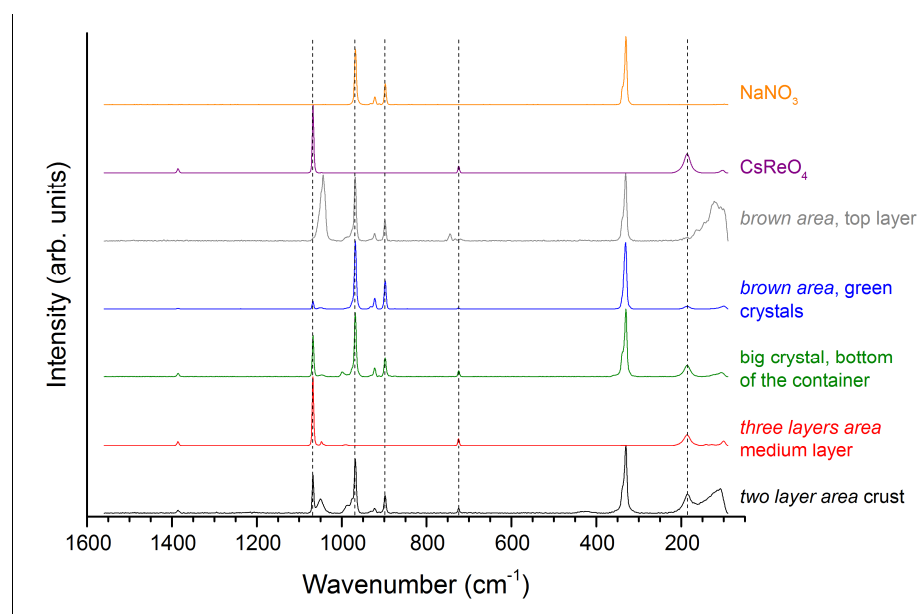


**Figure 75** Raman spectra of several samples from characteristic areas of the residual material compared to reference spectra of  $\text{NaNO}_3$  and  $\text{CsReO}_4$ .

### *Infrared Spectroscopy analyses*

The same set of samples was analyzed by IR spectroscopy. The results agree with the information obtained by Raman spectroscopy. However, IR analysis enabled the identification of  $\text{Ba}(\text{NO}_3)_2$  in the first crystals formed on the solutions surface and the wall of the steel container (cf. **Figure 76**). The absorption band at around  $900 \text{ cm}^{-1}$  can most likely be attributed to perhenate species. The main IR features of  $\text{CsReO}_4$  are reported to lie around  $900 \text{ cm}^{-1}$ .<sup>240</sup>

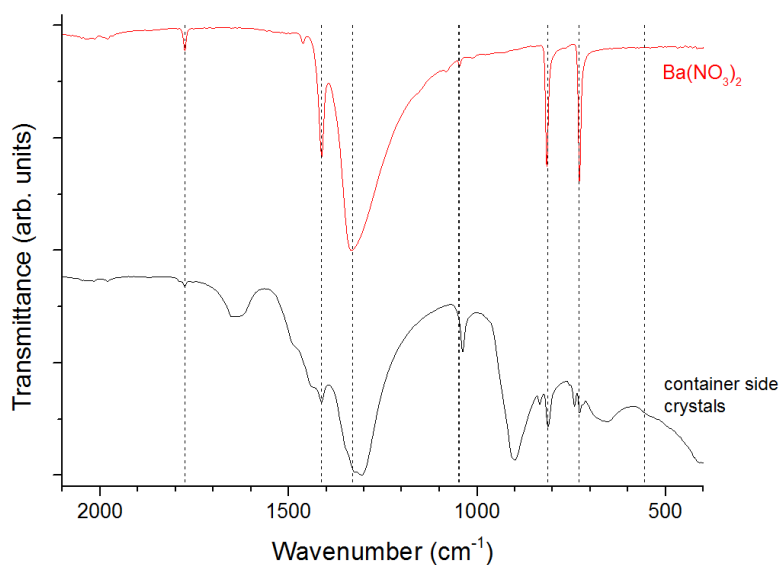


**Figure 76** IR spectrum of crystals formed early in the drying process on the solutions surface and the container wall. For comparison pure  $\text{Ba}(\text{NO}_3)_2$  reference spectrum is shown. The main absorption bands of  $\text{Ba}(\text{NO}_3)_2$  are indicated by vertical dashed black lines.

### 6.2.3. Discussion

Analysis of the liquid sampling reveal that the crystallization of several compounds is initiated during volume reduction where concentrations of nitric acid are high (more than 12 mol/L) and elements reach their solubility limit. The precipitating material contains nitrates and perrhenate salts, no oxide compounds are identified. Raman and IR spectroscopy have been a suitable tools to reveal those species. The hygroscopic nature of the material is a consequence of the nitrate and perrhenate compounds. The corrosive behavior of the residue when heated, revealed in XRD and TGA analysis (interrupted due to equipment corrosion), is another characteristic property of the material. The first compound to precipitated from the oversaturated solution is  $\text{Ba}(\text{NO}_3)_2$ . The flocculation of its white crystals on the solutions surface was accompanied by a loss of Ba in the solution. The crystals were found mainly at the wall of the container, not in the residue material sediment at the bottom. There, large  $\text{NaNO}_3$  crystals of several mm size with a well-defined geometry were identified by XRD, SEM-EDX, Raman and IR spectroscopy. They are found mainly in the top crust layers of the residue. The expected formation of relatively poorly soluble  $\text{NaReO}_4$  is not observed (cf. **Table 41** in the **Appendix**). Na is additionally found in La rich crystals embedded in a non-crystalline paste matrix. They consist most likely of  $\text{La}(\text{NO}_3)_3 \cdot \text{H}_2\text{O}$  and  $\text{NaNO}_3$ . XRD and Raman spectroscopy are not able to clearly identify their composition. The precipitation behavior of Re was identified

by liquid sampling and XRD/Raman analysis. CsReO<sub>4</sub> crystals are formed when the solution was evaporated to approximately 1/15<sup>th</sup> of its initial volume. At this filling level most of the other compounds precipitated also. If the dissolution of the residuals in the VEK receipt and evaporator tank is preferred over the solid state removal, about 150 L of nitric acid solution should be sufficient to re-dissolve the precipitated material from a thermodynamic point of view. CsNO<sub>3</sub> formation is not observed. Re is found by ICP-OES and SEM-EDX to be correlated with Fe. As Re is present in larger molar amounts than Cs, the excess Re may form an Fe salt such as Fe(ReO<sub>4</sub>)<sub>3</sub>·xH<sub>2</sub>O. Small crystal sizes and/or the presence of larger amounts of residual water may be responsible that no regular crystal lattices, detectable by XRD, form. The perrhenate band in the Raman spectrum of Fe(ReO<sub>4</sub>)<sub>3</sub>·xH<sub>2</sub>O might be superimposed by the high intense CsReO<sub>4</sub> band. It is likely that a major amount of the Fe forms nitrate salt together with Ni, Mn, and Cr. As their melting points are very low (Fe(NO<sub>3</sub>)<sub>3</sub>·9H<sub>2</sub>O 47°C, Cr(NO<sub>3</sub>)<sub>3</sub>·9H<sub>2</sub>O 60°C, Mn(NO<sub>3</sub>)<sub>2</sub>·4H<sub>2</sub>O 37°C, Ni(NO<sub>3</sub>)<sub>2</sub>·6H<sub>2</sub>O 56°C) and all compounds exhibit a hygroscopic character it is likely that these compounds form a non-crystalline material. SEM-EDX measurements support this hypothesis as they find considerable amounts of the mentioned cations correlated in a paste-like omnipresent matrix.

The macroscopic structure of the residue is of great interest with regard to its removal and further treatment. Areas with one, two or three separate layers were found. The layers differ in chemical composition but also consistency. Dry hard material is found at the container wall and in the crusts which are underlaid by wet bitumen-like layers. Whereas the former is difficult to remove, removing of the latter will be easier. As in the performed experiment the material was dried only a few days at approximately 45 °C it is possible that in the meantime all water in the receipt and evaporation tank was removed to complete dryness after several years (four years at this juncture) under dry-air flow. The material exhibits a very hygroscopic and when heated corrosive nature. Due to a late crystallization most of the material can be found on the bottom of the tanks. Nevertheless, some material, especially Ba(NO<sub>3</sub>)<sub>2</sub> will be deposited also at the container walls. Colored areas can give a hint for high concentration of Cs and Tc. The high radiotoxicity, the hardness and the hygroscopic character of the residue will make its removal a great challenge. Residue removal will, thus, be difficult and might require some redissolution steps.

Except of the mentioned small deviations the general drying process in the VEK tanks was most likely elapsed in the same manner as in the here discussed experiment. Most of the radiotoxic Tc and Cs is assumed to be bound in CsTcO<sub>4</sub> according to our experimental data for Re. In analogy to data obtained for ReO<sub>4</sub><sup>-</sup>, the rest of Tc will be associated with Fe. The formation of CsNO<sub>3</sub> was not confirmed. Most of the remaining cations form nitrate salts with low melting

point. A selective separation of the main activity carriers Cs-137 and Tc-99 by controlled evaporation appears to be impossible. Most dissolved components precipitate more or less simultaneously from the solution when precipitating as a consequence of decreasing solution volume.

#### 6.2.4. Immobilization

The immobilization of the Tc and Cs rich residual material is a great challenge due to their high volatility at elevated temperatures. As the material is highly radioactive an appropriate solidification such as for example vitrification is the favored immobilization method. The obtained glass products will be suitable for long-term storage in a deep underground repository. As the volatilization of the some elements occurs from the surface of the glass melt, low surface-to-volume ratios favor their retention. A so-called “in-can melting” process could be therefore favored for the immobilization of the discussed waste.<sup>241</sup> Thereby the glass forming components and the solid waste are mixed in a crucible with preferentially tall geometry and externally heated. As the size of the crucible can be varied this technique is able to immobilize wastes from mg to kg scale. The stainless steel container used in the operation of the VEK plant would be a suitable crucible in an in-can melting process. Therefore, a potential licensing process would be facilitated very much.<sup>242</sup>

There are a lot of different glassy systems available. In the following, several experiments are presented in order to determine a glass system and vitrification conditions suitable for the potential immobilization of the in **Section 6.2** discussed residual material. The main focus will be on evaluation of the final waste glass product and the volatilization behavior of relevant elements within the vitrification. As the vapor pressure of the volatile elements is mainly dependent on the temperature, glass systems with preferentially low processing temperature will be reviewed. The solid residual material presented previously is used in the following immobilization experiments. The elements which are of relevance for volatilization losses are Re and Cs.

##### 6.2.4.1. Ba rich borosilicate glass at 950 °C

The addition of Ba to a borosilicate glass lowers its melting range significantly by modifying the glass network structure.<sup>243</sup> In the here presented approach, a Ba rich borosilicate glass is used enabling the vitrification of the waste simulate at temperatures below 1000 °C. As

conventional vitrification with borosilicate glass is often performed at 1100-1200 °C, the reduced temperature should have a beneficial influence on the volatilization loss. To study this behavior samples are melted from 950 to 1200 °C. To compare the results a glass ("reference glass"), developed at INE, will be used as a reference system.<sup>226, 244</sup> The compositions of both glass frits are depicted in **Table 18**.

**Table 18** Target composition of the Ba rich<sup>243</sup> and reference glass frit<sup>226</sup>. The Al content of the Ba rich glass was slightly increased in order to enhance the chemical durability of the final glass product.

Compound	reference frit (wt%)	Ba rich frit (wt%)
SiO <sub>2</sub>	53.41	38.50
B <sub>2</sub> O <sub>3</sub>	14.60	24.00
BaO	4.17	23.00
Na <sub>2</sub> O	5.21	12.50
Al <sub>2</sub> O <sub>3</sub>	4.40	2.00
Li <sub>2</sub> O	2.60	-
CaO	8.00	-
MgO	5.21	-
Sb <sub>2</sub> O <sub>5</sub>	0.60	-
V <sub>2</sub> O <sub>5</sub>	1.80	-
<b>Total</b>	<b>100</b>	<b>100</b>

In the literature it is reported that Tc can be reduced from its heptavalent Tc(VII) state to its less volatile tetravalent Tc(IV) state.<sup>245</sup> In order to optimize the Tc retention reducing agents will be added to some samples and their influence on the Re which is used in the experiment as Tc surrogate will be carefully evaluated. The waste glass samples will be loaded with 5 wt% total waste simulate loading in the glass. In addition to the volatilization behavior study the final glass products are investigated with regard to phase separations by several microscopic and spectroscopic techniques. This should give first information on the possible suitability of the product for long-term storage in a deep underground repository.

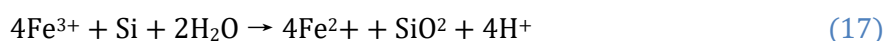
The here presented study was object of the "Vertiefungsprojekt", an extensive lab course project, of the Masters student Aaron Beck at KIT, Karlsruhe, Germany. The master project was supervised by S. Bahl. Following a short summary of the performed studies will be presented. For more details the reader is referred to the project report of Beck.<sup>246</sup>

## Experimental

The glass samples were synthesized using the same materials and tools as reported in **Section 6.1.1**. The characterization methods are described as well in **Section 6.1.1**. Detailed information are reported in the report of Beck.<sup>246</sup>

The simulate residue reported in **Section 6.2** was used without further manipulations. Attracted water was removed by drying at 90 °C. The residue was removed from the container wall and bottom. The paste-like material was well mixed to grant a homogenous distribution and added to the glass frits. The glass frits were pre-synthesized by melting of several oxide and carbonate compounds (cf. **Table 45** in the **Appendix**)

According to the following redox reactions elemental Si was added for vitrification in reducing conditions:



The samples nomenclature and the used amounts of waste, frit and reducing agent are listed in **Table 19**.

**Table 19** Overview of the samples which were synthesized from Ba rich and reference frit.

Sample	Ba rich frit (g)	reference frit (g)	Simulate residue (g)	Si (mg)
1.1	8.07	-	0.770	-
1.2	7.88	-	0.752	-
1.3	7.90	-	0.754	-
1.4	8.33	-	0.795	-
1.5	7.97	-	0.760	-
1.6	7.92	-	0.755	-
2.1	-	8.10	0.772	-
2.2	-	8.05	0.767	-
3.1	7.96	-	0.759	22.5
3.2	7.78	-	0.742	44.2
4.1	8.11	-	1.630	-

The mixture of waste simulate, glass frit powder and reducing agent was filled in a Pt crucible and heated to a temperature between 950 °C and 1200 °C with a heating rate of ca. 200 K/min.

For all samples the same crucible was used in order to keep the same surface-to-volume ratio of 3.0 cm<sup>-1</sup>. The sample was heated for 2 h at its vitrification temperature and afterwards quenched by pouring the melt on a stainless steel gutter. About half of each sample was milled for analysis. The samples are shown in **Figure 99** in the **Appendix**.

**Table 20** Overview of samples with waste loading, vitrification temperature and the amount of reducing agent added.

Sample	Frit	Waste loading (wt%)	Temperature (°C)	Si (wt%)
1.1	Ba rich	5	1200	-
1.2	Ba rich	5	1150	-
1.3	Ba rich	5	1100	-
1.4	Ba rich	5	1050	-
1.5	Ba rich	5	1000	-
1.6	Ba rich	5	950	-
2.1	reference glass	5	1200	-
2.2	reference glass	5	1100	-
3.1	Ba rich	5	1200	0.27
3.2	Ba rich	5	1200	0.54
4.1	Ba rich	10	950	-

## Results and Discussion

The samples are reviewed with regard to their homogeneity and volatilization losses by several microscopic, spectroscopic and analytic methods.

The absence of problematic water-soluble phase separations is a necessary prerequisite for the vitrification process and a criterion for quality assessment of the product. The samples, prepared as reported in the previous section, are investigated by XRD, Raman and SEM-EDX methods. XRD diffractograms do not show any crystalline reflexes for any of the investigated samples. Also samples with higher loading, low vitrification temperature or reducing conditions do not form any crystalline phases. Raman spectroscopy which is very sensitive to the formation of crystalline species does not show any narrow vibration bands characteristic for crystalline compounds. Nevertheless, a broader distribution of perrhenate species was observed in the Raman spectra. Their intensity decreases with increasing vitrification temperature which indicates an elevated Re loss with temperature. For a vitrification

temperature of 1200 °C the perrhenate band nearly vanishes. The same accounts for samples melted in reducing conditions. The perrhenate Re(VII) species is reduced to Re(IV) and/or metallic Re and therefore cannot be detected by Raman spectroscopy. As some small phase separations in the  $\mu\text{m}$  scale or Raman-inactive species can be invisible to Raman and especially XRD, the samples are also investigated by SEM-EDX microscopy. Only for one sample a phase separation is found. When the glass is melted with 0.54 wt% Si, metallic Re particles with 1-5  $\mu\text{m}$  form in the glass matrix. This minor heterogeneity should, however, not impair the performance of the waste glass product in a repository as the water-solubility of metallic Re is under repository reducing conditions very low.<sup>247</sup> In an “in-can melting” process a steel crucible would be used. It is possible that due to corrosion of the container additional Fe is introduced in the glass melt. As its solubility in borosilicate glasses is very high with 15-25 wt% no Fe phase separation is expected and also not observed in own experiments.<sup>245</sup>

Leaching experiments on the waste glasses need to be performed in order to allow for the assessment on the acceptability for disposal.

The chemical composition of the samples is analyzed by ICP-MS and ICP-OES after dissolution of samples glass powder. As expected significant deviations from the target composition are found for the volatile elements Re and Cs. **Figure 77** depicts their loss in the melted Ba rich and reference glass as function of the temperature. The measurements confirm the rising element loss with higher temperatures. The reasons therefore are most likely found in the increased vapor pressure and the enhanced element diffusion due to lower viscosity of the melt. The overall losses of Re and Cs in the Ba rich glass system are drastic. Whereas the Cs loss ranges from 61% to 80% the Re loss is 83% to 100%. Despite higher vitrification temperature the performance of the reference glass is even superior over the Ba rich glass. At 1200 °C the Cs loss accounts for 50% and the Re loss for 81%. It can be assumed that at the applied conditions the viscosity of the melt is a more important factor compared to the vapor pressure. From observation the viscosity of the Ba rich melt seemed to be at 950 °C even lower than the viscosity of the reference melt at 1200 °C.

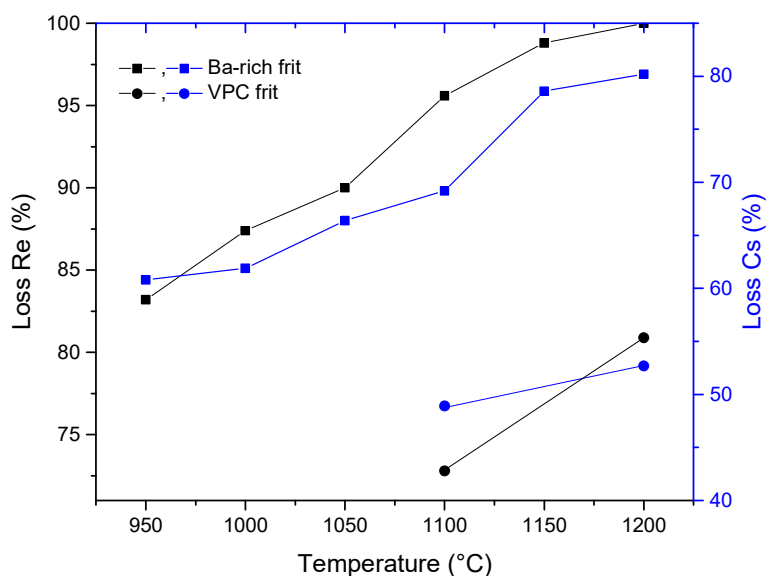


**Figure 77** Re and Cs loss for the Ba rich and reference glass samples synthesized at different vitrification temperatures. Whereas the Re loss is relates to the left y-axis the Cs loss is displayed at the right y-axis.

More Re can be retained in the glass matrix when it is reduced. At 1200 °C the addition of 0.27 wt% of elemental Si resulted in a Re retention of additional 3%, addition of 0.54 wt% of Si in an additional Re retention of 7%. The reduced loss of Re is a consequence of the lower vapor pressure of tetravalent and metallic Re compared to the perrhenate species. The rather low enhanced Re retention can have several reasons. As Re can be re-oxidized in the melt by air O<sub>2</sub> on the bath surface or by N from the nitrate salts which are reduced to NO<sub>x</sub> species the used amount of Si might not be sufficient. Also some of the Re might be already volatilized before a redox reaction with Si can occur. If this is the fact the efficiency of the reduction strategy would be decreased. Therefore, a very good mixture and small particle sizes of added components prior to melting are of great importance to establish a homogenous melt as fast as possible. By increasing the loading to 10 wt% the loss of Re and Cs raises from 83 to 91% and 61 to 67%.

In summary, it can be concluded that the discussed vitrification has the capability to be suited for immobilization with regard to the quality of the final glass product but in terms of Re and Cs volatilization the glass systems shows poor performance. Re and Cs loss of approximately 80% and 60% is not an acceptable solution for the immobilization of waste with volatile elements. Nevertheless, the use of reducing agent leads to enhanced Re retention. Further experiments are necessary to optimize the amount of reducing agent. As the reducing of perrhenate species has an advantageous effect on the Re retention it is possible to use this tool also in other glass systems for retention optimization. On basis of the performed experiments

the significant influence of the melt viscosity on the volatilization is indicated. More promising approaches might be done by reducing the vitrification temperature even more and to use glassy systems with higher viscosity at the processible temperature.

#### 6.2.4.2. Alternative approaches

As the Ba rich borosilicate glass discussed in the previous section did not emerge as suitable host matrix for the immobilization of the Tc and Cs rich waste a broader approach towards the immobilization of the waste was performed in which four potential host matrices are screened. They are shortly introduced in the following section. To address the volatilization loss of Re, samples with and without reducing agent were synthesized transforming Re(VII) in less volatile Re(IV) and/or Re(0) species (cf. also **Section 7**). The amount of reducing agent applied in the most reduced sample for each system was calculated taking into account the reduction of  $\text{NO}_3^-$  to NO, Fe(III) to Fe(II) and Re(VII) to Re(IV). The sample with half the reducing agent is half-stoichiometric to the redox reactions described above (cf. **a**, **b** and **c** in **Table 27**).

##### *Na rich borosilicate glass with addition of $\text{TiO}_2$*

Banerjee *et al.* studied the effect of  $\text{TiO}_2$  addition on the Cs volatilization from a borosilicate glass melted at 900 °C. The  $\text{TiO}_2$  was found to incorporate in the glass as a network former as well as a network modifier. It was suggested that  $\text{TiO}_2$  influences the Cs-O bonding nature and thereby increases the Cs retention. They optimized the  $\text{TiO}_2$  add-on to 5 wt% minimizing the Cs volatilization (loss: 4.2%). In addition this glass revealed a good leaching performance.<sup>248</sup> The optimized composition was used in the here presented study to vitrify the Cs and Re rich waste simulate adopting the vitrification conditions of Banerjee *et al.*

##### *Oxide ceramic $\text{CsAlTiO}_4$*

$\text{CsAlTiO}_4$  is a three-dimensional ordered macroporous ternary oxide whose structure is formed by tetrahedral  $\text{TiO}_4$  and  $\text{AlO}_4$  subunits.<sup>249</sup> It can be synthesized amongst other routes by simultaneously heating of  $\text{Cs}_2\text{CO}_3$ ,  $\text{TiO}_2$  and  $\text{Al}_2\text{O}_3$  for 5 h at 1000 °C without significant Cs loss. In the here presented study less  $\text{Cs}_2\text{CO}_3$  was added. As an additional Cs source the Cs from the waste simulate was used. Re is assumed to incorporate homogeneously as a  $\text{ReO}_4^-$ -tetrahedral subunit in the heated material.

### *Lead-tin fluorophosphate glass*

Whereas the most borosilicate glasses are obtained by melting the components to temperatures of more than 1000 °C, phosphate salt melts with a tailored composition can be melted at temperatures below 500 °C yielding a glassy material after quenching. A fluorophosphates glass with addition of Pb and Sn developed by Tick *et al.* can be processed at 450 °C.<sup>250, 251</sup> It is assumed that the vapor pressure of Cs and Tc/Re species is low at these temperatures (cf. **Table 42** in the **Appendix**). As a result the loss of Cs and Tc/Re might be significantly reduced compared to the previous experiments performed at 950-1200 °C melting temperatures.

### *Titanosilicate ETS-10*

The working group of Pavel *et al.* reported the loss-free immobilization of Cs in ETS-10 titanosilicate material. The Cs was incorporated into the ETS-10 structure by liquid ion exchange reaction prior to heating. Heating of the dried Cs loaded ETS-10 to 800 °C yielded a glassy composite material with homogenous Cs distribution.<sup>252</sup> This process was utilized for immobilization of the waste simulate. As the liquid ion exchange reaction might be difficult to realize for the genuine waste a second batch of samples was prepared. The solid ETS-10 matrix and the solid waste were sintered without liquid mixing and the volatilization loss reviewed.

In the following a summary of the investigation is presented. The study was performed within the first stage of the Master's thesis project of Aaron Beck supervised by S. Bahl. The aim of the study is to screen the Cs and Re retention performance of the different matrices. All samples were loaded with 5 wt% of waste simulate. In order to achieve reducing conditions suitable reducing agents were added (Si, Ti or Sn) following the general principle to introduce as few as possible additional elements in the system.

In the second stage of the Master project the most promising system will be selected and optimized with regard to the Cs and Tc/Re retention ability. In addition, the leaching performance of the immobilization product will be probed by a standard leaching test. These experiments will be completed in May 2017 and are not part of the here presented doctoral thesis of S. Bahl.

## Experimental

In the following section the synthesis of the materials is described. **Section 3** gives a general description of the applied characterization methods.

### Na rich borosilicate glass with addition of TiO<sub>2</sub>

The glass frit was synthesized by mixing 34.5 g SiO<sub>2</sub>, 26.7 g B<sub>2</sub>O<sub>3</sub>, 23.6 g Na<sub>2</sub>CO<sub>3</sub> and 5.09 g TiO<sub>2</sub> powders for ca. 15 min in a shake-mixer. The mixture was transferred into a platinum crucible, calcined at 800 °C for 1 hour and melted at 1200 °C for 2 hours. The molten glass was quenched by pouring it into a steel mold. To ensure homogeneity of the glass frit it was ground for 30 s in a vibrating cup mill and melted again at 1100 °C.

For waste immobilization the frit glass powder was mixed with simulated waste (cf. **Table 21**) in an agate mortar and transferred to an Al<sub>2</sub>O<sub>3</sub> crucible in which the mixture was heated to 900 °C for 2 h. Before pouring into a steel mold the melt was heated to 1000 °C for additional 15 min. Reducing conditions were obtained by adding Si powder to the vitrification feed mixture.

**Table 21** Amounts of starting materials used for immobilization of waste simulate in the Na rich borosilicate glass/TiO<sub>2</sub> glass system. **a**, **b** and **c** relate to the samples synthesized without reducing agent, half-stoichiometric and stoichiometric, respectively.

Material	a	b	c
glass frit	7.13 g	7.11 g	7.13 g
Si	-	45.5 mg	91.4 mg
waste simulate	680 mg	678 mg	680 mg

### Oxide ceramic CsAlTiO<sub>4</sub>

The waste simulate was immobilized in a CsAlTiO<sub>4</sub> matrix by mixing the components listed in **Table 22** in an agate mortar and for 15 min in a shake-mixer. The mixture was transferred to a Al<sub>2</sub>O<sub>3</sub> crucible and heated to 950 °C for 6 h. The solid material in the crucible was removed from the furnace and cooled at room temperature. By cutting with a low speed diamond saw (cooling agent: isopropanol) the material was separated from the Al<sub>2</sub>O<sub>3</sub> crucible. Reducing conditions were obtained by adding Ti powder to the starting materials. CsAlTiO<sub>4</sub> as suitable immobilization matrix for Cs and Tc rich solid waste was proposed by K. Popa from JRC-Karlsruhe.

**Table 22** Starting materials used for immobilization of the waste simulate in a CsAlTiO<sub>4</sub> matrix. **a**, **b** and **c** relate to the samples synthesized without reducing agent, half-stoichiometric and stoichiometric, respectively.

Material	a	b	c
Cs <sub>2</sub> CO <sub>3</sub>	4.23 g	4.23 g	4.23 g
TiO <sub>2</sub>	2.11 g	1.98 g	1.86 g
Al <sub>2</sub> O <sub>3</sub>	1.35 g	1.35 g	1.35 g
Ti	-	80.5 mg	156 mg
waste simulate	680 mg	679 mg	681 mg

### Lead-tin fluorophosphate glass

The waste simulate was immobilized in the ultra-low melting phosphate glass matrix by mixing the starting materials listed in **Table 23** in an agate mortar and for 15 min in a shake-mixer. The mixture was transferred to an Al<sub>2</sub>O<sub>3</sub> crucible and heated to 450 °C for 45 min. The solid material in the crucible was removed from the furnace and cooled at room temperature. By cutting with a low speed diamond saw (cooling agent: isopropanol) the material was separated from the Al<sub>2</sub>O<sub>3</sub> crucible. Reducing conditions were obtained by adding Sn powder to the starting materials.

**Table 23** Starting materials used for immobilization of the waste simulate in a fluorophosphates glass. **a**, **b** and **c** relate to the samples synthesized without reducing agent, half-stoichiometric and stoichiometric, respectively.

Material	a	b	c
PbF <sub>2</sub>	558 mg	558 mg	558 mg
SnF <sub>2</sub>	2.54 g	2.54 g	2.54 g
SnO	2.19 g	1.75 g	1.31 g
NH <sub>4</sub> H <sub>2</sub> PO <sub>4</sub>	2.99 g	2.99 g	2.99 g
Sn	-	384 mg	769 mg
waste simulate	681 mg	680 mg	680 mg

### Titanosilicate ETS-10

The immobilization of waste simulate in the ETS-10 matrix was performed by mixing the ETS-10 and the waste simulate listed in **Table 24** in an agate mortar and for 15 min in a shake-mixer. The ETS-10 material was provided by M. Ignat from Alexandru Ioan Cuza University in Iași, Romania. Samples **a**, **b** and **c** listed in the table were directly melted at 950 °C in an Al<sub>2</sub>O<sub>3</sub> crucible. Samples **a\***, **b\*** and **c\*** were preconditioned by transferring the mixture of the starting materials in a glass beaker adding 50 mL of deionized water and stirring for ca. 3 h. The suspension was left overnight without stirring. Heating the suspension to ca. 80-90 °C while stirring removed most of the water. Remaining moisture was removed in a drying furnace at 80 °C for three days. The solid material was then ground in a vibration mill for 30 s. The powder

was transferred to an Al<sub>2</sub>O<sub>3</sub> crucible and melted at 950 °C. By cutting with a low speed diamond saw (cooling agent: isopropanol) the materials from both sample series were separated from their crucibles. Reducing conditions were obtained by adding Si powder to the vitrification feed mixture before melting (cf. **Table 24**).

**Table 24** Starting materials used for immobilization of the waste simulate in the ETS-10 matrix. **a**, **b** and **c** relate to the samples synthesized without reducing agent, half-stoichiometric and stoichiometric, respectively. Sample **a\***, **b\*** and **c\*** were pre-conditioned for Cs ion exchange (Si was added after the pre-conditioning).

Material	a	b	c	a*	b*	c*
ETS-10	8.24 g	8.24 g	8.24 g	8.24 g	8.24 g	8.24 g
Si	-	45.5 mg	90.9 mg	-	45.6 mg	90.9 mg
waste simulate	680 mg	680 mg	680 mg	680 mg	680 mg	680 mg

\*starting materials were pre-conditioned with water

### Synchrotron-based X-ray fluorescence (XRF) measurements

Semi-quantitative X-ray fluorescence (XRF) analysis was performed at the INE-Beamline (cf. **Section 3**) for all heated sample materials. Pellets with a diameter of 4 mm and ca. 1 mm thickness were prepared by mixing sample powder (ground with agate mortar and pestle) with microcrystalline cellulose in a mass ratio of 2:1 and pressing with a hand press. The sample pellets were uniformly distributed on a 77 x 71 x 2 mm Plexiglass plate using self-adhesive polyimide Kapton tape. In addition to the prepared sample pellets, reference pellets were prepared for each system in order to quantify the Re and Cs content. Therefore, powder of the respective immobilization matrix was mixed with the solid waste simulate in a well defined ratio (cf. **Table 25**). From this mixture pellets were prepared according to the procedure describe above.

**Table 25** Amount of material used for XRF analysis.

	Respective glass frit (mg)	Cs <sub>2</sub> CO <sub>3</sub> (g)	Al <sub>2</sub> O <sub>3</sub> (g)	TiO <sub>2</sub> (g)	ETS-10 (mg)	waste simulate (mg)
Sodium borosilicate glass + TiO <sub>2</sub>	985	-	-	-	-	94.0
CsAlTiO <sub>4</sub> (oxide ceramic)	-	2.11	1.35	4.23	-	680
Tin fluorophosphate system	713	-	-	-	-	68.0
ETS-10 titanosilicate	-	-	-	-	824	68.0

For measurement the sample holder was placed on the goniometer at an angle of 45° with respect to the X-ray beam. The X-ray fluorescence was recorded with two silicon drift detectors in parallel (*Hitachi High-Technologies Science America*, 4-pixel Vortex ME4-multichannel system and the Vortex-60VX) perpendicular to the incident X-ray beam in a distance of about

85 mm. The incident beam was monochromatized by the DCM equipped with Si(111) and Ge(422) crystals for Cs (6.9 keV) and Re (10.6 keV) measurement, respectively. A toroidal mirror focused the beam to a spot size of approximately 500 x 300  $\mu\text{m}^2$  onto the sample. Its incident intensity was recorded using an Ar filled ionization chamber.

The obtained XRF data were analyzed by using the *PyMCA* software.<sup>94</sup> The Cs fluorescence was normalized to the Ti signal. In the phosphate glass system the Sn fluorescence signal was used instead. Re fluorescence intensities were quantified via the Re signal obtained from the prepared reference samples. It was assumed that there was no volatilization of Ti, Sn and Fe during the heating process.

The Re content for the Ti borosilicate glass and the ETS-10 system was additionally determined by ICP-OES. The findings were in agreement with the observed trend of the Re XRF analysis. For consistency reasons only the results obtained from XRF analysis are discussed.

## Results and Discussion

**Table 26** Systems used for waste simulate immobilization and their respective processing conditions.

System	Temperature	Reducing agent
Sodium borosilicate glass + TiO <sub>2</sub>	900 °C (2h)	Si
	1000 °C (15 min)	
CsAlTiO <sub>4</sub> (oxide ceramic)	950 °C (6 h)	Ti
Tin fluorophosphate system	450 °C (45 min)	Sn
ETS-10 titanosilicate	950 °C (2 h)	Si

An overview on the applied systems is depicted in **Table 26**. Cs volatilization was either addressed by significantly reduced heating temperature or by chemical retention. Re incorporation also profits from low-temperature processing but also from the addition of reducing agent which transforms highly volatile Re(VII) to its less volatile oxidation states (e.g., as Re(IV) and/or Re(0)). **Figure 78** depicts photographic images of selected synthesized samples.

The Ti borosilicate glass samples were glassy materials with homogenous appearance. The application of reducing agent transformed the yellow/brown glass which was obtained without a reducing agent into a nontransparent black glass.

The CsAlTiO<sub>4</sub> samples were porous ceramic material with predominantly greenish color. The surface of the samples revealed a brownish character.

The fluorophosphate samples were clearly heterogeneous black/grey composite materials. Residuals on the inner crucible wall indicated a significant bubbling of the melt while heated.

No difference was observed in the appearance of the ETS-10 samples with and without water pre-conditioning. All samples were obtained as nontransparent grey/black glassy materials with inclusion of bubbles. In these cavities and at the surface of the samples an isolated a water-soluble yellow phase was identified.

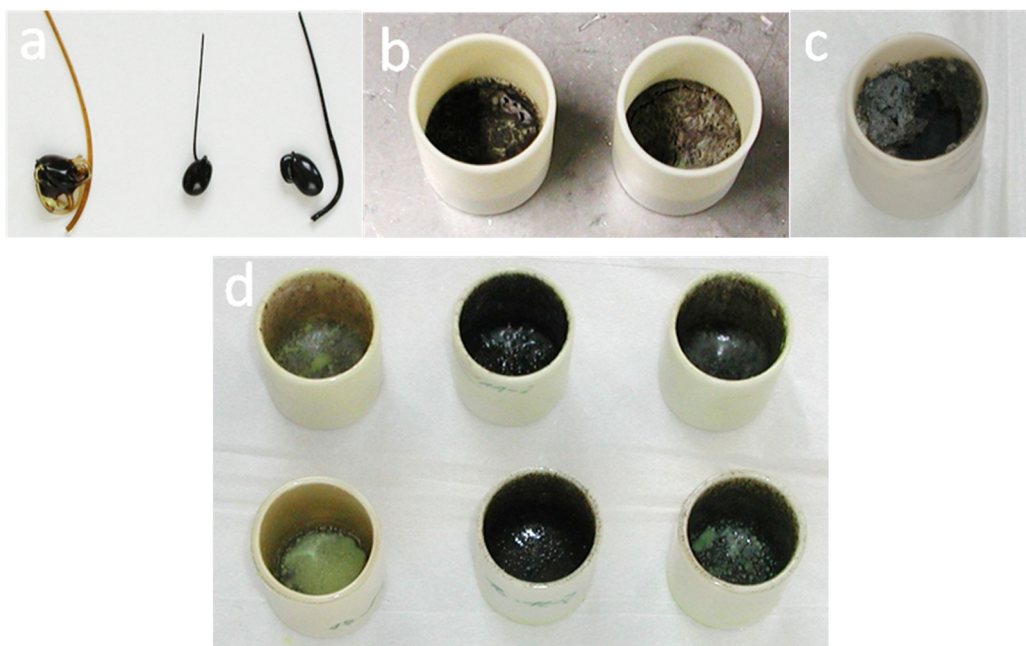


**Figure 78** Photographic images of the synthesized samples in different host matrices: a) TiO<sub>2</sub> borosilicate glass, b) CsAlTiO<sub>4</sub>, c) fluorophosphate glass, and d) ETS-10.

The Cs and Re content was determined by XRF spectroscopy by normalizing the emitted fluorescence intensity to the Fe signal of the respective sample. Fe is assumed to be a non-volatile element under the applied conditions. The obtained concentrations were compared to the target Cs and Re content and listed in [Table 27](#) as retention in percent for each studied system.

**Table 27** Volatilization and appearance characteristics of four immobilization matrices potentially suited for the immobilization of Tc and Cs rich waste. a) Samples synthesized without reducing agent, b) with half-stoichiometric amount of reducing agent, and c) with stoichiometric amount of reducing agent.

Matrix	Cs retention (%)			Re retention (%)			Appearance
	a	b	c	a	b	c	
TiO <sub>2</sub> borosilicate glass	45	41	43	19	17	16	Homogenous glass
CsAlTiO <sub>4</sub>	93	93	94	17	64	50	Homogenous ceramic
Fluorophosphates glass	122	82	130	123	104	103	Highly heterogeneous
ETS-10*	71 (69)	69 (67)	71 (64)	28 (14)	23 (14)	25 (15)	Glassy material, phase separation

\*Values in brackets relate to samples preconditioned in aqueous solution for Cs ion exchange.

The Ti in the borosilicate glass system which is assumed to have a retention effect on the Cs according to the literature showed rather poor performance. Heating at 900 °C for 2 h incorporated only ca. 40% of the Cs in the glass. This is comparable with the Cs loss observed for the waste simulate immobilization in the Ba rich borosilicate glass reported in the **Section 6.2.4.1**. Approximately 80% of the Re is volatilized within the heating process. As Re has a higher volatility than Cs, manifesting in lower melting and boiling points<sup>239, 253</sup> (see also **Table 42** in the **Appendix**), a lower retention is expected. Unexpectedly, no effect of the reducing agent on the Re volatilization was observed. Most likely the main fraction of the Re is already volatilized from the solid mixture before the required temperature is reached to melt the glass frit enabling redox reactions. Similar volatilization behavior is discussed in **Section 7**. Due to the high loss rates the Ti borosilicate glass system is not suitable for immobilization of the discussed waste form.

The CsAlTiO<sub>4</sub> was able to incorporate more than 90% of the total Cs inventory although the samples were heated for 6 h. It has to be noted that two sources of Cs were added to this system. The minority of the Cs (ca. 1.9%) originated from the waste simulate representing the radioactive Cs while most of the Cs (98.1%) was added as Cs<sub>2</sub>CO<sub>3</sub> for building-up the host matrix. Assuming that the total Cs loss of 10% is independent from its initial chemical form most of the “waste simulate Cs” was incorporated in the matrix and the “waste simulate Cs” loss is negligible (ca. 0.1%). This could be easily reviewed by repeating the experiment using radioactive marked Cs (e.g., Cs-137) in the waste simulate. By measuring the remaining activity of the CsAlTiO<sub>4</sub> product the retention of the waste Cs could be determined. The application of a reducing agent yielded an increased Re retention of 50-64% compared to ca. 17% when the solid mixture was heated without reducing agent. This confirmed the positive retention effect of a reducing agent on the Re retention. Considering the heating duration of 6h this is a reasonable performance. The fact that Re retention is not enhanced in the sample with

stoichiometric added reducing agent compared to the half-stoichiometric application indicates that some other effect might be also involved as consequence of the reducing agent addition (e.g., decreased bubbling or reduced viscosity of the melt). It is also possible that in the initial heating phase a fraction of Re is lost and the amount of reducing agent in the half-stoichiometric sample is sufficient to reduce all of the remaining Re. This would be in agreement with the Re retention of approximately 50%. Due to the revealed properties of the studied CsAlTiO<sub>4</sub> system it is recommended to continue with a more detailed study.

The Cs and the Re content of the phosphate glass system fluctuated drastically yielding an unrealistic Cs and Re retention of ca. 120% and 110%, respectively. The samples appeared heterogeneous. Due to the fact that the heating temperature of 450 °C is below the melting temperature of CsReO<sub>4</sub> of 620 °C (cf. **Table 42** in the **Appendix**) it can be assumed that most of the CsReO<sub>4</sub> did not incorporate in the matrix but rather was distributed heterogeneously within the samples. Pressed cellulose pellets were used for the XRF analysis. As only a fraction of the solid sample was ground to powder the analyzed specimen might not be representative for the averaged sample composition which could be an explanation for the analyzed Cs and Re concentrations above 100%. An additional source of Cs content uncertainty might be the XRF normalization method. For the phosphate glass the X-ray fluorescence was normalized to the Sn content whose fluorescence is absorbed significantly by the Ar content in the air. Therefore, small variations in the geometry of sample and detector had a considerable influence on the Cs determination in this system. Whether the remaining CsReO<sub>4</sub> material and the highly heterogeneous appearance of the samples have an effect on the immobilization performance of the material needs to be investigated.

The ETS-10 material showed an average Cs retention potential of ca. 70% independent of the aqueous preconditioning. The incorporation of the Cs in the ETS-10 network by ion exchange reaction as performed by Pavel *et al.*<sup>252</sup> did not yield an increased Cs retention. A poor Re retention of ca. 25% was achieved while the reducing agent did not have a positive effect similar to the Ti borosilicate glass system. The aqueous preconditioning had a negative impact on the Re retention (15%). The reason remains unknown. While the ETS-10 material might be a considerable immobilization system for Cs containing wastes it shows poor performance for Re immobilization.

One of the four investigated immobilization systems emerged as potential candidate for the immobilization of the in **Section 6.2** discussed waste. The CsAlTiO<sub>4</sub> host matrix incorporated up to 90% of Cs and 60% of Re notwithstanding the fact that the samples were heated for a relative long time of 6 h. Further optimization of the process could lead to higher retention

rates by lowering the heating time and/or temperature. Standard leaching test will provide a first estimation of the corrosion behavior of the material. A ceramic predominantly homogenous material was obtained which could potentially be suited for final disposal. The ETS-10 system might be a candidate for Cs immobilization by incorporating up to 70% Cs. But the reducing agent did not increase the Re retention which was found to be only 25%. Due to their poor retention rates and heterogeneous appearance both the Ti borosilicate and the phosphate glass systems are considered as inappropriate for immobilization of the Cs and Tc(Re) rich waste.

## **7. *In-situ* observation of noble metal particle (NMP) formation and their fate in a borosilicate melt**

FPs causing trouble in the vitrification of HLLW originating from SNF reprocessing can be grouped in two categories: Volatile and glass insoluble elements. Main representative of the first group are Cs and Tc. Both elements are radiologically of high importance as they account for a considerable share of the initial radioactivity of reprocessed waste. Cs and Tc exhibit high volatility under the high-temperature conditions of the vitrification process rendering their incorporation into the glass melt an essential challenge for this technology (see also **Section 6.2**).

The insoluble PGMs (Pd, Ru and Rh) are of less radiological relevance but play an important role in the processing behavior as they do not dissolve in the borosilicate glass melt and form immiscible particles, so-called noble metal particles (NMP). In a liquid-fed vitrification process these particles are primarily formed within the 2-5 cm thick reaction zone between the molten glass and the HLLW solution. This zone floating on the surface of the glass pool is called cold-cap and is described later in this section. The NMPs leave the lower part of the cold-cap and tend to sediment to the bottom of the melter forming sludge with high viscosity and increased electrical conductivity. This behavior can result in serious consequences for the vitrification process such as short circuits between the electrodes in a JHCM and plugging of the bottom drain.<sup>9</sup> Due to its great relevance the topic of NMP formation and management is widely discussed in several studies.<sup>8, 9, 254-256</sup> Nevertheless, no completely satisfying countermeasures could be presented yet.

The present study has the aim to contribute to the understanding of the behavior of the aforementioned troublesome elements on the vitrification process by *in-situ* application of an X-ray CT setup.<sup>7</sup> Thereby, 3D cross-section X-ray tomography images can be recorded and processed into a 3D model. The methodology is based on the average X-ray absorption reflecting the materials density and elemental composition. Glass frit and PGM doped HLLW simulate were adapted from the vitrification process of the Rokkasho vitrification plant in Japan.<sup>257</sup>

The formation mechanism of the NMPs was examined by reproducing the cold-cap vitrification conditions in which the NMP formation and precipitation was expected. The results were compared to existing hypotheses on the formation of the particles.<sup>8, 9</sup> Additionally, two approaches were studied aiming to suppress the formation of RuO<sub>2</sub> by adjustment of the vitrification parameters. RuO<sub>2</sub> is considered to have the most severe impact on the

sedimentation of NMPs. Therefore, waste glasses were synthesized using either reducing agents or glass frit powder (smaller than 500  $\mu\text{m}$ ). Krause and Luckscheiter predict a reduced  $\text{RuO}_2$  formation by application of these countermeasures.<sup>9</sup>

As the ongoing fate of the formed NMPs is of great importance to the technical process their sedimentation behavior was monitored *in-situ* by X-ray CT techniques. Two sedimentation hypotheses were reviewed: 1) The formation of felted NMP clusters in the melt and their subsequent sedimentation, as well as 2) The entrapment of convection-dragged particles on the bottom of the melter.<sup>258</sup> To track the particles movement it was necessary to develop a new melting furnace with reduced dimensions in order to increase the spatial resolution of the X-ray CT technique to the level of the NMP collectives.

In addition, the volatilization behavior of Cs and Re (as Tc surrogate) was monitored and the effect of the  $\text{RuO}_2$  countermeasures on the elements loss determined. From experience and literature it is known that decreased sample surface and the addition of a reducing agent can have a beneficial influence on the retention of volatile elements.

Briefly, the study was thematically divided into three stages:

- (1) Identification of the NMP formation in cold-cap mimicking conditions (section *NMP formation in a cold-cap*)
- (2) Evaluation of the effectiveness of countermeasures (reducing agents, size of glass particles) on the NMP formation (section *Countermeasures to the  $\text{RuO}_2$  formation*)
- (3) *In-situ* monitoring of the NMP fate in a convection driven circulating glass melt (section *In-situ monitoring of NMP sedimentation*)

As this is the first study of its kind the general applicability of the CT setup to questions arising from the vitrification of PGM-containing wastes is a valuable contribution to the scientific discussion of the characterization of NMP behavior in glass processing techniques.

#### *Properties of NMP and sedimentation mechanism*

HLLW originating from reprocessing of commercial SNF contains typically 2-6 g/L of the FP PGMs (Ru, Rh and Pd). A targeted waste loading of approximately 16 wt% yields a waste glass with ca. 1-3 wt% of PGMs. Their solubility in borosilicate glass melts is exceptional low (tens to thousands of ppm).<sup>259</sup> Therefore, they can be found as precipitated particles – predominantly  $\text{RuO}_2$  and Pd (alloyed with Rh and/or Te). In **Figure 79** a SEM micrograph of a NMP “collective” in which Pd particles are surrounded by  $\text{RuO}_2$  needles can be

seen. The NMPs tend to sediment in the glass melt to the bottom of the melter forming a viscous sludge which complicates their draining. Such behavior is the reason for the design of a new melter class with highly sloped bottoms angles (up to 60°) facilitating the drainage of PGM-containing glass melts.<sup>8, 33</sup>

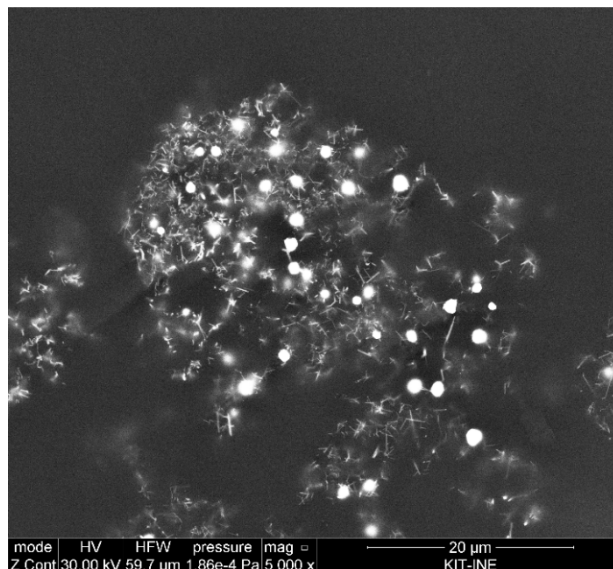


**Figure 79** SEM micrograph of a polished borosilicate glass (grey homogenous matrix) containing significant amounts of Pd (bright spherical particle of ca. 3 µm diameter) and RuO<sub>2</sub> (felted submicron needle particles).

The most severe impact on vitrification processes have needle-shaped RuO<sub>2</sub> particles.<sup>260</sup> RuO<sub>2</sub> forms a tetragonal rutil structure in which Ru is octahedrally coordinated by O atoms.<sup>261</sup> Whereas Pd or Pt particles exhibit excellent metallic electric conductivity, the conductivity of oxidic compounds is commonly lower by orders of magnitudes. Nevertheless, RuO<sub>2</sub> is an exception and is considered as ceramic material with metal-like electric conductivity.<sup>262</sup> This extraordinary behavior is attributed to a super-exchange of electrons between the Ru atoms via its dioxo-bridges. The electrical resistance of a glass melt containing 0.5-0.7 vol% RuO<sub>2</sub> was found to have an electric conductivity enhanced by several orders of magnitudes as demonstrated by Pflieger *et al.*<sup>263</sup> In combination with its tenacious settlement on the melter's bottom the increased electric conductivity leads to severe problems in a JHCM by reducing the effectiveness of the electric current heating. Even short-circuits are possible risking to damage parts of the melter installation.<sup>9</sup>

At vitrification conditions of up to 1200 °C RuO<sub>2</sub> is apparently the stable state in the glass melt.<sup>259</sup> At temperatures above 1200 °C the O<sub>2</sub> partial pressure of RuO<sub>2</sub> increases until its decomposition at 1580 °C.<sup>264</sup> The sedimentation mechanism of the NMPs is highly debated.<sup>9, 258, 265</sup> Calculations showed that applying the Stokes' law to Pd particles taking into account their shape, density and size distribution did not indicate any sedimentation behavior which is

in accordance to experimental findings. Subsequently, modelling of the settling behavior of the even smaller RuO<sub>2</sub> needles yielded sedimentation rates also negligible compared to the convection drag forces. Nevertheless, in industrial processes and laboratory based experiments drastically increased RuO<sub>2</sub> concentrations in the lower part of the glass melts are observed. The low viscosity of the formed RuO<sub>2</sub> sludge leads to the entrapment of Pd particles which finally enrich also on the bottom of the melter. Schill *et al.*<sup>258</sup> proposed a hypothesis of an interaction of the RuO<sub>2</sub> with the melter tank surface: The RuO<sub>2</sub> particles dragged horizontally above the bottom of the melter might be halted by obstacles on the floor such as roughness of the refractory or already deposited agglomerates when they enter a certain entrapment height. However, experimental evidence confirming the proposed mechanisms could not be found yet.

The research group of Kelm *et al.*<sup>266</sup> proposed a sedimentation hypothesis involving the felting of the RuO<sub>2</sub> particles in the 1990s. According to their experience RuO<sub>2</sub> needles agglomerate forming large compacts in which the incorporated glass melt serves as bonding agent. These stable compacts can build up to several hundred µm. Their density is decreased compared to pure Pd or RuO<sub>2</sub> but due to their large apparent particle size the sedimentation rate can be significantly enhanced.

#### *Description of cold-cap*

Closer attention has to be paid to the cold-cap which is the expected location of the NMP formation. The cold-cap (or sometimes called “batch blanket”) indicates a layer of melter feed floating on a pool of molten glass in an electrical glass-melting furnace.<sup>267</sup> In the one-stage vitrification process for nuclear waste (cf. **Section 2.1.2.3**) the melter feed typically consists of a HNO<sub>3</sub> slurry containing ca. 40-60% of water. In dependence of the liquid waste and glass frit feed rate the cold-cap can cover nearly the entire glass melt surface. An extensive coverage has a beneficial effect on the retention of volatile elements as the cap can reduce their volatilization by trapping them with its lower temperature. In the different layers numerous complex chemical reactions and physical processes take place. **Figure 80** illustrates a schematic model of a cold-cap fed by HLLW and glass beads. Due to the cold liquid waste on the top and the hot glass melt on the bottom of the cold-cap a strong temperature gradient in the cap is established determining its structuring. In the liquid evaporation layer water is transferred to the gas phase of the melter’s plenum. It is removed by the exhaust system. The remaining precipitated nitrate salts are calcined in the calcination layer from 100 °C on decomposing the salts to their respective oxidic compounds. The calcination is accompanied by strong NO<sub>x</sub> gas formation. At around 500-600 °C the glass beads soften and glass chemical reactions with the calcined HLLW

are initiated. This temperature region is called transformation layer. In a last step the waste components dissolve in the molten glass before convection forces distribute them in the entire pool. NMPs are here transported from the cold-cap into the molten glass.

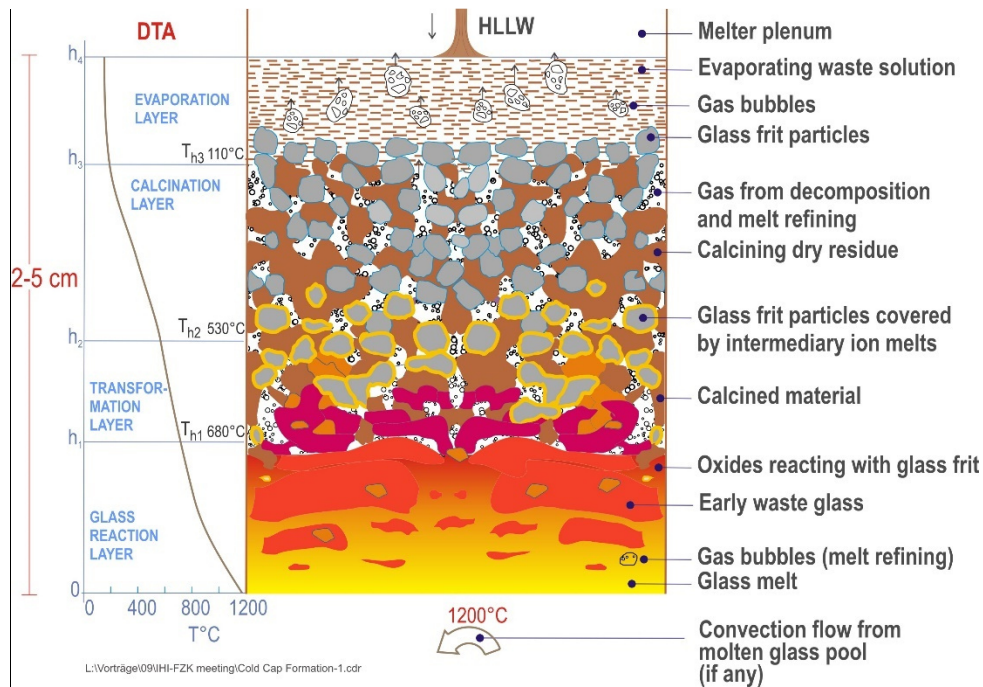


**Figure 80** Schematic illustration of a liquid fed cold-cap structuring. Its composition is related to the temperature gradient. (Reproduced with permission from Ref. <sup>268</sup>)

## 7.1. Experimental

### Methods and Materials

#### *Glass frit*

The composition of the glass used in this study was adapted from a glass which is used in the vitrification plant Rokkasho, Japan.<sup>257</sup> Its complete composition is not yet published. The glass frit contains about 60 wt% SiO<sub>2</sub> and 18.2 wt% B<sub>2</sub>O<sub>3</sub>. 21.8 wt% are composed by Na<sub>2</sub>O, Li<sub>2</sub>O, CaO, Al<sub>2</sub>O<sub>3</sub>, ZnO. The glass beads size distribution is given in **Table 46** in the **Appendix**.

Glass powder was obtained by milling of glass beads. Therefore, the glass beads were fused in an Al<sub>2</sub>O<sub>3</sub> crucible for 1 h at 600 °C. The glass block was quenched by pouring cold water on it before dried in a drying furnace at 90 °C for 10 min. The milling was performed first in an automatic mortar mill and final hand milling with mortar and pestle. A powder of 10 µm particle sizes was obtained by glass sieving.

### HLLW simulate

The commercially prepared HLLW simulate solution mimics the HLLW composition which is vitrified in the Rokkasho vitrification plant (cf. **Table 28**). Its quantitative composition will be published by JNFL in the future. Radioactive components of the genuine HLLW were replaced by inactive isotopes in the simulate solution on a mole-by-mole basis. Tc was surrogated by Mn while the *An* were replaced by *Ln*. The prepared HLLW simulate had significant amounts of fine dispersed deposits. Before using these undissolved solids were suspended (cf. **Figure 100** in the **Appendix**).

Re was additionally added to the HLLW simulate used for review of the RuO<sub>2</sub> formation countermeasures and their effect on Re/Tc volatilization. Therefore, 40 mg of Re powder were dissolved under strong NO<sub>x</sub> generation in 0.5 mL of HNO<sub>3</sub> (conc.). The yellow clear solution was mixed with 44.59 mL HLLW simulate solution.

**Table 28** Qualitative composition of the commercially prepared HLLW simulate solution.

<b>Compounds</b>	
Na <sub>2</sub> O	Rh <sub>2</sub> O <sub>3</sub>
P <sub>2</sub> O <sub>5</sub>	PdO
K <sub>2</sub> O	Ag <sub>2</sub> O
Cr <sub>2</sub> O <sub>3</sub>	ZnO
Fe <sub>2</sub> O <sub>3</sub>	TeO <sub>2</sub>
NiO	Cs <sub>2</sub> O
CoO	BaO
SrO	La <sub>2</sub> O <sub>3</sub>
Y <sub>2</sub> O <sub>3</sub>	Ce <sub>2</sub> O <sub>3</sub>
ZrO <sub>2</sub>	Pr <sub>2</sub> O <sub>3</sub>
MoO <sub>3</sub>	Nd <sub>2</sub> O <sub>3</sub>
MnO	Sm <sub>2</sub> O <sub>3</sub>
RuO <sub>2</sub>	Gd <sub>2</sub> O <sub>3</sub>

### Preparation of solid HLLW simulate mixed with glass frit

For vitrification the simulated HLLW solution was mixed with the glass beads/powder in the ratio 89.18 mL solution to 30 g of glass which relates to a waste oxide loading of 22 wt% in the glass product. The mix was transferred to a Teflon container and placed on a sand bath with temperature of ca. 120 °C. When most of the water was evaporated and a crust started to form on the surface the sand bath was dimmed to 90 °C. Occasional agitating was necessary in order to remove the solid crust which prevented the evaporation of the remaining water. The mixture was solidified within 6-10 h. The precipitated HLLW simulate compounds were mainly sticking to the surface of the glass beads (cf. [Figure 81](#)).



**Figure 81** Preparation of the dried HLLW simulate with glass beads. The mix was heated on a sand bath.

### X-ray CT setup and furnace

The X-ray CT furnace was designed and constructed by the research group of Yano *et al.* and the setup is described by Watanabe *et al.*<sup>7</sup> [Figure 82](#) illustrates the functionality of X-ray CT installation. The electrons of the X-ray tube were accelerated with 160-200 kV and a current of 90-200 mA is generated. The distance from X-ray source to sample (SOD) and from X-ray source to detector (SID) determined the magnification and resolution of the recorded CT data. For the vitrification process recorded with the CT setup the SOD was set to 180 mm and SID to 600 mm.

The resolution of all X-ray CT measurements was set to 1024 x 1024 pixels while the samples were turned either 360 degrees (CT of vitrification process) or 180 degrees (*in-situ* monitoring

of the NMP sedimentation). The measurements were performed mainly twice for every sample recording 600 or 1200 slices per sample.

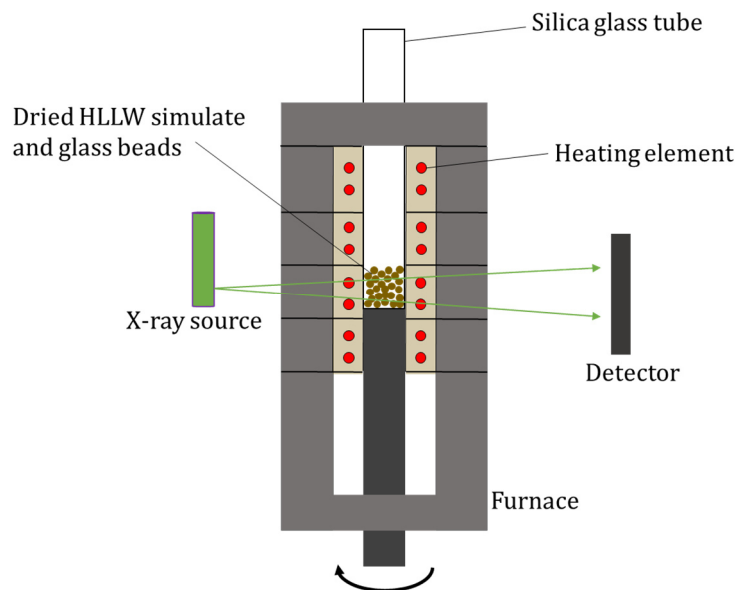


**Figure 82** Schematic illustrations of high-temperature furnace and X-ray CT setup. The sample stage can be turned for the CT measurement. The distance between the X-ray source, the sample and the detector can be varied in order to define magnification and spatial resolution.

The standard furnace used to observe the vitrification process was equipped with five independent heating circuits coupled with thermocouples for temperature monitoring. The samples were positioned in heating zone 3. For calibration of the furnace the temperature in the empty silica tube serving as crucible was measured and compared to the set temperature within the commissioning of the setup (cf. [Table 29](#)).<sup>7</sup> These data were used for temperature correction. Samples in the furnace were ramped with 11.5 K/min (heating and cooling) corresponding to a heating rate after correction of ca. 10 K/min. The temperature profiles of heating zone 3, the set temperature and the temperature of the silica tube are displayed in [Figure 101](#) in the **Appendix**).

The small furnace was uniformly heated by several heating circuits to the set temperature. No calibration data are available. Due to its reduced dimensions it is assumed that the set temperature correlated closely to the sample temperature. The maximum temperature of 1000 °C was reached by heating with 10K/min.

**Table 29** Calibration data of the standard X-ray CT furnace.

<b>Time (min)</b>	<b>Set temperature (°C)</b>	<b>Temperature in silica tube (°C)</b>
0	0	22
10	115	158
20	230	292
30	345	417
40	460	529
50	575	635
60	690	738
70	805	838
80	920	937
90	1035	1032
100	1150	1052

#### X-ray CT software

For processing of the X-ray CT data the software *VG studio max* version 2.2 was used. It was used to generate the X-ray CT 3D model of a glass fragment depicted in **Figure 84**.

#### Scanning electron microscope (SEM) and energy-dispersive X-ray spectroscopy (EDX)

A *JEOL JCM-6000* electron microscope was used for fast scanning of the samples in high-vacuum and ESEM mode. High resolution electron microscopic images were recorded using the electron microscope and EDX detector described in **Section 3**.

#### X-ray powder diffraction (XRD)

X-ray powder diffractograms were recorded with a *Bruker Advance D8* diffractometer using Cu-K $\alpha$ -radiation ( $\lambda = 0.15406$  nm) and Bragg-Brentano ( $\theta$ - $2\theta$ )-geometry (U = 35 kV, I = 300 mA). At room temperature the angle range from  $2\theta = 20$ - $60^\circ$  with a step size of  $0.023^\circ$  was measured. Diffractograms of the **ISV** samples were recorded with same integration time. Reflexes were identified by comparison with the *International Centre for Diffraction Data* (ICDD) database.<sup>269</sup> Integration of the diffraction signals was performed with the *Origin* software before the diffractograms were background corrected.<sup>95</sup> The Pd reflexes were integrated from  $39.7$ - $40.6^\circ$  whereas the RuO<sub>2</sub> reflexes between  $27.9$ - $28.4^\circ$  and  $35.0$ - $35.6^\circ$  were used for integration. Background correction and slight smoothing of the spectra was performed with the *EVA* software (*Bruker*).

#### Micro X-ray fluorescence spectroscopy ( $\mu$ -XRF)

Elemental distribution maps were recorded with a *Bruker M4 Tornado*  $\mu$ -XRF spectrometer. The X-ray source operated with 50 kV at a tube current of 600  $\mu$ A. The samples were evacuated to 20 mbar and the X-rays detected by a *XFlash* silicon drift detector with an energy resolution of less than 145 eV. The scanning step size was set to either 12 or 25  $\mu$ m and scanned in one or two cycles and from 2.2–30 s integration time per point.

#### Inductively coupled plasma optical emission spectroscopy (ICP-OES)

Elemental analysis was performed by digesting approximately 800 mg of the glass samples and determination of the Mo, Si, B, P, Mn and Re concentration. All measurements were performed as duplicates and the average value was used for evaluation. All concentrations were normalized to an average SiO<sub>2</sub> concentration of 50.71% (Raw data: **ISV-ox** 51.18%, **ISV-powder** 49.29% and **ISV-red** 51.65%). The analyses were performed with an *Optima 8300* optical emission spectrometer.

## **Experiments**

#### NMP formation in transformation and glass reaction layer of a cold-cap

For each sample 44.59 mL HLLW simulate were dried mixed with 15 g glass beads according to the procedure described in the previous section. The material was transferred to a small Al<sub>2</sub>O<sub>3</sub> crucible and placed at room temperature into a high-temperature furnace and heated with 5 K/min to the desired temperature which was maintained for 2 h. To avoid contamination of the furnace chamber by splashing the small crucible was placed into a bigger Al<sub>2</sub>O<sub>3</sub> crucible and covered with an Al<sub>2</sub>O<sub>3</sub> cap (cf. **Figure 102** in the **Appendix**). Afterwards the crucible was removed from the furnace and quenched in air being covered by a bigger graphite crucible. The synthesized samples **B500-B1200** are shown in **Figure 83**. They are labeled according to their maximum vitrification temperature: **B500**: 500 °C, **B600**: 600 °C, **B700**: 700 °C, **B800**: 800 °C **B900**: 900 °C, **B1000**: 1000 °C, **B1200**: 1200 °C.

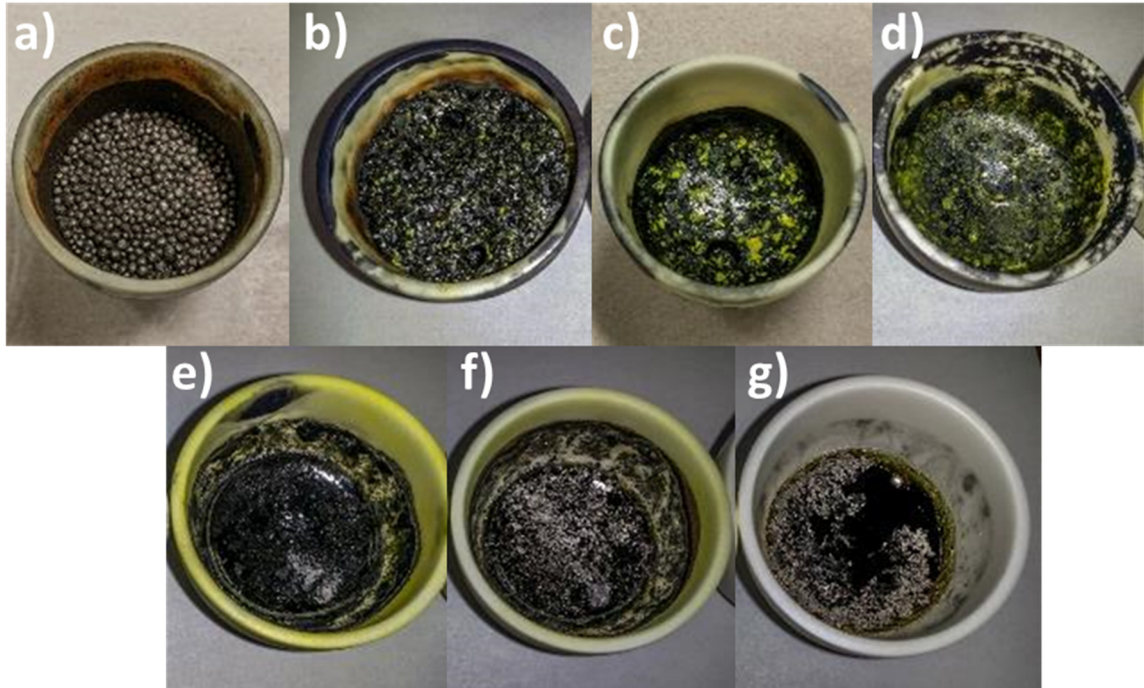


**Figure 83** Synthesized glass samples from 500-1200 °C: a) **B500**, b) **B600**, c) **B700**, d) **B800**, e) **B900**, f) **B1000**, g) **B1200**.

For analysis the glass samples were cut with a water-cooled buzz saw and ground on a disc turning table with sandpaper (grain size 400 and 1500). Polishing of the glass surface was done with 9 µm and 3 µm water based diamond paste. In-between the grinding and polishing steps the specimens were cleaned in ultrasonic bath with deionized water for 5 min respectively. Polished samples of **B600** and **B800-B1200** are shown in **Figure 103** in the **Appendix**.

#### Countermeasures to the RuO<sub>2</sub> formation

For vitrification in the CT furnace Re doped simulated HLLW solution was used to synthesize the mixture of solid HLLW simulate and glass beads or powder (10 µm particle size). Ca. 17 g of this mixture were used in each experiment. For the application of reducing conditions 1 wt% of Si powder (ca. 0.17 g) was added to the mixture prior heating. The furnace was ramped with 10 K/min to the set temperature of 1200 °C which was maintained for 2 h. According to the calibration curve of the furnace the sample reached a maximum temperature of 1050–1100 °C instead of 1200 °C (cf. **Table 29** and **Figure 101** in the **Appendix**). Cooling of the sample was performed with 10 K/min to ca. 400-600 °C. Hereupon the silica tube was removed from the furnace and cooled in air where the tube and the containing melted glass cracked after a few seconds. Within the heating and cooling process X-ray CT pictures were recorded every 2, 5 or 10 min. Photographic pictures of the upper part of the silica tube were taken every 15 s with a *Nikon D5300 camera*\* (18-55 mm VR II objective with polarization filter). For evaluation both X-ray CT and camera images were processed to time lapse videos with 25 fps.

### *In-situ monitoring of NMP sedimentation*

These experiments were performed in a furnace with reduced dimensions in order to decrease the SOD to 100 mm (SID = 1000 mm) for optimized resolution. The glass product **B1200** was used for NMP movement monitoring. Therefore, ca. 0.59 g of the glass was filled in a small silica glass tube with inner diameter of approximately 6.8 mm in form of powder (less than 500  $\mu\text{m}$ ) or glass fragments. The sample was heated with 10 K/min to 1000 °C and kept at this temperature for some time. Every 2 min an X-ray CT measurement was performed. The recording of a measurement took ca. 30 s.

## 7.2. Results

### *NMP formation in a cold-cap*

In order to mimic the conditions of the lower part of a cold-cap (cf. **Figure 80**) glass samples were synthesized at vitrification temperatures from 500-1200 °C. To simulate the drying process which the HLLW undergoes before reaching the calcination layer the HLLW simulate was dried in the presence of glass frit beads to whose surface most of the dried HLLW simulate was attached. The melting process is described in **Section 7.1**. **Figure 83** and **Figure 103** in the **Appendix** depict photographs of the synthesized samples. Heating up to 500 °C lead to the calcination of the dried HLLW simulate but did not melt the glass beads. The obtained material was brittle and disintegrated while sawing. In **B600** the glass beads were just melted incorporating the waste components. The sample revealed large cavities (cf. **Figure 103** in the **Appendix**). From 700-1200 °C glassy materials with dense amorphous appearance were obtained.

X-ray CT measurement of the solid samples revealed a heterogeneous X-ray absorption pattern which can be attributed to differences in the density and/or elemental distribution of the samples. Due to the quenched solid state of the specimens high-quality X-ray CT scans were performed (recording time: ca. 1 h) and processed generating 3D models illustrating the spatial X-ray absorption. **Figure 84** left shows exemplary the 3D CT model of **B1200**. Increased concentrations of heavier elements were found at the bottom, the surface and in certain areas within the solidified melt. 3D evaluation revealed pronounced “channels” of heavier elements crossing the glass. On contrary, some areas of the glass were free of heavier elements.  $\mu$ -XRF investigation identified areas with increased X-ray absorption which is assigned to the presence of significant amounts of Ru and Pd while other waste elements were homogeneously distributed in the **B1200** glass sample (cf. **Figure 84**, middle). The Al concentration fluctuated

continuously within a small range in the samples. Areas with increased PGM concentration were also possible to distinguish by careful optical observation in agreement with results from CT and  $\mu$ -XRF (cf. **Figure 84**, right). Similar results were obtained for **B1000**. Minor heterogeneity of additional waste elements (Ce, Cr and Nd) appear for the **B900**, whereas all waste components were heterogeneously distributed in **B800** and **B600** samples.

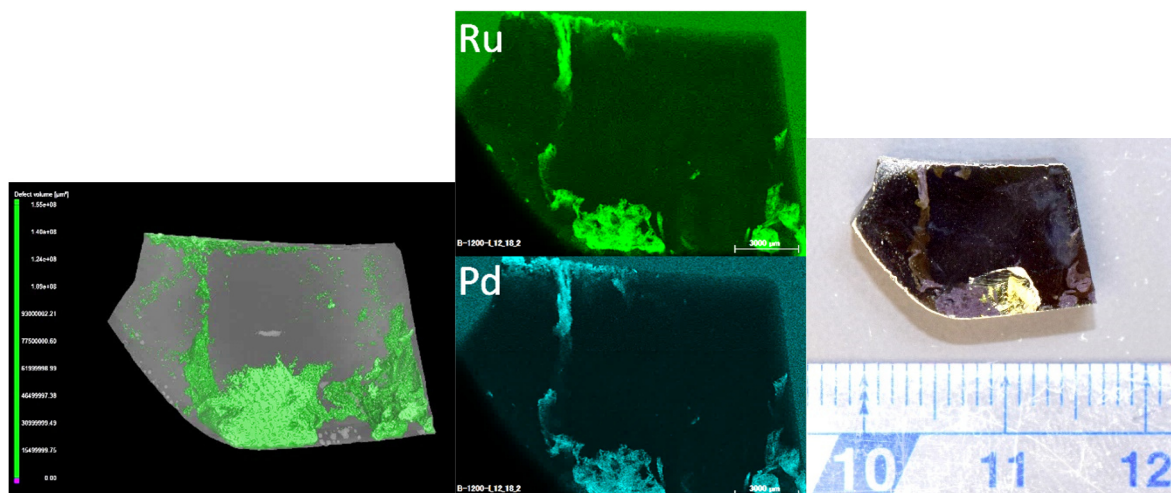


**Figure 84** X-ray CT measurement of a **B1200** specimen (left). Green areas indicate areas with high X-ray absorption. This can be due to higher material density and/or the presence of heavier elements.  $\mu$ -XRF mapping of Ru and Pd of **B1200** specimen (middle). Brighter areas indicate high concentration of Re/Pd. Photograph of a **B1200** specimen (right). The units of the scale are in cm.

Five main species ( $\text{RuO}_2$  needles, Ru big particle, Pd particle, Ce particles, Nd particles) were identified by SEM-EDX investigations (cf. **Figure 85**). The results are in good agreement with the findings of the  $\mu$ -XRF investigations and are summarized in **Table 30**. In **B600** and **B700** big Ca-molybdate crystals with 200  $\mu\text{m}$  size are identified too (not shown). The  $\text{RuO}_2$  needles appear in all samples as felted collectives while other areas of the samples are entirely free of  $\text{RuO}_2$ . Spherical Pd particles are predominantly embedded in  $\text{RuO}_2$  collectives. For **B700** only small number of Pd particles is detected. Large Ru particles with more than 10  $\mu\text{m}$  diameter exhibit a spinose structure while growing from a big bulky part. They are found in all samples except **B1200** and **B700**. As the prepared surface of **B700** is very small it is assumed that the particles are also present in this sample but are not detected by SEM. To check whether the formation of these particles can be attributed to the slow cooling rate (10 K/min) a glass sample was synthesized under the same conditions and at 800  $^\circ\text{C}$  but quenched by pouring its glass melt on a stainless steel plate which cooled the melt within several seconds to room temperature. In the quenched glass sample no large Ru particles are found by electron microscopy. However, the presence of large Ru particles in areas other than investigated cannot be completely excluded.

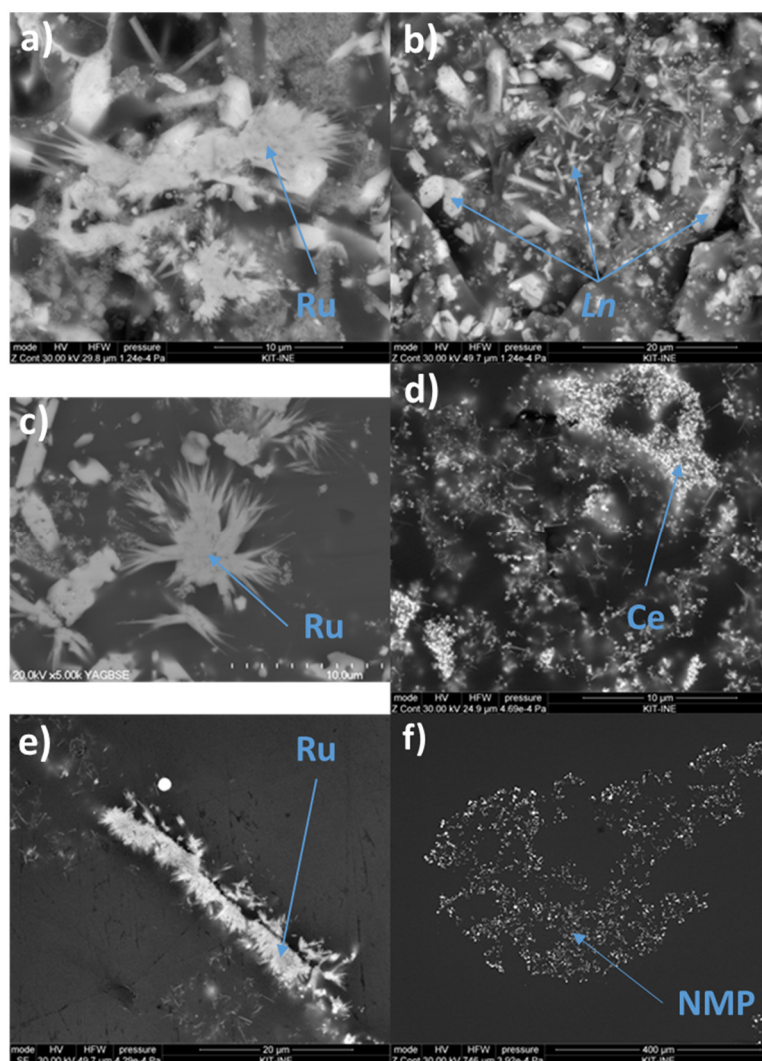


**Figure 85** Backscattered electron micrographs of a polished glass sample a) **B600**, b) **B700**, c) **B800**, d) **B900**, e) **B1000**, f) **B1200**.

**Table 30** Results of SEM-EDX investigations. The secondary and backscattered electron signals in combination with EDX results help to identify five main species in the glass samples **B600-B1200**. **B600** and **B700** contain minor amounts of  $\text{RuO}_2$  and Pd particles, respectively, which is shown with brackets in the table.

	<b><math>\text{RuO}_2</math> needles</b>	<b>Ru big particle</b>	<b>Pd particles</b>	<b>Ce particles</b>	<b>Nd particles</b>
500 °C*	n.a.	n.a.	n.a.	n.a.	n.a.
600 °C	(✓)	✓		✓	✓
700 °C	✓	□†	(✓)	✓	✓
800 °C	✓	✓	✓	✓	✓
900 °C	✓	✓	✓	✓	✓
1000 °C	✓	✓	✓		
1200 °C	✓		✓		

\*preparation of applicable SEM sample was not possible

†particles were not found in the prepared sample but their existence is likely

XRD analyses were performed with samples **B500-B1200**. As an unprocessed reference material dried HLLW simulate mixed with glass powder was also measured (cf. **Figure 86**).

The diffraction patterns are compared to data from a crystal structure database. RuO<sub>2</sub> is clearly identified for **B700-B1200**. For **B600** only weak reflexes are observed. These results are in accordance with results from SEM and  $\mu$ -XRF analyses. The intensities of the RuO<sub>2</sub> reflexes increase from **B600** to **B1000**. Sample **B1200** shows similar RuO<sub>2</sub> intensity as **B900**. **B500** does not reveal RuO<sub>2</sub> typical reflexes. Metallic Pd is clearly identified in **B800-B1000**. The XRD pattern for **B1200** does not exhibit a pronounced Pd signal whereas SEM-EDX analyses illustrate large amounts of micrometer-sized Pd particles (cf. [Figure 85](#)). Vitrification temperatures of 600 °C and 700 °C lead to the significant contribution of Ln-silicates and/or Ln-oxides in the glass samples; those are identified mainly as Ce and Nd phases by SEM-EDX. In accordance with its decomposition temperature of 600-700 °C NaNO<sub>3</sub> is still present in **B500** in addition to several Ru and Mo salts.<sup>270</sup> Broad silicate reflexes visible in the non-heated mixture vanish after heating to 500 °C.

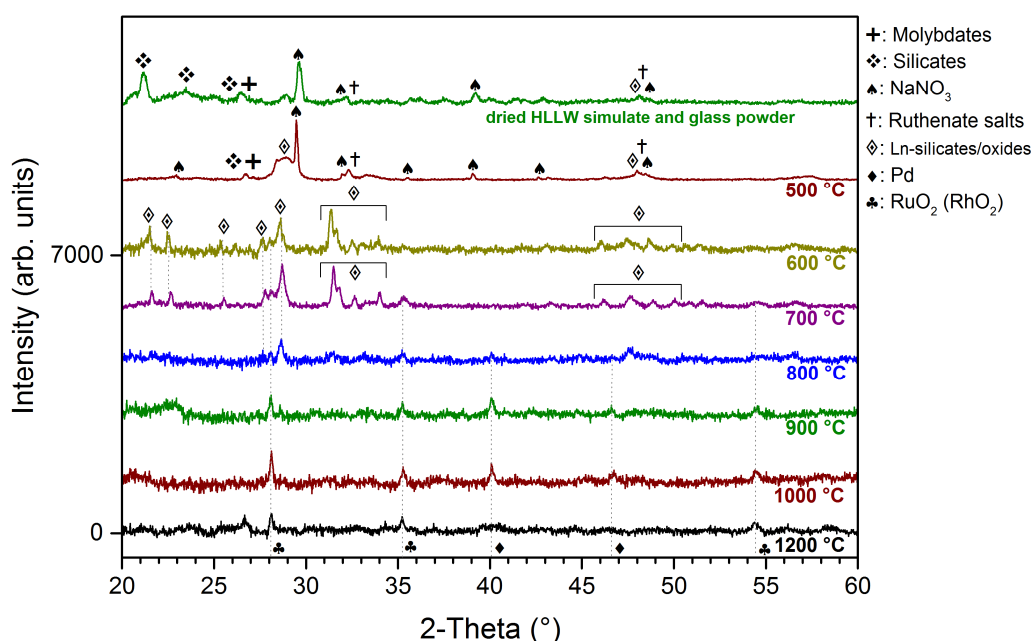


**Figure 86** Powder XRD pattern of glass samples **B500-B1200** in addition to an unprocessed reference material of dried HLLW simulate mixed with glass powder.

#### *Countermeasures to the RuO<sub>2</sub> formation*

In order to evaluate the countermeasures for formation of RuO<sub>2</sub> particles proposed by Krause and Luckscheiter three experiments were performed: 1) Melting of Re containing dried HLLW simulate with glass beads, 2) Melting of Re containing dried HLLW simulate with sieved glass powder (particle size less than 10  $\mu$ m), 3) Melting of Re containing dried HLLW simulate with glass beads and addition of 1 wt% metallic Si (cf. [Section 7.1](#)). The experiments are denoted by **ISV-ox**(idizing), **ISV-powder** and **ISV-red**(ucing) according to the applied conditions. All

samples were heated to a target temperature of 1200 °C for 2 h. The set temperature, the temperature of the heating zone and the sample temperature differ according to the calibration data (cf. [Table 29](#)). The temperature profiles are plotted in [Figure 101](#) in the **Appendix**. The sample temperature is extrapolated from calibration measurement of an empty silica tube. Due to phase transitions and chemical reactions the temperature in the sample might be a bit lower than indicated.

The CT data suggests two main transformation processes illustrated exemplarily in [Figure 87](#) for **ISV-ox**. In contrast to the 3D model analysis presented in [Figure 84](#) only cross-section measurements were possible for *in-situ* investigations. High-quality data required for 3D CT processing were in need of several minutes/hours recording time.

At ca. 370 °C the dried HLLW simulate and the glass beads rearrange and compact while the glass beads stay in shape. At approximately 740 °C a massive bubbling is initiated. Within this transformation the glass beads melt and the waste components are dissolved. From ca. 940 °C on a melt with minor bubble formation remains. At temperatures from 1050 °C on a dense homogenous glass melt is observed by the CT. It is possible to correlate the discussed phenomena to observations of exhaust gas formation (cf. [Figure 88](#)). At ca. 200 °C remaining water, most likely crystallization water, leaves the sample and steam up at the upper glass tube wall. Afterwards, two major stages of NO<sub>x</sub> release are observed. The first stage starts at ca. 300 °C producing significant amounts of the gas, the second stage is initiated at approximately 640 °C generating less NO<sub>x</sub>. Above 1000 °C no gas formation is detected.

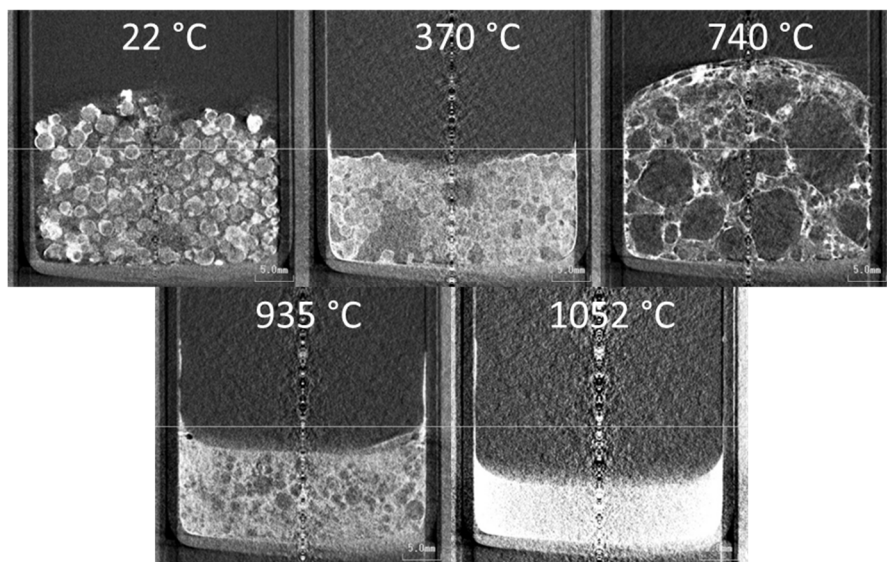


**Figure 87** CT cross-sections of experiment **ISV-ox**. The pictures represent the whole sample volume melted in a silica tube.

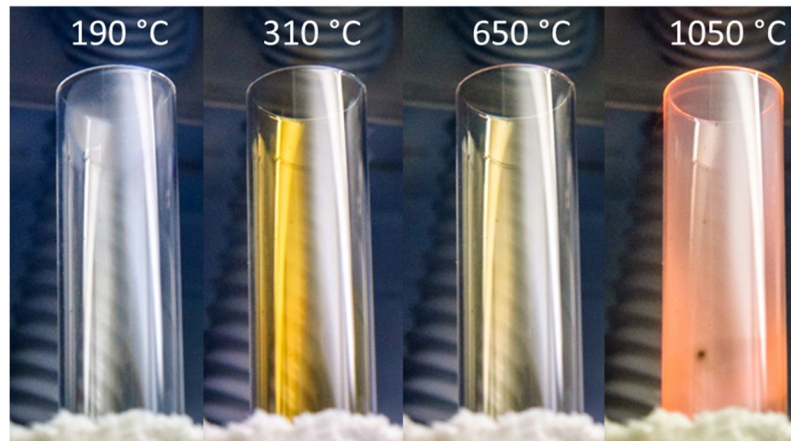


**Figure 88** Photographic observation of the exhaust gas formation in the upper silica tube end of **ISV-ox**. Yellow-brown colouring indicates the formation of  $\text{NO}_x$  gasses. In the first photograph a steaming of the upper glass wall can be observed.

**Figure 104–Figure 107** in the **Appendix** depict the CT cross-sections and the photographs for **ISV-powder** and **ISV-red**. The compaction of the dried waste simulate mixed with the glass powder is found to appear at an elevated temperature of 570 °C. The material symmetrically shrinks together building a sintered body before it suddenly liquidates. Between **ISV-ox** and **ISV-red** no differences are observed by CT and photographic analysis.

SEM-EDX analysis of the samples report an amorphous glass with numerous inclusions of Pd and  $\text{RuO}_2$  particles similar to the samples from the previous experiments melted at higher than 1000 °C.  $\text{RuO}_2$  needles are found for all **ISV** samples with comparable size distributions. Spherical Pd particles with typical 1-2  $\mu\text{m}$  diameter are always associated with a collective of  $\text{RuO}_2$  needles. Some of the Pd particles from **ISV-red** have a larger diameter of approximately 5  $\mu\text{m}$  (cf. **Figure 108** in the **Appendix**). A peculiar structure is found for the **ISV-powder**. It is best described as a spinous, sometimes closed agglomerate of small crystals with predominant formation direction and a typical size of 10-40  $\mu\text{m}$ . Two examples are shown in **Figure 89**. According to SEM-EDX this collective exclusively consists of Ru (~30 at%) and O (~46 at%). This leads to the conclusion that these agglomerates are similar to the large Ru particles which are identified in **B600-B1000** (cf. **Figure 85**). The formation of these isolated phases seem to be correlated to the presence of Pd particles which often reside inside but are not necessarily directly connected to the  $\text{RuO}_2$ .

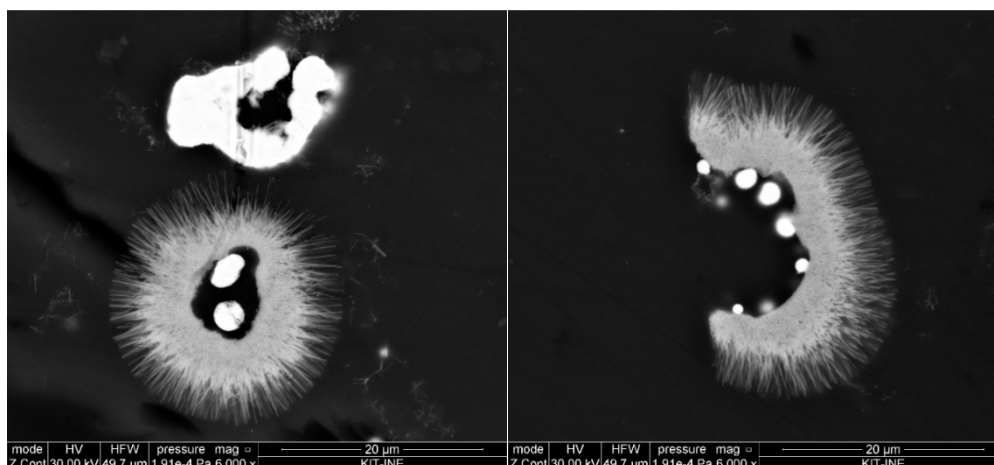


**Figure 89** RuO<sub>2</sub> agglomerates of ca. 20 μm size formed in sample **ISV-powder**. The bright object in the left micrograph is a Pd particle alloyed with ca. 6 wt% of Te. Bright spots neighbouring the spinous RuO<sub>2</sub> structures are also Pd particles.

To evaluate the effectiveness of the applied countermeasures, powder XRD analysis was performed (cf. **Figure 90**). Pd and RuO<sub>2</sub> reflexes can be identified in all three samples. In addition, in **ISV-powder**, some broad reflexes at diffraction angles characteristic for silicate compounds appear. As the samples were measured with the same integration time the intensities of the reflexes can be compared. The peak areas of reflexes can in general be correlated to the amount of crystal phase present in the sample whereas the broadness of the reflex reflects the size of the crystals (e.g., well defined large crystals obtain sharper reflexes). The intensities of the reflexes for both Pd and RuO<sub>2</sub> clearly change for the different samples. Whereas the RuO<sub>2</sub> signals are most pronounced in **ISV-ox** the Pd diffraction is most significant for both **ISV-ox** and **ISV-powder**. In **ISV-red** the Pd peak at around 40° is broader (FWHM 0.50°) compared to **ISV-ox** and **ISV-powder** (FWHM 0.25° and 0.33°).

The peaks at 28.2, 35.3 and 40.1° were integrated with the same integration windows for all three samples. **Figure 91** depicts the peak areas of the Pd and the sum of the main RuO<sub>2</sub> reflexes. While the contribution of Pd particles is higher for both countermeasures the formation of RuO<sub>2</sub> is significantly reduced. Considering **ISV-ox** as reference system the Pd formation is increased by a factor of 1.3 and 1.1 while the RuO<sub>2</sub> is decreased by a factor of 1.6 and 1.4 for **ISV-powder** and **ISV-red**, respectively.

The broad reflex at approximately 39.4° for the **ISV-powder** is not present in the other diffractograms. This un-assigned peak might misleadingly be contributed to the area of the Pd peak.

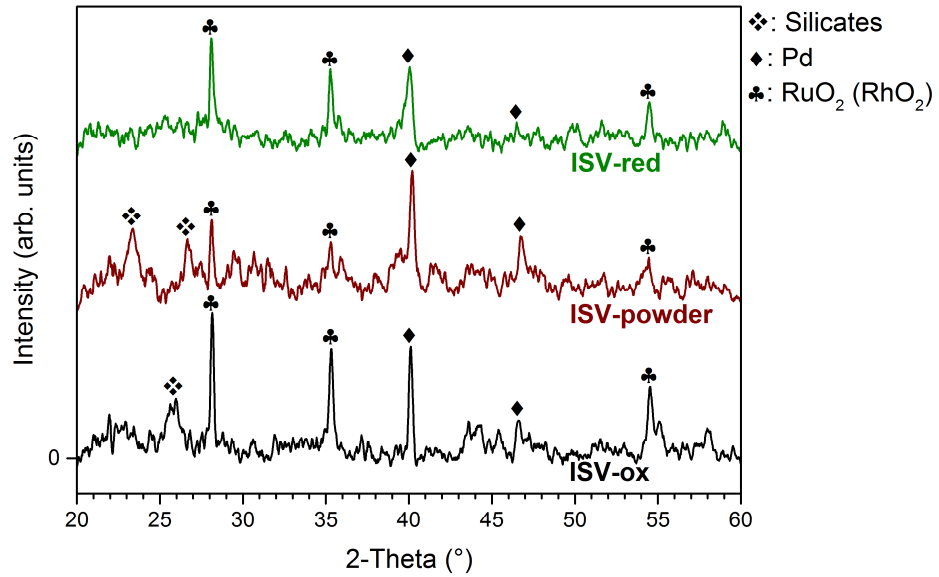


Figure 90 Powder XRD diffractograms of the ISV samples. Identified phases are labelled with symbols.

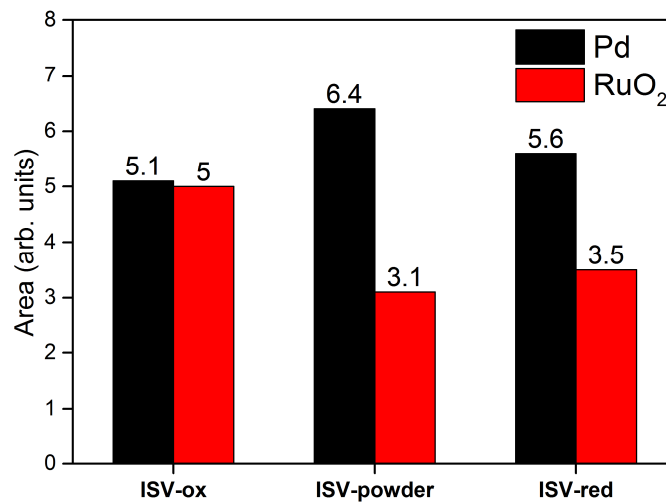


Figure 91 Peak areas of the Pd reflex at 40.1° and the peak area sum of the RuO<sub>2</sub> reflexes at 28.2° and 35.3°.

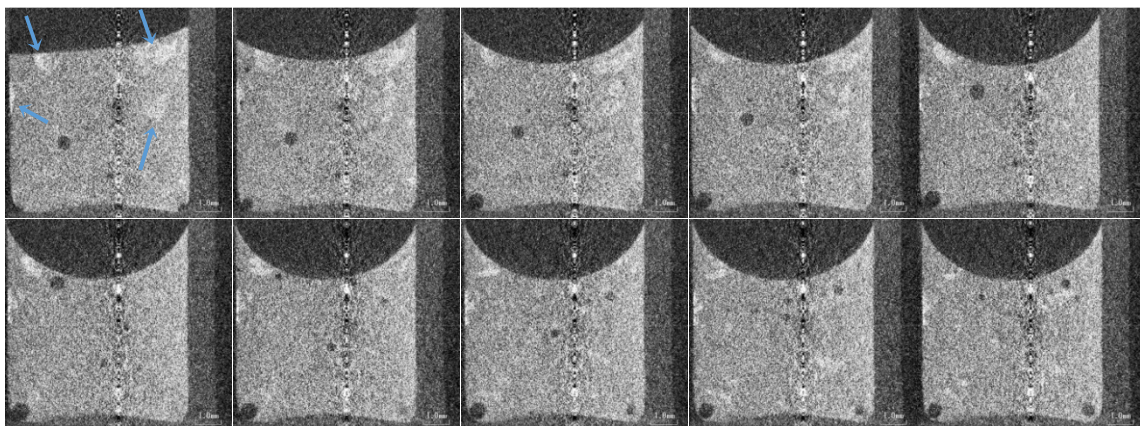
The contents of the elements in the glasses were determined using KOH digestion and ICP-OES analysis and are reported in Table 31. The use of 10 μm glass powder instead of glass beads improves Re retention by a factor of approximately 3 while the addition of Si as reducing agent retains Re by a factor of ca. 2 relative to ISV-ox.

Table 31 Re ICP-OES analysis of the ISV experiments after KOH digestion of the glass samples.

	ICP-OES ReO <sub>4</sub> (wt%)	Target ReO <sub>4</sub> (wt%)	Retention ReO <sub>4</sub> (%)
ISV-ox	0.037	0.31	12
ISV-powder	0.110	0.31	35
ISV-red	0.070	0.31	23

### *In-situ monitoring of NMP sedimentation*

To monitor the movement of the NMPs in a convection dragged glass melt several identical experiments were performed and evaluated as a collective. A well characterized glass from the cold-cap layer experiment (**B1200**) was used in the melting process. NMPs appeared in this sample as spherical Pd particles with size of ca. 1-3  $\mu\text{m}$  and as submicron  $\text{RuO}_2$  needles felted in larger collectives with size of more than 500  $\mu\text{m}$ . Glass fragments of **B1200** were transferred into a small silica tube which was heated in a furnace with reduced dimensions. The recording of one X-ray CT measurement took ca. 30 s while processing occupied another 1-2 min. Therefore, about every 2 min a scan was performed sufficient to record a smooth movement of the NMPs. Time lapse videos were produced from the recorded CT images with durations of 1-8 s at 7 frames per second (fps) (0-2 s at 25 fps). The progress of one experiment is illustrated in **Figure 92**. Black gas bubbles rise in an ascending movement to the surface of the glass melt. As the spatial and the image quality is not sufficient to identify single Pd or  $\text{RuO}_2$  particles only the larger NMP collectives were monitored. Bright areas of ca. 200-1000  $\mu\text{m}$  move in a defined way in all directions of the melt. From this movement convection currents can be deduced. In all performed experiments the predominant movement direction at the glass tube walls is downwards before flowing horizontally over the tube bottom in a distance of less than 1 mm followed by an upwards movement in the center of the melt. Independent from the convection flows, larger NMP agglomerates of approximately 1 mm size seem to exhibit a preferential downwards movement suggesting a sedimentation behavior. Due to repeated failure of the X-ray CT machine the duration of the videos is limited and the potential settlement could not be finally observed. In one experiment a central spiral movement of the NMP collectives involving approximately 70% of the glass melt was identified.



**Figure 92** X-ray CT images of a glass melt containing large NMP agglomerates, recorded every 4 min. Clearly the rising movement of black gas bubbles can be tracked. NMP domains appear as bright areas, dragged by convection forces in a directed pattern (marked in the first image with blue arrows).

### 7.3. Discussion

#### *NMP formation in a cold-cap*

To investigate the formation of the NMPs dried HLLW simulate was vitrified at different temperatures between 500-1200 °C mimicking the conditions in the different lower cold-cap layers (transformation and glass reaction layer). Generally, the comparability of the synthesized samples with a genuine liquid fed cold-cap is limited. Heat and mass transfer, gas evolution and thickness differ. Nevertheless, the formation of NMPs is expected to depend mainly on the temperature. Temperatures similar to a real vitrification process are applied, hence, NMP formation in the synthesized samples is similar to their formation in a cold-cap. The general assumption is made that the particles of interest are present in the glass melt and do not change in composition or structure while the glass melt solidifies. This assumption seems to be justified by insights from earlier studies.<sup>8,9</sup>

Heating to 500 °C led to a calcination of the waste components, temperature of 600 °C melted the glass beads forming an early waste glass whose melt is highly viscous as revealed from the encapsulated gas bubbles.  $\mu$ -XRF and X-ray CT gave complementary information on the PGM distribution. The 3D distribution of heavier elements was determined by CT while  $\mu$ -XRF identified these areas as Ru and Pd rich agglomerates. These areas were preferentially found on the bottom of the crucible and on the melt surface. While the first represents the characteristic NMP behavior of sedimentation, the latter might be due to surface effects such as surface tension entrapping some of the NMPs. In the bulk of the samples PGM rich “channel” were observed while other areas were entirely free of the heavy elements. It can be assumed that some sort of interaction between the NMPs leads to growing agglomeration while the particles move in the glass melt. This observation is in accordance with the experiences of Kelm *et al.*<sup>266</sup> Most likely the felting of RuO<sub>2</sub> needles is responsible for the build-up trapping also spherical Pd particles while being dragged through the melt.

The fluctuations in the Al concentration can be explained by an Al release from the Al<sub>2</sub>O<sub>3</sub> crucible as consequence of glass corrosion.<sup>271, 272</sup> As Al is a well soluble element in the borosilicate glass melt no influence on the performed investigations is assumed.

$\mu$ -XRF, XRD and SEM-EDX report in agreement the presence of Ce and Nd separated phases for a vitrification temperature lower than 900 °C. As the calcination of their respective nitrate salts is expected to be completed at 600 °C,<sup>273</sup> the elements are most likely present in their oxidic form. XRD supports this assumption. Temperatures of more than 900 °C are required in order to dissolve these Ln in the glass.

The discovery of the large Ru rich crystals with up to 10  $\mu\text{m}$  in diameter for most vitrification temperatures except 1200  $^{\circ}\text{C}$  was unexpected. According to the calculations of Schill *et al.* these particles should have the potential to sediment due to their size and density providing a possible Ru sedimentation route.<sup>258</sup> The phases looked like undamaged well crystallized structures. Therefore, it is suspected that they are not present in the glass melt but form while the glass melt solidifies while slowly being cooled down in air (several minutes for solidification). To check whether the formation of these particles can be attributed to the slow cooling rate a similar glass sample was melted at 800  $^{\circ}\text{C}$  and quenched by pouring the glass melt on a stainless steel plate causing the melt to cool very rapidly within seconds. In a specimen prepared from these samples no big Ru particles were found. As the SEM investigations were limited by the prepared specimens surface and machine time the presence of bigger Ru particle can not necessarily be excluded. For a final statement on the formation of the large Ru structures further studies are necessary.

The first characteristic needle  $\text{RuO}_2$  particles are observed consistently by SEM and XRD at vitrification at 700  $^{\circ}\text{C}$  suggesting that they form predominantly in the temperature range of 600-700  $^{\circ}\text{C}$ .

While numerous Pd particles were identified for melting at 1200  $^{\circ}\text{C}$  by SEM-EDX the corresponding diffraction pattern reveals an unexpectedly low Pd signal. Also the  $\text{RuO}_2$  reflexes are significantly reduced. Due to the heterogeneous distribution of the PGMs it is possible that glass fragments with low NMP concentration were used for preparation of the glass powder for XRD analysis. In analogy to the Ru particles Pd was also found to be first formed in relevant amounts at 700  $^{\circ}\text{C}$ . As this is the lowest temperature for liquidation of the glass beads it can be assumed that the presence of a liquid glass melt is necessary to enable the precipitation of  $\text{RuO}_2$  needles and metallic Pd particles. Comparing the formation temperature to the texture of the cold-cap (cf. [Figure 80](#)), the NMP precipitation starts in the top of the glass reaction layer.

#### *Countermeasures to the $\text{RuO}_2$ formation*

In a second stage the effect of two countermeasures proposed by Krause and Luckscheiter<sup>9</sup> on the formation of  $\text{RuO}_2$  particles was evaluated. For this purpose a set of three *in-situ* vitrification experiments (**ISV**) was performed. In a reference experiment (**ISV-ox**) standard vitrification conditions were applied by vitrifying dried HLLW simulate mixed with glass beads used also in the previous experiments. Krause and Luckscheiter assume that molybdate compounds dissolved in an alkali melt oxidize Ru to its hexavalent oxidation state which then decomposes subsequently to  $\text{RuO}_2$ . This process takes place predominantly within the small

cavities between the glass beads. Reduction of this reaction space might lead to formation of less RuO<sub>2</sub> particles. Thus, glass powder of less than 10 µm size was used for vitrification in the **ISV-powder** experiment. An alternative suggestion by Krause and Luckscheiter addresses directly the redox process aiming to prevent the oxidation of Ru to RuO<sub>3</sub> in the first place. Therefore, 1 wt% of metallic Si powder was added to the vitrification mixture of **ISV-red**. It is known from the literature that maintaining reducing vitrification conditions can have a beneficial effect on the volatilization behavior of Tc/Re by reducing them to their less volatile tetravalent state (cf. **Section 6.2.4** and **Table 42** in the **Appendix**). A more homogenous and denser waste/glass mixture might also favor the retention of volatile elements. To evaluate these effects the dried HLLW simulate contained approximately 0.89 g/L Re. The maximum heating temperature was limited by the setup to ca. 1050 °C (cf. **Figure 101** in the **Appendix**). From the previous experiments it was known that no significant difference in the NMP formation was observed for samples synthesized at 1000 °C and 1200 °C. Therefore, a maximum temperature of approximately 1050 °C can be considered as suitable to obtain the desired information.

Combination of the gas formation observation and the CT measurements give complementary picture of the vitrification process. In a first step the crystallization water is removed from the solid mix at ca. 200 °C. The thermal decomposition of the first nitrate salts is observed at approximately 310 °C and accompanied by a compaction of the waste/glass mix. Kawai *et al.* studied the thermal decomposition of dried HLLW simulate with the same composition.<sup>273</sup> According to their study Fe(NO<sub>3</sub>)<sub>3</sub> and Pd(NO<sub>3</sub>)<sub>2</sub> decompose first at around 150 °C followed by the decomposition of Zr and Mn nitrate at ca. 200 °C. Some nitrate salts are in a first reaction decomposed to mixed oxidic nitrate species, e.g., Zr<sub>2</sub>O<sub>3</sub>(NO<sub>3</sub>). Zr and Mn decompose finally from 250 °C to 300 °C to its pure oxidic compound together with Ce. The decomposition of the *Ln* nitrates salts is initiated at ca. 400 °C ranging up to 600 °C. Ba and Sr nitrate decompose in a range of ca. 550-800 °C. Na nitrate is decomposed at 380 °C to NaNO<sub>2</sub> which decomposes at temperature well above 600 °C. Kawai *et al.* showed that in the presence of a borosilicate glass NaNO<sub>2</sub> decomposes from approximately 400 °C to ca. 700 °C.<sup>273</sup> These results can be correlated to the two observed stages of NO<sub>x</sub> gas formation. The first phase at ca. 300 °C is most likely caused by the thermal decomposition of the transition metal nitrates which is expected to occur from 200 °C to 300 °C followed by a rearrangement and compaction of the solid material observed at 370 °C. The second phase at approximately 650 °C is caused by the NO<sub>x</sub> release from *Ln* salts. This goes along with massive bubbling observed at 740 °C as the glass starts to liquefy. From that point chemical reactions and dissolution of the waste components in the molten glass are occurring. These processes were observed in all **ISV** experiments.

With one exception the obtained results for the NMP formation probed by SEM do not reveal significant differences between the **ISV** samples in both shape and quantity. The presence of larger Pd particles of up to 5  $\mu\text{m}$  size in **ISV-red** can most likely be attributed to the effect of the reducing agent. In agreement with previous experiments Pd precipitates were found in vicinity the of  $\text{RuO}_2$  domains.

The formation of large spinous  $\text{RuO}_2$  crystals is most likely due to the slow cooling rate of the glass samples as has been already discussed before. The spatial correlation with Pd particles indicates that the Pd serves as some kind of seed crystal from which the growing of bulk material starts in all spatial directions ending into its spinous structure.

The  $\text{RuO}_2$  countermeasures can be best quantified considering the powder XRD results. Qualitative evaluation of the diffractograms indicates a positive effect (suppression) on the  $\text{RuO}_2$  formation by both methods. The application of 10  $\mu\text{m}$  sized glass powder decreased the  $\text{RuO}_2$  formation by ca. 40% compared to the reference experiment. From the X-ray CT time lapse video no cavities can be identified available for alkali melt reactions while the stacking of glass beads (mixed with dried waste simulate) in the other experiments led to mm sized empty cavities (cf. [Figure 87](#)). The waste and glass mixed material which is compacted even more at 570  $^\circ\text{C}$  does not show any changes before the sudden liquidation of the material. The application of the reducing agent minimized the  $\text{RuO}_2$  formation by ca. 30%. No other apparent differences to the reference experiment were observed when adding 1 wt% Si to the vitrification feed. This behavior supports the hypothesis of Krause and Luckscheiter who investigated the redox behavior also in independent experiments. The broad Pd reflex in the reducing glass indicates that Pd is formed in a less ordered crystal lattice. Its larger peak area compared to the reference experiment confirms that more XRD detectable metallic Pd is formed.

The increased Pd peak in the sample where glass powder has been used is not expected. The formation of Pd from a supersaturated glass melt should not depend on the initial size of the glass frit. Possibly Pd particles are formed prior to the melting of the glass frit. Nevertheless, the broad peak at approximately  $39.4^\circ$  in the **ISV-powder** diffractogram might add a misleading contribution to the peak area.

As both countermeasures show a positive effect the use of glass powder in combination with addition of a reducing agent can most effectively prevent  $\text{RuO}_2$  formation. The technical implementation of direct feeding of glass powder into a Joule-heated melter such as illustrated in [Figure 5](#) is challenging. The feeding mechanism tends to clog due to the moist atmosphere arising from the melter's plenum.<sup>274</sup> However, glass frit in a powder form can be pre mixed

with HLLW to form a wet slurry which can be transferred with suitable pumps into the melter.<sup>274</sup> Addition of reducing agent is challenging too. Direct contact with the oxidizing HNO<sub>3</sub> will dissolve the reducing agent removing its reducing power. One solution might be the encapsulation of the reducing agent in a material, e.g., a low melting glass which disintegrates at temperatures higher than 100 °C.

During vitrification the main part of Re is volatilized. The samples exhibit Re losses of 65-88%. Both RuO<sub>2</sub> countermeasures have a positive influence on the Re retention. While the addition of 1 wt% Si retains 1.9 times more Re than in the reference experiment the use of 10 µm glass powder yields a retention factor of 3.0. As the application of the glass powder should not have any influence on the Re volatilization when the glass is already molten its influence has to be attributed to the temperature range below 660 °C. The application of the powder degrades the amount of cavities and results in a denser waste/glass material. Therefore, possibly less Re is volatilized from the dried HLLW simulate in the calcination phase. This early loss of Re might also be the reason for the relative low Re retention when applying a reducing agent. If the main part of the Re is already lost before a glass melt is established the retention effectiveness of the Re reduction is significantly decreased.

#### *In-situ monitoring of NMP sedimentation*

As a first experiment of its kind the X-ray CT setup proved to be able to identify 200 µm and larger agglomerates of NMPs in a liquid glass melt and was able to track their movements. Essential for the increase of resolution was the design and the assembly of a high-temperature furnace with decreased dimensions allowing a significantly smaller distance from the X-ray source to the sample. Due to a missing water cooling the heating temperature of the furnace was limited to 1000 °C. From the previous experiments it was known that the nature of the samples synthesized at 1000 °C and at 1200 °C are comparable concerning the NMP behavior. The higher melt viscosity at lower temperature was even beneficial to the experiment as it slowed down the movement of the particles. The processing of the CT images recorded every 2 min resulted in time lapse videos with smooth particle movements. It needs to be noted that the heating mechanism of the experiment differed from the heating in most JHCM. These heat the glass pool by applying an electrical current through the melt which is delivered by several electrodes which are in contact with the melt. The external heating in the CT furnace causes the melt to be heated primarily on the outer silica tube walls. The observed convection behavior of the glass melt in the experiments is therefore different to the glass flow observed in industrial melters.<sup>258</sup> However, this should have only minor influence on the mechanisms which are the object of interest. A more important difference is the relation between particle

size, volume of the melt and the crucible surface area. Due to these effects the observed behavior might only be partially comparable to the situation in an industrial melter.

In general, the analysis of the NMPs movement by the X-ray CT technique was challenging due to the low quality of the images and the limited duration of the videos. In addition, only NMP movement in the cross-section plane was trackable (i.e., vertical and horizontal particle movement). Due to the fast movement of the melt relative to the time-consuming high-quality measurement, *in-situ* 3D modelling (cf. [Figure 84](#)) of the glass melt was not possible.

Analysis of movements of high-density regions in the melt is facilitated when replaying the videos rather than evaluating the single X-ray images collected as a function of time. While smaller NMP agglomerates were dragged by the convection force in ascending and descending manner, larger domains tend to reveal a sedimentation behavior. Due to the limited time of the recordings their final state could not be determined. An entrapment of the particles by obstacles on the crucibles bottom as proposed by Schill *et al.*<sup>258</sup> is less likely from the video observations but can also not be excluded.

It can be noticed that coherence of the agglomerates is rather high. Whereas their shape is influenced by the drag forces the collectives remain predominantly intact. It can be assumed that the shear forces are not strong enough to disintegrate the felted RuO<sub>2</sub> needles. The accumulations could be described as immiscible viscous drop dragged by a thin fluid. The significantly increased viscosity of NMP containing glass melt supports this picture.<sup>9</sup> It is most likely that continuous convection in a glass melter favors the merging of smaller drops. Due to this association some areas of the glass melt remain entirely free of NMPs.

The performed experiments and preparations of the NMP observations were aimed to review the applicability of the X-ray CT setup with increased spatial resolution for the *in-situ* analysis of NMP movement patterns. Extended experiments with longer observation times are essential in order to reliably evaluate the suggested sedimentation routes. A monitoring duration of at least 200 min is necessary.

## 7.4. Conclusion

The formation mechanisms of NMPs in a liquid fed cold-cap is challenging and therefore has never been studied in detail. In this dissertation it is aimed to contribute to the understanding of their formation by mimicking the cold-cap conditions and performing chemical and structural investigations of samples quenched at different temperatures. Precipitates of RuO<sub>2</sub> and Pd particles are detected in the borosilicate glass at 600 °C and 700 °C whereas dissolution of the most temperature resistant FP phases (Mo and Ln) is found at 900 °C. In addition to the expected formation of small RuO<sub>2</sub> particles a Ru rich phase with spinous appearance and approximately 10 µm size is found in most of the samples. To the best of our knowledge this agglomerate was never described before in the context of PGM vitrification. Most likely the formation of these large particles can be attributed to crystallization processes caused by the slow cooling of the glass melt. Nevertheless, their presence in the molten glass cannot definitely be excluded. As these phases could have a major impact on the NMP sedimentation behavior clarification of this question is of great interest and should be studied in further experiments.

The two applied counter-measures emerge as highly effective for prevention of RuO<sub>2</sub> formation. The application of 10 µm sized glass powder achieved a decreased RuO<sub>2</sub> formation of ca. 40% for vitrification at 1050 °C while the application of a reducing agent in form of 1 wt% Si reduced the RuO<sub>2</sub> formation by 30%. In an industrial vitrification it is usually attempted to remove the NMPs by increasing the slope of the melter's bottom which has only partial success.<sup>265</sup> The here presented counter-measures are to our knowledge the first chemical approaches significantly reducing the formation of the NMPs. The combination of both counter-measures could prove as a powerful tool in the commercial vitrification of PGM rich HLLW. In addition, the experimental results indicate a potential Tc retention by a factor of approximately 2-3 by the same measures. Therefore, the discussed counter-measures should strongly be considered for further optimization and application in the vitrification of PGM rich wastes.

The *in-situ* X-ray CT setup with improved furnace dimensions enables the successful tracking of large NMP agglomerates. Due to a limited machine time the duration of the recordings was not sufficiently long to determine the fate of the NMPs. Nevertheless, the obtained results indicate a predominantly descending movement for mm sized NMP agglomerates favoring the hypothesis of Kelm *et al.*<sup>266</sup> The entrapment of the particles on the crucible walls as proposed by Schill *et al.*<sup>258</sup> was not observed but can also not be completely excluded on the basis of the obtained data. The developed X-ray CT setup has a high potential to reveal the debated sedimentation mechanism of the NMPs.

## 8. Summary and Outlook

The application of advanced synchrotron based X-ray methods coupled with conventional microscopic and spectroscopic techniques proved to be a powerful combination for characterization of nuclear waste materials. The here presented studies contribute to the understanding of the properties of those waste materials which is necessary to improve vitrification processes and predict their fate in storage and repository conditions. The U, Np and Pu  $M_{4,5}$  edge high-energy resolution X-ray absorption near edge structure (HR-XANES) methods were applied for the first time here for investigations of U and Pu oxidation states in genuine and model waste glasses and SNF. The obtained results provide new insights and therefore they will stimulate new controversial discussions:

- 1) Within this doctoral project for the first time Pu(III), Pu(IV) and Pu(VI) were characterized simultaneously present in a borosilicate glass using the Pu  $M_5$  edge HR-XANES technique. Only Pu(III) and Pu(IV) were identified by the conventional Pu  $L_3$  edge XANES method. It was illustrated that the Pu  $M_5$  edge HR-XANES can be very efficiently used to verify Pu oxidation states which determine the solubility limit of Pu in a glass matrix. The analysis showed that initially added Pu(VI) was partly preserved during vitrification at 1200/1400 °C in an Ar atmosphere. Pu(VI) could be very advantageous for vitrification of Pu rich wastes since it might reach high solubility limits in the glass melt. Evidences were provided that the glass matrix likely accommodates Pu(VI) in a similar manner to U(VI) which incorporates in borosilicate glass with up to 40 wt%  $UO_2$ . HR-XANES results demonstrated that the addition of excess  $Si_3N_4$  is not sufficient for complete reduction of Pu to Pu(III) which has a relatively high solubility limit (10-25 wt%  $PuO_2$ ) due to its network-modifying behavior in glasses. Measurements of suitable reference compounds will allow quantitative oxidation states analyses.

In the bulk of the investigated genuine nuclear waste glass U was found to incorporate as hexavalent species while Pu was present in its tetravalent oxidation state. The glass has been sampled from the vitrification process performed in the vitrification plant Karlsruhe. Np was identified as a mixture of Np(IV) and Np(V). The Np reduction is possibly the consequence of a synchrotron X-ray radiation induced process. The same is true for U where a drastic reduction of U(VI) to U(IV) upon irradiation with synchrotron X-rays with energies of 3728 eV was observed which was not found for the U doped model glasses. This difference must be attributed to charge transfer processes from atoms surrounding U and/or X-ray triggered interactions with reactive species and free charges present only in the highly radioactive HLW glass. U  $L_3$  EXAFS revealed ordered agglomerates where

U(VI) surrounded by O atoms is coordinated by Al or more likely Si atoms in the second coordination sphere. Those inclusions were found only for the HLW glass but not for the model glasses and therefore they might be related to the observed radiation damage effects. Si and Al K edge EXAFS and TEM (planned in collaboration with Thierry Wiss, *JRC-Karlsruhe*) studies can help to verify the composition and structure of those ordered particles which were not detected by SEM-EDX investigations possibly due to their small size (less than 200 nm). The obtained results demonstrate that surrogate glasses are not for all studies representative models for HLW glass.

In analogy to the synchrotron X-ray induced redox processes the reduction of the *An* might as well be initiated on a long-term by the  $\alpha$ ,  $\beta$ ,  $\gamma$  and X-ray internal radiation of the nuclear waste glass. The importance of the effect needs to be evaluated since it can have an influence on the long-term speciation of *An* in the glass. SEM-EDX analysis revealed a homogeneous glass matrix with expected numerous inclusions of Pd and RuO<sub>2</sub> particles with spherical and needle-like shapes, respectively.

Np and Pu L<sub>1</sub> edge EXAFS studies of the waste glass recently became available at the CAT-ACT-Beamline at ANKA commissioned in 2016. Such investigations will verify if Np and Pu have similar to U local coordination environment.

- 2) The benchmark investigation of reference UO<sub>2</sub> samples revealed that the U M<sub>4</sub> edge HR-XANES is a bulk probe in comparison to the surface sensitive XPS technique. In agreement with the literature it was shown that UO<sub>2</sub> has limitations as a model for oxidation processes of SNF. It was demonstrated that studies of footprint reference and SNF samples composed of small powder particles yield results being not representative for the bulk of irradiated SNF since the large surface to volume ratio of the small particles lead to ongoing oxidation of U.

The investigations of SNF revealed the presence of predominant tetravalent U and Pu oxidation states. Variable contributions of U<sub>4</sub>O<sub>9</sub> (U(IV) and U(V)) were found in the bulk of the SNF and in the reference samples. These results indicate that limited O<sub>2</sub> access in dry storage conditions prevents phase transformation of UO<sub>2</sub> to U<sub>3</sub>O<sub>8</sub> (U(V) and U(VI)) in the irradiated SNF. In general, the transformation of UO<sub>2</sub> to U<sub>3</sub>O<sub>8</sub> or UO<sub>3</sub> with higher U oxidation states is considered critical as phase transformation induces drastic volume increase and potentially cracking of zircaloy cladding.

Analysis of a high burn-up SNF structure showed essentially the same *An* redox states as found for the low burn-up samples. However, at least for Pu there are indications that higher oxidation states are present. This is certainly surprising and requires further studies.

Within this project the procedure for the preparation of the samples was developed and the feasibility of the U/Pu M<sub>4,5</sub> edge HR-XANES investigations of the highly active SNF and a genuine waste glass was demonstrated. On this basis further synchrotron based experiments will be performed continuing the cooperation with the *JRC-Karlsruhe*. The recently implemented HR-XANES technique proved to be a powerful tool for bulk investigation of challenging materials. In the same time new phenomena not known from the respective L<sub>3</sub> edge XANES measurements were observed and require further studies by systematic approaches for elucidation.

- 3) The formation of a Cs and Tc rich highly radioactive residual material in the vitrification plant Karlsruhe was simulated and the formed compounds were identified. The relevance of the results for potential conditioning of the material were discussed. Several conceptually different immobilization approaches were reviewed addressing the challenge of the Cs and Tc retention. Different matrices potentially suitable for immobilization were screened and compared serving as a fundament for more detailed studies currently carried out in the Master Project of Aaron Beck, KIT. The application of CsAlTiO<sub>4</sub> as host material for the immobilization of the volatile elements achieved a Cs and Re retention of 90% and 60% respectively. Due to its predominantly homogenous appearance the material is a promising candidate to serve as immobilization matrix. Its leaching performance and the optimization of the immobilization process will be further investigated.

Cs<sub>3</sub>PMo<sub>12</sub>O<sub>40</sub> appears to be a main component of waste originating from precipitation of HLLW during storage at the site of the reprocessing plant Karlsruhe. Despite the initial compound was decomposed in the melt, vitrification in a borosilicate glass at 1000 °C and 3.5 wt% waste loading emerges as a favorable immobilization strategy with minimal Cs losses of approximately 5%. The formed glass-composite material is likely suitable for disposal in a final repository since the formed Ca- and BaMoO<sub>4</sub> phases in the glass matrix show poor solubility in water.

- 4) Most HLLW contains considerable amounts of platinum group metals (PGM). They form particles with different shapes and size in the micrometer range in glass melts which is a major issue in the HLLW vitrification process. By sedimentation these particles can cause severe problems such as drain plugging and short circuits. A novel X-ray computer tomography setup of the TIT University Tokyo was tested for the possibility to study the formation and deposition of the spherical Pd particles and needle-like RuO<sub>2</sub>. The doctoral candidate S. Bahl was granted a KHYS scholarship to work for three months on this project

at TIT University in Tokyo, Japan. First results demonstrate the feasibility of the arrangement and suggest that PGM particles form in the lower part of the cold-cap. First indications for a directed sedimentation mechanism via agglomeration to larger PGM collectives was observed. Two tested countermeasures including the use of a reducing agent or glass frit powder instead of mm sized glass beads reduce the formation of RuO<sub>2</sub> by 30% or 40% by possibly influencing Ru redox reactions. Both measures had another beneficial effect since the loss of volatile Re used as a surrogate for Tc was reduced. Within this project initiated cooperation with the working group of Prof. T. Yano will be continued in the next years.



## Appendix

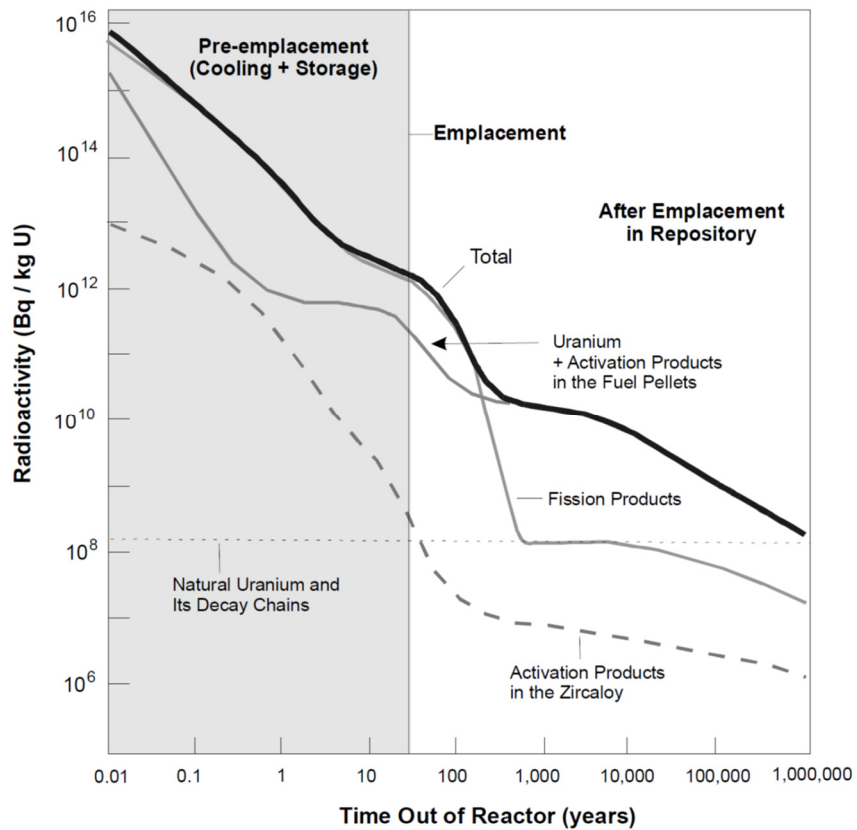


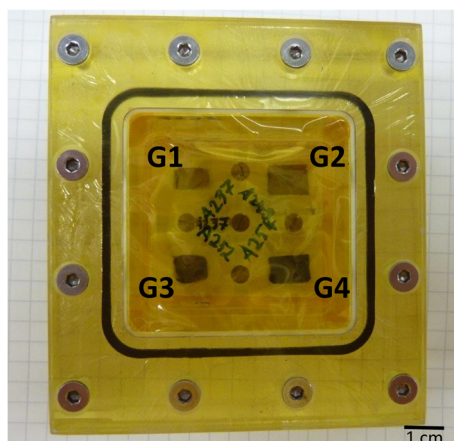
Figure 93 Decrease of radioactivity in Canadian SNF over time. (adapted from NEA/RWM/IGSC(2006)3)<sup>27</sup>

Table 32 X-ray absorption edges of U and Pu with the detected emission line and the corresponding crystals and Bragg angles  $\theta$  including the intermediate and final state lifetime broadenings.

Element	Absorption edge	Absorption energy (eV) <sup>114</sup>	Transition	Emission line	Emission energy (eV) <sup>114</sup>	Crystal	$\theta$ (°)	$\Gamma_{INT}$ (eV)	$\Gamma_{FIN}$ (eV)
U	L <sub>3</sub>	17166	$3d_{5/2} \rightarrow 2p_{3/2}$	L $\alpha_1$	13614	Ge(777)	77.39	8.2 <sup>79</sup> 7.43 <sup>70</sup>	3.5 <sup>79</sup>
U	M <sub>4</sub>	3728	$4f_{5/2} \rightarrow 3d_{3/2}$	L $\beta$	3339.8	Si(220)	75.18	3.5 <sup>79</sup>	0.37 <sup>79</sup>
Pu	L <sub>3</sub>	18057	$3d_{5/2} \rightarrow 2p_{3/2}$	L $\alpha_1$	14282	Si(777)	75.70	8.7 <sup>54</sup>	4.1 <sup>54</sup>
Pu	M <sub>5</sub>	3775	$4f_{7/2} \rightarrow 3d_{5/2}$	M $\alpha$	3339	Si(220)	75.22	-	-

**Table 33** Isotopic composition of the Pu used for sample preparation.

Isotope	Pu-238	Pu-239	Pu-240	Pu-241	Pu-242	Pu-244
Concentration (at%)	0.025 ±0.001	91.98 ±0.02	7.577 ±0.015	0.305 ±0.003	0.115 ±0.001	Not detectable



**Figure 94** G1-G4 glass samples mounted in a Plexiglass cell and sealed with two Kapton windows 10 + 12.5 μm.

**Table 34** The energy positions of the Gaussian and arctangent profile functions used to model the spectral features of the G1-G4 and G1\*/G4\* spectra in order to determine their energy positions. The energy position of the b profile function was fixed during the fit. The spectra of the G1 and G4 glasses recorded with high experimental energy resolution are marked with asterisk (G1\* and G4\*). The fitting of G1 is exemplarily shown in Figure 95 in the Appendix.

Sample/Fitting function	a ± 0.1 (eV)	b ± 0.1 (eV)	c ± 0.1 (eV)	d ± 0.1 (eV)	e ± 0.1 (eV)
<b>G1</b>	3773.4	3774.9	3776.1	3777.9	3791.7
<b>G2</b>	3773.6	3774.9	3775.8	3778.2	3790.1
<b>G3</b>	3773.2	3774.9	-	3776.1	3789.3
<b>G4</b>	3773.3	3774.9	-	3777.1	3786.5
<b>G1*</b>	3773.1	3774.6	3775.7	3777.3	3789.2
<b>G4*</b>	3773.2	3774.6	-	3776.9	3787.4

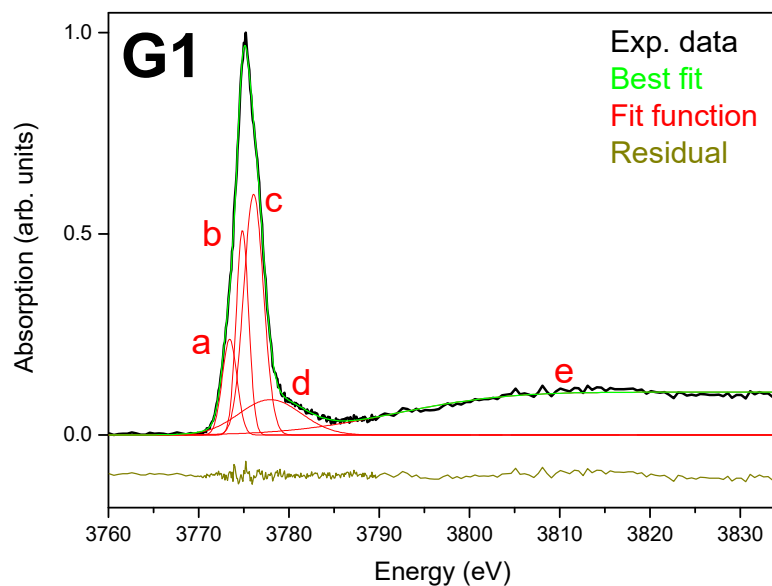


**Figure 95** Pu  $M_5$  edge HR-XANES **G1** spectrum (black) with its best fit (green). The fitting functions used to fit features a-e are shown in red. The difference between the best fit sum and the experimental spectrum is given below the spectrum as residual.

**Table 35** EXAFS fit results for Pu glass samples (SP – scattering path, N – coordination number, R – bond distance,  $\sigma^2$  - Debye-Waller factor,  $\Delta E_0$  – energy shift,  $S_0^2$  – amplitude reduction factor and r - goodness of fit parameter.

Sample	SP	N	R (Å)	$\sigma^2$ (Å <sup>2</sup> )	$\Delta E_0$ (eV)	$s_0^2$	r
<b>G1</b>	Pu-O1	$5.7 \pm 0.3$	$2.25 \pm 0.01$	$0.011 \pm 0.001$	$-7.2 \pm 0.6$	0.9	0.001
<b>G2</b>	Pu-O1	$5.7 \pm 0.4$	$2.27 \pm 0.01$	$0.017 \pm 0.002$	$-7.4 \pm 0.8$	0.9	0.001
<b>G3</b>	Pu-O1	$5.3 \pm 0.4$	$2.34 \pm 0.01$	$0.016 \pm 0.001$	$-5.7 \pm 0.7$	0.9	0.002
<b>G4</b>	Pu-O1	$5.8 \pm 0.5$	$2.34 \pm 0.01$	$0.016 \pm 0.001$	$-5.7 \pm 0.8$	0.9	0.002

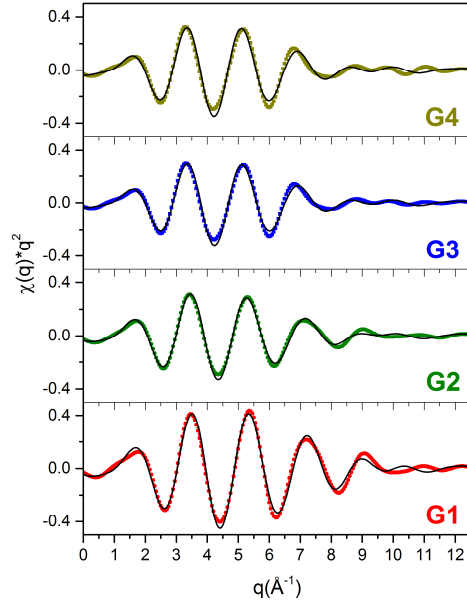


**Figure 96** Backtransformed Pu L<sub>3</sub> edge FT-EXAFS spectra of G1-G4 in q space. Experimental data are shown with colored symbols whereas solid black lines represent best fit results.

**Table 36** EXAFS fit results of U doped glass with 5 wt% (N – coordination number, R – bond distance,  $\sigma^2$  - Debye-Waller factor,  $\Delta E_0$  – energy shift and r - goodness of fit parameter).

	backscatterer	N	R (Å)	$\sigma^2$ (Å <sup>2</sup> )	$\Delta E_0$ (eV)	r
U L <sub>3</sub> -edge (2.6-14.0 Å <sup>-1</sup> )	O <sub>ax</sub>	2.0	1.84	0.0058	0.97	0.0007
	O <sub>eq</sub> (1)	5.4	2.29	0.012		
	O <sub>eq</sub> (2)	3.0	2.62			
	-	-	-	-		

**Table 37** EXAFS fit results of VEK glass performed by Dardenne *et al.* (N – coordination number, R – bond distance,  $\sigma^2$  - Debye-Waller factor,  $\Delta E_0$  – energy shift and r - goodness of fit parameter).

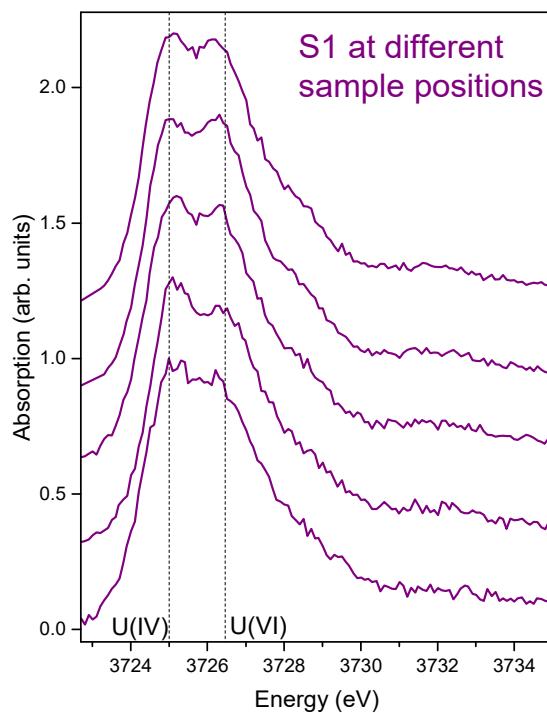
	backscatterer	N	R (Å)	$\sigma^2$ (Å <sup>2</sup> )	$\Delta E_0$ (eV)	r
U L <sub>3</sub> -edge (2.6-10.0 Å <sup>-1</sup> ) S <sub>0</sub> <sup>2</sup> =0.78	O <sub>ax</sub>	2.0	1.80	0.0009	5.19	0.0051
	O <sub>eq</sub> (1)	5.0	2.27	0.0075		
	O <sub>eq</sub> (2)	1.2	2.82	0.0009		
	Si/Al	2.6	3.97	0.0008		



Figure 97 Empty sample holder used for  $AnM_{4.5}$  HR-XANES investigation (left). The inlay (right) can be exchanged for different designs.

Table 38 Fitting results of U2 XPS spectrum.

Position (eV)	Pos_rel (ev)	FWHM (eV)	Intensity	%Gauss	Area	%Area	Oxidation state	U(IV) (%)	U(V) (%)	U(VI) (%)
379.78	0	1.50	17059	98	27453	19.86	U(IV)	19.86		
380.91	1.13	1.50	17589	74	31530	22.81	U(V)		22.81	
382.44	2.66	2.02	2600	73	6301	4.56	U(VI)			4.56
386.13	6.35	2.81	1889	15	7924	5.73	U(IV)	5.73		
388.73	8.95	2.81	1496	38	5793	4.19	U(V)		4.19	
390.58	10.80	1.50	11282	70	20590	14.89	U(IV)	14.89		
391.71	11.93	1.50	12876	68	23648	17.10	U(V)		17.1	
393.24	13.46	2.02	1696	38	4726	3.42	U(VI)			3.42
396.93	17.15	2.81	1608	50	5943	4.30	U(IV)	4.3		
399.53	19.75	2.81	1360	85	4345	3.14	U(V)		3.14	
<b>Total</b>								<b>44.78</b>	<b>47.24</b>	<b>7.98</b>



**Figure 98** U  $M_4$  edge HR-XANES spectra of **S1** at different sample positions. The maximum of the U(IV) and U(VI) reference main peaks are indicated by vertical dashed lines.

**Table 39** Absorption feature (Feature), height (Height), position (Position), half width at half maximum (HWHM) and area (Area) parameters of the Gaussian functions used to model the U  $M_4$  edge HR-XANES spectra and the arctangent function used to model the edge jump. <sup>a</sup>For the arctangent function the width of the function is given instead of the HWHM

Spectrum	Feature	Height $\pm$ 0.01	Position $\pm$ 0.1 (eV)	HWHM $\pm$ 0.1 (eV)	Area
S3	A	5.07	3724.97	0.99	5.34
UO <sub>2</sub>	A	6.08	3724.95	0.92	5.97
S3	B	4.43	3726.12	2.37	11.16
UO <sub>2</sub>	B	4.60	3726.05	2.39	11.67
S3	C	0.71	3728.33	2.30	1.73
UO <sub>2</sub>	C	0.65	3728.33	2.27	1.58
S3	D	0.61	3730.53	8.96	5.81
UO <sub>2</sub>	D	0.62	3730.39	8.95	5.92
S3	E	0.72	3745.82	10.77	8.23
UO <sub>2</sub>	E	0.78	3746.23	11.09	9.19
S3	F	0.20	3760.86	5.86	1.26
UO <sub>2</sub>	F	0.29	3759.92	7.08	2.21
S3	arctan	1	3752.49	4.74 <sup>a</sup>	-
UO <sub>2</sub>	arctan	1	3753.09	4.75 <sup>a</sup>	-

**Table 40** Calculated Pu inventory of commercial SNF performed by E. Gonzalez-Robles.

	mass (g/t <sub>HM</sub> )	mass (wt%)
Pu-238	300	2.9
Pu-239	5700	54.8
Pu-240	2900	27.9
Pu-241	560	5.4
Pu-242	950	9.1
<b>Total</b>	<b>10410</b>	<b>100</b>

**Table 41** ICP-MS analysis results from liquid sampling of VEK rinsing solution (cf. also **Table 13**). The remaining solid compounds from drying of the solution were calculated according to their solubility limits (cf. **Table 42** in the **Appendix**).

ICP-MS analysis			Calculated data				
Element	g/l	mmol/l	Solid compound	mmol/l	Species in glass	g/l	wt%
Tc ± 0.7%	4.24	43.3	CsTcO <sub>4</sub>	26.7	Cs <sup>+</sup> TcO <sub>4</sub> <sup>-</sup>	7.86	46.22
Cs ± max. 5%	3.54	26.7					
Na ± 3.54%	1.26	55.0	NaTcO <sub>4</sub>	16.6	Na <sup>+</sup> TcO <sub>4</sub> <sup>-</sup>	3.07	18.05
			NaNO <sub>3</sub>	38.4	Na <sub>2</sub> O	1.18	6.96
Fe ± 1.88%	1.67	29.9	Fe(NO <sub>3</sub> ) <sub>3</sub>	29.9	Fe <sub>2</sub> O <sub>3</sub>	2.39	14.04
La ± 0.38%	1.22	8.8	La(NO <sub>3</sub> ) <sub>3</sub>	8.8	La <sub>2</sub> O <sub>3</sub>	1.43	8.41
Cr ± 2.24%	0.33	6.4	Cr(NO <sub>3</sub> ) <sub>3</sub>	6.4	Cr <sub>2</sub> O <sub>3</sub>	0.48	2.84
Ni ± 6.74%	0.24	4.1	Ni(NO <sub>3</sub> ) <sub>2</sub>	4.1	NiO	0.30	1.78
Ba ± 9.87%	0.13	0.9	Ba(NO <sub>3</sub> ) <sub>2</sub>	0.9	BaO	0.15	0.85
Mn ± 1.66%	0.09	1.6	Mn(NO <sub>3</sub> ) <sub>2</sub>	1.6	MnO <sub>2</sub>	0.14	0.82
<b>Total</b>						<b>17</b>	<b>100</b>

**Table 42** Physical properties of selected compounds.

Constituent	Melting point (°C)	Boiling point (°C)	Solubility (mol/l)
Tc <sub>2</sub> O <sub>7</sub>	120 <sup>275</sup>	311 <sup>275</sup>	
CsTcO <sub>4</sub>	595 <sup>276</sup>	Dissociation	0.014 <sup>277</sup>
NaTcO <sub>4</sub>	378 <sup>276</sup>	Dissociation	1.48 <sup>278</sup>
Re <sub>2</sub> O <sub>7</sub>	300 <sup>275</sup>	360 <sup>275</sup>	-
CsReO <sub>4</sub>	620 <sup>279</sup>	(Dissociation)	0.02 <sup>280</sup>
NaReO <sub>4</sub>	420 <sup>279</sup>	(Dissociation)	3.66 <sup>280</sup>
ReO <sub>2</sub>	1000 <sup>270</sup>	-	-

**Table 43** Overview about the volume, the sampling dates and the temperature of the solution within the drying process.

Time	T <sub>solution</sub>	Volume (L)	Time	T <sub>solution</sub>	Volume (L)
06/08/2014			12/08/2014		
15:20	30.0 °C	4.85	11:10	49.5 °C	0.83
16:13	1.0 mL sample 1		12:10	49.5 °C	0.82
16:17	35.0 °C	4.85	14:10	49.5 °C	0.79
17:30	40.0 °C	4.85	15:10	49.0 °C	0.79
07/08/2014			16:10	49.5 °C	0.77
9:13	49.0 °C	4.23	16:20	1.0 mL sample 7	
11:12	47.5 °C	4.19	17:10	49.0 °C	0.74
14:10	46.5 °C	4.14	13/08/2014		
16:36	1.0 mL sample 2		9:10	47.0 °C	0.59
17:25	47.5 °C	4.09	9:40	1.0 mL sample 8	
08/08/2014			10:10	47.0 °C	0.57
9:20	49.0 °C	3.40	11:10	47.5 °C	0.57
11:16	49.0 °C	3.33	12:10	47.5 °C	0.54
12:45	49.0 °C	3.29	13:10	48.0 °C	0.52
13:42	49.5 °C	3.28	14:27	48.0 °C	0.52
14:47	49.5 °C	3.25	15:10	47.5 °C	0.49
15:47	49.0 °C	3.20	16:10	48.0 °C	0.49
16:25	1.0 mL sample 3		16:15	1.0 mL sample 9	
16:47	48.5 °C	3.19	17:10	48.0 °C	0.48
17:22	48.0 °C	3.16	14/08/2014		
11/08/2014			9:10	46.0 °C	0.34
9:10	52.5 °C	1.23	9:20	1.0 mL sample 10	
9:17	1.0 mL sample 4		10:10	51.0 °C	0.32
10:55	47.0 °C	1.20	11:10	51.0 °C	0.31
12:30	46.0 °C	1.17	12:10	50.0 °C	0.29
first crystals			13:10	49.5 °C	0.26
13:40	46.5 °C	1.12	14:20	49.0 °C	0.25
14:50	47.0 °C	1.11	15:20	49.5 °C	0.23
15:45	47.0 °C	1.11	16:20	48.0 °C	0.22
16:25	1.0 mL sample 5		17:20	48.0 °C	0.20
16:30	47.5 °C	1.11	15/08/2014		
17:10	47.5 °C	1.09	solution dried		
12/08/2014			9:15	50.0 °C	-
9:10	49.0 °C	0.86	16:50	46.0 °C	-
9:20	1.0 mL sample 6				
10:10	49.5 °C	0.85			

**Table 44** Results of liquid sampling S1–S10 by ICP-OES/AAS analysis. The results are given in g/L.

sample	S1	S2	S3	S4	S5	S6	S7	S8	S9	S10
Ba	0.14	0.17	0.22	0.28	0.19	0.11	0.08	0.07	0.09	0.10
Cr	0.33	0.42	0.52	1.49	1.64	2.11	2.49	3.55	4.18	8.34
Fe	1.67	1.94	2.44	7.36	8.05	10.37	11.31	17.68	20.23	37.71
La	1.25	1.53	1.92	5.62	6.13	7.99	8.99	12.86	15.64	7.84
Mn	0.09	0.11	0.14	0.39	0.43	0.55	0.64	0.91	1.07	1.94
Na	1.27	1.58	1.91	5.71	6.13	7.90	8.99	13.16	15.83	15.41
Ni	0.26	0.32	0.40	1.09	1.20	1.55	1.79	2.41	2.74	5.20
Re	7.84	9.61	1.22	3.47	3.77	49.57	56.14	80.18	93.69	146.30
Cs	3.49	4.24	5.57	15.29	16.50	23.06	27.00	36.91	43.34	57.70
	±0.78%	±2.68%	±0.6%	±1.89%	±2.33%	±3.99%	±0.93%	±1.9%	±3.56%	±0.73%

**Table 45** Amounts used to synthesize the Ba rich and reference glass frit.

Compound	Ba rich frit (g)	Reference frit (g)
SiO <sub>2</sub>	32.80	20.49
B <sub>2</sub> O <sub>3</sub>	20.82	5.60
BaCO <sub>3</sub>	25.42	2.07
Na <sub>2</sub> CO <sub>3</sub>	18.36	3.42
Al(OH) <sub>3</sub>	2.60	2.58
Li <sub>2</sub> CO <sub>3</sub>	-	2.48
CaCO <sub>3</sub>	-	5.48
MgO	-	2.00
Sb <sub>2</sub> O <sub>5</sub>	-	0.23
V <sub>2</sub> O <sub>5</sub>	-	0.69
<b>Total</b>	<b>100</b>	<b>45.04</b>



**Figure 99** Pictures of glass fragments from all synthesized waste glass samples.

**Table 46** Size distribution of used glass beads.

Size of glass beads (mm)	Ratio (%)
> 2.8	0.1
> 2.0	50
> 1.0	50
< 1.0	0.1



**Figure 100** HLLW simulate solution with sedimented solid particles (left) and after slurring (right).

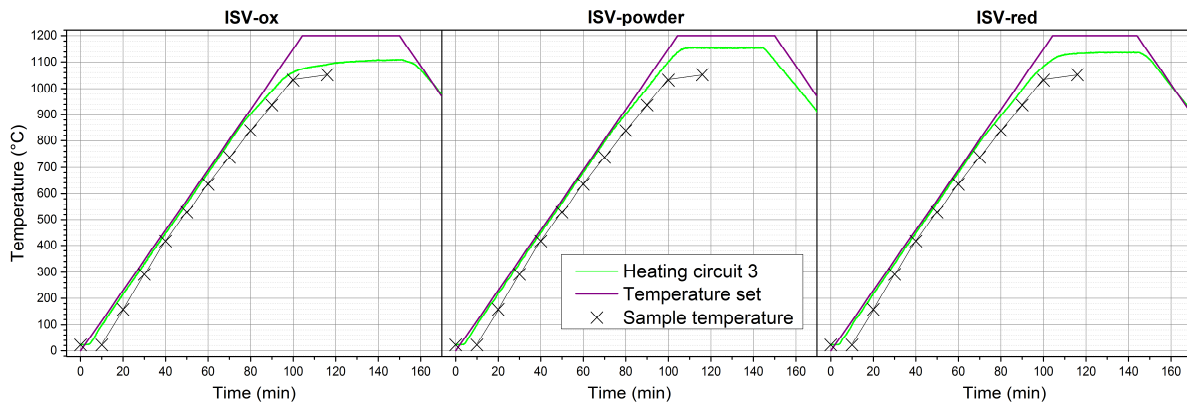


**Figure 101** Temperature profiles of set temperature, temperature of sample zone and sample temperature.



**Figure 102** Dried HLLW simulate covering glass beads in an Al<sub>2</sub>O<sub>3</sub> crucible (left), hot glass melt in a second Al<sub>2</sub>O<sub>3</sub> crucible without cap (right).

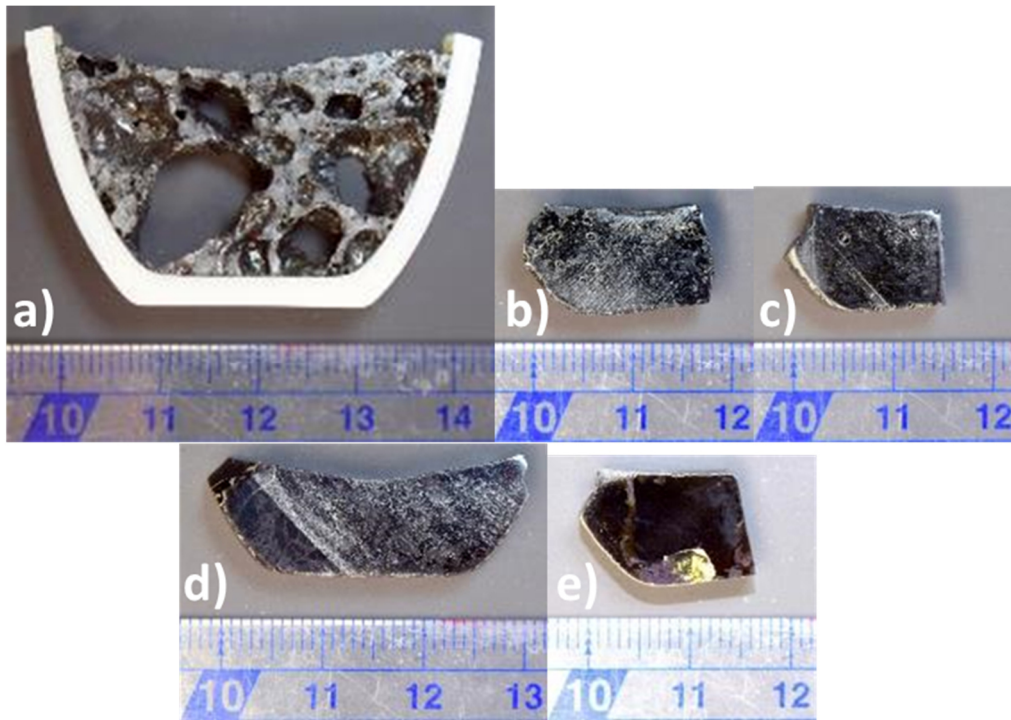


Figure 103 Photographs of polished glass specimens of sample a) B600, b) B800, c) B900, d) B1000 and e) B1200.

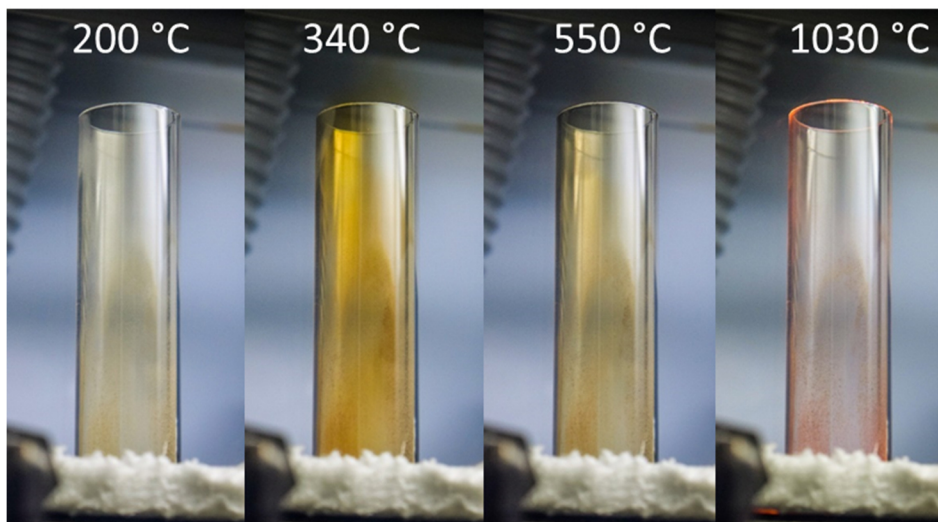


Figure 104 Exhaust gas formation observation of ISV-powder.

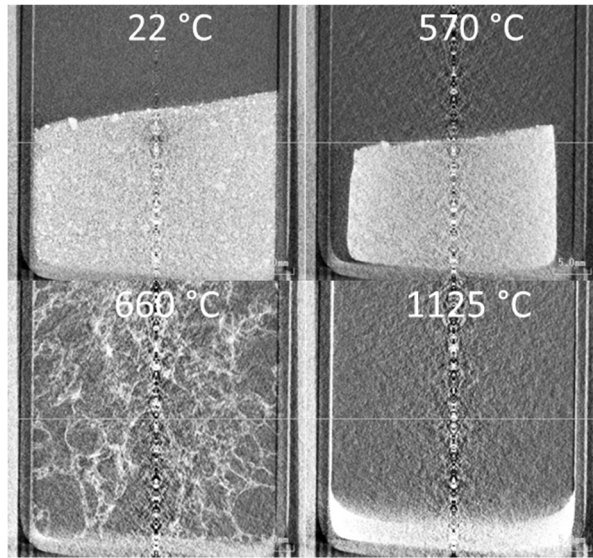


Figure 105 CT observations of ISV-powder.

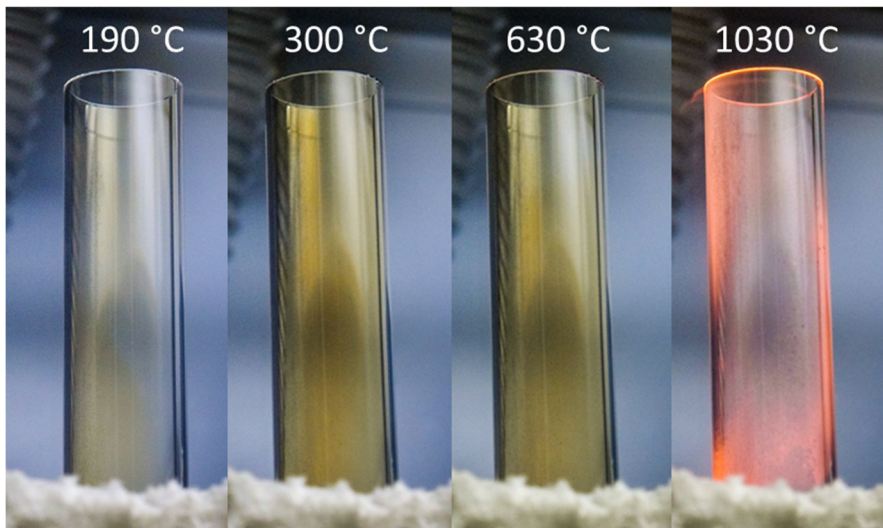


Figure 106 Exhaust gas formation observation of ISV-red.

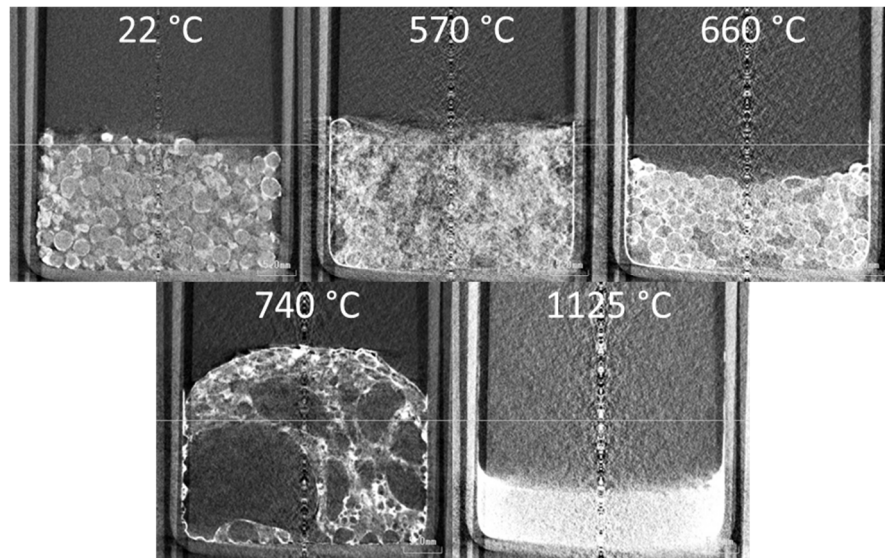


Figure 107 CT observations of ISV-red.

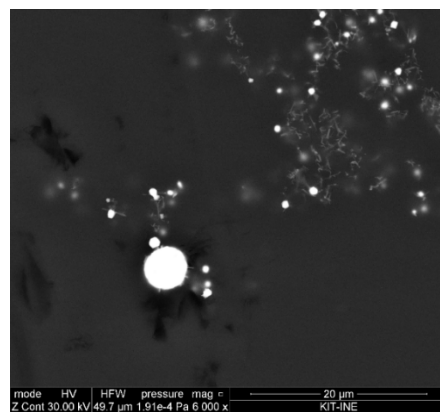


Figure 108 Pd particle with increased size of ca. 5  $\mu\text{m}$  found in the ISV-red sample.



## List of Tables and Figures

TABLE 1 BEAMTIME CHARACTERISTICS OF THE AN M <sub>4,5</sub> HR-XANES MEASUREMENTS. ....	38
TABLE 2 REDOX REFERENCE SAMPLES USED IN DIFFERENT BEAMTIMES. ....	39
TABLE 3 GLASS FRIT COMPOSITIONS USED TO VITRIFY PU. <sup>35</sup> .....	43
TABLE 4 FABRICATION CHARACTERISTICS OF PU DOPED GLASSES; $R = M(\text{Si}_3\text{N}_4)/M(\text{PUO}_2)$ . ....	44
TABLE 5 GLASS FORMING PRECURSORS USED TO PRODUCE THE VEK GLASS. ....	57
TABLE 6 TARGET OXIDE COMPOSITION OF U AND PU MODEL GLASS SAMPLES. ....	58
TABLE 7 AVERAGED EDX RESULTS FROM 5 MEASUREMENTS OF U DOPED MODEL GLASSES. ....	66
TABLE 8 RESULTS FROM QUANTITATIVE FIT OF THE XPS SPECTRUM OF THE 3 WT% UO <sub>2</sub> GLASS SAMPLE SHOWN IN FIGURE 36. ....	69
TABLE 9 EDX RESULTS OF THE NMPS AND THE GLASS MATRIX AVERAGED FROM THREE MEASUREMENTS (ONLY SELECTED ELEMENTS ARE LISTED). ....	75
TABLE 10 OVERVIEW OF SAMPLES STUDIED IN THIS PROJECT AND THEIR DESCRIPTION. ....	90
TABLE 11 GLASS FORMING PRECURSORS USED TO SYNTHESIZE THE GLASS FRIT. <sup>226</sup> .....	105
TABLE 12 SUMMARY OF THE RESULTS FROM RAMAN SPECTROSCOPY OF SAMPLES VK-03-600 TO - 1200. ....	109
TABLE 13 ICP-MS ANALYSIS RESULTS OF LIQUID SAMPLING OF THE EVAPORATOR CONCENTRATE TANK ON 14 <sup>TH</sup> OF MARCH 2011. THE ELEMENTS WITH THE MOST RELEVANT CONCENTRATIONS ARE LISTED. STANDARD DEVIATIONS AND MORE DETAILS RESULTS ARE LISTED IN TABLE 41 IN THE APPENDIX. ....	115
TABLE 14 TARGET COMPOSITION OF THE EXPERIMENTAL SOLUTION USED FOR THE DRYING EXPERIMENT. IT IS BASED ON THE ANALYSIS RESULTS REPORTED IN TABLE 13. ....	117
TABLE 15 CHEMICALS USED FOR THE SYNTHESIS OF THE EXPERIMENTAL SOLUTION. ....	118
TABLE 16 H <sub>3</sub> O <sup>+</sup> CONCENTRATION AND SOLUTION DENSITY CALCULATED FOR S1-S10. ....	122
TABLE 17 ICP-OES AND AAS RESULTS FROM SAMPLING OF THE SOLID RESIDUAL MATERIAL FROM DIFFERENT AREAS. THE RESULTS ARE GIVEN IN AT%. THE RELATIVE STANDARD DEVIATION OF THE CS CONCENTRATION IS GIVEN BY MAX. 2.74% WHEREAS THE DEVIATION FOR THE OTHER ELEMENTS IS MAX. 5%. ....	124
TABLE 18 TARGET COMPOSITION OF THE BA RICH <sup>243</sup> AND REFERENCE GLASS FRIT <sup>226</sup> . THE AL CONTENT OF THE BA RICH GLASS WAS SLIGHTLY INCREASED IN ORDER TO ENHANCE THE CHEMICAL DURABILITY OF THE FINAL GLASS PRODUCT. ....	130
TABLE 19 OVERVIEW OF THE SAMPLES WHICH WERE SYNTHESIZED FROM BA RICH AND REFERENCE FRIT. ....	131
TABLE 20 OVERVIEW OF SAMPLES WITH WASTE LOADING, VITRIFICATION TEMPERATURE AND THE AMOUNT OF REDUCING AGENT ADDED. ....	132
TABLE 21 AMOUNTS OF STARTING MATERIALS USED FOR IMMOBILIZATION OF WASTE SIMULATE IN THE NA RICH BOROSILICATE GLASS/TIO <sub>2</sub> GLASS SYSTEM. A, B AND C RELATE TO THE SAMPLES SYNTHESIZED WITHOUT REDUCING AGENT, HALF-STOICHIOMETRIC AND STOICHIOMETRIC, RESPECTIVELY. ....	137
TABLE 22 STARTING MATERIALS USED FOR IMMOBILIZATION OF THE WASTE SIMULATE IN A CSALTIO <sub>4</sub> MATRIX. A, B AND C RELATE TO THE SAMPLES SYNTHESIZED WITHOUT REDUCING AGENT, HALF-STOICHIOMETRIC AND STOICHIOMETRIC, RESPECTIVELY. ....	138
TABLE 23 STARTING MATERIALS USED FOR IMMOBILIZATION OF THE WASTE SIMULATE IN A FLUOROPHOSPHATES GLASS. A, B AND C RELATE TO THE SAMPLES SYNTHESIZED WITHOUT REDUCING AGENT, HALF-STOICHIOMETRIC AND STOICHIOMETRIC, RESPECTIVELY. ....	138
TABLE 24 STARTING MATERIALS USED FOR IMMOBILIZATION OF THE WASTE SIMULATE IN THE ETS-10 MATRIX. A, B AND C RELATE TO THE SAMPLES SYNTHESIZED WITHOUT REDUCING AGENT, HALF-STOICHIOMETRIC AND STOICHIOMETRIC, RESPECTIVELY. SAMPLE A*, B* AND C*	

WERE PRE-CONDITIONED FOR CS ION EXCHANGE (SI WAS ADDED AFTER THE PRE-CONDITIONING).....	139
TABLE 25 AMOUNT OF MATERIAL USED FOR XRF ANALYSIS. ....	139
TABLE 26 SYSTEMS USED FOR WASTE SIMULATE IMMOBILIZATION AND THEIR RESPECTIVE PROCESSING CONDITIONS. ....	140
TABLE 27 VOLATILIZATION AND APPEARANCE CHARACTERISTICS OF FOUR IMMOBILIZATION MATRICES POTENTIALLY SUITED FOR THE IMMOBILIZATION OF TC AND CS RICH WASTE. A) SAMPLES SYNTHESIZED WITHOUT REDUCING AGENT, B) WITH HALF-STOICHIOMETRIC AMOUNT OF REDUCING AGENT, AND C) WITH STOICHIOMETRIC AMOUNT OF REDUCING AGENT.....	142
TABLE 28 QUALITATIVE COMPOSITION OF THE COMMERCIALY PREPARED HLLW SIMULATE SOLUTION.....	150
TABLE 29 CALIBRATION DATA OF THE STANDARD X-RAY CT FURNACE. ....	153
TABLE 30 RESULTS OF SEM-EDX INVESTIGATIONS. THE SECONDARY AND BACKSCATTERED ELECTRON SIGNALS IN COMBINATION WITH EDX RESULTS HELP TO IDENTIFY FIVE MAIN SPECIES IN THE GLASS SAMPLES B600-B1200. B600 AND B700 CONTAIN MINOR AMOUNTS OF RUO <sub>2</sub> AND PD PARTICLES, RESPECTIVELY, WHICH IS SHOWN WITH BRACKETS IN THE TABLE. ....	158
TABLE 31 RE ICP-OES ANALYSIS OF THE ISV EXPERIMENTS AFTER KOH DIGESTION OF THE GLASS SAMPLES.....	163
TABLE 32 X-RAY ABSORPTION EDGES OF U AND PU WITH THE DETECTED EMISSION LINE AND THE CORRESPONDING CRYSTALS AND BRAGG ANGLES $\theta$ INCLUDING THE INTERMEDIATE AND FINAL STATE LIFETIME BROADENINGS. ....	177
TABLE 33 ISOTOPIC COMPOSITION OF THE PU USED FOR SAMPLE PREPARATION. ....	178
TABLE 34 THE ENERGY POSITIONS OF THE GAUSSIAN AND ARCTANGENT PROFILE FUNCTIONS USED TO MODEL THE SPECTRAL FEATURES OF THE G1-G4 AND G1*/G4* SPECTRA IN ORDER TO DETERMINE THEIR ENERGY POSITIONS. THE ENERGY POSITION OF THE B PROFILE FUNCTION WAS FIXED DURING THE FIT. THE SPECTRA OF THE G1 AND G4 GLASSES RECORDED WITH HIGH EXPERIMENTAL ENERGY RESOLUTION ARE MARKED WITH ASTERISK (G1* AND G4*). THE FITTING OF G1 IS EXEMPLARILY SHOWN IN FIGURE 95 IN THE APPENDIX. ....	178
TABLE 35 EXAFS FIT RESULTS FOR PU GLASS SAMPLES (SP – SCATTERING PATH, N – COORDINATION NUMBER, R – BOND DISTANCE, $\Sigma^2$ - DEBYE-WALLER FACTOR, $\Delta E_0$ – ENERGY SHIFT, $S_0^2$ – AMPLITUDE REDUCTION FACTOR AND R - GOODNESS OF FIT PARAMETER. ....	179
TABLE 36 EXAFS FIT RESULTS OF U DOPED GLASS WITH 5 WT% (N – COORDINATION NUMBER, R – BOND DISTANCE, $\Sigma^2$ - DEBYE-WALLER FACTOR, $\Delta E_0$ – ENERGY SHIFT AND R - GOODNESS OF FIT PARAMETER. ....	180
TABLE 37 EXAFS FIT RESULTS OF VEK GLASS PERFORMED BY DARDENNE ET AL. (N – COORDINATION NUMBER, R – BOND DISTANCE, $\Sigma^2$ - DEBYE-WALLER FACTOR, $\Delta E_0$ – ENERGY SHIFT AND R - GOODNESS OF FIT PARAMETER.....	180
TABLE 38 FITTING RESULTS OF U2 XPS SPECTRUM.....	181
TABLE 39 ABSORPTION FEATURE (FEATURE), HEIGHT (HEIGHT), POSITION (POSITION), HALF WIDTH AT HALF MAXIMUM (HWHM) AND AREA (AREA) PARAMETERS OF THE GAUSSIAN FUNCTIONS USED TO MODEL THE U M <sub>4</sub> EDGE HR-XANES SPECTRA AND THE ARCTANGENT FUNCTION USED TO MODEL THE EDGE JUMP. <sup>A</sup> FOR THE ARCTANGENT FUNCTION THE WIDTH OF THE FUNCTION IS GIVEN INSTEAD OF THE HWHM.....	182
TABLE 40 CALCULATED PU INVENTORY OF COMMERCIAL SNF PERFORMED BY E. GONZALEZ-ROBLES. ....	183
TABLE 41 ICP-MS ANALYSIS RESULTS FROM LIQUID SAMPLING OF VEK RINSING SOLUTION (CF. ALSO TABLE 13). THE REMAINING SOLID COMPOUNDS FROM DRYING OF THE SOLUTION WERE CALCULATED ACCORDING TO THEIR SOLUBILITY LIMITS (CF. TABLE 42 IN THE APPENDIX). ....	183

TABLE 42 PHYSICAL PROPERTIES OF SELECTED COMPOUNDS.....	183
TABLE 43 OVERVIEW ABOUT THE VOLUME, THE SAMPLING DATES AND THE TEMPERATURE OF THE SOLUTION WITHIN THE DRYING PROCESS. ....	184
TABLE 44 RESULTS OF LIQUID SAMPLING S1–S10 BY ICP-OES/AAS ANALYSIS. THE RESULTS ARE GIVEN IN G/L.....	185
TABLE 45 AMOUNTS USED TO SYNTHESIZE THE BA RICH AND REFERENCE GLASS FRIT.....	185
TABLE 46 SIZE DISTRIBUTION OF USED GLASS BEADS.....	186
FIGURE 1 ILLUSTRATION OF SNF MICROSTRUCTURE AND DISTRIBUTION OF FPS AND AN. (REPRODUCED WITH PERMISSION FROM REF. <sup>3</sup> ).....	7
FIGURE 2 SCHEMATIC ILLUSTRATION OF CHEMICAL PROCESSES INVOLVED IN THE SNF MATERIAL DISSOLUTION IN THE NEAR-FIELD OF A GEOLOGICAL REPOSITORY. (REPRODUCED WITH PERMISSION FROM REF. <sup>26</sup> ).....	9
FIGURE 3 FIELD OF CONSTRAINTS AND REQUIREMENTS A GLASS FORMULATION HAS TO CONSIDER AND TO FULFIL, RESPECTIVELY, IN ORDER TO SERVE AS A RELIABLE HOST MATRIX FOR NUCLEAR WASTE. (REPRODUCED WITH THE PERMISSION FROM REF. <sup>32</sup> ).....	12
FIGURE 4 SCHEMATIC ILLUSTRATION OF AN ALKALI-SILICATE GLASS NETWORK. THE BLUE TETRAHEDRAL STRUCTURES REPRESENT $\text{SiO}_4$ NETWORK FORMING UNITS, B ATOMS FORM EITHER $\text{BO}_3$ TRIGONAL PLANAR OR $\text{BO}_4$ TETRAHEDRAL UNITS. CHARGED S, MO OR CR TETRAHEDRA ARE NOT CONNECTED TO THE GLASS NETWORK BUT INCORPORATED IN ITS GAPS. FREE CATIONS SUCH AS ALKALI AND EARTH-ALKALI ELEMENTS COMPENSATE THE NEGATIVE CHARGE OF NBO. (ILLUSTRATION BY S. WEISENBURGER) .....	14
FIGURE 5 CROSS-SECTION OF A JHCM DEVELOPED BY KIT-INE WITHIN THE VEK PROJECT.(ILLUSTRATION ADAPTED FROM GRÜNEWALD ET AL.) <sup>36</sup> .....	16
FIGURE 6 ABSORPTION CROSS-SECTION $\mu/P$ OF PB, CD, FE AND O OVER A LARGE X-RAY ENERGY RANGE. THE ELEMENT SPECIFIC ABSORPTION EDGES ARE CAN BE RECOGNIZED BY A SHARP RISE IN $\mu/P$ . (REPRODUCED WITH PERMISSION FROM REF. <sup>51</sup> ) .....	20
FIGURE 7 ILLUSTRATION OF THE PHOTOELECTRIC EFFECT. A PHOTON EXCITES A CORE ELECTRON FROM THE K SHELL INTO THE CONTINUUM (LEFT). THE ELECTRON HOLE IS FILLED BY AN OUTER M OR L SHELL ELECTRON EMITTING EITHER X-RAY FLUORESCENCE (MIDDLE) OR AN AUGER ELECTRON (RIGHT). (ADAPTED WITH PERMISSION FROM REF. <sup>51</sup> ).....	20
FIGURE 8 XAS SPECTRUM OF $\text{PuO}_2$ (CF. SECTION 3). THE XANES REGION IS MARKED GREEN, THE EXAFS REGION RED. THE MOST INTENSE PEAK IN THE XANES REGION IS THE WL. (CRYSTAL STRUCTURE OF $\text{PuO}_2$ ADAPTED WITH PERMISSION FROM REF. <sup>55</sup> ).....	21
FIGURE 9 SCHEMATIC ILLUSTRATION OF THE TWO-STEP RIXS PROCESSES. (ADAPTED WITH PERMISSION FROM REF. <sup>54</sup> ).....	24
FIGURE 10 3D4F RIXS OF $\text{PuO}_2$ . <sup>69</sup> THE COLORS REPRESENT THE INTENSITY OF FLUORESCENCE FROM BLUE (LOW) TO RED (HIGH). THE YELLOW HORIZONTAL LINE INDICATES THE EMISSION ENERGY AT WHICH PU $M_5$ EDGE HR-XANES SPECTRA ARE MEASURED. ....	24
FIGURE 11 SCHEMATIC ILLUSTRATION OF ELECTRON TRANSITIONS AT THE AN $L_3$ AND $M_{4,5}$ EDGES. ....	25
FIGURE 12 XANES SPECTRA OF METASCHOEPITE MEASURED WITH CONVENTIONAL AND HIGH-ENERGY RESOLUTION SETUP.....	26
FIGURE 13 U $M_4$ EDGE (LEFT) AND $L_3$ EDGE (RIGHT) HR-XANES SPECTRA OF U COMPOUNDS CONTAINING DIFFERENT, PURE U OXIDATION STATES SHOWN IN RED AND BLACK. THE BLUE SPECTRUM IS DERIVED BY LINEAR COMBINATION MODELLING OF 90% U(VI) AND 10% U(IV) OF THE PURE SPECTRA. ....	27
FIGURE 14 3D4F RIXS CONTOUR MAP OF $\text{PuO}_2^{2+}$ (LEFT). WHEN INTEGRATED WITH DIFFERENT EMISSION ENERGY WIDTH (GREEN: 0.05 EV, PINK: 0.25 EV, CYAN: 1 EV, YELLOW: 5 EV,	

ORANGE: 10 EV) HR-XANES SPECTRA WITH DIFFERENT ENERGY RESOLUTION CAN BE OBTAINED (RIGHT).....	28
FIGURE 15 U M <sub>4</sub> EDGE HR-XANES SPECTRA OF THE U MINERAL UMOHOITE. THE SPECTRA WERE RECORDED AFTER THE SAMPLE WAS EXPOSED TO INTENSE X-RAY RADIATION OF THE MEASUREMENT FOR 0, 10 AND 60 S. ....	29
FIGURE 16 SCHEMATIC ILLUSTRATION OF A SYNCHROTRON FACILITY. IT CONSISTS OF AN ELECTRON GUN (1), A LINEAR ACCELERATOR (2), A BOOSTER RING (3), A STORAGE RING (4) AND SEVERAL BEAMLINES (5). (© SOLEIL SYNCHROTRON. ADAPTED WITH PERMISSION FROM REF. <sup>84</sup> ).....	30
FIGURE 17 SCHEMATIC ILLUSTRATION OF A TYPICAL BEAMLINE (ANGLES AND DISTANCES ARE NOT TO SCALE). THE SYNCHROTRON RING WITH ITS RADIATION PRODUCING DEVICES ARE NAMED AS "SOURCE". THE IONIZATION CHAMBERS ARE ABBREVIATED AS IC <sub>N</sub> . (REPRODUCED WITH PERMISSION FROM REF. <sup>54</sup> ).....	31
FIGURE 18 3D CAD MODEL (LEFT) AND PICTURES OF THE MAC-SPECTROMETER SETUP INCLUDING THE HE ENVIRONMENT CHAMBER. ....	32
FIGURE 19 SCHEMATIC ILLUSTRATION OF THE ACT-BEAMLINE AND PHOTOGRAPHIC PICTURES OF THE INSTALLED SPECTROMETER INCLUDING HE ENVIRONMENT CHAMBER.....	32
FIGURE 20 SCHEMATIC ILLUSTRATION OF THE JOHANN GEOMETRY APPLIED FOR THE MAC-SPECTROMETER (LEFT). (REPRODUCED WITH PERMISSION FROM REF. <sup>90</sup> ) PICTURE OF THE INSTALLED SPECTROMETER AT THE INE-BEAMLINE AT ANKA. THE PATHS OF THE INCIDENT AND FLUORESCENCE X-RAY BEAMS ARE INDICATED IN RED. ....	33
FIGURE 21 CRYSTAL POSITIONING STAGES WITH FOUR DEGREES OF FREEDOM FOR EACH CRYSTAL TO FULFIL THE BRAGG CONDITION FOR THE DESIRED ENERGY. ONLY FOUR OF THE FIVE CRYSTALS ARE MOUNTED. (FIGURE TAKEN FROM PRÜßMANN, DOCTORAL THESIS) <sup>54</sup> .....	33
FIGURE 22 HE ENVIRONMENT FOR THE MAC- SPECTROMETER FOR LOW ENERGY HR-XANES MEASUREMENTS WITH ENERGIES OF 3-4 KEV. ....	34
FIGURE 23 PU M <sub>5</sub> HR-XANES SPECTRA OF PUO <sub>2</sub> MEASURED WITH DIFFERENT EXPERIMENTAL ENERGY RESOLUTIONS.....	45
FIGURE 24 PU L <sub>3</sub> EDGE XANES SPECTRA OF THE G1-G4 GLASSES AND THE PU(III), PU(IV), PU(VI) REFERENCES.....	47
FIGURE 25 (A) PU M <sub>5</sub> EDGE HR-XANES SPECTRA OF THE G1-G4 GLASSES AND (B) THE G1, G4 GLASSES RECORDED WITH MEDIUM AND HIGH EXPERIMENTAL ENERGY RESOLUTIONS, RESPECTIVELY. THE PU(III) <sub>AQ</sub> AND PU(VI) <sub>AQ</sub> SPECTRA WERE MEASURED WITH LOW EXPERIMENTAL ENERGY RESOLUTION.....	49
FIGURE 26 (A) PU L <sub>3</sub> EDGE EXAFS SPECTRA OF THE G1-G4 GLASS IN K SPACE, (B) MAGNITUDE AND IMAGINARY PART OF THE EXPERIMENTAL FT-EXAFS SPECTRA AND THEIR BEST FITS (RIGHT). EXPERIMENTAL DATA ARE SHOWN WITH COLORED SYMBOLS WHEREAS SOLID BLACK LINES REPRESENT FIT RESULTS.....	51
FIGURE 27 STATISTICS OF PU-O DISTANCES FOR CA. 100 PU CONTAINING COMPOUNDS REPORTED IN THE ICSD DATABASE. <sup>133</sup> THE PU-O DISTANCES OBTAINED FROM THE EXAFS FITS FOR THE G1-G4 SAMPLES ARE INDICATED WITH BLACK ARROWS. ....	52
FIGURE 28 PHOTOGRAPHS OF PU AND U MODEL GLASSES. UO <sub>2</sub> CONTENT: A) 1.19 WT%, B) 3 WT%, C) 5 WT%. PUO <sub>2</sub> CONTENT: D) 0.2 WT% E) 0.5 WT% F) 1 WT% G) 1.5 WT%. ....	63
FIGURE 29 LIGHT MICROSCOPE IMAGE OF THE VEK GLASS PARTICLE.....	63
FIGURE 30 POWDER XRD DIFFRACTOGRAMS OF THE PU AND U MODEL GLASSES.....	64
FIGURE 31 RAMAN SPECTRA OF THE VEK AND U MODEL GLASSES RECORDED WITH A 785 NM LASER.....	65
FIGURE 32 CORRELATION DIAGRAM BETWEEN VIBRATION BAND INTENSITY AND U CONTENT IN THE THREE U DOPED MODEL GLASS SAMPLES. ....	65

FIGURE 33 SEM MICROGRAPH OF THE 1.19 WT% (LEFT), 3 WT% (MIDDLE) AND 5 WT% (RIGHT) UO <sub>2</sub> MODEL GLASSES. THE HOMOGENOUS SURFACE IS COVERED WITH SMALL GLASS PIECES AND DUST PARTICLES RESULTING FROM SAMPLE PREPARATION. ....	66
FIGURE 34 RAMAN SPECTRA OF THE PU MODEL GLASSES RECORDED WITH A 785 NM LASER. ....	67
FIGURE 35 PU M <sub>5</sub> (LEFT) AND U M <sub>4</sub> (RIGHT) EDGE HR-XANES OF MODEL GLASSES AND REFERENCE COMPOUNDS. ....	67
FIGURE 36 XPS SPECTRA OF POWDERED U MODEL GLASS SAMPLES (LEFT) AND FIT OF THE 3 WT% UO <sub>2</sub> SAMPLE XPS SPECTRUM (RIGHT). FIT RESULTS ARE SHOWN IN TABLE 8. ....	69
FIGURE 37 XPS SPECTRA OF AS-PREPARED GLASS CHIP SAMPLE 5 WT% UO <sub>2</sub> MEASURED AT 5 DIFFERENT POSITIONS (LEFT) AND 30 SCANS MEASURED AT ONE POSITION OF THE SAME SAMPLE (RIGHT). EACH SCAN TOOK APPROXIMATELY 10 MIN. ....	70
FIGURE 38 U L <sub>3</sub> EDGE EXAFS SPECTRUM OF THE U MODEL GLASS SAMPLE WITH 5 WT% UO <sub>2</sub> IN K SPACE. EXPERIMENTAL DATA ARE SHOWN AS SOLID LINE WHEREAS BLACK SYMBOLS REPRESENT FIT RESULTS (LEFT). FT-EXAFS SPECTRA OF THE SAME SAMPLE IN R SPACE. MAGNITUDE AND REAL PART OF THE EXPERIMENTAL DATA ARE SHOWN AS SOLID LINES; SYMBOLS REPRESENT THE FIT RESULTS (RIGHT). ....	71
FIGURE 39 PU M <sub>5</sub> EDGE HR-XANES SPECTRA OF THE VEK GLASS AND THE 0.2 WT% PUO <sub>2</sub> MODEL GLASS (LEFT), U M <sub>4</sub> EDGE HR-XANES SPECTRA OF THE VEK GLASS RECORDED AFTER DIFFERENT IRRADIATION TIME OF THE SAME SAMPLE SPOT (RIGHT). ....	71
FIGURE 40 U M <sub>4</sub> EDGE HR-XANES SPECTRUM OF THE VEK WASTE GLASS SAMPLE IN COMPARISON TO THE U DOPED GLASS WITH 1.19 WT% UO <sub>2</sub> . THE VEK GLASS SPECTRUM REPRESENTS THE MERGED SPECTRA DEPICTS IN FIGURE 39 (RIGHT). ....	72
FIGURE 41 U L <sub>3</sub> EDGE EXAFS SPECTRUM OF THE VEK GLASS IN K SPACE. EXPERIMENTAL DATA ARE SHOWN AS SOLID LINE WHEREAS BLACK SYMBOLS REPRESENT FIT RESULTS (LEFT). FT-EXAFS SPECTRA OF THE SAME SAMPLE IN R SPACE. MAGNITUDE AND REAL PART OF THE EXPERIMENTAL DATA ARE SHOWN AS SOLID LINES, SYMBOLS REPRESENT THE FIT RESULTS (RIGHT). DATA WERE OBTAINED AND EVALUATED BY DARDENNE ET AL. ....	74
FIGURE 42 MICROGRAPH OF A 1 MM VEK GLASS PARTICLE (LEFT). NMP AGGLOMERATES OF RUO <sub>2</sub> NEEDLES AND SPHERICAL PD PARTICLES (RIGHT). ....	75
FIGURE 43 HR-XANES SPECTRA OF THE VEK GLASS AND THE NP DOPED R7T7 REFERENCE GLASS IN COMPARISON WITH NP REDOX REFERENCES (NP(IV)O <sub>2</sub> , CA <sub>0.5</sub> NP(V)O <sub>2</sub> (OH) <sub>2</sub> ·1.3H <sub>2</sub> O AND NA <sub>2</sub> NP(VI) <sub>2</sub> O <sub>7</sub> ). ....	76
FIGURE 44 SEM MICROGRAPH OF HIGH BURN-UP SNF FROM THE CORE REGION OF A PELLETT (LEFT) AND FROM THE RIM REGION OF A PELLETT (RIGHT). THE LATTER REVEALS THE TYPICAL CHARACTERISTICS OF THE HBS MORPHOLOGY. THESE TWO RADIAL PELLETT REGIONS WERE USED FOR PREPARATION OF SAMPLES S1 AND S2. (REPRODUCED WITH PERMISSION FROM REF. <sup>176</sup> ) ....	80
FIGURE 45 MACROGRAPH OF THE COMMERCIAL IRRADIATED SNF VERTICAL CROSS SECTION (LEFT). PREPARED FOOTPRINT OF CORE PARTICLE S2 AND HBS DUST MATERIAL S1 ON KAPTON TAPE (RIGHT) FOR AN M EDGE INVESTIGATIONS. RED ARROWS INDICATE THE ORIGIN OF THE FOOTPRINT SAMPLES MATERIAL. (CROSS SECTION IMAGE ADAPTED WITH PERMISSION FROM REF. <sup>215</sup> ) ....	87
FIGURE 46 SAMPLE HOLDER FOR AN M <sub>4,5</sub> EDGES HR-XANES (CEA DESIGN, ACKNOWLEDGMENTS TO PHILIPPE MARTIN, PHILIPPE VALENZA AND RENAUD BELIN) MEASUREMENTS. (1) OUTER CONTAINMENT (AL); (2) OUTER CONTAINMENT RING WITH 13 μM KAPTON FOIL; (3) INNER CONTAINMENT (AL) WITH A 3 MM DUMP FOR AN SAMPLE; (4) INNER CONTAINMENT RING WITH 8 μM KAPTON FOIL; (5) COVER FOR THE FIRST CONTAINMENT; (6) SCREWS FOR THE FIRST CONTAINMENT RING (LEFT). SNF SAMPLE S3 MOUNTED IN THE ILLUSTRATED AL CELL SEALED WITH TWO KAPTON WINDOWS (RIGHT). <sup>216</sup> ....	87

FIGURE 47 SAMPLE HOLDER OF UO <sub>2</sub> BENCHMARK SAMPLE U1 AND U3. THE EMPTY CELL ILLUSTRATING THE CONTAINMENT CONCEPT IS SHOWN IN FIGURE 97 IN THE APPENDIX. ....	88
FIGURE 48 XPS SPECTRUM OF U2 (BLACK). FITTING OF THE MAIN AND SATELLITE PEAKS RESULTED IN THE FIT SPECTRUM SHOWN IN RED. THE EVALUATION RESULTS OF THE BEST FIT CAN BE FOUND IN TABLE 38 IN THE APPENDIX. ....	91
FIGURE 49 U M <sub>4</sub> EDGE HR-XANES SPECTRA OF SAMPLES U1, U3, UF1 AND DIFFERENT U OXIDE REFERENCES SAMPLES WITH EMPHASIZE ON THE WL REGION (LEFT) AND ON THE POST-EDGE REGION (RIGHT). THE EXPERIMENTAL RESOLUTION BETWEEN THE TWO SETS OF SPECTRA DIFFER SLIGHTLY. THE POST-EDGE FEATURES ARE MARKED WITH SOLID BLACK LINES.....	92
FIGURE 50 U M <sub>B</sub> FLUORESCENCE MAP OF S1 AND S2. BLUE AND RED INDICATE AREAS OF LOW AND HIGH U FLUORESCENCE INTENSITY, RESPECTIVELY. SAMPLE S1 WAS MEASURED AT POSITIONS MARKED WITH WHITE STARS. NO FLUORESCENCE DATA WERE RECORDED FOR THE AREA IN GREY.....	93
FIGURE 51 U M <sub>4</sub> EDGE HR-XANES SPECTRA (SHORT (LEFT) AND EXTENDED (RIGHT) ENERGY RANGE) OF THE HBS SAMPLE S1, SNF SAMPLE S2 AND THE UO <sub>2</sub> REFERENCE U3 MEASURED IN MARCH 2015, NOVEMBER 2015 AND 2016. THE ENERGY POSITIONS OF THE MOST INTENSE ABSORPTION PEAKS OF U(IV) (UO <sub>2</sub> ), U(V) (U <sub>4</sub> O <sub>9</sub> ) AND U(VI) (Γ-UO <sub>3</sub> ) ARE MARKED WITH LINES. THE SHORT ENERGY RANGE SPECTRA ARE NORMALIZED BY THE MAXIMUM OF THE MOST INTENSE ABSORPTION PEAK WHEREAS THE EXTENDED ENERGY RANGE SPECTRA ARE NORMALIZED BY THE PRE- AND POST-EDGE. ....	94
FIGURE 52 U M <sub>4</sub> EDGE HR-XANES SPECTRA (SHORT (LEFT) AND EXTENDED (RIGHT) ENERGY RANGE) OF THE HBS SAMPLE S1, AND UNIRRADIATED UF1 MEASURED IN NOVEMBER 2015 AND 2016. THE ENERGY POSITIONS OF THE MOST INTENSE ABSORPTION PEAKS OF U(IV) (UO <sub>2</sub> ), U(V) (U <sub>4</sub> O <sub>9</sub> ) AND U(VI) (Γ-UO <sub>3</sub> ) ARE MARKED WITH LINES. THE SHORT ENERGY RANGE SPECTRA ARE NORMALIZED BY THE MAXIMUM OF THE MOST INTENSE ABSORPTION PEAK WHEREAS THE EXTENDED ENERGY RANGE SPECTRA ARE NORMALIZED BY THE PRE- AND POST-EDGE. THE NOVEMBER 2016 MEASUREMENT OF UF1 WAS ABORTED PREMATURELY....	95
FIGURE 53 U M <sub>4</sub> EDGE HR-XANES SPECTRA OF S3 AND UO <sub>2</sub> REFERENCE U3 MEASURED IN NOVEMBER 2016. FOR EVALUATION, THE SPECTRA WERE NORMALIZED TO THE PRE- AND POST-EDGE REGION (LEFT) AND TO THE MAXIMUM OF THE MAIN PEAK (RIGHT). THE ENERGY POSITION OF THE MOST INTENSE ABSORPTION PEAKS OF UO <sub>2</sub> IS MARKED WITH A VERTICAL LINE. ....	96
FIGURE 54 S3 AND UO <sub>2</sub> SPECTRA (BLACK) PLOTTED WITH THEIR BEST FIT (GREEN). THE FITTING FUNCTIONS USED TO FIT FEATURES A-F ARE SHOWN IN RED. THE DIFFERENCE BETWEEN THE BEST FIT SUM AND THE EXPERIMENTAL SPECTRUM IS GIVEN BELOW THE RESPECTIVE SPECTRA AS RESIDUAL.....	97
FIGURE 55. PU M <sub>5</sub> EDGE HR-XANES SPECTRA (SHORT (LEFT) AND EXTENDED (RIGHT) ENERGY RANGE) OF THE HBS SAMPLE S1, SNF SAMPLE S2 AND THE PUO <sub>2</sub> REFERENCE. THE ENERGY POSITIONS OF THE MOST INTENSE ABSORPTION PEAKS OF PU(III), PU(IV) AND PU(VI) IS MARKED WITH VERTICAL DASHED LINES. ....	98
FIGURE 56 PU M <sub>5</sub> EDGE HR-XANES SPECTRA (SHORT (LEFT) AND EXTENDED (RIGHT) ENERGY RANGE) OF THE HBS SAMPLE S3 AND THE PUO <sub>2</sub> REFERENCE. THE ENERGY POSITIONS OF THE MOST INTENSE ABSORPTION PEAKS OF PU(III), PU(IV) AND PU(VI) ARE MARKED WITH VERTICAL DASHED LINES. ....	99
FIGURE 57 KEGGIN STRUCTURE OF [PMO <sub>12</sub> O <sub>40</sub> ] <sup>3-</sup> . THE TETRAHEDRAL PO <sub>4</sub> <sup>3-</sup> -UNIT (PURPLE) IS CAGED BY 12 OCTAHEDRAL MOO <sub>4</sub> <sup>2-</sup> -UNITS (GREY). (REPRODUCED WITH PERMISSION FROM REF. <sup>232</sup> )	103
FIGURE 58 SEM MICROGRAPH OF CS <sub>3</sub> PMO <sub>12</sub> O <sub>40</sub> PARTICLES.....	103
FIGURE 59 POWDERED CS <sub>3</sub> PMO <sub>12</sub> O <sub>40</sub> IN A BEAKER. ....	104
FIGURE 60 GLASS FRAGMENTS OF SYNTHESIZED SAMPLES. ....	107

FIGURE 61 IR-SPECTRA OF THE GLASS FRIT, $CS_3PMO_{12}O_{40}$ AND THREE GLASS SAMPLES. ....	108
FIGURE 62 NORMALIZED AND BACKGROUND CORRECTED RAMAN SPECTRA OF THE SYNTHESIZED GLASS SAMPLES AND THREE CRYSTALLINE REFERENCES. ....	109
FIGURE 63 SEM PICTURE OF AN UNDISSOLVED $CS_3PMO_{12}O_{40}$ GRAIN IN SAMPLE VK-03-600.....	110
FIGURE 64 XRD PATTERN OF THE GLASS SAMPLES AND THREE CRYSTALLINE MOLYBDATE- REFERENCES. ....	110
FIGURE 65 CS LOSS AS FUNCTION OF THE VITRIFICATION TEMPERATURE DETERMINED BY CS AAS OF THE KOH DIGESTED GLASS SAMPLES.....	111
FIGURE 66 (A) TEM IMAGE OF A GLASS FRAGMENT WITH SEVERAL CRYSTALLINE STRUCTURES. (B) ONE CRYSTALLINE STRUCTURE WHICH WAS MEASURED AT DIFFERENT SPOTS. (C-E) DIFFRACTION PATTERN RECORDED AT SPOTS 1–3 (F-G) DARK FIELD IMAGES WHICH SHOW THE LATTICE DISTRIBUTION OF $BAMOO_4$ AND $CAMOO_4$ .....	112
FIGURE 67 FILLING LEVELS IN THE RECEIPT AND EVAPORATOR CONCENTRATE TANK AS FUNCTION OF THE TIME (LEFT). TEMPERATURE PROFILE OF THE SOLUTIONS IN BOTH TANKS UNTIL DRYNESS AND BEYOND (RIGHT). THE MOMENT OF DRYNESS IS INDICATED. (DATA FROM KTE GMBH <sup>10</sup> ).....	114
FIGURE 68 PHOTOGRAPHS OF THE EXPERIMENTAL SOLUTION IN THE DRYING PROCESS.....	120
FIGURE 69 MEASUREMENT OF THE VOLUME DECREASE BY TIME IN BLACK. THE SAMPLING TIME OF SAMPLE S1 TO S10 IS INDICATED BY LABELLED RED MARKS. THE FIRST OBSERVATION OF FLOATING CRYSTALS IS INDICATED WITH A GREEN VERTICAL BAR, THE DRYNESS OF THE MATERIAL WITH A BLUE VERTICAL BAR. ....	121
FIGURE 70 ELEMENT CONCENTRATION OF SELECTED ELEMENTS RE, CS, FE AND NA IN THE SIMULATE SOLUTION AS FUNCTION OF THE SOLUTIONS VOLUME (LEFT). DECREASE OF ELEMENT FRACTION WITH DECREASING VOLUME (RIGHT). THE VOLUME OF 0.34 L WHEN MOST COMPOUNDS START TO CRYSTALLIZE IS INDICATED WITH A VERTICAL DASHED BLACK LINE.....	121
FIGURE 71 PHOTOGRAPHS OF AREAS IN THE RESIDUAL MATERIAL WITH SIGNIFICANT DIFFERENT CHARACTERISTICS. “TWO LAYERS AREA” (LEFT), “ONE LAYER AREA” (MIDDLE) AND “BROWN AREA” (RIGHT).....	122
FIGURE 72 XRD PATTERN OF HOMOGENIZED RESIDUAL MATERIAL IN COMPARISON WITH REFLEX POSITIONS OBTAINED FROM AMCSD CRYSTAL STRUCTURE DATABASE. ....	123
FIGURE 73 SEM IMAGES OF SAMPLE MATERIAL FROM CRUST OF THE “TWO LAYER AREA” (LEFT) AND THE MIDDLE LAYER OF THE “THREE LAYER AREA” (RIGHT).....	125
FIGURE 74 SEM IMAGES OF LA AND NA RICH CRYSTALS IN NON-CRYSTALLINE MATRIX. ....	125
FIGURE 75 RAMAN SPECTRA OF SEVERAL SAMPLES FROM CHARACTERISTIC AREAS OF THE RESIDUAL MATERIAL COMPARED TO REFERENCE SPECTRA OF $NANO_3$ AND $CSREO_4$ . ....	126
FIGURE 76 IR SPECTRUM OF CRYSTALS FORMED EARLY IN THE DRYING PROCESS ON THE SOLUTIONS SURFACE AND THE CONTAINER WALL. FOR COMPARISON PURE $BA(NO_3)_2$ REFERENCE SPECTRUM IS SHOWN. THE MAIN ABSORPTION BANDS OF $BA(NO_3)_2$ ARE INDICATED BY VERTICAL DASHED BLACK LINES.....	127
FIGURE 77 RE AND CS LOSS FOR THE BA RICH AND REFERENCE GLASS SAMPLES SYNTHESIZED AT DIFFERENT VITRIFICATION TEMPERATURES. WHEREAS THE RE LOSS IS RELATES TO THE LEFT Y-AXIS THE CS LOSS IS DISPLAYED AT THE RIGHT Y-AXIS. ....	134
FIGURE 78 PHOTOGRAPHIC IMAGES OF THE SYNTHESIZED SAMPLES IN DIFFERENT HOST MATRICES: A) $TIO_2$ BOROSILICATE GLASS, B) $CSALTO_4$ , C) FLUOROPHOSPHATE GLASS, AND D) ETS-10.....	141
FIGURE 79 SEM MICROGRAPH OF A POLISHED BOROSILICATE GLASS (GREY HOMOGENOUS MATRIX) CONTAINING SIGNIFICANT AMOUNTS OF PD (BRIGHT SPHERICAL PARTICLE OF CA. 3 $\mu$ M DIAMETER) AND $RUO_2$ (FELTED SUBMICRON NEEDLE PARTICLES).....	147

FIGURE 80 SCHEMATIC ILLUSTRATION OF A LIQUID FED COLD-CAP STRUCTURING. ITS COMPOSITION IS RELATED TO THE TEMPERATURE GRADIENT. (REPRODUCED WITH PERMISSION FROM REF. 268) .....	149
FIGURE 81 PREPARATION OF THE DRIED HLLW SIMULATE WITH GLASS BEADS. THE MIX WAS HEATED ON A SAND BATH .....	151
FIGURE 82 SCHEMATIC ILLUSTRATIONS OF HIGH-TEMPERATURE FURNACE AND X-RAY CT SETUP. THE SAMPLE STAGE CAN BE TURNED FOR THE CT MEASUREMENT. THE DISTANCE BETWEEN THE X-RAY SOURCE, THE SAMPLE AND THE DETECTOR CAN BE VARIED IN ORDER TO DEFINE MAGNIFICATION AND SPATIAL RESOLUTION. ....	152
FIGURE 83 SYNTHESIZED GLASS SAMPLES FROM 500-1200 °C: A) B500, B) B600, C) B700, D) B800, E) B900, F) B1000, G) B1200.....	155
FIGURE 84 X-RAY CT MEASUREMENT OF A B1200 SPECIMEN (LEFT). GREEN AREAS INDICATE AREAS WITH HIGH X-RAY ABSORPTION. THIS CAN BE DUE TO HIGHER MATERIAL DENSITY AND/OR THE PRESENCE OF HEAVIER ELEMENTS. $\mu$ -XRF MAPPING OF RU AND PD OF B1200 SPECIMEN (MIDDLE). BRIGHTER AREAS INDICATE HIGH CONCENTRATION OF RE/PD. PHOTOGRAPH OF A B1200 SPECIMEN (RIGHT). THE UNITS OF THE SCALE ARE IN CM. ....	157
FIGURE 85 BACKSCATTERED ELECTRON MICROGRAPHS OF A POLISHED GLASS SAMPLE A) B600, B) B700, C) B800, D) B900, E) B1000, F) B1200.....	158
FIGURE 86 POWDER XRD PATTERN OF GLASS SAMPLES B500-B1200 IN ADDITION TO AN UNPROCESSED REFERENCE MATERIAL OF DRIED HLLW SIMULATE MIXED WITH GLASS POWDER. ....	159
FIGURE 87 CT CROSS-SECTIONS OF EXPERIMENT ISV-OX. THE PICTURES REPRESENT THE WHOLE SAMPLE VOLUME MELTED IN A SILICA TUBE.....	160
FIGURE 88 PHOTOGRAPHIC OBSERVATION OF THE EXHAUST GAS FORMATION IN THE UPPER SILICA TUBE END OF ISV-OX. YELLOW-BROWN COLOURING INDICATES THE FORMATION OF NO <sub>x</sub> GASSES. IN THE FIRST PHOTOGRAPH A STEAMING OF THE UPPER GLASS WALL CAN BE OBSERVED.....	161
FIGURE 89 RUO <sub>2</sub> AGGLOMERATES OF CA. 20 $\mu$ M SIZE FORMED IN SAMPLE ISV-POWDER. THE BRIGHT OBJECT IN THE LEFT MICROGRAPH IS A PD PARTICLE ALLOYED WITH CA. 6 WT% OF TE. BRIGHT SPOTS NEIGHBOURING THE SPINOUS RUO <sub>2</sub> STRUCTURES ARE ALSO PD PARTICLES..	162
FIGURE 90 POWDER XRD DIFFRACTOGRAMS OF THE ISV SAMPLES. IDENTIFIED PHASES ARE LABELLED WITH SYMBOLS. ....	163
FIGURE 91 PEAK AREAS OF THE PD REFLEX AT 40.1° AND THE PEAK AREA SUM OF THE RUO <sub>2</sub> REFLEXES AT 28.2° AND 35.3°. ....	163
FIGURE 92 X-RAY CT IMAGES OF A GLASS MELT CONTAINING LARGE NMP AGGLOMERATES, RECORDED EVERY 4 MIN. CLEARLY THE RISING MOVEMENT OF BLACK GAS BUBBLES CAN BE TRACKED. NMP DOMAINS APPEAR AS BRIGHT AREAS, DRAGGED BY CONVECTION FORCES IN A DIRECTED PATTERN (MARKED IN THE FIRST IMAGE WITH BLUE ARROWS).....	164
FIGURE 93 DECREASE OF RADIOACTIVITY IN CANADIAN SNF OVER TIME. (ADAPTED FROM NEA/RWM/IGSC(2006)3) <sup>27</sup> .....	177
FIGURE 94 G1-G4 GLASS SAMPLES MOUNTED IN A PLEXIGLASS CELL AND SEALED WITH TWO KAPTON WINDOWS 10 + 12.5 $\mu$ M.....	178
FIGURE 95 PU M <sub>5</sub> EDGE HR-XANES G1 SPECTRUM (BLACK) WITH ITS BEST FIT (GREEN). THE FITTING FUNCTIONS USED TO FIT FEATURES A-E ARE SHOWN IN RED. THE DIFFERENCE BETWEEN THE BEST FIT SUM AND THE EXPERIMENTAL SPECTRUM IS GIVEN BELOW THE SPECTRUM AS RESIDUAL. ....	179
FIGURE 96 BACKTRANSFORMED PU L <sub>3</sub> EDGE FT-EXAFS SPECTRA OF G1-G4 IN Q SPACE. EXPERIMENTAL DATA ARE SHOWN WITH COLORED SYMBOLS WHEREAS SOLID BLACK LINES REPRESENT BEST FIT RESULTS. ....	180
FIGURE 97 EMPTY SAMPLE HOLDER USED FOR AN M <sub>4,5</sub> HR-XANES INVESTIGATION (LEFT). THE INLAY (RIGHT) CAN BE EXCHANGED FOR DIFFERENT DESIGNS. ....	181

FIGURE 98 U M <sub>4</sub> EDGE HR-XANES SPECTRA OF S1 AT DIFFERENT SAMPLE POSITIONS. THE MAXIMUM OF THE U(IV) AND U(VI) REFERENCE MAIN PEAKS ARE INDICATED BY VERTICAL DASHED LINES. ....	182
FIGURE 99 PICTURES OF GLASS FRAGMENTS FROM ALL SYNTHESIZED WASTE GLASS SAMPLES. ....	185
FIGURE 100 HLLW SIMULATE SOLUTION WITH SEDIMENTED SOLID PARTICLES (LEFT) AND AFTER SLURRYING (RIGHT).....	186
FIGURE 101 TEMPERATURE PROFILES OF SET TEMPERATURE, TEMPERATURE OF SAMPLE ZONE AND SAMPLE TEMPERATURE.....	186
FIGURE 102 DRIED HLLW SIMULATE COVERING GLASS BEADS IN AN AL <sub>2</sub> O <sub>3</sub> CRUCIBLE (LEFT), HOT GLASS MELT IN A SECOND AL <sub>2</sub> O <sub>3</sub> CRUCIBLE WITHOUT CAP (RIGHT).....	186
FIGURE 103 PHOTOGRAPHS OF POLISHED GLASS SPECIMENS OF SAMPLE A) B600, B) B800, C) B900, D) B1000 AND E) B1200.....	187
FIGURE 104 EXHAUST GAS FORMATION OBSERVATION OF ISV-POWDER.....	187
FIGURE 105 CT OBSERVATIONS OF ISV-POWDER.....	188
FIGURE 106 EXHAUST GAS FORMATION OBSERVATION OF ISV-RED.....	188
FIGURE 107 CT OBSERVATIONS OF ISV-RED.....	189
FIGURE 108 PD PARTICLE WITH INCREASED SIZE OF CA. 5 μM FOUND IN THE ISV-RED SAMPLE. ....	189



## List of Symbols and Abbreviations

$\alpha$	Alpha
$\beta$	Beta
$\gamma$	Gamma
%	Percent
Å	Angstrom
$E_0$	Absorption edge energy
An	Actinides
ANKA	Angströmquelle Karlsruhe
at%	Atom percent
AAS	Atomic absorption spectroscopy
OES	Atomic emission spectroscopy
CANDU	Canada Deuterium Uranium
CAD software	Computer aided design software
FEFF	Computer program for quantum-chemical calculations
FITYK	Computer program for spectra analysis and modelling
N	Coordination number
DW	Debye-Waller factor
DCM	Double crystal monochromator
EDX	Energy dispersive X-ray spectroscopy
$\Delta E_0$	Energy shift
ESEM	Environmental Scanning Electron Microscope
ESRF	European Synchrotron Radiation Facility
EXAFS	Extended X-Ray absorption fine structure
FP	Fission products
FT	Fourier transform
FPS	Frames per second
FWHM	Full width half maximum
GWd/t <sub>HM</sub>	Giga-Watt-days per t heavy metals (U, Pu, ...)
r	Goodness of fit parameter
HWHM	Half width half maximum
HBRP	High Burnup Rim Project
HLLW	High liquid level waste
HLW	High-level waste
HR-XANES	High-resolution X-ray absorption near edge structure
ICP	Inductively coupled plasma
ICSD	Inorganic crystal structure database

<b>INE</b>	Institute for Nuclear Waste Disposal
<b>ATHENA</b>	Interactive program for XAFS analysis
<b>ARTEMIS</b>	Interactive program for XAFS fitting
<b>R</b>	Interatomic distance
<b>JHCM</b>	Joule-heated ceramic melter
<b>KIT</b>	Karlsruhe Institute of Technology
<b>Ln</b>	Lanthanides
<b>LWR</b>	Light water reactor
<b>MS</b>	Mass Spectroscopy
<b>MA</b>	Minor Actinides
<b>MAC-spectrometer</b>	Multi analyzer crystal spectrometer
<b>NMP</b>	Noble metal particles
<b>PNNL</b>	Pacific Northwest National Laboratory
<b>k</b>	Photoelectron's wavenumber
<b>h</b>	Planck's constant
<b>PGM</b>	Platinum group metals
<b>RIXS</b>	Resonant inelastic X-ray scattering
<b>SEM</b>	Scanning electron microscopy
<b>PNL</b>	<i>See PNNL</i>
<b>SAED</b>	Selected-area electron diffraction
<b>SSD</b>	Solid state detector
<b>SNF</b>	Spent nuclear fuel
<b>IFEFFIT</b>	Suite of interactive programs for XAFS analysis
<b>TEM</b>	Transmission electron microscopy
<b>UV-Vis</b>	Ultraviolet-visible
<b>U-235</b>	Uran with atomic mass of 235 u
<b>wt%</b>	Weight percent
<b>WL</b>	White line
<b>dk</b>	Width of the slit used in the FT windows
<b>XAFS</b>	X-ray absorption fine structure
<b>XANES</b>	X-ray absorption near edge structure
<b>XAS</b>	X-ray absorption spectroscopy
<b>XRD</b>	X-ray diffraction
<b>XES</b>	X-ray emission spectroscopy
<b>XRF</b>	X-ray fluorescence spectroscopy
<b>XPS</b>	X-ray photoelectron spectroscopy
<b>Zircaloy</b>	Zirconium alloy for fuel cladding

## List of Publications and Contributions

### Publications

Y. Podkovyrina, I. Pidchenko, T. Prüßmann, S. Bahl, J. Göttlicher, A. Soldatov, T. Vitova (2016). *Probing Covalency in the UO<sub>3</sub> Polymorphs by U M<sub>4</sub> edge HR-XANES*. 16th International Conference on X-ray Absorption Fine Structure, Karlsruhe.

### Conference contributions

S. Bahl *et al.*; *Comparative U, Np and Pu M edge high energy resolution X-ray absorption spectroscopy (HR-XANES) investigations of model and genuine active waste glass*, Second Joint Workshop on f-Element Chemistry **2015**, Karlsruhe, Deutschland. (Oral presentation)

S. Bahl *et al.*; *Advanced spectroscopic investigations of genuine active waste glass*, 2nd International Workshop on Advanced Techniques in Actinide Spectroscopy **2014**, Dresden, Deutschland. (Oral presentation)

S. Bahl, S.P. *et al.*; GDCh Wissenschaftsforum Chemie **2015**, Dresden, Deutschland. (Poster contribution)

S. Bahl, S.P. *et al.*; 16th International Conference on X-ray Absorption Fine Structure **2015**, Karlsruhe, Deutschland. (Poster contribution)

S. Bahl, S.P. *et al.*; Energy, Science & Technology Conference **2015**, Karlsruhe, Deutschland. (Poster contribution)

S. Bahl, S.P. *et al.*; European f-Element Chemistry Research Conference **2015**, Lissabon, Portugal. (Poster contribution)

S. Bahl, S.P. *et al.*; Actinide XAS Conference **2014**, Schloss Böttstein, Schweiz. (1<sup>st</sup> poster price)

S. Bahl, S.P. *et al.*; 22nd International Congress on X-Ray Optics and Microanalysis **2013**, Hamburg, Deutschland. (Poster contribution)



## **Curriculum Vitae**

Not available in the electronic version.



## List of References

1. W. N. Association, Radioactive Waste Management, <http://www.world-nuclear.org/information-library/nuclear-fuel-cycle/nuclear-wastes/radioactive-waste-management.aspx>, (accessed 20.02.17).
2. R. Böhler, A. Quaini, L. Capriotti, P. Çakır, O. Beneš, K. Boboridis, A. Guiot, L. Luzzi, R. J. M. Konings and D. Manara, *J Alloy Compd*, 2014, **616**, 5-13.
3. R. C. Ewing, *Nature Materials*, 2015, **14**, 252-257.
4. H. Geckeis, J. Lutzenkirchen, R. Polly, T. Rabung and M. Schmidt, *Chem Rev*, 2013, **113**, 1016-1062.
5. J. Rothe, S. Butorin, K. Dardenne, M. A. Denecke, B. Kienzler, M. Loble, V. Metz, A. Seibert, M. Steppert, T. Vitova, C. Walther and H. Geckeis, *Rev Sci Instrum*, 2012, **83**.
6. K. O. Kvashnina, S. M. Butorin, P. Martin and P. Glatzel, *Phys Rev Lett*, 2013, **111**.
7. K. Watanabe, T. Yano, K. Takeshita, K. Minami and E. Ochi, *Glass Technology: European Journal of Glass Science and Technology Part A*, 2012, **53**, 273-278.
8. W. Grunewald, G. Roth, W. Tobie, K. Weiss and S. Weisenburger, *Glass Technol-Part A*, 2008, **49**, 266-278.
9. C. Krause and B. Luckscheiter, *J Mater Res*, 1991, **6**, 2535-2546.
10. WAK-GmbH, Wiederaufarbeitungsanlage Karlsruhe, <http://www.ewn-gmbh.de/wak/rueckbauprojekte/wiederaufarbeitungsanlage-karlsruhe.html>, (accessed 03.01.17).
11. I. P. o. F. Materials, *Managing Spent Fuel from Nuclear Power Reactors - Experience and Lessons from Around the World*, International Panel on Fissile Materials, IPFM, 2011.
12. N. Bundesministerium für Umwelt, Bau und Reaktorsicherheit, *Journal*, 2015, 26.
13. O. N. a. IAEA, *Uranium 2014: Resources, Production and Demand - NEA No. 7209*, OECD, 2014.
14. B. Raj and P. R. V. Rao, For sustainable nuclear energy, a closed fuel cycle, <http://thebulletin.org/reprocessing-poised-growth-or-deaths-door/sustainable-nuclear-energy-closed-fuel-cycle>, (accessed 27.01.17).
15. H. Kleykamp, *Journal of Nuclear Materials*, 1985, **131**, 221-246.
16. R. J. M. Konings, T. Wiss and O. Beneš, *Nature Materials*, 2015, **14**, 247-252.
17. K. Lassmann, C. T. Walker, J. Vandelaar and F. Lindstrom, *Journal of Nuclear Materials*, 1995, **226**, 1-8.
18. N. E. A. (NEA), *Radioactive Waste in Perspective - NEA No. 6350*, OECD, 2010.
19. T. Wiss, J. P. Hiernaut, D. Roudil, J. Y. Colle, E. Maugeri, Z. Talip, A. Janssen, V. Rondinella, R. J. M. Konings, H. J. Matzke and W. J. Weber, *Journal of Nuclear Materials*, 2014, **451**, 198-206.
20. M. Kuroda and S. Yamanaka, *J Nucl Sci Technol*, 2002, **39**, 234-240.
21. D. W. Shoosmith, *Journal of Nuclear Materials*, 2000, **282**, 1-31.
22. B. Kienzler, A. Loida, W. Maschek and A. Rineiski, *Nucl Technol*, 2003, **143**, 309-321.
23. E. González-Robles, V. Metz, D. H. Wegen, M. Herm, D. Papaioannou, E. Bohnert, R. Gretter, N. Müller, R. Nasyrow, W. de Weerd, T. Wiss and B. Kienzler, *Journal of Nuclear Materials*, 2016, **479**, 67-75.
24. L. O. Werme and K. Spahiu, *J Alloy Compd*, 1998, **271**, 194-200.
25. B. Kienzler, M. Altmaier, C. Bube and V. Metz, *Radionuclide Source Term for HLW Glass, Spent Nuclear Fuel, and Compacted Hulls and End Pieces (CSD-C Waste)*, KIT, Karlsruhe, 2010.
26. B. Grambow, *Source Term for Performance Assessment of Spent Nuclear Fuel as a Waste Form EUR19140 Report*, 2000.

27. NEA, *CONSIDERATION OF TIMESCALES IN POST-CLOSURE SAFETY OF GEOLOGICAL DISPOSAL OF RADIOACTIVE WASTE - NEA/RWM/IGSC(2006)3*, NUCLEAR ENERGY AGENCY (NEA), 2006.
28. NEA-OECD, *SAFIR 2: Belgian R&D Programme on the Deep Disposal of High-level and Long-lived Radioactive Waste*, 2003.
29. B. Grambow, C. Landesman and S. Ribet, *Appl Geochem*, 2014, **49**, 237-246.
30. K. Maher, J. R. Bargar and G. E. Brown, *Inorg Chem*, 2013, **52**, 3510-3532.
31. A. Hedin, *Spent Nuclear Fuel - How Dangerous is it?*, Technical Report TR-97-13, SKB, 1997.
32. E. Vernaz, S. Gin and C. Veyer, in *Comprehensive Nuclear Materials*, Elsevier, Oxford, 2012, DOI: <http://dx.doi.org/10.1016/B978-0-08-056033-5.00107-5>, pp. 451-483.
33. M. I. Ojovan and W. E. Lee, in *An Introduction to Nuclear Waste Immobilisation (Second Edition)*, Elsevier, Oxford, 2014, DOI: <http://dx.doi.org/10.1016/B978-0-08-099392-8.00017-6>, pp. 245-282.
34. A. Dietzel, *Zeitschrift für Elektrochemie und angewandte physikalische Chemie*, 1942, **48**, 9-23.
35. X. Deschanel, S. Peugeot, J. N. Cachia and T. Charpentier, *Prog Nucl Energ*, 2007, **49**, 623-634.
36. R. Grünwald, Tobie, Fleisch, Schmitz, Weishaupt, *Proceedings of GLOBAL 2011*, 2011.
37. P. Frugier, S. Gin, Y. Minet, T. Chave, B. Bonin, N. Godon, J. E. Lartigue, P. Jollivet, A. Ayrat, L. De Windt and G. Santarini, *Journal of Nuclear Materials*, 2008, **380**, 8-21.
38. E. Vernaz, S. Gin, C. Jegou and I. Ribet, *Journal of Nuclear Materials*, 2001, **298**, 27-36.
39. E. Y. Vernaz and J. L. Dussossoy, *Appl Geochem*, 1992, **7**, 13-22.
40. S. Ribet and S. Gin, *Journal of Nuclear Materials*, 2004, **324**, 152-164.
41. T. Chave, P. Frugier, S. Gin and A. Ayrat, *Geochim Cosmochim Acta*, 2011, **75**, 4125-4139.
42. S. Gin, N. Godon, J. P. Mestre, E. Y. Vernaz and D. Beaufort, *Appl Geochem*, 1994, **9**, 255-269.
43. A. Abdelouas, J. L. Crovisier, W. Lutze, B. Grambow, J. C. Dran and R. Muller, *Journal of Nuclear Materials*, 1997, **240**, 100-111.
44. A. Abdelouas, J. L. Crovisier, W. Lutze, R. Muller and W. Bernotat, *Eur J Mineral*, 1995, **7**, 1101-1113.
45. P. Zimmer, E. Bohnert, D. Bosbach, J. I. Kim and E. Althaus, *Radiochim Acta*, 2002, **90**, 529-535.
46. O. Bouty, L. Ramond, P. L. Solari and S. Cammelli, *J Mater Sci*, 2016, **51**, 7918-7928.
47. S. Peugeot, J. N. Cachia, C. Jegou, X. Deschanel, D. Roudil, V. Broudic, J. M. Delaye and J. M. Bart, *Journal of Nuclear Materials*, 2006, **354**, 1-13.
48. J. de Bonfils, S. Peugeot, G. Panczer, D. de Ligny, S. Henry, P. Y. Noel, A. Chenet and B. Champagnon, *Journal of Non-Crystalline Solids*, 2010, **356**, 388-393.
49. J. M. Delaye, S. Peugeot, G. Bureau and G. Calas, *Journal of Non-Crystalline Solids*, 2011, **357**, 2763-2768.
50. B. Kienzler and A. Loida, *Endlagerrelevante Eigenschaften von hochradioaktiven Abfallprodukten. Charakterisierung und Bewertung. Empfehlung des Arbeitskreises HAW-Produkte.*, Forschungszentrum Karlsruhe, Karlsruhe, 2001.
51. M. Newville, *Fundamentals of XAFS*, University of Chicago, Chicago, 2004.
52. A. Einstein, *Annalen der Physik*, 1905, **322**, 132-148.
53. H. Hertz, *Annalen der Physik*, 1887, **267**, 983-1000.
54. T. Prüßmann, Characterization of bonding differences by advanced synchrotron based X-ray spectroscopy - KITopen ID: 1000052760, Doctoral Thesis, KIT, 2016.
55. S. D. Conradson, B. D. Begg, D. L. Clark, C. den Auwer, M. Ding, P. K. Dorhout, F. J. Espinosa-Faller, P. L. Gordon, R. G. Haire, N. J. Hess, R. F. Hess, D. W. Keogh, L. A. Morales,

- M. P. Neu, P. Paviet-Hartmann, W. Runde, C. D. Tait, D. K. Veirs and P. M. Vilella, *J Am Chem Soc*, 2004, **126**, 13443-13458.
56. I. Pidchenko, Characterization of structural properties of U and Pu in model systems by advanced synchrotron based X-ray spectroscopy - KITopen ID: 1000054271, , KIT, 2016.
  57. T. Vitova, K. O. Kvashnina, G. Nocton, G. Sukharina, M. A. Denecke, S. M. Butorin, M. Mazzanti, R. Caciuffo, A. Soldatov, T. Behrends and H. Geckeis, *Phys Rev B*, 2010, **82**.
  58. K. O. Kvashnina, S. M. Butorin and P. Glatzel, *J Anal Atom Spectrom*, 2011, **26**, 1265-1272.
  59. J. Stöhr, *NEXAFS Spectroscopy*, Springer-Verlag Berlin Heidelberg, Heidelberg, 1992.
  60. J. J. Rehr and R. C. Albers, *Rev Mod Phys*, 2000, **72**, 621-654.
  61. M. P. Seah and W. A. Dench, *Surface and Interface Analysis*, 1979, **1**, 2-11.
  62. J. Wong, *Materials Science and Engineering*, 1986, **80**, 107-128.
  63. M. Katsikini and E. C. Paloura, EXAFS: Extended X-ray Absorption Fine Structure, [http://users.auth.gr/~katsiki/EXAFS\\_IN.htm](http://users.auth.gr/~katsiki/EXAFS_IN.htm), (accessed 21.01.17).
  64. T. Vitova, X-ray absorption spectroscopy investigation of structurally modified lithium niobate crystals Doctoral thesis, 2008.
  65. L. J. P. Ament, M. van Veenendaal, T. P. Devereaux, J. P. Hill and J. van den Brink, *Rev Mod Phys*, 2011, **83**.
  66. K. O. Kvashnina, Y. O. Kvashnin and S. M. Butorin, *J Electron Spectrosc*, 2014, **194**, 27-36.
  67. P. Glatzel and U. Bergmann, *Coordin Chem Rev*, 2005, **249**, 65-95.
  68. T. Vitova, M. A. Denecke, J. Göttlicher, K. Jorissen, J. J. Kas, K. Kvashnina, T. Prüßmann, J. J. Rehr and J. Rothe, *Journal of Physics: Conference Series*, 2013, **430**.
  69. T. Vitova, I. Pidchenko, D. Fellhauer, P. S. Bagus, Y. Joly, T. Prüßmann, S. Bahl, E. Gonzalez-Robles, J. Rothe, M. Altmaier, M. Denecke and H. Geckeis, *Nature Communications*, 2017, **submitted**.
  70. M. O. Krause and J. H. Oliver, *J Phys Chem Ref Data*, 1979, **8**, 329-338.
  71. G. Bunker, *Introduction to XAFS*, Cambridge University Press, Cambridge, 2010.
  72. F. M. F. de Groot, M. H. Krisch and J. Vogel, *Phys Rev B*, 2002, **66**.
  73. K. Hamalainen, D. P. Siddons, J. B. Hastings and L. E. Berman, *Phys Rev Lett*, 1991, **67**, 2850-2853.
  74. K. Dardenne, E. Gonzalez-Robles, J. Rothe, N. Muller, G. Christill, D. Lemmer, R. Praetorius, B. Kienzler, V. Metz, G. Roth and H. Geckeis, *Journal of Nuclear Materials*, 2015, **460**, 209-215.
  75. B. Brendebach, N. L. Banik, C. M. Marquardt, J. Rothe, M. A. Denecke and H. Geckeis, *Radiochim Acta*, 2009, **97**, 701-708.
  76. A. Walshe, T. Prüßmann, T. Vitova and R. J. Baker, *Dalton T*, 2014, **43**, 4400-4407.
  77. P. J. Panak and A. Geist, *Chem Rev*, 2013, **113**, 1199-1236.
  78. T. Vitova, J. C. Green, R. G. Denning, M. Löble, K. Kvashnina, J. J. Kas, K. Jorissen, J. J. Rehr, T. Malcherek and M. A. Denecke, *Inorg Chem*, 2015, **54**, 174-182.
  79. J. L. Campbell and T. Papp, *Atom Data Nucl Data*, 2001, **77**, 1-56.
  80. T. Vitova, J. C. Green, R. G. Denning, M. Löble, K. Kvashnina, J. J. Kas, K. Jorissen, J. J. Rehr, T. Malcherek and M. A. Denecke, *Inorg Chem*, 2014, DOI: 10.1021/ic5020016.
  81. H. Dau, J. Dittmer, L. Iuzzolino, H. Schiller, W. Dörner, I. Heinze, V. A. Sole and Nolting, *Journal De Physique. IV : JP*, 1997, **7**, C2-607-C602-610.
  82. V. Veselská, R. Fajgar, S. Číhalová, R. M. Bolanz, J. Göttlicher, R. Steininger, J. A. Siddique and M. Komárek, *J Hazard Mater*, 2016, **318**, 433-442.
  83. I. Mantouvalou, K. Witte, D. Grotzsch, M. Neitzel, S. Gunther, J. Baumann, R. Jung, H. Stiel, B. Kanngiesser and W. Sandner, *Rev Sci Instrum*, 2015, **86**.
  84. Synchrotron Soleil, France, <http://www.synchrotron-soleil.fr/portal/page/portal/IndustrieValorisation/EquipementIndustrie>, (accessed 11.01.17).
  85. F. de Groot and A. Kotani, *Core Level Spectroscopy of Solids*, CRC Press, Boca Ratn, 2008.

86. S. Bahl, HYIG Webpage, <http://www.ine.kit.edu/127.php>, (accessed 08.01.16).
87. H. O. Moser, *J Alloy Compd*, 2001, **328**, 42-49.
88. A. Zimina, K. Dardenne, M. A. Denecke, J. D. Grunwaldt, E. Huttel, H. Lichtenberg, S. Mangold, T. Pruessmann, J. Rothe, R. Steininger and T. Vitova, *Journal of Physics: Conference Series*, 2016, **712**, 012019.
89. H. H. Johann, *Zeitschrift für Physik*, 1931, **69**, 185-206.
90. E. Kleymenov, J. A. van Bokhoven, C. David, P. Glatzel, M. Janousch, R. Alonso-Mori, M. Studer, M. Willmann, A. Bergamaschi, B. Henrich and M. Nachtegaal, *Rev Sci Instrum*, 2011, **82**.
91. B. L. Henke, E. M. Gullikson and J. C. Davis, *Atom Data Nucl Data*, 1993, **54**, 181-342.
92. Bruker, OPUS Spektroskopiesoftware, <https://www.bruker.com/de/products/infrared-near-infrared-and-raman-spectroscopy/opus-spectroscopy-software.html>, (25.02.17).
93. C. Gauthier, V. A. Sole, R. Signorato, J. Goulon and E. Moguiline, *J Synchrotron Radiat*, 1999, **6**, 164-166.
94. V. A. Sole, E. Papillon, M. Cotte, P. Walter and J. Susini, *Spectrochim Acta B*, 2007, **62**, 63-68.
95. OriginLab, <http://www.originlab.de/>, (accessed 21.02.17).
96. D. Prieur, U. Carvajal-Nunez, T. Vitova and J. Somers, *Eur J Inorg Chem*, 2013, DOI: 10.1002/ejic.201201294, 1518-1524.
97. D. Fellhauer, V. Neck, M. Altmaier, J. Lutzenkirchen and T. Fanghanel, *Radiochim Acta*, 2010, **98**, 541-548.
98. D. Fellhauer, J. Rothe, M. Altmaier, V. Neck, J. Runke, T. Wiss and T. Fanghaenel, *Radiochim Acta*, 2016, **104**, 355-379.
99. X. Gaona, D. Fellhauer and M. Altmaier, *Pure Appl Chem*, 2013, **85**, 2027-2049.
100. D. Fellhauer, V. Neck, M. Altmaier, J. Lützenkirchen and T. Fanghänel, *Radiochimica Acta International journal for chemical aspects of nuclear science and technology*, 2010, **98**, 541-548.
101. D. Fellhauer, J. Rothe, M. Altmaier, V. Neck, J. Runke, T. Wiss and T. Fanghänel, *Radiochimica Acta*, 2016, **104**, 355-379.
102. A. L. Smith, P. Martin, D. Prieur, A. C. Scheinost, P. E. Raison, A. K. Cheetharn and R. J. M. Konings, *Inorg Chem*, 2016, **55**, 1569-1579.
103. A. L. Smith, P. E. Raison and R. J. M. Konings, *Journal of Nuclear Materials*, 2011, **413**, 114-121.
104. C. M. Jantzen, *Journal of Non-Crystalline Solids*, 1986, **84**, 215-225.
105. C. P. Kaushik, *Procedia Materials Science*, 2014, **7**, 16-22.
106. G. Deissmann, S. Neumeier, F. Brandt, G. Modolo and D. Bosbach, *Materials Research Society Symposium Proceedings*, 2014, **1665**, 23-30.
107. J. D. Vienna, D. L. Alexander, H. Li, M. J. Schweiger, D. K. Peeler and T. F. Meaker, *Plutonium dioxide dissolution in glass*, Pacific Northwest National Laboratory, Richland, 1996.
108. X. Feng, H. Li, L. L. Li, J. G. Darab, M. J. Schweiger, J. D. Vienna, B. C. Bunker, P. G. Allen, J. J. Bucher, I. M. Craig, N. M. Edelstein, D. K. Shuh, R. C. Ewing, L. M. Wang and E. R. Vance, *Ceramic Transactions*, 1999, **93**.
109. H. D. Schreiber and G. B. Balazs, *Phys Chem Glasses*, 1982, **23**, 139-146.
110. I. Pidchenko, Y. O. Kvashnin, T. Yokosawa, N. Finck, S. Bahl, D. Schild, R. Polly, E. Bohnert, A. Rossberg, J. Göttlicher, K. Dardenne, J. Rothe, T. Schäfer, H. Geckeis and T. Vitova, *Environmental Science & Technology*, 2017.
111. K. Popa, D. Prieur, D. Manara, M. Najji, J. F. Vigier, P. M. Martin, O. D. Blanco, A. C. Scheinost, T. Prussmann, T. Vitova, P. E. Raison, J. Somers and R. J. M. Konings, *Dalton T*, 2016, **45**, 7847-7855.
112. J. M. Delaye and D. Ghaleb, *CEA/Valrho Summer Session Proceedings*, 1997, 87.

113. J. N. Cachia, X. Deschanel, C. Den Auwer, O. Pinet, J. Phalippou, C. Hennig and A. Scheinost, *Journal of Nuclear Materials*, 2006, **352**, 182-189.
114. B. Ravel and M. Newville, *J Synchrotron Radiat*, 2005, **12**, 537-541.
115. S. Kelly, Basics of EXAFS data analysis,  
[http://xafs.org/Tutorials?action=AttachFile&do=get&target=Basics\\_of\\_XAFS\\_to\\_chi.pdf](http://xafs.org/Tutorials?action=AttachFile&do=get&target=Basics_of_XAFS_to_chi.pdf),  
(accessed 06.03.17).
116. J. J. Rehr, J. J. Kas, F. D. Vila, M. P. Prange and K. Jorissen, *Phys Chem Chem Phys*, 2010, **12**, 5503-5513.
117. S. D. Conradson, B. D. Begg, D. L. Clark, C. Den Auwer, F. J. Espinosa-Faller, P. L. Gordon, N. J. Hess, R. Hess, D. W. Keogh, L. A. Morales, M. P. Neu, W. Runde, C. D. Tait, D. K. Veirs and P. M. Vilella, *Inorg Chem*, 2003, **42**, 3715-3717.
118. D. Hudry, C. Apostolidis, O. Walter, A. Janssen, D. Manara, J. C. Griveau, E. Colineau, T. Vitova, T. Prussmann, D. Wang, C. Kubel and D. Meyer, *Chem-Eur J*, 2014, **20**, 10431-10438.
119. D. L. Clark, in *Challenges in Plutonium Science*, 2000, vol. 26, pp. 364-381.
120. P. C. Burns, R. C. Ewing and F. C. Hawthorne, *Can Mineral*, 1997, **35**, 1551-1570.
121. Y. Podkovyrina, I. Pidchenko, T. Pruessmann, S. Bahl, J. Göttlicher, A. Soldatov and T. Vitova, *16th International Conference on X-ray Absorption Fine Structure (XAFS16)*, 2016.
122. G. G. Christoph, A. C. Larson, P. G. Eller, J. D. Purson, J. D. Zahrt, R. A. Penneman and G. H. Rinehart, *Acta Crystallographica Section B*, 1988, **44**, 575-580.
123. L. R. Morss, N. M. Edelstein, J. Fuger and J. J. Katz, eds., *The chemistry of the actinide and transactinide elements: Neptunium, Plutonium and Americium*, Springer, Dordrecht, 2006.
124. B. O. Loopstra, *Acta Crystallogr*, 1964, **17**, 651-&.
125. L. Desgranges, G. Baldinozzi, D. Simeone and H. E. Fischer, *Inorg Chem*, 2016, **55**, 7485-7491.
126. N. J. Hess, W. J. Weber and S. D. Conradson, *Journal of Nuclear Materials*, 1998, **254**, 175-184.
127. A. J. Gaunt, I. May, M. P. Neu, S. D. Reilly and B. L. Scott, *Inorg Chem*, 2011, **50**, 4244-4246.
128. F. Farges, C. W. Ponader, G. Calas and G. E. Brown, *Geochim Cosmochim Ac*, 1992, **56**, 4205-4220.
129. K. Servaes, C. Hennig, I. Billard, C. Gaillard, K. Binnemans, C. Görrler-Walrand and R. Van Deun, *Eur J Inorg Chem*, 2007, DOI: 10.1002/ejic.200700475, 5120-5126.
130. J. C. Taylor and M. H. Mueller, *Acta Crystallogr*, 1965, **19**, 536-&.
131. N. A. Stump, R. G. Haire and S. Dai, *Materials Research Society Symposium - Proceedings*, 1997, **465**, [d]47-54.
132. S. V. Stefanovsky, A. A. Shiryayev, Y. V. Zubavichus and J. C. Marra, *Materials Research Society Symposium Proceedings*, 2010, **1264**, 21-26.
133. C. Buchsbaum, S. Hohler-Schlimm and S. Rehme, *Struct Bond*, 2010, **134**, 37-58.
134. *Waste Acceptance Product Specifications (WAPS) For Vitrified High Level Waste Forms*, United States Department of Energy, 2012.
135. G. R. Lumpkin, *Elements*, 2006, **2**, 365-372.
136. W. J. Weber and F. P. Roberts, *Nucl Technol*, 1983, **60**, 178-198.
137. G. Calas, *Geochim Cosmochim Ac*, 1979, **43**, 1521-1531.
138. H. R. Halse, Using synchrotron radiation to determine the oxidation state of uranium in magmas Ph.D. thesis, Imperial College London.
139. R. J. Short, R. J. Hand, N. C. Hyatt and G. Mobus, *Journal of Nuclear Materials*, 2005, **340**, 179-186.
140. G. Roth and S. Weisenburger, *Nucl Eng Des*, 2000, **202**, 197-207.
141. H. Geckeis and T. Stumpf, *Annual Report 2010 - Institute for Nuclear Waste Disposal*, Institute for Nuclear Waste Disposal, Karlsruhe, 2010.

142. C. Hahlweg, W. Zhao and H. Rothe, 2012, **8487**, 84870S-84870S-84879.
143. R. J. P. Driscoll, D. Wolverson, J. M. Mitchels, J. M. Skelton, S. C. Parker, M. Molinari, I. Khan, D. Geeson and G. C. Allen, *Rsc Adv*, 2014, **4**, 59137-59149.
144. S. Matsika, Z. Zhang, S. R. Brozell, J. P. Baudeau, Q. Wang and R. M. Pitzer, *J Phys Chem A*, 2001, **105**, 3825-3828.
145. P. J. Hay, R. L. Martin and G. Schreckenbach, *J Phys Chem A*, 2000, **104**, 6259-6270.
146. M. J. Sarsfield, R. J. Taylor, C. Puxley and H. M. Steele, *Journal of Nuclear Materials*, 2012, **427**, 333-342.
147. J. Petiau, G. Calas, D. Petitmaire, A. Bianconi, M. Benfatto and A. Marcelli, *Phys Rev B*, 1986, **34**, 7350-7361.
148. N. Ollier, M. J. Guittet, M. Gautier-Soyer, G. Panczer, B. Champagnon and P. Jollivet, *Opt Mater*, 2003, **24**, 63-68.
149. G. Gasperi, L. Amidani, F. Benedetti, F. Boscherini, P. Glatzel, S. Valeri and P. Luches, *Phys Chem Chem Phys*, 2016, **18**, 20511-20517.
150. W. Grünewald, G. Roth, W. Tobie and K. Weiß, *Waste Management WM'00 Conference*, 2000.
151. N. Metrich, J. Susini, L. Galois, G. Calas, M. Bonnin-Mosbah and B. Menez, *J Phys Iv*, 2003, **104**, 393-397.
152. M. Wilke, P. J. Jugo, K. Klimm, J. Susini, R. Botcharnikov, S. C. Kohn and M. Janousch, *Am Mineral*, 2008, **93**, 235-240.
153. S. J. Wu, O. Beermann, S. A. Wang, A. Holzheid, W. Depmeier, T. Malcherek, G. Modolo, E. V. Alekseev and T. E. Albrecht-Schmitt, *Chem-Eur J*, 2012, **18**, 4166-4169.
154. F. Demartin, C. M. Gramaccioli and T. Pilati, *Acta Crystallogr C*, 1992, **48**, 1-4.
155. D. P. Shashkin, E. A. Lure and N. V. Belov, *Kristallografiya+*, 1974, **19**, 958-963.
156. D. Ginderow, *Acta Crystallogr C*, 1988, **44**, 421-424.
157. J. J. Yang, T. Regier, J. J. Dynes, J. Wang, J. Y. Shi, D. Peak, Y. D. Zhao, T. D. Hu, Y. X. Chen and J. S. Tse, *Anal Chem*, 2011, **83**, 7856-7862.
158. J. Goettlicher, A. Kotelnikov, N. Suk, A. Kovalski, T. Vitova and R. Steininger, *Z Kristallogr*, 2013, **228**, 157-171.
159. H. Geckeis and T. Stumpf, *Annual Report 2011 - Institute for Nuclear Waste Disposal*, Institute for Nuclear Waste Disposal, Karlsruhe, 2011.
160. P. Frugier, C. Martin, I. Ribet, T. Advocat and S. Gin, *Journal of Nuclear Materials*, 2005, **346**, 194-207.
161. D. Fellhauer, Untersuchungen zur Redoxchemie und Löslichkeit von Neptunium und Plutonium, Heidelberg, Univ., Diss., 2013, 2013.
162. M. S. Grigor'ev and N. N. Krot, *Radiochemistry*, 2010, **52**, 375-381.
163. P. Carbol, D. H. Wegen, T. Wiss and P. Fors, in *Comprehensive Nuclear Materials*, Elsevier, Oxford, 2012, DOI: <http://dx.doi.org/10.1016/B978-0-08-056033-5.00106-3>, pp. 389-420.
164. V. V. Rondinella and T. Wiss, *Mater Today*, 2010, **13**, 24-32.
165. T. Sonoda, M. Kinoshita, I. L. F. Ray, T. Wiss, H. Thiele, D. Pellottiero, V. V. Rondinella and H. Matzke, *Nuclear Instruments and Methods in Physics Research Section B: Beam Interactions with Materials and Atoms*, 2002, **191**, 622-628.
166. M. L. Bleiberg, R. M. Berman and B. Lustman, *Effects of high burn-up on oxide ceramic fuels*, IAEA, International Atomic Energy Agency (IAEA), 1963.
167. D. Klein, W. Baer and G. G. Smith, *Nucl Sci Eng*, 1958, **3**, 698-706.
168. J. Spino and D. Papaioannou, *Journal of Nuclear Materials*, 2000, **281**, 146-162.
169. C. Ronchi, M. Sheindlin, D. Staicu and M. Kinoshita, *Journal of Nuclear Materials*, 2004, **327**, 58-76.
170. J. Spino, J. Rest, W. Goll and C. T. Walker, *Journal of Nuclear Materials*, 2005, **346**, 131-144.
171. R. Manzel and C. T. Walker, *Journal of Nuclear Materials*, 2002, **301**, 170-182.

172. D. Baron, *HBEP Steering Committee Meeting*, 1986.
173. M. Kinoshita, T. Sonoda, S. Kitajima, A. Sasahara, T. Kameyama, T. Matsumura, E. Kolstad, V. V. Rondinella, C. Ronchi, J. P. Hiernaut, T. Wiss, F. Kinnart, J. Ejton, D. Papaioannou and H. Matzke, *Proceedings of the 2004 International Meeting on LWR Fuel Performance*, 2004, 207-213.
174. O. N. a. IAEA, *Fission gas release and fuel rod chemistry related to extended burnup*, IAEA, Austria, 1992.
175. IAEA, *Water reactor fuel element modelling at high burnup and its experimental support*, Austria, 1994.
176. D. H. Wegen, S. Bremier and D. Pellottiero, *SEM Study on High Burn-up Fuel - JRC104732*, 2016.
177. P. Taylor, D. D. Wood, D. G. Owen and G. I. Park, *Journal of Nuclear Materials*, 1991, **183**, 105-114.
178. R. J. McEachern and P. Taylor, *Journal of Nuclear Materials*, 1998, **254**, 87-121.
179. F. Valdivieso, V. Francon, F. Byasson, M. Pijolat, A. Feugier and V. Peres, *Journal of Nuclear Materials*, 2006, **354**, 85-93.
180. E. Gonzalez-Robles, *Study of Radionuclide Release in Commercials UO<sub>2</sub> Spent Nuclear Fuels Docoral Thesis*, Universitat Politècnica de Catalunya, 2011.
181. I. J. Hastings, D. H. Rose, J. R. Kelm, D. A. Irvine and J. Novak, *Journal of the American Ceramic Society*, 1986, **69**, C-16-C-17.
182. B. D. Hanson, *The Burnup Dependence of Light Water Reactor Spent Fuel Oxidation - PNNL-11929*, PNNL, 1998.
183. H. R. Hoekstra and S. Siegel, *Journal of Inorganic and Nuclear Chemistry*, 1961, **18**, 154-165.
184. P. Taylor, D. D. Wood, A. M. Duclos and D. G. Owen, *Journal of Nuclear Materials*, 1989, **168**, 70-75.
185. J. Novak, I. J. Hastings, E. Mizzan and R. J. Chenier, *Nucl Technol*, 1983, **63**, 254-265.
186. D. G. Boase and T. T. Vandergraaf, *Nucl Technol*, 1977, **32**, 60-71.
187. R. E. Einziger and J. A. Cook, *Nucl Technol*, 1985, **69**, 55-71.
188. L. E. Thomas and R. E. Einziger, *Mater Charact*, 1992, **28**, 149-156.
189. S. Aronson, R. B. Roof Jr and J. Belle, *The Journal of Chemical Physics*, 1957, **27**, 137-144.
190. P. E. Blackburn, J. Weissbart and E. A. Gulbransen, *J Phys Chem-Us*, 1958, **62**, 902-908.
191. I. F. Ferguson and J. D. M. McConnell, *Proceedings of the Royal Society of London. Series A. Mathematical and Physical Sciences*, 1957, **241**, 67-79.
192. P. Taylor, D. D. Wood and A. M. Duclos, *Journal of Nuclear Materials*, 1992, **189**, 116-123.
193. K. K. Bae, B. G. Kim, Y. W. Lee, M. S. Yang and H. S. Park, *Journal of Nuclear Materials*, 1994, **209**, 274-279.
194. T. K. Campbell, E. R. Gilbert, G. D. White, G. F. Piepel and B. J. Wrona, *Nucl Technol*, 1989, **85**, 160-171.
195. J. S. Anderson, L. E. J. Roberts and E. A. Harper, *J Chem Soc*, 1955, DOI: <http://dx.doi.org/10.1039/jr9550003946>, 3946-3959.
196. P. Taylor, E. A. Burgess and D. G. Owen, *Journal of Nuclear Materials*, 1980, **88**, 153-160.
197. K. M. Wasywich, W. H. Hocking, D. W. Shoemsmith and P. Taylor, *Nucl Technol*, 1993, **104**, 309-329.
198. C. Jegou, M. Gennisson, S. Peugeot, L. Desgranges, G. Guimbretiere, M. Magnin, Z. Talip and P. Simon, *Journal of Nuclear Materials*, 2015, **458**, 343-349.
199. J. Cobos, D. Papaioannou, J. Spino and M. Coquerelle, *J Alloy Compd*, 1998, **271**, 610-615.
200. T. Fanghänel, V. V. Rondinella, J. P. Glatz, T. Wiss, D. H. Wegen, T. Gouder, P. Carbol, D. Serrano-Purroy and D. Papaioannou, *Inorg Chem*, 2013, **52**, 3491-3509.
201. T. K. Campbell, E. R. Gilbert, C. K. Thornhill and B. J. Wrona, *Nucl Technol*, 1989, **84**, 182-195.

202. P. Taylor, *Journal of Nuclear Materials*, 2005, **344**, 206-212.
203. J. M. Haschke and V. M. Oversby, *Journal of Nuclear Materials*, 2002, **305**, 187-201.
204. M. Altmaier, X. Gaona and T. Fanghänel, *Chem Rev*, 2013, **113**, 901-943.
205. R. Vauchy, A. C. Robisson, R. C. Belin, P. M. Martin, A. C. Scheinost and F. Hodaj, *Journal of Nuclear Materials*, 2015, **465**, 349-357.
206. P. N. Laboratory, *Characterization of Spent Fuel Approved Testing Material-ATM-103 - PNL-5109-103*, Materials Characterization Center - PNL, 1988.
207. A. J. Kropf, J. A. Fortner, R. J. Finch, J. C. Cunnane and C. Karanfil, *Physica Scripta T*, 2005, **T115**, 998-1000.
208. J. A. Fortner, A. J. Kropf, J. L. Jerden and J. C. Cunnane, *Materials Research Society Symposium Proceedings*, 2007, **985**, 21-26.
209. S. Anthonysamy, K. Joseph, T. Gnanasekaran and P. R. V. Rao, *Journal of Nuclear Materials*, 2000, **280**, 25-32.
210. J. A. Fortner, R. J. Finch, A. J. Kropf and J. C. Cunnane, *Geochim Cosmochim Acta*, 2005, **69**, A475-A475.
211. R. J. Ackermann, R. J. Thorn and G. H. Winslow, *J. Opt. Soc. Am.*, 1959, **49**, 1107-1111.
212. R. Bohler, M. J. Welland, D. Prieur, P. Cakir, T. Vitova, T. Pruessmann, I. Pidchenko, C. Hennig, C. Gueneaud, R. J. M. Konings and D. Manara, *Journal of Nuclear Materials*, 2014, **448**, 330-339.
213. L. Troger, D. Arvanitis, K. Baberschke, H. Michaelis, U. Grimm and E. Zschech, *Phys Rev B*, 1992, **46**, 3283-3289.
214. V. Metz, E. González-Robles and B. Kienzler, *Characterization of UOX fuel segments irradiated in the Gösgen pressurized water reactor*, KIT, Karlsruhe 2014.
215. K. Lemmens, E. González-Robles, B. Kienzler, E. Curti, D. Serrano-Purroy, R. Sureda, A. Martínez-Torrents, O. Roth, E. Slonszki, T. Mennecart, I. Günther-Leopold and Z. Hózer, *Journal of Nuclear Materials*, 2017, **484**, 307-323.
216. F. Cappia, M. Uhlig, L. Velnom, K. Sauer, M. Kirschner, G. Montagnier, G. Paperini, B. Cremer, M. Ernstberger, T. Wiss and V. Rondinella, *Spent nuclear fuel (SNF) sample preparation for synchrotron measurements - JRC report JRC-Karlsruhe*, Eggenstein-Leopoldshafen, 2016.
217. M. Kelm and E. Bohnert, *P Indian as-Chem Sci*, 2002, **114**, 697-704.
218. DuPont, Material specifications - Kapton Films, [http://www.goba.de/pics/service\\_support/c/Eigenschaften%20und%20Daten%20-%20Kapton.pdf](http://www.goba.de/pics/service_support/c/Eigenschaften%20und%20Daten%20-%20Kapton.pdf), (accessed 16.02.17).
219. L. Desgranges, G. Baldinozzi, G. Rousseau, J.-C. Nièpce and G. Calvarin, *Inorg Chem*, 2009, **48**, 7585-7592.
220. K. O. Kvashnina and F. M. F. de Groot, *J Electron Spectrosc*, 2014, **194**, 88-93.
221. G. C. Allen, P. A. Tempest and J. W. Tyler, *Philos Mag B*, 1986, **54**, L67-L71.
222. *Journal*, 2015.
223. S. Van Winckel, C. Apostolidis, D. Bouexière, M. Ernstberger, R. Konings, B. Negreanu, G. Pagliosa, D. Papaioannou, P. Raison, A. Walschburger, O. Walther and J.-P. Glatz, *JRC Scientific and Technical Reports*, 2011.
224. W. Lutze and R. Ewing, *Radioactive Wasteforms for the Future*, Amsterdam, 1988.
225. S. Bahl, Diploma thesis, Karlsruhe Institut für Technology (KIT), 2013.
226. W. Grünewald, G. Roth, S. Hilpp, W. Tobie, A. Salimi, S. Weisenburger and B. Brendebach, Paris, 2009.
227. V. Koldeisz, Structural investigations of caesium phosphomolybdate and uranium loaded borosilicate glass systems, Budapest University of Technology and Economics, 2014.
228. M. T. Pope and A. Müller, *Angewandte Chemie International Edition in English*, 1991, **30**, 34-48.
229. N. Mizuno and M. Misono, *Chemical Reviews*, 1998, **98**, 199-218.

230. I. V. Kozhevnikov, *Chemical Reviews*, 1998, **98**, 171-198.
231. T. Okuhara, N. Mizuno and M. Misono, *Journal*, 1996, **41**, 113-252.
232. Keggin Anion, <http://verahill.blogspot.de/2012/03/molecules.html>, (accessed 15.02.17).
233. K. Eguchi, N. Yamazoe and T. Seiyama, *Nippon Kagaku Kaishi*, 1981, 336-342.
234. T. Ressler, J. Wienold and O. Timpe, *Physica Scripta T*, 2005, **T 115**, 66-71.
235. B. Grambow, R. Müller, A. Rother and W. Lutze, *Radiochim Acta*, 1991, **52-53**, 501-506.
236. G. Roth and S. Weisenburger, *Verifizierung der Eintrocknung der hochradioaktiven Lösungen in den VEK Behältern 841 BB 02 und 845 BB 03 nach der HAWC Verglasung* Report Bestell-Nr. 722/3000/4500129886, KIT-INE, 2014.
237. A. Seither, *Analysis No. KZ-43*, KIT-INE, 2011.
238. P. Estevenon, *Characterization of Tc- and Cs- rich solid waste residuals originating from operations of high level liquid waste vitrification*, ENSCM, 2014.
239. J. G. Darab and P. A. Smith, *Chem Mater*, 1996, **8**, 1004-1021.
240. L. Bencivenni, H. M. Nagarathna and K. A. Gingerich, *Chem Phys Lett*, 1983, **99**, 258-261.
241. H. T. Blair, *Nucl Technol*, 1980, **49**, 267-273.
242. M. Lüdeke, H. Tietze-Jaensch and R. Odoj, *Handbuch zur Verfahrensqualifikation (HVQ) der Verglasungseinrichtung Karlsruhe (VEK) : PKS\_TECDOC-04-003-01 ; Index: 01 vom 13.04.2005*, FZJ, Institut für Sicherheitsforschung und Reaktortechnik, Jülich, 2005.
243. C. P. Kaushik, R. K. Mishra, P. Sengupta, A. Kumar, D. Das, G. B. Kale and K. Raj, *Journal of Nuclear Materials*, 2006, **358**, 129-138.
244. S. Bahl, *Spektroskopische und mikroskopische Charakterisierung verglasteter Mo/P/Zr/Cs-reicher HLW-Simulat-Rückstände* Diploma thesis, KIT, 2013.
245. L. Ojovan, *An Introduction to Nuclear Waste Immobilisation*, Elsevier Science, 2005.
246. A. Beck, *Verglasung rhenium- und cäsiumreicher HLW-Simulatrückstände in einem bariumreichen Borosilikatglas bei 950 °C*, KIT-INE, Karlsruhe, 2016.
247. B. Allard and B. Torstenfelt, *On the solubility of technetium in geochemical systems*, Report SKBF-KBS-TR-83-60, 1983.
248. D. Banerjee, V. K. Sudarsan, A. Joseph, R. Mishra, I. Singh, P. K. Wattal and D. Das, *Journal of the American Ceramic Society*, 2010, **93**, 3252-3258.
249. S. Madhavi, C. Ferraris and T. White, *J Solid State Chem*, 2006, **179**, 866-872.
250. P. A. Tick, *Journal of the American Ceramic Society*, 1983, **66**, 716-719.
251. J. Leissner, K. Sebastian, H. Roggendorf and H. Schmidt, *Materials Science Forum*, 1991, **67-68**, 137-142.
252. C. C. Pavel, M. Walter, P. Poml, D. Bouexiere and K. Popa, *J Mater Chem*, 2011, **21**, 3831-3837.
253. W. M. Haynes, D. R. Lide and T. J. Bruno, *CRC handbook of chemistry and physics : a ready-reference book of chemical and physical data*, 2015.
254. R. Pflieger, L. Lefebvre, M. Malki, M. Allix and A. Grandjean, *Journal of Nuclear Materials*, 2009, **389**, 450-457.
255. W. Lutze, W. Gong, F. C. Perez-Cardenas, K. S. Matlack, I. L. Pegg and P. Schill, *Glass Technol-Part A*, 2007, **48**, 263-275.
256. M. Puyou, N. Jacquetfrancillon, J. P. Moncouyoux, C. Sombret and F. Teulon, *Nucl Technol*, 1995, **111**, 163-168.
257. A. Sakai, H. Koikegami, N. Miura and E. Ochi, *International Conference on Nuclear Engineering, Proceedings, ICONE*, 2014, **4**.
258. P. Schill, W. Lutze, W. Gong and I. L. Pegg, *Glass Technol-Part A*, 2007, **48**, 276-289.
259. H. D. Schreiber, F. A. Settle, P. L. Jamison, J. P. Eckenrode and G. W. Headley, *J Less-Common Met*, 1986, **115**, 145-154.
260. S. R. Butler and J. L. Gillson, *Mater Res Bull*, 1971, **6**, 81-&.
261. C. E. Boman, *Acta Chem Scand*, 1970, **24**, 116-&.

262. J. M. Fletcher, W. E. Gardner, B. F. Greenfield, M. J. Holdoway and M. H. Rand, *J Chem Soc A*, 1968, DOI: DOI 10.1039/j19680000653, 653-+.
263. R. Pflieger, M. Malki, Y. Guari, J. Larionova and A. Grandjean, *Journal of the American Ceramic Society*, 2009, **92**, 1560-1566.
264. H. G. Wiedemann and G. Bayer, *Chemtech*, 1977, **7**, 381-389.
265. G. Roth and S. Weisenburger, *Role of Noble Metals in Electrically Heated Ceramic Waste Glass Melters*, Forschungszentrum Karlsruhe, Institut für Nukleare Entsorgung (INE), 2003.
266. M. Kelm, B. Oser, B. Luckscheiter, W. Bernotat and H. Pentinghaus, *High Level Radioactive Waste and Spent Fuel Management*, 1989, 171-176.
267. P. Hrma, A. A. Kruger and R. Pokorny, *Journal of Non-Crystalline Solids*, 2012, **358**, 3559-3562.
268. S. Weisenburger, *IHI-KIT/INE Meeting/Workshop*, 2016.
269. I. C. f. D. Data, ICDD, <http://www.icdd.com/>, (accessed 03.03.17).
270. Thieme Römpf Lexikon, <https://roempp.thieme.de/roempp4.0/do/data/RD-14-00448>, (accessed 02.02.17).
271. I. M. G. Dos Santos, R. C. M. Moreira, A. G. De Souza, E. R. Leite, J. A. Varela and E. Longo, *InterCeram: International Ceramic Review*, 2003, **52**, 268-275.
272. L. B. Deng, X. F. Zhang, B. W. Li, X. L. Jia, M. X. Zhang, S. L. Ouyang and H. Li, *Rengong Jingti Xuebao/Journal of Synthetic Crystals*, 2015, **44**, 3133-3139 and 3171.
273. K. KAWAI, T. FUKUDA, Y. NAKANO, K. TAKESHITA, Y. MIURA and N. KANEHIRA, *Proceedings of Global 2015*, 2015.
274. G. Roth, personal communication.
275. A. F. Holleman and E. Wiberg, *Lehrbuch der anorganischen Chemie*, de Gruyter, Berlin [u.a.], 2007.
276. M. H. Langowski, J. G. Darab and P. A. Smith, *Volatility Literature of Chlorine, Iodine, Cesium, Strontium, Technetium, and Rhenium; Technetium and Rhenium Volatility Testing - PNNL-11052*, Pacific Northwest National Laboratory, Richland, 1996.
277. M. E. Vol'pin, *Soviet Scientific Reviews, Section B - Chemistry Reviews*, harwood academic publishers, Amsterdam, 1981.
278. *Chemical Thermodynamic of Technetium*, Elsevier, 1990.
279. W. Lukas and M. Gaune-Escard, *The Journal of Chemical Thermodynamics*, 1982, **14**, 593-597.
280. K. Schwochau, *Radiochim Acta*, 1983, **32**, 139-152.